A MULTI-STACK FRAMEWORK IN MAGNETIC RESONANCE IMAGING

A Thesis
Presented to
The Academic Faculty

by

Richard Z. Shilling

In Partial Fulfillment
of the Requirements for the Degree
Doctor of Philosophy in the
School of Electrical and Computer Engineering

Georgia Institute of Technology
May 2009

A MULTI-STACK FRAMEWORK IN MAGNETIC RESONANCE IMAGING

Approved by:

Dr. Marijn E. Brummer, Co-advisor
School of Electrical and Computer Engineering
Georgia Institute of Technology

Dr. Russell M. Mersereau, Co-advisor
School of Electrical and Computer Engineering
Georgia Institute of Technology

Dr. Aaron D. Lanterman
School of Electrical and Computer Engineering
Georgia Institute of Technology

Dr. Allen R. Tannenbaum
School of Electrical and Computer Engineering
Georgia Institute of Technology

Dr. Justin Romberg
School of Electrical and Computer Engineering
Georgia Institute of Technology

Date Approved: May 1 2009

To my parents, Eleanor and Norman Shilling.

To my sister and her family, Beth, Neil, Emily, and Sydney Peraza.

To my family friend, Gary Annett.

ACKNOWLEDGEMENTS

I would like to thank my advisor, Marijn Brummer, for his guidance, support, and patience.

I would like to thank the Emory University School of Medicine, Departments of Pediatrics and Radiology for making their facilities available.

I would like to thank my co-advisor, Russell Mersereau, for his help at Georgia Tech.

I would also like to extend special thanks to Greg Krudysz, Brendan Sullivan, and Loran Jatunov for their help and support.

I would also like to thank Jim Chrencik, Chris Alvino, Trevor Robbie, Senthil Ramamurthy, Klaus Mewes, Rosa Younessi, Jee Choi, Nicole Tendon, Jennifer Alexander, and Walter Huang.

TABLE OF CONTENTS

LIST OF TABLES

LIST OF FIGURES

SUMMARY

Magnetic resonance imaging (MRI) is the preferred imaging modality for visualization of intracranial soft tissues. Surgical planning, and increasingly surgical navigation, use high resolution 3-D patient-specific structural maps of the brain. However, the process of MRI is a multi-parameter tomographic technique where high resolution imagery competes against high contrast and reasonable acquisition times.

Resolution enhancement techniques based on super-resolution are particularly well-suited in solving the problems of resolution when high contrast with reasonable times for MRI acquisitions are needed. Super-resolution is the concept of reconstructing a high resolution image from a set of low-resolution images taken at different viewpoints or foci. The MRI encoding techniques that produce high resolution imagery are often sub-optimal for the desired contrast needed for visualization of some structures in the brain.

A novel super-resolution reconstruction framework for MRI is proposed in this thesis. Its purpose is to produce images of both high resolution and high contrast desirable for image-guided minimally invasive brain surgery. The input data are multiple 2-D multi-slice Inversion Recovery MRI scans acquired at orientations with regular angular spacing rotated around a common axis. Inspired by the computed tomography domain, the reconstruction is a 3-D volume of isotropic high resolution, where the inversion process resembles a projection reconstruction problem. Iterative algorithms for reconstruction are based on the projection onto convex sets formalism. Results demonstrate resolution enhancement in simulated phantom studies, and in ex- and in-vivo human brain scans, carried out on clinical scanners. In addition, a novel motion correction method is applied to volume registration using an iterative technique in which super-resolution reconstruction is estimated in a given iteration following motion correction in the preceding iteration. A comparison study of our method with previously published methods in super-resolution shows favorable characteristics of the proposed approach.

CHAPTER I

INTRODUCTION

1.1 Motivation

New therapies for treatment of a variety of neurological disorders require accurate determination of locations within small deep-brain gray matter structures, such as the internal and external parts of the Globus Pallidus, Thalamus, and Sub-Thalamic Nucleus, as shown in Fig. 1 [64, 75, 82]. Such therapies include thermal ablation or implantation of Deep Brain Stimulators at sites in the brain, which are associated with severe symptoms in medically intractable Parkinson's disease, other movement disorders, and more recently also for epileptic disorders. In the future, additional novel treatment methods, using targeted implantation of stem cells and cell lines with neuro-transmitter replacement capabilities, are anticipated to augment these current options.

Magnetic resonance imaging (MRI)[1] is the preferred imaging modality for visualization of intracranial soft tissues. Surgical planning, and increasingly surgical navigation, use high resolution (HR) 3-D patient-specific structural maps of the brain. Commonly, such maps are provided by pre-operatively acquired MRI scans, stereotactically co-registered with a rigid frame attached to the head of the patient. In planning the surgery, the location of a burr hole craniotomy and the approach towards the surgical target structures are determined based on anatomical landmark information from these maps. Surgical navigation for movement disorder surgery employs interactive co-registration of 3-D anatomy from pre-acquired HR MRI with intra-operatively acquired electrophysiological data. Electrical brain activity is recorded at the tip of a micro-electrode along a linear trajectory through the brain. This intra-operative use of pre-acquired non-realtime MRI provides patient-specific structural boundary information and a mechanism to compensate for bulk spatial offsets in the stereotactic MRI registration.

[1] Appendix I lists the acronyms used throughout this work.

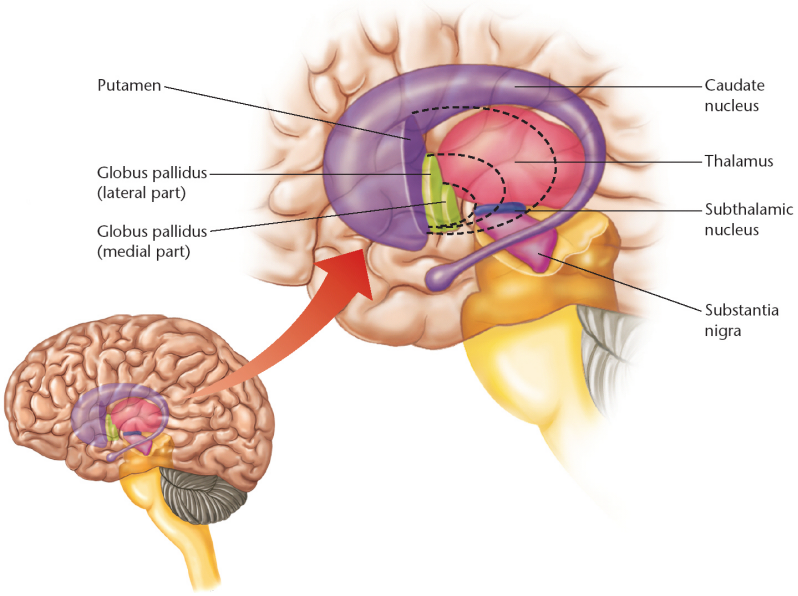

Figure 1: Basal Ganglia region of the brain [1].

However, MRI produces images that are never exactly equal to the true anatomy. The true information is not directly available for measurement. There are trade-offs between timing, spatial resolution, contrast, and signal-to-noise ratio (SNR) in the MRI acquisition process. MRI simultaneously captures the proton density of an object and its magnetization decay or relaxation rates whose different values create image contrast. In the case of delineating the Globus Pallidus internal and surrounding white matter, an acquisition method in MRI, known as Inversion Recovery (IR), is currently the preferred clinical approach for optimized contrast [62]. The minimum slice thickness for such a sequence is 1.5 – 2mm, which presents a challenge for further improvement of targeting accuracy in the associated areas of the brain when used as a navigational map for neuro-surgery.

To overcome the poor resolution associated with high contrast IR MRI acquisitions, algorithms for resolution enhancement have been explored based on super-resolution (SR) techniques [10, 27, 30, 56, 57]. Super-resolution reconstruction (SRR) creates an estimate of an unaliased HR image (HRI) from several observed and aliased low-resolution images (LRIs) of the same scene, taken either simultaneously or sequentially at different viewpoints or foci. The differences between the LRIs contribute information to the reconstruction process. The resultant estimate of the HRI can then exceed the Nyquist rate of the imaging

sensor. When the imaging sensor technology is limited to trade-offs, as in the case for MRI, exceeding the Nyquist limit of the sensor makes SR an ideal candidate for resolution enhancement. Potential cost benefits of using multiple LRIs instead of one HR imaging system also makes SR an attractive alternative to improving the available sensor hardware.

Prior to their application for MRI, SR techniques were applied to imagery from charged-coupled device cameras. Such techniques have been well-studied. Numerous SRR algorithms have gained interest because of the improving computational feasibility of these demanding, usually iterative, methods. An overview of SR is in [53, 39]. SR not only includes recovering a HRI from LRIs, but it can also include compensation for aspects of motion between the LRIs. Typically, these are treated as separate problems. However, coupling motion estimation and SR has been applied in some numerical experiments [47]. Advantages of coupling these problems together depend partly on their individual complexity.

1.2 Outline of thesis

This thesis presents a SR technique for MRI based on a novel sampling configuration that combines both high resolution and contrast otherwise not available in MRI. Chapter 2 explains MRI and its spatial resolution limitations. It includes a chronology of previous SR experiments applied to MRI that highlights its atypical signal processing aspects relative to other imaging methods. Chapter 3 presents a novel extension of this study from existing SR techniques for MRI that defines a sampling configuration known as Multi-Stack (MS). The estimation of the HRI is cast into a Bayesian framework, and iterative algorithms derived from computed tomography, which MS model resembles, are applied. Maximum-likelihood estimators based on this technique are derived that impose known conditions. A validation study is presented in Chapter 4. Its purpose is to show feasibility of MS in the clinical setting for surgical navigation applications. Chapter 4 also includes simulating the forwarding model so that extraneous unknown error in the input data is ruled out. MS is also validated on real multi-slice MRI-type data and comparisons are made of a SRR result and one single acquisition with equivalent resolution. Chapter 5 discusses algorithms for motion correction

in-between LRIs. The algorithms include intensity and mutual information metrics that are then applied to real multi-slice MRI data that are known to have motion between LRIs. In general, SRR is an ill-posed problem. Chapter 6 incorporates an image prior on the HR estimate by using Tikohonov regularization to make the SRR more stable from numerical anomalies. Chapter 6 continues with comparisons between the MS and the traditional SR technique. Conclusions are presented in Chapter 7 with recommendations on areas for future work.

1.3 Specific Contributions

Our specific contributions made in this body of work are as follows.

- A new sampling strategy is proposed for SR in MRI. Previous SR constructs have assumed translational motion whereas this thesis contributes to a new observation model.
- A novel algorithm for constructing the matrix in the SR forwarding model is derived, for which approximation error can be directly controlled.
- A formal maximum-likelihood estimator is derived for using complex-valued MRI data.
- An adaptation of standard computed tomography algorithms based on projection reconstruction algorithms and their application to the new sampling model is presented.
- A feasibility study of the new SR technique using simulated experiments with parametric variation is validated.
- A head-to-head experimental performance comparison between MS SR and traditional MRI SR is given. Observations from singular value decomposition are also given.
- An application of Tikhonov regularization for maximum a-posteriori estimation in SR is given.
- Motion is intermittently estimated with the SR problem. The novelty is based on the application of an existing matching metric not previously applied to SR.

- A validation study consisting of seven real scans, which includes measuring edges of the SRR and LRI in each study is given. Results demonstrate high quality images that are faithfully reconstructed.

CHAPTER II

BACKGROUND

MRI is a non-linear multi-parameter imaging system with working principles based on quantum mechanics. Using nuclear magnetic resonance signals, the internal physical and chemical characteristics of an object can be imaged. Lauterbur and Liang describe MRI in useful signal processing terms [44]. This chapter summarizes only the main steps in MRI. For more detail we refer to [76, 44]. In particular, this chapter explains the limitations of spatial resolution, image contrast, and signal-to-noise ratio (SNR) in MRI. The second part of the chapter explains SR with a chronology of related SR experiments for MRI.

2.1 MRI Fundamentals

Magnetic fields and radio frequency (RF) waves are applied to the object for imaging. These magnetic fields are controlled, manipulated, and then detected into an image that can be explained by the high-level linkage in [44]:

$$u \rightarrow \mathbf{M} \rightarrow \mathbf{M}_{xy} \rightarrow S(t) \rightarrow S(\boldsymbol{k}) \rightarrow y(\boldsymbol{s}). \tag{1}$$

Microscopic magnetic moments, i.e., protons, of the object to be imaged, u, are exposed to a homogeneous magnetic field, $\mathbf{B}_0$, creating a bulk magnetization, $\mathbf{M}$, as shown in Fig. 2. These magnetic moments precess at the Larmor frequency, ω_0, which is proportional to the magnetic field strength. When an external RF pulse is applied, the protons sharing the precessional frequencies with the frequency band of the RF pulse are governed by the Bloch differential equations [80]. These magnetic moments become excited and tip away from their equilibrium state of alignment with $\mathbf{B}_0$ to create a coherent transverse magnetization, $\mathbf{M}_{xy}$. When the RF pulse is turned off, the magnetic moments thermally relax to a lower energy state by precessing back and re-aligning with $\mathbf{B}_0$. Relaxation generates new RF waves coming from the magnetic moments with a frequency equal to their Larmor frequency, which are then detected through induction on a receiving coil, $\mathbf{M}_{xy} \rightarrow S(t)$. The process,

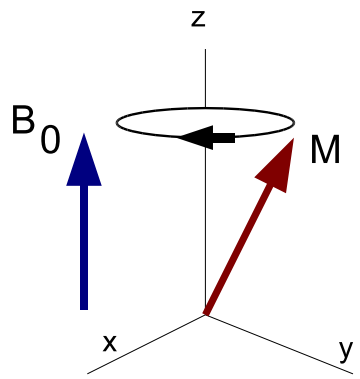

Figure 2: A magnetic moment, $\mathbf{M}$, precessing around the direction of the external magnetic field $\mathbf{B}_0$.

$S(t) \rightarrow S(\boldsymbol{k})$, is central to MRI during relaxation. An additional magnetic field with a gradient, $\mathbf{G} = (\mathbf{G}_x, \mathbf{G}_y, \mathbf{G}_z)$, is superimposed onto $\mathbf{B}_0$ so that the effective magnetic field at spatial location, $\mathbf{s} = (\mathbf{s}_x, \mathbf{s}_y, \mathbf{s}_z)$ is

$$\mathbf{B}(\mathbf{s}) = \mathbf{B}_0 + (\mathbf{G}_x\mathbf{s}_x, \mathbf{G}_y\mathbf{s}_y, \mathbf{G}_z\mathbf{s}_z). \tag{2}$$

This magnetic field yields a linear spatially varying precessional frequency along the direction of $\mathbf{G}$ so that

$$\omega_0(\mathbf{s}) = \gamma||\mathbf{B}(\mathbf{s})||, \tag{3}$$

where γ and $||.||$ denote the gyromagnetic ratio and magnitude, respectively. The phase component, ϕ, of the complex-valued magnetization is the integral over time in angular velocity, i.e., precessional frequency. In a system with a time-dependent magnetic field gradient, $\mathbf{G}(t)$, the phase of the magnetization becomes

$$\begin{aligned} \phi(\mathbf{s}, t) &\propto \int_0^t \gamma \left\langle \mathbf{G}(\tau), \mathbf{s} \right\rangle d\tau & (4) \\ &= \gamma \left\langle \int_0^t \mathbf{G}(\tau)\, d\tau, \mathbf{s} \right\rangle & (5) \\ &= \gamma \left\langle \boldsymbol{k}(t), \mathbf{s} \right\rangle, & (6) \end{aligned}$$

where

$$\boldsymbol{k}(t) = \int_0^t \mathbf{G}(\tau)\, d\tau, \tag{7}$$

Table 1: Relative Echo (T_E) and Repetition (T_R) times needed to weigh the appropriate parameter.

$T_E \in [20, 100]$ msec	$T_R \in [250, 3000]$ msec	Image Weighting
short	long	ρ
short	short	T_1
long	long	T_2

and $\langle ., . \rangle$ denotes the inner product. The measured signal, $S(t)$, is a superposition of all magnetic moments emitting RF waves during relaxation so that it becomes

$$S(t) \propto \int_{\Omega_u} \rho(\mathbf{s}) e^{-i2\pi \langle \boldsymbol{k}(t), \mathbf{s} \rangle} \, d\mathbf{s}, \tag{8}$$

where Ω_u is the region of space containing only the excited magnetic moments and $\rho(\mathbf{s})$ is the magnitude of the magnetization, also known as the proton density function. Effectively, $\boldsymbol{k}(t)$ are a specified subset of locations for the Fourier samples of $\rho(\mathbf{s})$, which are controlled by both the time and the gradient of the magnetic field. Hence, $\boldsymbol{k}$-space is synonymous with Fourier space. The sampling of locations and their values, $S(\boldsymbol{k})$, given by Eq. (7), is known as $\boldsymbol{k}$-space traversal. The Fourier image reconstruction process is represented by the final thread, $S(\boldsymbol{k}) \rightarrow y(\boldsymbol{s})$, where $y(\boldsymbol{s})$ is the resultant image.

In addition to the proton density function, the signal acquired is exponentially weighted by the different decay rates of magnetic relaxation, which are crucial in delineating contrast among anatomical structures like cerebral spinal fluid, gray and white brain matter [19]. These decay rates are the T_1 and T_2 values of a proton that characterize the longitudinal recovery (spin-lattice) and transverse de-phasing times (spin-spin) of the magnetization, respectively:

$$S(t) \propto \rho(1 - e^{-t/T_1}) e^{-t/T_2}. \tag{9}$$

Different locations with different parameter values create image contrast. Associated with a particular acquisition in $S(t) \rightarrow S(\boldsymbol{k})$ are timing variables weighting the three parameters of the image in Eq. (9). Two timing variables known as the echo (T_E) and repetition (T_R) times weight the parameters of the object differently, as shown in the Table 1. T_E is the time between an RF excitation and the signal acquisition, while T_R is the time period between two consecutive RF excitations.

Using Eq. (7), the magnetic moments can be either frequency- or phase-encoded by a correspondence of spatial locations and linear magnetic field gradients. The spatial resolution of MRI is intrinsically linked to the time duration of the acquisition. This is because $\boldsymbol{k}$-space is sampled over time and thus $\boldsymbol{k}(t)$ is limited to the T_1 and T_2 exponential decay rates given in Eq. (9). Thus, the total number of samples is bounded by a time window, T_{acq}. In general, the mapping relationship of $\boldsymbol{k}$-space and time is either

$$\boldsymbol{k}(t) \propto \int_0^t \mathbf{G}_{fe}(\tau) d\tau \tag{10}$$

or

$$\boldsymbol{k} \propto \int_0^{T_{pe}} \mathbf{G}_{pe}(\tau) d\tau, \tag{11}$$

where fe and pe denote the frequency- and phase-encoding directions, respectively, for the magnetic field gradient. There are numerous sampling patterns, i.e., $\boldsymbol{k}$-space traversals. For instance, one common type of $\boldsymbol{k}$-space coverage in 2-D imaging involves using frequency- and phase-encoding along the x- and y-direction, respectively. Specifically,

$$\boldsymbol{k}_x = \mathbf{G}_x t \tag{12}$$

$$\boldsymbol{k}_y = n \Delta \mathbf{G}_y T_{pe}, \tag{13}$$

where n refers to the n^{th} RF excitation. $\Delta \mathbf{G}_y$ is the change in magnetic field strength for the phase-encoding gradient between two consecutive RF excitations. The sequence of events for this spatial encoding is given as a timing diagram in Fig. 3 with its corresponding $\boldsymbol{k}$-space traversal pattern given in Fig. 4. The varying phase-encoding strength puts the frequency-encoding readout line along the direction of the $\boldsymbol{k}_x$-axis at different $\boldsymbol{k}_y$ values.

Fundamentally, the spatial resolution of MRI can be increased by (1) decreasing the field of view (FOV), (2) increasing the number of samples in the frequency-encoding, or (3) increasing the phase-encoding direction(s). The FOV in the Fourier reconstructed image is determined by the sampling density of $\boldsymbol{k}$-space, i.e., Δk. Decreasing the density is limited to the support region of the object to be imaged. The volume can either be selected in its entirety and Fourier encoding spans 3-D, or the volume can be imaged by sequential 2-D imaging techniques.

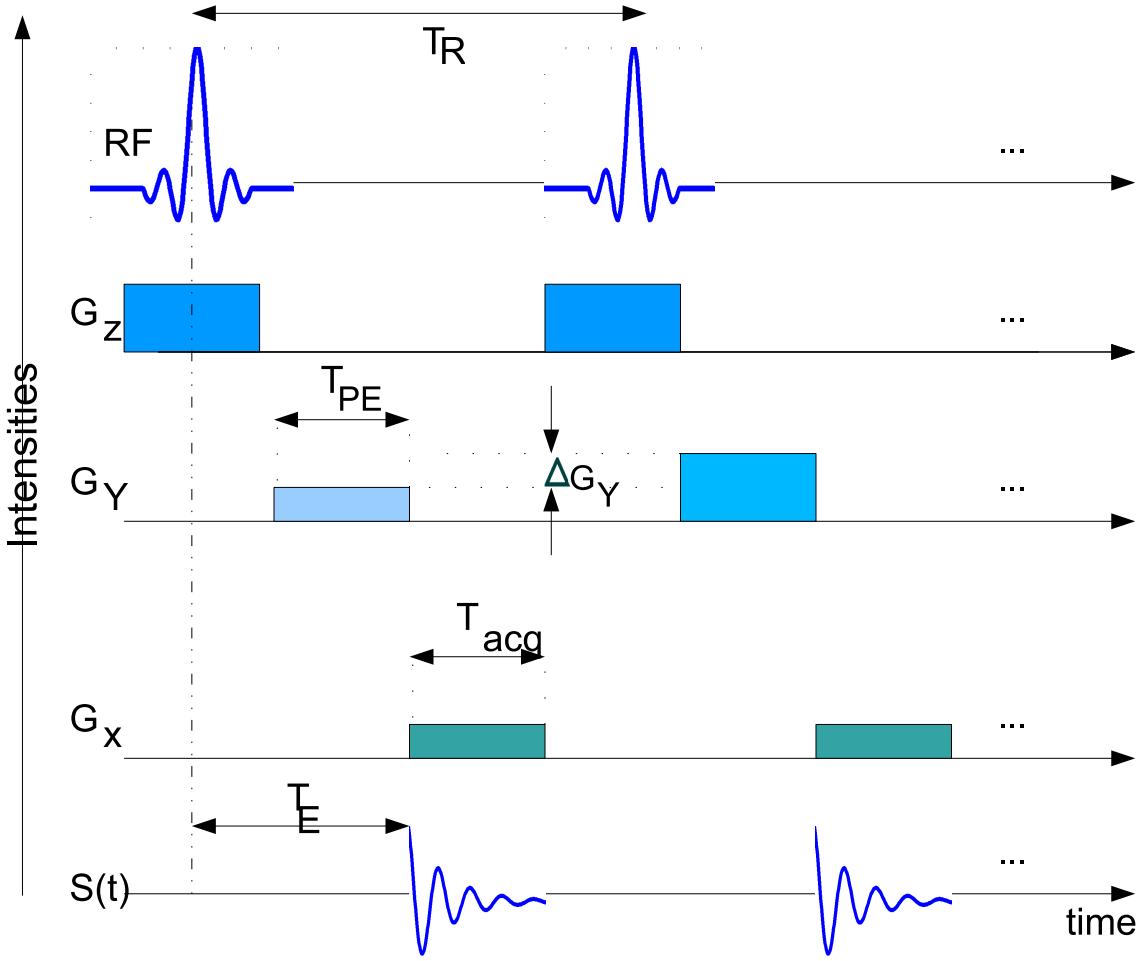

Figure 3: Timing diagram for 2-D $\boldsymbol{k}$-space traversal. (1) An RF pulse is simultaneously applied during presence of a magnetic field gradient, $\mathbf{G}_z$, for excitation. (2) Selected magnetic moments excite. (3) Selected magnetic moments relax. (4) During relaxation, a varying phase-encoding gradient, $\mathbf{G}_y$, and constant frequency-encoding gradient, $\mathbf{G}_x$, is then applied for signal acquisition, $S(t)$. T_E is the time between the RF excitation and signal acquisition. T_R is the time between two consecutive RF excitations. $\Delta\mathbf{G}_y$ is the change in magnetic field strength for the phase-encoding gradient between two consecutive read-out lines. T_{acq} is the time window of acquisition for the frequency-encoded samples. The corresponding $\boldsymbol{k}$-space traversal is given in Fig. 4.

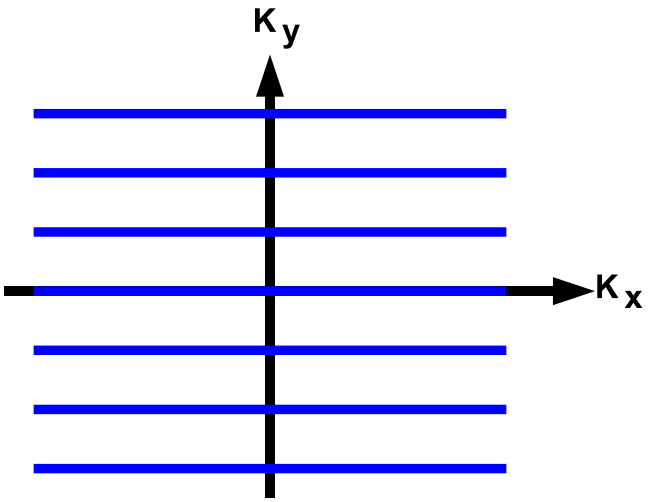

Figure 4: $\boldsymbol{k}$-space traversal pattern for Fig. 3 (denoted in blue). $\boldsymbol{k}_x$ and $\boldsymbol{k}_y$ is frequency- and phase-encoded, respectively. One repetition gives the samples of $\boldsymbol{k}_x$-space along a constant value $\boldsymbol{k}_y$, i.e., a read-out line.

2.2 Spatial Encoding in MRI

2.2.1 3-D Methods

In true 3-D MRI, the bulk magnetization of an entire imaging volume is selected onto the transverse plane and gradient encoding is applied in all three dimensions. Thus, ***k***-space is 3-D. The complex phase evolution under the extent of the gradient defines the ***k***-space traversal and it must include at least one dimension that is frequency-encoded, while the other two can be either phase- or frequency-encoded. This is notably different from the 2-D imaging process shown in Fig. 3. The RF pulse is nonselective and it is unnecessary to include a magnetic field gradient, $\mathbf{G}_z$, during the excitation phase. However, the z-dimension must include a magnetic field gradient, which is applied simultaneously with the $\mathbf{G}_y$ gradient for T_{PE} seconds. Its strength also varies for the different RF excitations as a way to Fourier encode spatial information.

Referring to Table 1, short T_R times are needed for T_1-weighted image contrast. This results in a smaller time window, T_{acq}, for ***k***-space traversal at the cost of strength in the acquired signal. Conversely, for T_2-weighted imaging, true 3-D is difficult to obtain in a reasonable imaging time because of the long repetitions between excitations. Other problems of true 3-D MRI include a dynamic range of values across the volume that creates quantization error during digitization and thus decreases SNR [48].

2.2.2 Multi-slice Methods

In 2-D multi-slice MRI, a stack of thin slices are sequentially collected through multiple RF excitations and magnetic field gradients. Unlike true 3-D, the magnetic field applied during the acquisition stage of RF pulse excitation in 2-D multi-slice includes a linear gradient component. Then, the desired slice to excite may be expressed in terms of a bandlimited RF pulse. A Fourier relationship exists between the profile of the slice to select and the RF pulse. However, the finite imaging time limited by the T_1 and T_2 decay rates prevents a sinc pulse of infinite duration for an ideal box slice selection profile. Consequently, a temporal truncation of the RF pulse gives an undesired non-uniform weighting or profile of the slice. Truncation effects are shown in Fig. 5.

Within the 2-D plane, data is sampled in the frequency domain; one direction is frequency encoded and the other is either phase- or frequency-encoded. The number of frequency-encoded samples is limited by T_2 times, and extending the sampling significantly beyond this time decreases the SNR, thus limiting the frequency bandwidth. The time between the RF excitation and its corresponding signal echo suffers from a latency long enough to include a subsequent RF excitation for a different imaging plane within the duration of the repetition (T_R). In practice, an acquisition technique, known as interlacing, excites the next slice while the current slice is completing T_1 relaxation before the next repetition (T_R). This method of interlacing allows for significant scan time reduction that can be achieved in clinical practice without a loss in image SNR or contrast [20]. Albeit, there are overlapping slices that contribute to each other's slice selection profiles. To circumvent this so-called cross-talk artifact, slice gaps are often inserted at the cost of increased slice widths [44].

The 2-D multi-slice Fast Spin Echo Inversion Recovery (FSE-IR) acquisition has been compared with other competing MRI acquisitions for brain imaging, such as the gradient-echo or fast field echo sequences [62]. In IR, magnetic spins are forced in the opposite direction or 180° from the main magnetic field vector, so the duration of the longitudinal relaxation is maximized. The time between the 180° excitation and the 90° rotation is the inversion time, T_I. Re-phasing by the 180° RF pulse allows acquisition of another $\boldsymbol{k}$-space line within the same T_R time. The re-phasing of magnetic spins may be repeated while longitudinal recovery continues and is known as the echo train length. Likewise in FSE, magnetic spins are re-phased so that the duration of the transverse relaxation is maximized. An echoing effect is produced by applying another RF pulse that rotates the magnetic spins 180° around the y-axis. Figures 7 and 6 illustrate these new effects.

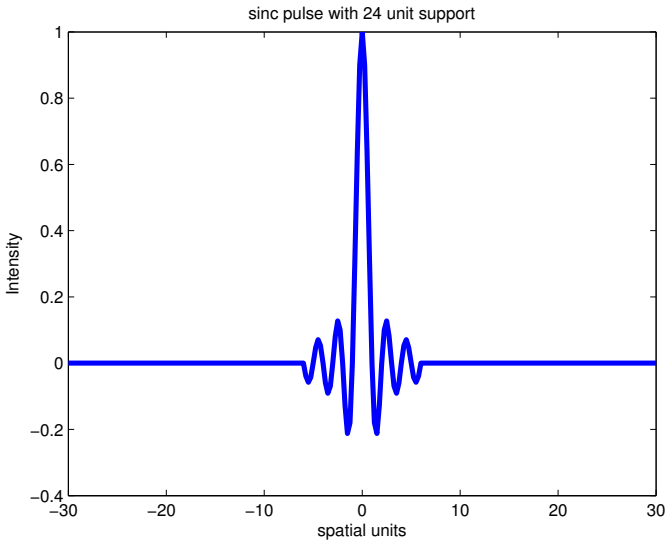

(a)

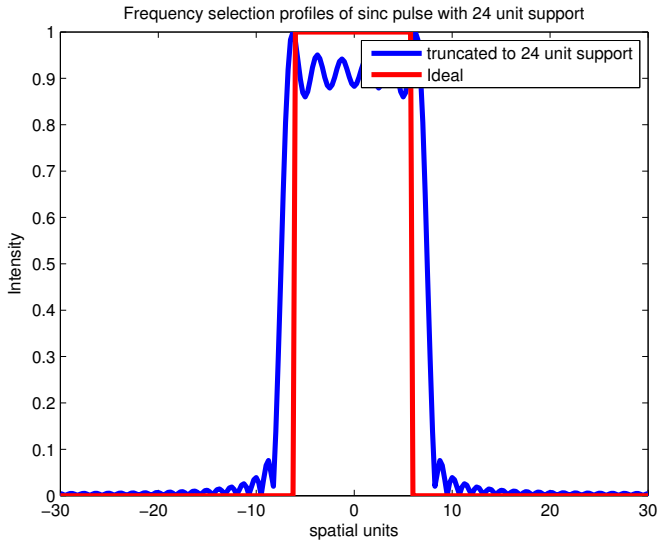

(b)

Figure 5: Effects of truncating a (a) sinc pulse to 24 support units (b) with its frequency selection profile with ideal selection pulse

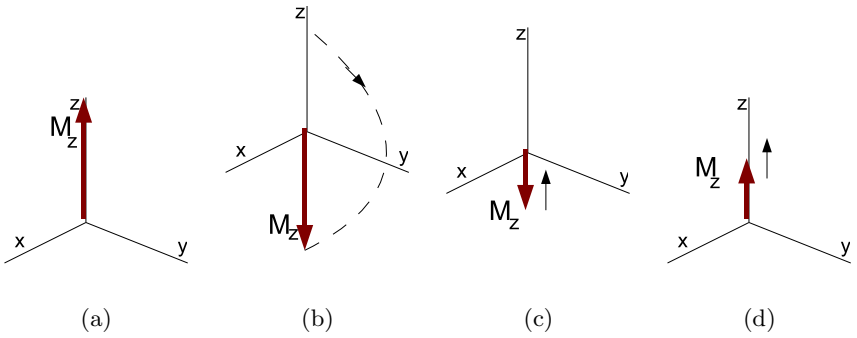

Figure 6: Inversion Recovery (IR) effect with longitudinal magnetization component, M_z, of a spin: (a) immediately before excitation, (b) immediately after excitation (180° flip angle), (c) during relaxation, (d) finishing relaxation.

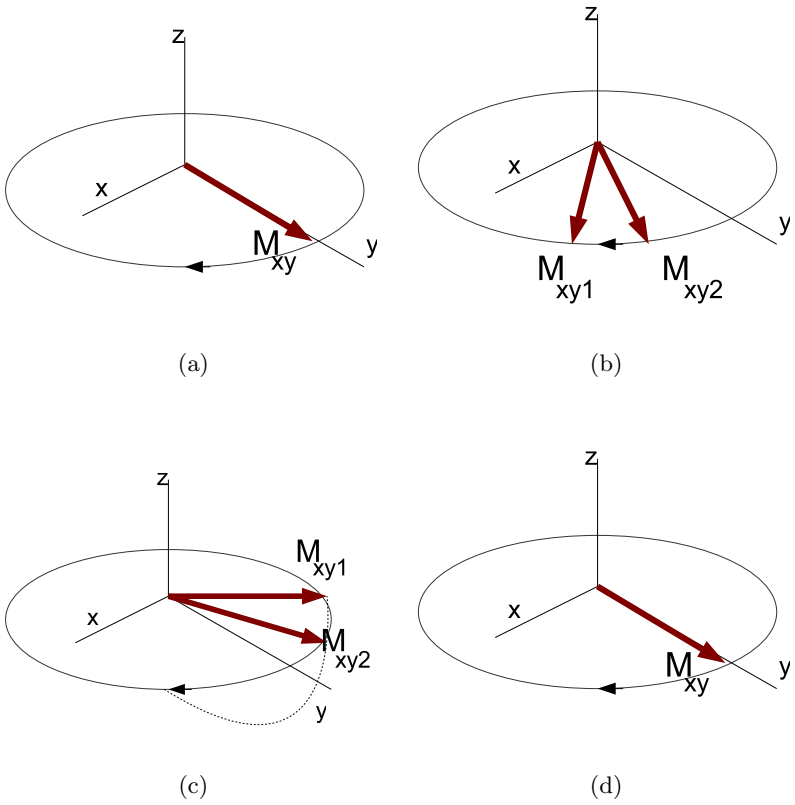

Figure 7: Spin Echo (SE) effect with transverse magnetization components of two spins of different magnetic properties overlayed with each other, M_{xy1} and M_{xy2}: (a) immediately after excitation (M_{xy1} and M_{xy2} are initially aligned), (b) during relaxation (precessional frequency of M_{xy1} faster than M_{xy2}), (c) immediately after echo pulse (i.e., M_{xy1} and M_{xy2} rotated around y-axis) (d) during further relaxation (i.e., M_{xy1} and M_{xy2} re-align for echo effect).

2.2.3 Hybrid Methods

A hybrid approach, using a multiple overlapping thin slab acquisition (MOTSA) to combine high resolution 3-D encoding with interleaved timing of multi-slice imaging, has been used successfully for angiographic applications. Angiography images fluids that have long T_2 times and are relatively insensitive to noise by the nature of commonly used maximum intensity projection algorithms used for viewing [54, 16]. Maximum intensity projection algorithms are visualization methods for 3-D data that only render those voxels along a ray having the maximum intensity. In MOTSA, the time lost waiting for a true 3-D T_2-weighted signal is avoided by providing excitation and acquisition parallelism to sub-volumes similar to the multi-slice imaging. The intention is to combine the HR from 3-D MRI with high contrast from 2-D multi-slice FSE-IR MRI. MOTSA may also be applied as an FSE-IR acquisition, but instead of imaging slices, slabs or sub-volumes are excited and acquired. Unfortunately, new image artifacts persist. The overlapping areas of neighboring slabs experience irregular RF excitation, causing cross-talk interference. The result is a non-uniform profile along the slab-select dimension, causing deterioration in signal power at its edges. The samples collected in the slab-select dimension are truncated, which contributes to a wider point spread function (PSF) [25]. For more complex and sensitive contrast requirements, like the visualization of dilute gray matter nuclei embedded within white matter, early experiments using MOTSA yielded very low SNR, inconsistent contrast and signal intensity across the thin slabs, and substantial additional penalties in imaging time to further increase overlap in the slabs to ameliorate these effects. A MOTSA and 2-D multi-slice acquisition using FSE-IR were acquired on an in-vivo subject as an experiment to illustrate some of these effects. Our results in Fig. 8 show an axial view of a MOTSA scan that highlights some of the mentioned artifacts and compares with Multi-Stack technology introduced in this document. Table 2 gives the SNR and scan times measured from two acquisitions. Inconsistent signal intensity from slab boundary artifacts between two neighboring MOTSA slices is apparent, as shown in Figs. 9(a) and (b). A recently proposed method for reducing slab boundary artifacts may eventually contribute to improved consistency of image intensities across the slab, but has not been demonstrated for IR pulse

sequences to date and does not offer improvement of SNR [45].

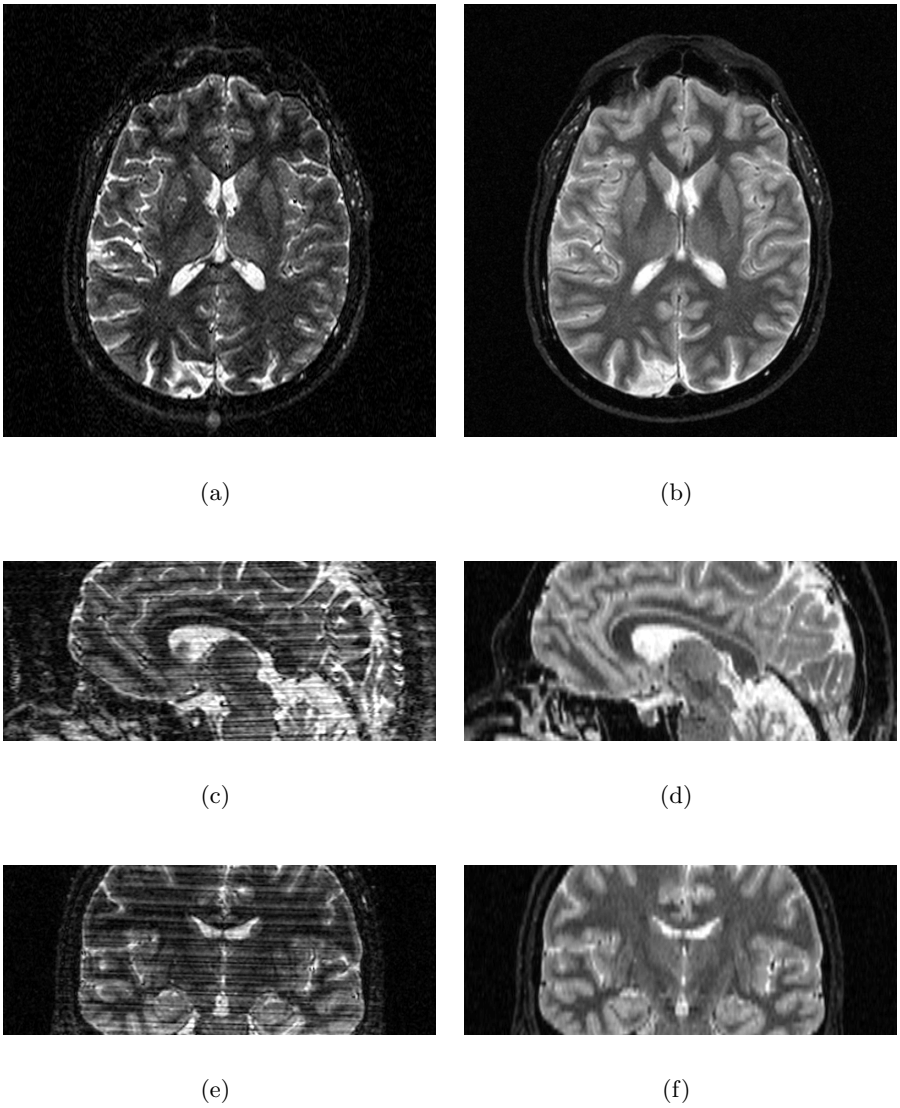

Figure 8: Preliminary Results: MOTSA and 2-D multi-slice both using FSE-IR. Magnitude images of an in-vivo subject: Axial views of a (a) MOTSA, pixel size = $0.43 \times 0.43 mm^2$, (b) 2-D multi-slice, pixel size = $0.43 \times 0.43 mm^2$; sagittal views of a (c) MOTSA, pixel size = $0.43 \times 0.80 mm^2$, (d) 2-D multi-slice, pixel size = $0.43 \times 2 mm^2$; coronal view of a (e) MOTSA, pixel size = $0.80 \times 0.43 mm^2$, (f) 2-D multi-slice, pixel size = $2 \times 0.43 mm^2$

2.3 MRI of deep-brain structure for image-guided neurosurgery

The three different MRI methods of 3-D, 2-D multi-slice, and MOTSA each have their own unique advantage for brain imaging. Two-dimensional multi-slice MRI has been shown to generate greater T_1 contrast than other sequences and is more useful for differentiation

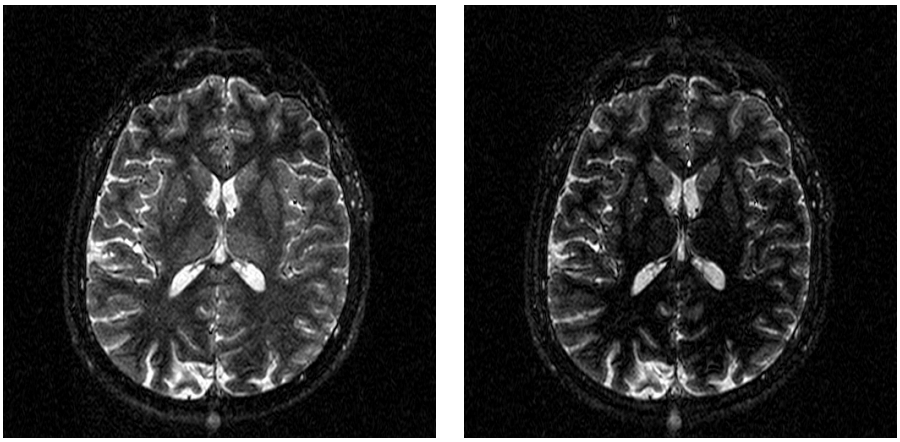

(a) (b)

Figure 9: Axial views of two neighboring MOTSA magnitude image slices separated 2 mm apart, pixel size = $0.43 \times 0.43 mm^2$.

Table 2: Measured SNR and scan times of two MRI acquisitions.

Acquisition	SNR	voxel size (mm^3)	Resolution	Time(min:sec)
MOTSA	26	$0.43 \times 0.43 \times 0.80$	$512 \times 512 \times 120$	6:00
Multi-slice FSE-IR	66	$0.43 \times 0.43 \times 2.0$	$512 \times 512 \times 52$	2:36

of tissues having similar spin density and T_2 values but slightly different T_1 values [62]. For clinical use in brain scanning, the pre-operative scan is acquired in the axial direction to cover the whole brain and takes 15 minutes to scan for the desired SNR, as shown in Fig. 10. Reich et al. compared this FSE-IR scanning protocol with other previously used protocols to assess differences in contrast and contrast-to-noise ratios, i.e., mean intensity difference of two regions, in the region of the Globus Pallidus [62]. The parameters of the FSE-IR acquisition given in Table 3 give one of the most favorable contrast mechanisms known. Three-dimensional MRI can provide HR imagery but for T_1 weighted contrast. In contrast, multi-slice methods yield poor resolution across the slice selection direction. The slice thickness is inversely related to the magnetic gradient strength and RF pulse duration. Narrowing the slice thickness through stronger magnetic gradients has been shown to increase geometric distortions in the reconstructed image [24, 40]. Otherwise, for those clinical applications that need thin slices, acquisitions may have to perform signal averaging to increase SNR. These adverse factors in the slice-selective direction result in anisotropic

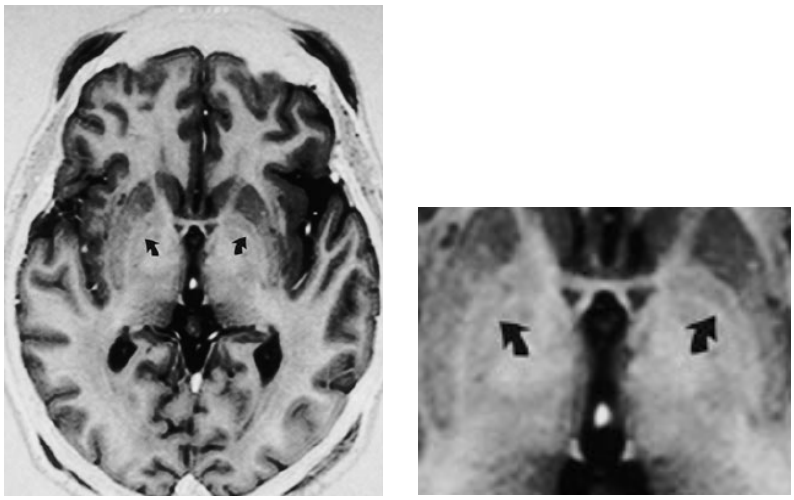

(a) (b)

Figure 10: (a) Axial images from the 2-D multi-slice FSE-IR acquisition ($2mm$ slice thickness) (b) Interpolated close up of Globus Pallidus [62].

resolution, which is problematic for visualizing white matter fibers in brain disease imaging [4]. For brain diseases such as Parkinson's Disease, long T_E and T_R times in the acquisition process would promote a useful navigational map for neurosurgery. However, the issue of unreasonable acquisition times for 3-D imaging methods exacerbates the problem of obtaining high resolution [2]. Our initial MOTSA experiment showed a significant variation in the intensity profile, detracting from its effectiveness for navigational mapping in neurosurgery. While 3-D methods are used widely and often successfully, they are not optimal for visualization of the Globus Pallidus and Sub-Thalamic Nucleus structures of the brain. None of these methods fully satisfies the functional requirements needed for image-guided minimally invasive neurosurgery.

Table 3: Parameters of the FSE-IR acquisition used by Reich [62].

Magnet	T_R/T_E (ms)	T_I (ms)	echo train length	slice thickness (mm)
1.5 T	3000/40	200	5	2

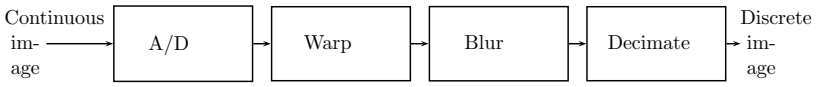

Figure 11: Block diagram of an SR system model.

2.4 Super-resolution in previous work

SR shares some of the same concepts with multi-channel reconstruction [53]. Sub-Nyquist sampling of the HRI introduces aliasing, and the objective is to recover the aliased spatial content to obtain the HRI. In general terms, a continuous image is sampled above the Nyquist rate for a desired unaliased discrete HRI that is then warped and blurred followed by down-sampling and additive noise, as shown in Fig. 11. The warping is typically a one-to-one geometric transformation and the blur comes from the point-spread function (PSF) of the imaging sensor. Decimating causes the effective sub-Nyquist sampling and gives aliasing effects. Deblurring or image restoration reconstructs the original image using a degraded image that shares the same resolution. The SR error is typically contributed by the imaging device and can come from thermal noise, quantization noise, registration noise, etc.

An often-cited SR observation model for Fig. 11 developed by Elad and Feuer (E&F) assumes that each warp, blur, and down-sampling for each of the degradation channels is independent, linear, and space-variant and can be composed into a series of linear transformations [22]. In the E&F model, the r^{th} discrete LRI is lexicographically ordered into the vector $\mathbf{y}_r$. The original continuous image, $x(\mathbf{s})$, is sampled above the Nyquist rate and is also lexicographically ordered into the vector, $\mathbf{x}$, such that

$$\mathbf{y}_r = D_r C_r F_r \mathbf{x} + \mathbf{e}_r \qquad 1 \leq r \leq P, \tag{14}$$

where each matrix is described in Table 4. The decimator, D_r, is the down-sampling rate. C_r is the blur matrix and is Toeplitz when the blur is shift-invariant. If the warp, F_r,

Table 4: Matrices from the SR observation model of Elad and Feuer [22].

Matrix	Description	sizes for 1-D case	sizes for 2-D case
$\mathbf{x}$	discrete unaliased HRI	$N \times 1$	$N_1N_2 \times 1$ or $N \times 1$
$\mathbf{y}_r$	discrete LRI	$M_r \times 1$	$M_{r1}M_{r2} \times 1$
D_r	decimator	$M_r \times N$	$M_{r1}M_{r2} \times N_1N_2$
C_r	blur	$N \times N$	$N_1N_2 \times N_1N_2$
F_r	warp	$N \times N$	$N_1N_2 \times N_1N_2$
e_r	additive noise	$M_r \times 1$	$M_{r1}M_{r2} \times 1$
$\mathbf{y}$	All discrete LRIs	$\sum_{r=1}^{P} M_r \times 1$ or $M \times 1$	$\sum_{r=1}^{P} M_{r1}M_{r2} \times 1$ or $M \times 1$
$\mathbf{e}$	All additive noise	$\sum_{r=1}^{P} M_r \times 1$	$\sum_{r=1}^{P} M_{r1}M_{r2} \times 1$
$\mathbf{H}$	System Matrix	$\sum_{r=1}^{P} M_r \times N$	$\sum_{r=1}^{P} M_{r1}M_{r2} \times N_1N_2$

is unknown, then geometric registration algorithms can be applied for calculating motion estimates so that all the LRIs can be superimposed onto one sampling lattice. Equation (14) can be concatenated over all P LRIs to form the SR problem into one linear problem:

$$\begin{pmatrix} \mathbf{y}_1 \\ \vdots \\ \mathbf{y}_P \end{pmatrix} = \begin{pmatrix} D_1C_1F_1 \\ \vdots \\ D_PC_PF_P \end{pmatrix} \mathbf{x} + \begin{pmatrix} \mathbf{e}_1 \\ \vdots \\ \mathbf{e}_P \end{pmatrix} \tag{15}$$

or

$$\mathbf{y} = \mathbf{H}\mathbf{x} + \mathbf{e}. \tag{16}$$

The direct inversion of $\mathbf{H}$ is computationally infeasible, even for modest sized SR problems. For example, four LRIs with pixel dimensions of 32×128 and a HRI with pixel dimensions of 128×128 is a matrix with 16384 rows and columns. Lower upper matrix decomposition applied to an $n \times n$ matrix takes $O(n^3)$ time, thus requiring approximately $4.4e + 12$ computations in this case [26]. Instead of direct inversion, other methods of SRR must be explored. Generally, the methodologies for determining $\mathbf{x}$ can be classified into three different techniques: frequency domain, interpolation domain, and spatial domain.

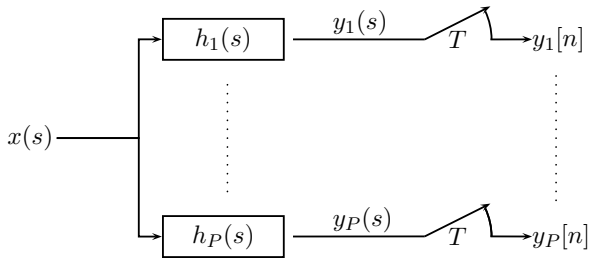

Figure 12: Multi-channel linear shift invariant (LSI) system

2.4.1 Frequency Domain Techniques for Super-resolution

Frequency domain methods transform the LRIs into the frequency domain using the discrete Fourier transform (DFT). The spectral data is combined and the inverse DFT is applied. The sub-Nyquist spatial sampling of the HRI causes overlapping spectrum copies in the spectra of the LRIs. The recovery of the HRI from these spectra depends on the bandwidth of the HRI, the number of LRIs, and the independence of the blurs. Kim et al. derive the relationship for HR recovery explained here [41]. In the frequency domain, the SR observation model is treated as a multi-channel linear shift-invariant (LSI) system with dimensionality reduced to 1-D, as shown in Fig. 12. The conditions that must be satisfied by the σ-bandlimited function, $x(s) : \mathbb{C} \rightarrow \mathbb{C}$, are described with its continuous Fourier transform (CFT), $X(\omega)$:

$$X(\omega) = 0 \quad |\omega| \geq \sigma, \tag{17}$$

$$\frac{1}{2\pi} \int_{-\sigma}^{\sigma} |X(\omega)|^2 d\omega < \infty. \tag{18}$$

Then, the CFT of $y_r(s)$ is

$$Y_r(\omega) = H_r(\omega) X(\omega), \tag{19}$$

where

$$Y_r(\omega) = 0 \quad |\omega| \geq \frac{L}{T} \geq \sigma, \tag{20}$$

for some positive integer L. Assuming that all the LR signals share the same size of M_0 samples using a sub-Nyquist sampling rate of $\frac{1}{T}$:

$$y_r[n] = y_r(nT) \qquad n = 0, ..., M_0 - 1 \qquad r = 1, ..., P. \tag{21}$$

Then, the M_0-point DFT of $\mathbf{y}_r[n]$ is

$$\mathbf{Y}_r^s[l] = \sum_{n=0}^{M_0-1} y_r[n] e^{-j2\pi \frac{ln}{M_0}}, \quad l = 0, ..., M_0 - 1, \quad r = 1, ..., P, \tag{22}$$

and it can be combined with the key aliasing relationship from [49]:

$$\mathbf{Y}_r^s[l] = \frac{1}{T} \sum_{m=-\infty}^{\infty} Y_r(\omega)|_{\omega = \frac{l}{M_0 T} + \frac{m}{T}}. \tag{23}$$

Using the bound from Eq. (20), $Y_r[l]$ is expressed in a finite number of shifted copies from Eq. (23), indicating that the bandwidth, in terms of its counter variable, m, is 2L. In other words, $Y_r[l]$ is expressed with no more than $2L$ combinations of $Y_r(\omega)$ evaluated on

$$\Omega = \left\{ \frac{-L}{T}, \frac{-L}{T} + \frac{1}{M_0 T}, ..., \frac{L}{T} - \frac{1}{M_0 T} \right\}. \tag{24}$$

Subsequent analysis shows PM_0 linear equations from $Y_r[l]$ and $2LM_0$ unknown spectrum values from $Y_r(\omega)|_\Omega$ that must satisfy

$$P \geq 2L, \tag{25}$$

for complete SRR to be possible. Then, recovery of $X(\omega)|_\Omega$ depends only on the invertibility of $H_r(\omega)|_\Omega$. Tsai and Huang were the first to apply these principles toward SRR based on Eq. (25) [32]. They studied uniformly spaced pixel shifts between the LRIs that accounted for neither blur nor noise in the filters:

$$h_r(s) = \delta(s + \phi_r) \qquad \phi_r = \frac{T(r-1)}{P}. \tag{26}$$

Thus, the invertible phase modulations in the Fourier domain permits recovery of $x(s)$. Kim et al. extended their work by introducing both blur and noise using recursive properties from the frequency domain in the reconstruction [41]. Their recursive updating proceeds from an existing solution of a structured smaller set of linear equations. Frequency domain techniques are relatively limited in comparison to interpolation and spatial methods in SRR.

If the degradation blur model becomes shift-variant, then frequency domain methods must be abandoned. Furthermore, if there are any non-linear known spatial constraints, then it is difficult to apply them in this domain.

2.4.2 Interpolation Domain Techniques for Super-resolution

With interpolation-based SRR techniques, a continuous estimate of the HRI, $x(s)$, is weighted by the samples from the LRIs, $\mathbf{y}$. The weighting is expressed by a set of kernel functions, $\{\varphi_r(s)\}_{r=1}^{P}$:

$$\widehat{x}(s) = \sum_{r=1}^{P} \sum_{n=-\infty}^{\infty} y_r(nT)\varphi_r(s - nT). \tag{27}$$

The most commonly used methods are nearest neighbor, linear, cubic, p^{th} order, and spline interpolation. However, these approaches are severely limited in accuracy because they disregard both the noise and blur characteristics caused by the degradation process. Nevertheless, some of these simple methods are often applied and shown in the results of published SR experiments as a way to visually compare performance against another SRR techniques [22]. Only after the samples from the LRIs are interpolated onto an estimate of the HRI is the degradation process addressed.

There have been hybrid interpolation-frequency methods that alternately constrain frequency and spatial information so that the estimate to the HRI has band-limited properties [67]. These techniques share the same underlying principle as the Papoulis-Gerchberg band-limited extrapolation algorithm [51]. That is, if the data is sampled on $\{nT\}_{n=0}^{M_0-1}$, then the l^{th} estimate for $x(s)$ is

$$\widehat{x}^{(l)}(nT) = y(nT) \tag{28}$$

that is then frequency constrained:

$$\widehat{X}^{(l+1)}(\omega) = \left\{ \begin{array}{cc} \widehat{X}^{(l)}(\omega) & |\omega| < \sigma \\ 0 & |\omega| \geq \sigma \end{array} \right\}. \tag{29}$$

In the case of multiple LRIs for SR used in [67], each iteration includes applying the spatial constraint successively from each of the P LRIs.

To account for blurring in interpolation-based SR, Papoulis's generalized sampling expansion (GSE) theorem is applicable [52]. The GSE theorem extends Shannon's sampling

theorem by providing the necessary condition for signal reconstruction from multiple channels when sampled at a fraction of the Nyquist rate [36, 23]. The GSE theorem provides the interpolation kernels needed for reconstruction using the filtered down-sampled available data and has been used in SRR.

Generalized Sampling Expansion Theorem 1 *It is possible to reconstruct a σ-bandlimited signal, $x(s)$, that is passed through P different channels, $h_r(s)$, that are then sampled each at $\frac{1}{P}^{th}$ the Nyquist rate with sampling period, $T = \frac{P}{2\sigma}$, if*

$$\mathbf{H}(\omega) = \begin{pmatrix} H_1(\omega) & ... & H_P(\omega) \\ H_1(\omega + \frac{2\sigma}{P}) & ... & H_P(\omega + \frac{2\sigma}{P}) \\ \vdots & & \vdots \\ H_1(\omega + (P-1)\frac{2\sigma}{P}) & ... & H_P(\omega + (P-1)\frac{2\sigma}{P}) \end{pmatrix} \tag{30}$$

is non-singular $\forall \omega \in [-\sigma, -\sigma + \frac{2\sigma}{P}]$. If so, then if

$$\Phi(\omega, s) = \begin{pmatrix} \Phi_1(\omega, s) \\ \vdots \\ \Phi_P(\omega, s) \end{pmatrix}, \tag{31}$$

is a solution to

$$\mathbf{H}(\omega)\Phi(\omega, s) = \boldsymbol{b}(s), \tag{32}$$

where

$$\boldsymbol{b}(s) = \begin{pmatrix} 1 \\ e^{j\frac{2\sigma}{P}s} \\ \vdots \\ e^{j(P-1)\frac{2\sigma}{P}s} \end{pmatrix}, \tag{33}$$

then the r^{th} interpolation kernel is

$$\varphi_r(s) = \frac{P}{2\sigma} \int_{-\sigma}^{-\sigma+\frac{2\sigma}{P}} \Phi_r(\omega, s) e^{j\omega s} d\omega, \qquad r = 1, ..., P. \tag{34}$$

Thus, the original signal is expressed by

$$x(s) = \sum_{r=1}^{P} \sum_{n=-\infty}^{\infty} y_r(nT)\varphi_r(s - nT), \tag{35}$$

where $y_r(nT)$ is the output from the r^{th} channel.

Brown et al., Sabata et al., and Cheung extended the GSE theorem to multiple dimensions so that it can be readily applied to band-limited imagery [7, 17, 11]. In addition, Cheung et

al. and Brown et al. further investigated the stability and robustness of the interpolation kernels constructed by the GSE when noise is added to the input [12, 7]. In general, this relates to the condition of an inverse problem: how a small error perturbation from the input affects the output. If the total energy from any of the interpolation kernels is infinite, then the GSE reconstruction is ill-posed with respect to error added to the input [12]. A useful result by Brown et al. leads to a sufficient condition for the well-posedness of the GSE theorem [7]:

Corollary to the Generalized Sampling Theorem 1 *The GSE theorem is well-posed if the* $|det(\mathbf{H}(\omega))|$ *given in Eq. (30) is bounded away from zero on* $-\sigma < \omega < -\sigma + \frac{2\sigma}{P}$.

Hence, the uniform delays used previously by Kim et al. result in a well-posed matrix so that

$$|det(\mathbf{H}(\omega))| = |\prod_{i>r}^{P}(e^{j\phi_i \frac{2\sigma}{P}} - e^{j\phi_r \frac{2\sigma}{P}})| = c > 0, \tag{36}$$

for some constant c. This is precisely the method Ur and Gross used to improve the resolution from sub-pixel shifted pictures in the spatial domain [81].

2.4.3 Spatial Domain Techniques for Super-resolution

If the observation model of E&F can be accurately and directly represented with the matrix, $\mathbf{H}$, in Eq. (16), then it is straightforward to apply a SR technique in the spatial domain. A straightforward energy to minimize in the spatial domain is the magnitude of the residual error from the forwarded HR estimate and the observations:

$$\hat{\mathbf{x}} = \arg\min_{\mathbf{x}} \|\mathbf{y} - \mathbf{H}\mathbf{x}\|_2^2, \tag{37}$$

where $\|.\|_2$ is the L^2 norm. This is a least squares estimate for the HRI that can be solved with gradient descent-type optimization algorithms [3]. The energy term is required to be analytic with respect to $\mathbf{x}$, which proceeds to step in a direction governed by the gradient at the current location (or estimate) until it reaches a neighborhood of a local minimum. However, the formulation of this energy used in Eq. (37) ignores the stochastic properties of the observation model and gradient descent techniques do not work on non-analytic functions. Instead, SRR techniques based on a Bayesian formalism have been used

in the spatial domain, providing a natural way to incorporate prior knowledge into the HR estimate.

In the Bayesian framework, each variable from the E&F model becomes a random variable (RV) with a probability density function (PDF), where actual data is an element from the sample space. Commonly used estimators in SR maximize the likelihood of the parameters, $p(\mathbf{y}|\mathbf{x})$, or maximize the posterior distribution, $p(\mathbf{x}|\mathbf{y})$:

$$\hat{\mathbf{x}}_{ML} = \arg\max_{\mathbf{x}} p(\mathbf{y}|\mathbf{x}), \tag{38}$$

$$\hat{\mathbf{x}}_{MAP} = \arg\max_{\mathbf{x}} p(\mathbf{x}|\mathbf{y}) \tag{39}$$

$$= \arg\max_{\mathbf{x}} (\log p(\mathbf{y}|\mathbf{x}) + \log p(\mathbf{x})), \tag{40}$$

where ML and MAP denote maximum-likelihood and maximum a posteriori, respectively. The additive noise from the E&F model is typically independent and identically distributed (IID) for most systems, which can simplify both the algebra and computation involved in the SRR. To avoid excessive noise amplification that sometimes results from ML estimation, the prior, $p(\mathbf{x})$, serves to regularize the problem. For imagery, it often penalizes the total energy (i.e., $||\mathbf{x}||_2^2$), or promotes (piecewise) smoothness:

$$p(\mathbf{x}) \propto \exp(-\sum_{n=1}^{N} \upsilon(||\nabla \mathbf{x}_n||_2, \beta)), \tag{41}$$

where

$$\upsilon(z, \beta) = \left\{ \begin{array}{cc} z^2 & |z| < \beta \\ 2\beta|z| - \beta^2 & |z| \geq \beta \end{array} \right\}, \tag{42}$$

∇ is the spatial gradient, and $\upsilon(.,.)$ is the Huber potential. The β-threshold relaxes the penalty for high frequency content, resulting in edge preservation, where higher frequency content is expected. Otherwise, uniform smoothness is achieved as $\beta \rightarrow \infty$. Other image priors assigned to the HR image are surveyed in [39].

If the LRIs are unregistered (i.e., different coordinate systems), then the existing E&F model becomes incomplete. The LRIs need to be either registered as a SR preprocessing step or combined directly into the observation model. Hardie et al. modeled the unknown motion parameters of the LRIs, denoted by $\mathbf{v} = [\mathbf{v}_1 ... \mathbf{v}_P]^T$, as Gaussian RVs and combined

them into the E&F warp [29]:

$$\mathbf{y}_r = D_r C_r F_r(\mathbf{v}_r)\mathbf{x} + \mathbf{e}_r \qquad 1 \leq r \leq P. \tag{43}$$

The statistical independence of the HRI and the motion (i.e., $p(\mathbf{v}|\mathbf{x}) = p(\mathbf{v})$) in their joint MAP estimate leads to

$$\begin{aligned} \hat{\mathbf{x}}_{MAP}, \hat{\mathbf{v}}_{MAP} &= \arg\max_{\mathbf{x},\mathbf{v}} p(\mathbf{x}, \mathbf{v}|\mathbf{y}), & (44) \\ &= \arg\max_{\mathbf{x},\mathbf{v}} (\log p(\mathbf{x}) + \log p(\mathbf{v}) + \log p(\mathbf{y}|\mathbf{x}, \mathbf{v})). & (45) \end{aligned}$$

However, $\mathbf{y}_r$ is non-linear with respect to $\mathbf{v}_r$ in Eq. (43) and solving this optimization problem over multiple variables simultaneously is not as straightforward as it is for a linear expression. One such solution to solving this problem by Tipping et al. included marginalizing over the motion parameters and HRI to solve for the ML component in Eq. (45) [58, 79]:

$$\begin{aligned} \hat{\mathbf{v}}_{ML} &= \arg\max_{\mathbf{v}} \int p(\mathbf{y}|\mathbf{x}, \mathbf{v}) p(\mathbf{x}) d\mathbf{x} & (46) \\ \hat{\mathbf{x}}_{ML} &= \arg\max_{\mathbf{x}} \int p(\mathbf{y}|\mathbf{x}, \mathbf{v}) p(\mathbf{v}) d\mathbf{v} & (47) \end{aligned}$$

Another approach is made possible through alternate minimization algorithms. Each of the two estimates from Eq. (44) can be alternately updated as the other is fixed. The sufficient conditions and correctness for these algorithms are given in [15]. However, the E&F model now depends on the motion estimates, $\hat{\mathbf{v}}$. Hence, every other iteration requires re-computing $\mathbf{H}$, which can be formidable if accuracy and speed are required. Another alternative is to simply compute the motion parameters as an effective pre-processing step and then perform SRR.

In cases where the system matrix, $\mathbf{H}$, in Eq. (16), cannot be computed directly, alternatives exist that work in the spatial domain, such as the iterative back projection (IBP) algorithm [35]. The algorithm sequentially back projects[1] the current HR estimate in the spatial domain by reversing the warping, blurring, and down-sampling that are then subtracted from the observed data and averaged into the new HR estimate. If the r^{th} warp,

[1] To avoid ambiguity in the nomenclature, "projection" or "project" will refer to an algebraic operation, which is semantically different from a tomographic projection in computed tomography.

blur, and down-sampling are denoted as c_r, $\mathbf{h}$, and $\downarrow$, then the l^{th} estimate for the r^{th} LRI is

$$\hat{\mathbf{y}}_r^{(l)} = (c_r(\hat{\mathbf{x}}^{(l)}) * \mathbf{h}) \downarrow d, \tag{48}$$

where d is the down-sampling rate. This is similar to the E&F observational model but the IBP algorithm assumes a shift-invariant blur. The back-projection expression becomes

$$\hat{\mathbf{x}}^{(l+1)} = \hat{\mathbf{x}}^{(l)} + \frac{1}{P}\sum_{r=1}^{P} c_r^{-1}(((\mathbf{y}_r - \hat{\mathbf{y}}_r^{(l)}) \uparrow d) * \mathbf{g}), \tag{49}$$

where c_r^{-1} is the inverse warp, $\mathbf{g}$ is the back projection kernel, and $\uparrow$ is the up-sampling operator. Unlike imaging blur, the back-projection kernel can be chosen to satisfy the convergence condition

$$||\delta - \mathbf{h} * \mathbf{g}||_2 < \frac{1}{\frac{1}{P}\sum_{r=1}^{P} ||c_r||_2}, \tag{50}$$

where δ and $||c_r||$ are the Kronecker delta and operator norm of T_r, respectively. The back-projection kernel determines the characteristic of the solution. However, the IBP algorithm is unable to apply a priori constraints, making it limited in a Bayesian setting.

Other iterative methods in the spatial domain have been generalized to set-theoretic approaches. In this case, the HR estimate is treated as an element in a subset of a Euclidean space that makes up the admissible solutions. More general than linear methods, if the set is convex, then it becomes straightforward to apply the projection onto convex sets (POCS) methods. The ellipsoid algorithm is geometrically based and is applicable when the constraints are convex functions. The IBP algorithm is an example of a row action projection method, which updates the current best guess according to data constraints. The authors in [74, 77, 55] formalized SRR into a POCS framework using data consistency as the constraint. In general, the method finds a vector contained in all of the imposed convex sets:

$$\hat{\mathbf{x}}^{(l+1)} = P_M P_{M-1} \dots P_2 P_1 \hat{\mathbf{x}}^{(l)}, \tag{51}$$

where P_k is the operator that projects a vector onto the convex set, C_k. Stark et al. and Tekalp et al. used the POCS formalism in their SRR incorporating warping without any blurring [74, 77]. Patti et al. proposed a POCS algorithm accounting for space-varying

blur with arbitrary sampling lattices [55]. Aside from the data consistency, additional types of convex constraints can include output energy, smoothness, phase, support, amplitude windowing, etc. All these priors may be expressed in the MAP estimate given in Eq. (40). For quadratic constraints, projecting the estimate can be a computationally expensive and the use of the steepest descent algorithms can be used instead. However, steepest descent algorithms require the functions to be analytic and may not permit some of these priors. As an alternative, Elad and Feuer built a hybrid SRR algorithm that separates constraints if the error function is analytic [22]. Their algorithm proceeds to use the steepest descent methods on the analytic error whose estimate is then projected sequentially onto the remaining non-analytic constraints. In this context, their hybrid method combined the stochastic approach with the POCS formalism.

2.5 Previous Super-resolution Research in Magnetic Resonance Imaging

Our investigation of SR techniques has the same underlying purpose much as the previous research. The current limits in HR imagery and high SNR in MRI are not due to the acquisition system resolution but rather to the acquisition time. The acquisition times for 3-D HR imaging are impractical for desired T_2-weighted contrast.

Herment et al. were one of the first groups to experiment with SR in MRI [30, 66]. They combined partial $\boldsymbol{k}$-space data of the same object but with different frequency domain sampling boundaries using three successive 3-D MRI volumes, as shown in Figs. 13(a-c). To reconstruct an image using $\boldsymbol{k}$-space data, their method zero-"pads" the unknown regions contained in the bounding box from the union of the three $\boldsymbol{k}$-space data volumes (Fig. 13(d)). The shared center cube portion of acquired $\boldsymbol{k}$-space samples is averaged, while the remaining exclusive partial volumes of acquired $\boldsymbol{k}$-space samples are left unchanged for Fourier reconstruction. The total acquisition time of the three 3-D MRI volumes is shorter than the acquisition time of an equivalent 3-D MRI scan with $\boldsymbol{k}$-space data extending to the bounding box from the union of the three volumes. Their results show anisotropic HR imagery, but only in the directions shared by the high-frequency $\boldsymbol{k}$-space data samples. This makes their method readily useful for imaging tissues with specific direction such as

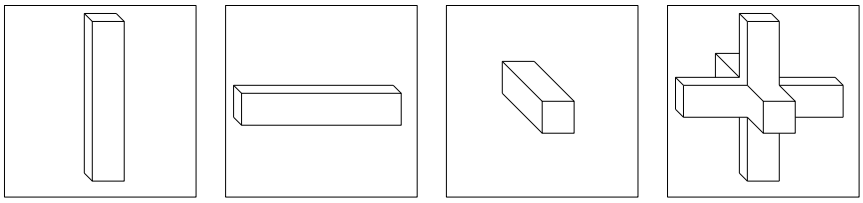

(a) (b) (c) (d)

Figure 13: The LR ***k***-space boundaries for the SRR experiments for MRI used by Herment et al. [30] (a-c) Bounding boxes of sampled ***k***-space data from three 3-D MRI acquisitions of different boundaries (d) Effective ***k***-space sampling boundary in HRI.

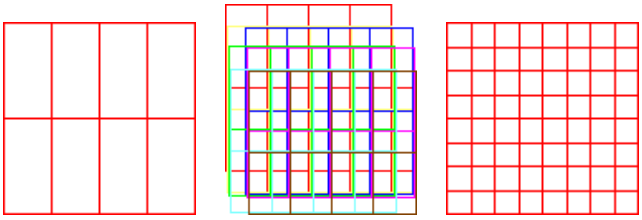

(a) (b) (c)

Figure 14: The SRR for MRI experiment of Peled and Yeshurun showing phase- and frequency-encoding direction [57] (a) Sampling Configuration for one LRS, one LR pixel = 2×4 HR pixel units (b) Eight shifted LRSs with 1×1 HR pixel unit shift increments (c) HR scan of 8×8 pixel units.

arteries, but not for brain imaging where isotropic resolution is desired.

Peled and Yeshurun applied the IBP algorithm to a set of eight spatially shifted LR diffusion tensor images with equal resolutions and field of views using 2-D multi-slice acquisitions, as shown in Fig. 14 [57]. Diffusion tensor imaging relies on the Brownian motion of water molecules in brain tissue, which helps visualize white matter fibers (or tracts) of the brain as a way to detect strokes [28]. While Peled and Yeshurun claimed resolution improvement in the frequency- and phase-encoding directions, their results were subsequently invalidated by Scheffler [68].

The argument is rooted in ***k***-space with a dimensionality reduced to 1-D. The separability of the Fourier transform permits a dimensionality reduction without any loss of generality.

In a homogeneous magnetic field, the samples of k-space are equivalent to samples from the continuous Fourier transform and are not discrete Fourier transform coefficients. That is, if an arbitrary LRS, $y(s)$, has a sampling period of Δk in the frequency domain and has neither any blurring nor warping then

$$Y(\omega) = \sum_{n=-M_0/2}^{M_0/2-1} \delta(\omega - n\Delta k) \int_{-\infty}^{\infty} x(s) e^{-j2\pi\omega s} ds. \tag{52}$$

It is readily apparent that the T_1 and T_2 decay rates from Eq. (9) limit the duration of time available to acquire a signal so that only a finite number of frequency samples in k-space is collected, i.e., $M_0 < \infty$. Also, Eqs. (10) and (11) indicate that low-frequency values arrive temporally earlier than high-frequency values, effectively creating a low-pass filter in the acquisition. So, there does not exist any spatial aliasing or fold-over in the frequency domain samples of the LRIs whatsoever. Otherwise, if there was spatial sampling, then the discrete-to-continuous Fourier transform relationship given in Eq. (23) would be applicable. Therefore, there does not exist any frequency information at locations exceeding the location limits of the LRIs finitely sampled in the frequency domain. Furthermore, Poisson re-summation of Eq. (52) is

$$x(s) = \Delta k \sum_{n=-\infty}^{\infty} Y(n\Delta k) e^{j2\pi n\Delta k s} \qquad |s| < \frac{1}{\Delta k}. \tag{53}$$

Hence, the field of view in the spatial domain is directly controlled by the choice of $\frac{1}{\Delta k}$. As is the case for the SR experiments of Peled and Yeshurun, if the finite resolutions and field of views of the LRIs are identical, then, according to Eq. (53), the locations of the frequency samples must also be identical. Consequently, a LRS has neither any high-frequency information present nor any sampling lattice different from any other LRS. The spatial shifts of the LRSs used by Peled et al. then only correspond to a phase modulation of the same information added with noise in the Fourier domain. Thus, the sampled continuous Fourier transform of the r^{th} LRS is

$$Y_r(n\Delta k) = e^{j\phi_r n\Delta k} Y_1(n\Delta k) + E(n\Delta k) \qquad 2 \le r \le P \quad -\frac{M_0}{2} \le n \le \frac{M_0}{2} - 1, \tag{54}$$

where $E(n\Delta k)$ is the measurement error and ϕ_r is the relative spatial shift to an arbitrary

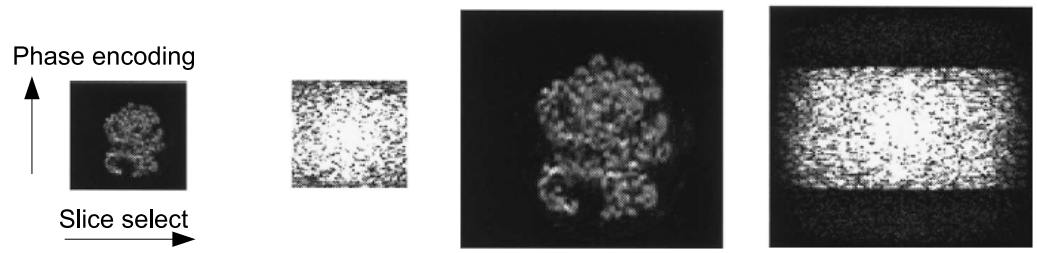

(a) (b) (c) (d)

Figure 15: Spectrum Analysis of phase-encoding and slice select direction from the experiments of Greenspan et al.[27] (a) LRI and its (b) Frequency Spectrum; (c) HRI estimate and its (d) Frequency Spectrum using the iterative back-projection algorithm.

reference LRS, i.e., $r = 1$. So, while the source data is identical, the spatial shifts are merely post-processing steps as a way to increase SNR.

Greenspan et al. verified the statements of Scheffler by applying SRR techniques to 2-D multi-slice MRI scans [27]. They also showed that the SRR results based on the Peled and Yeshurun experiments can be replicated with zero-padding interpolation from the LRIs. The slice selection and phase- and frequency-encoding directions of the LRIs shared uniformly spaced voxel shifts. Applying the 3-D iterative back-projection algorithm, the frequency spectrum of the HR estimates showed a sharp cut-off in the phase encoded direction, as shown in Fig. 15. Conversely, spectrum analysis in the slice selection direction revealed approximately twice the extent of bandwidth, thus providing a basis for SRR in this direction. Consequently, further SRR experiments of Greenspan et al. relied on spatial shifts in only the slice selection direction from both real and phantom 2-D multi-slice MRI data. To account for the PSF needed in the iterative back projection algorithm, Greenspan et al. measured the slice profile to be well approximated by Gaussian functions, where the slice thickness is its full width at half maximum. The SNR per unit acquisition time or SNR efficiency of the LRI data sets was greater than the equivalent scan with equal spatial resolution in the HR estimate as their data is shown in Table 5. It also shows that edge width is comparable to the HRI in the slice selection direction.

Table 5: Comparison of times and edges measured for SRR estimates with different PSFs against a HR scan in the experiments of Greenspan et al.[27].

	SRR Zero pad	SRR Box-PSF	SRR Gaussian-PSF	HR scan
Time (sec)	88	264	264	260
SNR	287	170	124	95
Edge width	3.7	2.9	2.2	2.3
SNR $/\sqrt{time}$	30.59	10.46	7.63	5.89

Peeters et al. also considered SR in the slice selection direction, but for functional MRI data used in the 2-D multi-slice acquisition [56]. As opposed to anatomical structure, functional MRI visualizes the temporal activity or physiology of the brain, which gives a dynamic time series of 3-D activation areas. Peeters et al. used an additive model, computing the volume of shared space from any given LR and HRI pixel. That is, if S_i and S_j is the space at the i^{th} LR and j^{th} HRI pixel, respectively, then the E&F matrix is

$$[\mathbf{H}]_{ij} = \int_{S_i \bigcap S_j} d\boldsymbol{s}. \tag{55}$$

The pixels from the LRIs of parallel spatial shifts shared boundaries with the HR pixels, thereby simplifying the computation for $\mathbf{H}$. Their error to minimize promoted piecewise smoothness for their HR estimate:

$$\hat{\mathbf{x}} = \arg\min_{\mathbf{x}} \|\mathbf{y} - \mathbf{H}\mathbf{x}\|_2^2 + \alpha \sum_{n=1}^{N_1 N_2} (\upsilon([D_1\mathbf{x}]_n, \beta) + \upsilon([D_2\mathbf{x}]_n, \beta)), \tag{56}$$

where D_1 and D_2 are finite difference approximations to the first derivatives in the slice selection and phase-encoding directions, $\upsilon(.,.)$ is Huber potential from Eq. (42), and α weighs fidelity against the smoothness. Their results based on only two LR fMRI scans showed a reconstruction of both higher SNR than that of the HRI equivalent and with sharper edges.

Carmi et al. explored SR further using 2-D multi-slice MRI data sets and recognized emerging problems caused by spatially shifted LRIs like those used by Greenspan et al. [10]. Their main contribution is a new sampling condition for the LRIs that goes beyond MRI and into SR in general. Specifically, they show how a set of LRIs with equal sampling periods of uniform spatial shifts can propagate localized spatial error globally to all the pixels of the HR estimate during the SRR process. They also show that in fully-determined

SR scenarios, pixels of the HR estimate may remain unresolved despite the absence of any error. If input error is limited to some physical location such as scanner vibration or non-rigid motion of the object, then it may be desirable to keep this spatial error localized. This means any pixel from the estimate of the HRI should be expressed by only a small combination of neighboring pixels in the LRIs. In other words, each row in the inverse of the E&F matrix, when non-singular, would only have a small number of non-zero entries. While a small support region of the PSF equates to a small number of HR pixels expressed in the linear combination of any pixel in the LRI (i.e., a sparse $\mathbf{H}$), it does not, however, guarantee sparsity for its inverse.

To guarantee localization of SRR error, Carmi et al. introduce a set of LRIs with two different pixel sizes, where both are integer multiples of the pixel size from the estimate of the HRI, denoted as $1 \times a$ and $1 \times b \quad a, b \in \mathbb{Z}$. Then, all a and b possible integer offsets of the LRIs with the $1 \times a$ and $1 \times b$ pixel sizes are acquired, respectively. An algorithm proceeds to compute an image estimate with pixels of size $1 \times \gcd(a, b)$, where $\gcd(.,.)$ is the greatest common divisor. Consequently, if $\gcd(a, b) = 1$, then the estimate of the HRI can be recovered. Moreover, the number of LRI pixels needed to recover any HR pixel is shown to be bounded by $O(ab)$. More importantly, it means the propagation of error is also bounded. The major caveat to this approach is the number of LRIs needed, which in this case is ab. Obviously this may lead to more LRIs than used in the previously studied SRR methods of spatial shifts. However, in cases where keeping error localized is crucial, their method is the only proven candidate for SRR.

2.6 Summary

MRI is a tomographic technique that continues to suffer from LR when both high contrast and reasonable acquisition times are needed. The absence of aliasing in the frequency- and phase-encoding directions in MRI only allows SR in the slice selection direction. So far, all the successful SR experiments for MRI have only included sub-pixel spatial shifts of the LRIs in the slice selection direction. If isotropic resolution is required, this implies

that the degree of resolution enhancement is bounded by the pixel resolution in the phase-encoding or frequency-encoding direction. When an application requires isotropic resolution that exceeds resolution of the phase- and frequency-encoding directions, the SR methods for MRI described in this chapter may be inadequate. If this is the case, then a new SR methodology for MRI would be needed to improve resolution in these dimensions. While the elegant sampling strategy given by Carmi et al. localizes the input error in the HR estimate of the SR process, this result was not shown to hold when registration correction is applied. Our SR work focuses on these missing and remaining issues. We show that an approach to combine multiple SRR views at different scanning orientations offers a more natural avenue toward isotropic image resolution than multiple acquisitions at the same orientation with sub-pixel offsets.

CHAPTER III

THEORY OF MULTI-STACK

This chapter introduces a novel SR observation model for 2-D multi-slice MRI. To date, only sub-pixel spatial shifts in the SR experiments of MRI have been studied. Instead of multiple parallel multi-slice scans, an approach to combine multiple scans with different slice directions, each acquired with high in-plane resolution, is investigated. In this work a new SR model, known here on as "Multi-Stack" (MS), is introduced. It combines the benefits of long-T_R multi-slice imaging, in terms of contrast and acquisition efficiency, with the benefits of SRR to overcome the intrinsic resolution limitations of multi-slice imaging. In this chapter, MS is defined, a formal ML estimator for SRR in MRI is derived and the approach to discretizing the observation model is presented with supporting experiments.

3.1 Definition of Multi-Stack

The Multi-Stack approach combines multiple 2-D multi-slice scans or stacks, as shown in cross-section in Fig. 16(a). Except for slice orientation, all scans share the same acquisition parameters. The data input conditions are as follows.

- Slices are equidistant and parallel within each slice stack, and have identical slice selection profiles.
- Slice centers in each stack are aligned along the slice plane normal.
- Scans are spatially co-registered.
- Contrast parameters are equal.
- The slice orientations are at equal angular sampling intervals. The same frequency-encoding (or read-out) direction across all stacks, orthogonal to the planes shown in

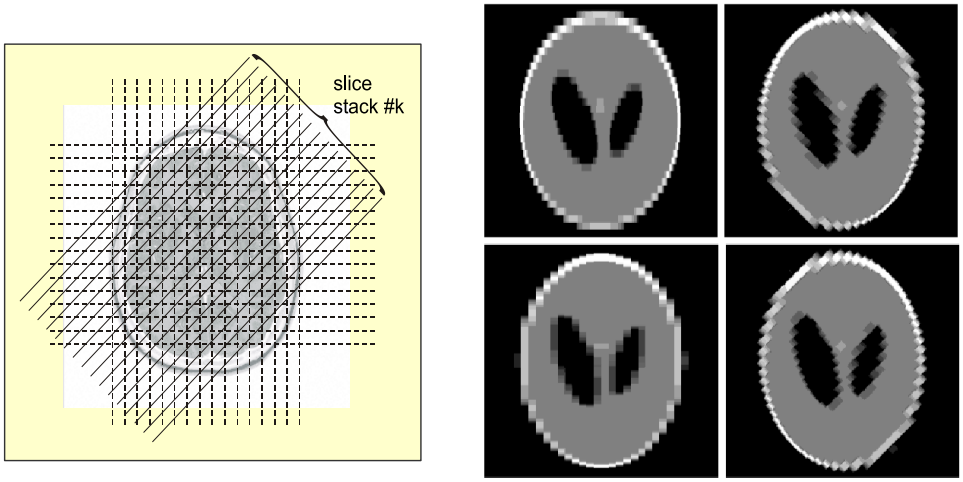

(a) (b)

Figure 16: (a) Coverage of the volume by multiple overlapping slice stacks (b) Simulation showing a cross-section through stacks of the Shepp-Logan Phantom with 45^o increments.

Fig. 16 results in consistent chemical shift artifacts[1], which can thus be ignored for reconstruction in this direction.

Under these conditions the problem of reconstructing a 3-D data volume from a set of such slice stacks possesses translational symmetry along the readout direction. Thus, the problem is reduced to a series of identical 2-D inversion problems with different measurement data. Figure 16(b) shows a simulated 2-D input data set using the Shepp-Logan phantom (SLP) with four stacks. The equal contrast parameters means the timing parameters, T_E and T_R, are consistent among all the LRSs.

The issue of representing the MS framework in either the frequency or spatial domain depends primarily on the frequency content of the brain. The compact region of support in the brain has an infinite frequency bandwidth that violates the preconditions needed by the SRR methods used in the frequency domain. Therefore, as an alternative, MS SRR consists of the individual LR scans (LRSs) from the spatial domain after Fourier reconstruction.

[1]Chemical shift artifact is a misregistration effect caused by different materials (i.e., water and fat) that are at the same spatial location in the frequency-encoding direction but will be measured at different spatial locations.

The scanning (or slice excitation) direction for the r^{th} stack undergoes a coordinate transformation by a rotation matrix, $\mathrm{R}_r \in SO(3)$, of the form

$$\mathrm{R}_r = \begin{pmatrix} 1 & 0 & 0 \\ 0 & \cos\theta_r & -\sin\theta_r \\ 0 & \sin\theta_r & \cos\theta_r \end{pmatrix}, \tag{57}$$

where θ_r is the rotation around the frequency-encoding axis. The angles, $\{\theta_r\}_{r=1}^{P}$, are uniformly distributed 180^o around this axis so that

$$\theta_r = \frac{180(r-1)}{P}. \tag{58}$$

The slice-selective excitation process is modeled by a convolution of the image by a slice profile function, followed by uniform sampling described by a diagonal sampling matrix V. The diagonal structure of V represents a rectangular sampling process:

$$\mathrm{V} = \begin{pmatrix} T_{FE} & 0 & 0 \\ 0 & T_{PE} & 0 \\ 0 & 0 & T_{SS} \end{pmatrix}, \tag{59}$$

where T_{FE}, T_{PE}, and T_{SS} are the pixel sizes or sampling periods in the frequency-encoding, phase-encoding, and slice selection directions, respectively. These are the parameters to the down-sampling process from the E&F model. The LRI, $y_r[\mathbf{n}] : \mathbb{Z}^3 \rightarrow \mathbb{C}$, from the r^{th} stack is related to the HRI, $x(\mathbf{s}) : \mathbb{R}^3 \rightarrow \mathbb{C}$, by

$$y_r[\mathbf{n}] = \int_{\Omega} x(\mathbf{s}) h(\mathrm{R}_r(\mathbf{s} - \mathrm{V}\mathbf{n})) d\mathbf{s} + e_r[\mathbf{n}], \tag{60}$$

where $\Omega \subset \mathbb{R}^3$ is the region of support for $x(\mathbf{s})$. The other functions, $h(\mathbf{s})$ and $e_r[\mathbf{n}]$, are the slice selection function and measurement noise, respectively. The warp and down-sampling operation in Eq. (60) is applied to $h(\mathbf{s})$ and not to $x(\mathbf{s})$, so it does not readily follow the E&F SR observation model. However, Appendix A.1 derives Eq. (60) by changing the variables so that

$$y_r[\mathbf{n}] = \int_{\Omega} x(\mathrm{R}_r^{-1}\mathbf{s} + \mathrm{V}\mathbf{n}) h(\mathbf{s}) d\mathbf{s} + e_r[\mathbf{n}]. \tag{61}$$

Thus, the forwarding model follows from the E&F SR observation model given in Eq. (14), and is shown as a block diagram in Fig. 17. Sampling followed by a lexicographical ordering

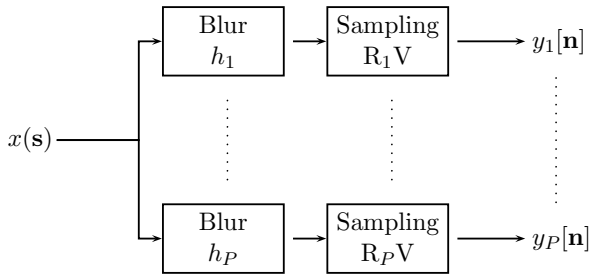

Figure 17: Multi-Stack degradation model.

of $y_r[\mathbf{n}]$ creates the LRI vector, $\mathbf{y}$, by replacing stack index, r, and sampled location indices, $\mathbf{n}$, with a composite pixel index i[2]. The measurements can then be described as the linear system,

$$\mathbf{y} = \mathrm{H}\mathbf{x} + \mathbf{e}, \tag{62}$$

where $\mathbf{e}$ is the measurement error. The matrix H represents the integral convolution operator and each of its non-negative entries is evaluated as

$$[\mathrm{H}]_{ij} = \int_{S_j} h(\mathrm{R}_r(\mathbf{s} - \mathrm{V}\mathbf{n}))d\mathbf{s}, \tag{63}$$

where S_j is the space for the j^{th} voxel of $\mathbf{x}$. The contribution from the HR voxel, j, to the LR voxel, i, is weighted by the slice excitation profile over the shared area, as illustrated in Fig. 18.

The maximum possible resolution improvement for the estimate of the HRI is bounded by the dimensions of H. In this case, $\mathrm{H} \in \mathbb{R}^{M \times N}$, where M and N are the total number of measurements and unknowns, respectively (see Table 4). The isotropic voxel size of the HRI must allow H to be non-singular. This means $M \geq N$. The uniformly spaced angles of the LRSs in MS creates sampling symmetry around the origin, resulting in an equal number of samples per dimension on average. If the in-plane resolution of the LR slices is equal and the number of stacks is greater than or equal to the slice thickness (expressed in number of LR pixels), then the SRR is fully-defined and has isotropic resolution. If there are P LRIs,

[2]If there are $M_1 \times M_2 \times M_3$ measurements for each LRS with $\mathbf{n} = (n_1, n_2, n_3)$, then $i = n_1 + (n_2 - 1)M_1 + (n_3 - 1)M_1M_2 + (r - 1)M_1M_2M_3$.

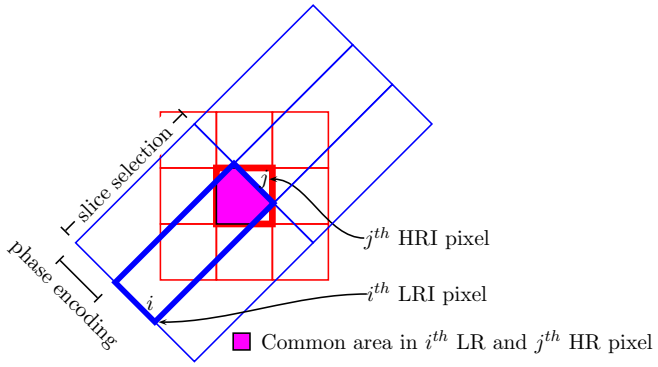

Figure 18: Contribution of a HR pixel to a LR data pixel.

S slices per stack, and K voxels per stack in the phase-encoding direction, then $M = KSP$ and the necessary condition for signal recovery becomes

$$N \leq KSP. \tag{64}$$

Otherwise, if $M < N$, then the inversion problem is under-determined, and the image cannot be recovered completely and image artifacts may be expressed. If $M > N$, then the system is over-determined. In cases of contamination, noise will be attenuated.

Since each measured voxel is integrated over the support region of the slice selection profile we treat it as a localized tomographic projection. Given the angular sampling pattern represented by the stack orientations, the MS problem will use existing projection reconstruction algorithms from the computed tomography domain.

3.2 Noise Model of Multi-Stack

The real and imaginary components of the intrinsically complex-valued MRI data in $x(\mathbf{s})$ are each independently corrupted by zero-mean Gaussian thermal noise in the frequency domain that remain independently distributed as Gaussian RVs with respect to its real and imaginary components from the spatial domain [83]. Bayesian estimation can be applied for $\mathbf{x}$, but the restriction that the RV must be real makes samples of the magnitude data meaningful for estimation. Otherwise, each sample must be treated as a joint PDF of two RVs, i.e., real and imaginary. However, transforming the complex-valued data to its signal amplitude changes the PDF from a Gaussian to a Rician. That is, if $\mathbf{x}(\mathbf{s})$ is corrupted with

IID error as

$$\tilde{x}(\mathbf{s}) = x(\mathbf{s}) + e(\mathbf{s}), \tag{65}$$

$$\Re(e(\mathbf{s})) \sim \mathsf{N}(0, \sigma_e^2), \tag{66}$$

$$\Im(e(\mathbf{s})) \sim \mathsf{N}(0, \sigma_e^2), \tag{67}$$

$$\mathsf{Cov}(\Re(e(\mathbf{s}))\Re(e(\mathbf{t}))) = \delta(\mathbf{s}-\mathbf{t})\sigma_e^2, \tag{68}$$

$$\mathsf{Cov}(\Im(e(\mathbf{s}))\Im(e(\mathbf{t}))) = \delta(\mathbf{s}-\mathbf{t})\sigma_e^2, \tag{69}$$

then the likelihood of the corrupted amplitude is

$$p(\tilde{x}_A(\mathbf{s})|x_A(\mathbf{s})) = \frac{x_A(\mathbf{s})}{\sigma_e^2} e^{-\frac{\tilde{x}_A(\mathbf{s})^2 + x_A(\mathbf{s})^2}{2\sigma_e^2}} I_0\left(\frac{\tilde{x}_A(\mathbf{s}) x_A(\mathbf{s})}{\sigma_e^2}\right) \qquad \tilde{x}_A(\mathbf{s}) \geq 0, \tag{70}$$

where

$$x_A(\mathbf{s}) = \sqrt{\Re(x(\mathbf{s}))^2 + \Im(x(\mathbf{s}))^2}, \tag{71}$$

$$\tilde{x}_A(\mathbf{s}) = \sqrt{\Re(\tilde{x}(\mathbf{s}))^2 + \Im(\tilde{x}(\mathbf{s}))^2}, \tag{72}$$

and $I_0(.)$ is the zeroth-order Bessel function of the first kind [73]. Brummer et al. show that as the SNR (i.e., $\frac{\tilde{x}_A(\mathbf{s})}{\sigma_\mathbf{e}}$) increases, the PDF of Eq. (70) approaches a Gaussian PDF [8]. Figure 19 shows several Rician PDFs with increasing values of SNR that begin to approximate a Gaussian PDF. The sampled amplitudes from the corrupted and true HRIs, denoted as $\tilde{\mathbf{x}}_A = [\tilde{x}_A(\mathbf{s}_1)\ \tilde{x}_A(\mathbf{s}_2)\ ...\ \tilde{x}_A(\mathbf{s}_N)]^T$ and $\mathbf{x}_A = [x_A(\mathbf{s}_1)\ x_A(\mathbf{s}_1)\ ...\ x_A(\mathbf{s}_N)]^T$, respectively, have a joint likelihood that is a product of their individual likelihoods after Gaussian substitution:

$$p(\tilde{\mathbf{x}}_A|\mathbf{x}_A) = \left(\frac{1}{2\pi\sigma_e^2}\right)^N \prod_{n=1}^{N} e^{-\frac{(\tilde{x}_A(\mathbf{s}_n) - x_A(\mathbf{s}_n))^2}{2\sigma_e^2}}. \tag{73}$$

It remains to determine the likelihood of parameters, $p(\mathbf{y}_A|\mathbf{x}_A)$, from Eq. (60) if $\tilde{x}(\mathbf{s})$ is the input to this observation model. The linearity of integration permits separation of the error term when substituting Eq. (65) into Eq. (60) so that

$$e_r[\mathbf{n}] = \int_\Omega e(\mathbf{s}) h(\mathrm{R}_r(\mathbf{s} - \mathrm{V}\mathbf{n})) d\mathbf{s}. \tag{74}$$

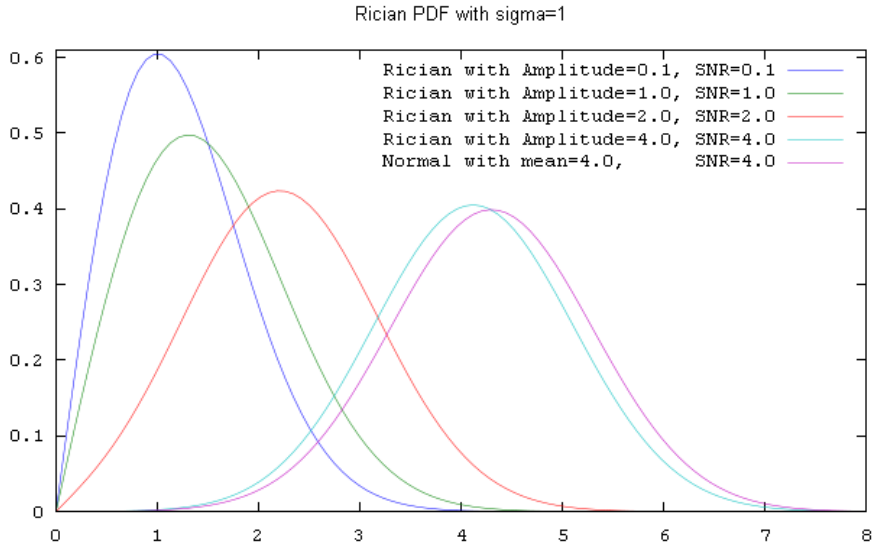

Figure 19: Rician Distribution for different SNR values.

Appendix B derives the PDFs of Eq. (74) as

$$\Re(e_r[\mathbf{n}]) \sim \mathsf{N}(0, \sigma_e^2 \hat{h}_r(\mathbf{n}, \mathbf{n})) \tag{75}$$

$$\Im(e_r[\mathbf{n}]) \sim \mathsf{N}(0, \sigma_e^2 \hat{h}_r(\mathbf{n}, \mathbf{n})), \tag{76}$$

with the covariance and autocorrelation of two samples, $\mathbf{n}$ and $\mathbf{m}$, as

$$\mathsf{Cov}(\Re(e_r[\mathbf{n}])\Re(e_r[\mathbf{m}])) = \sigma_e^2 \hat{h}_r(\mathbf{n}, \mathbf{m}) \tag{77}$$

$$\mathsf{Cov}(\Im(e_r[\mathbf{n}])\Im(e_r[\mathbf{m}])) = \sigma_e^2 \hat{h}_r(\mathbf{n}, \mathbf{m}) \tag{78}$$

$$\mathsf{R}_{\Re(e_r[\mathbf{n}])\Re(e_r[\mathbf{n}])}(\mathbf{n}, \mathbf{m}) = \sigma_e^2 \hat{h}_r(\mathbf{n}, \mathbf{m}) \tag{79}$$

$$\mathsf{R}_{\Im(e_r[\mathbf{n}])\Im(e_r[\mathbf{n}])}(\mathbf{n}, \mathbf{m}) = \sigma_e^2 \hat{h}_r(\mathbf{n}, \mathbf{m}), \tag{80}$$

where

$$\hat{h}_r(\mathbf{n}, \mathbf{m}) = \int_\Omega h(\mathrm{R}_r(\mathbf{s} - \mathrm{V}\mathbf{n}))h(\mathrm{R}_r(\mathbf{s} - \mathrm{V}\mathbf{m}))d\mathbf{s}. \tag{81}$$

The variance of the error from the LRI is thus amplified by the total energy of the slice selection profile. Furthermore, two different error samples may correlate with each other. If the sampling distances given by the diagonal entries in V is less than the support region of the slice selection profile, then there will be overlapping volumes between the samples, which will give the product in the integrand of Eq. (81) a non-zero value for some values

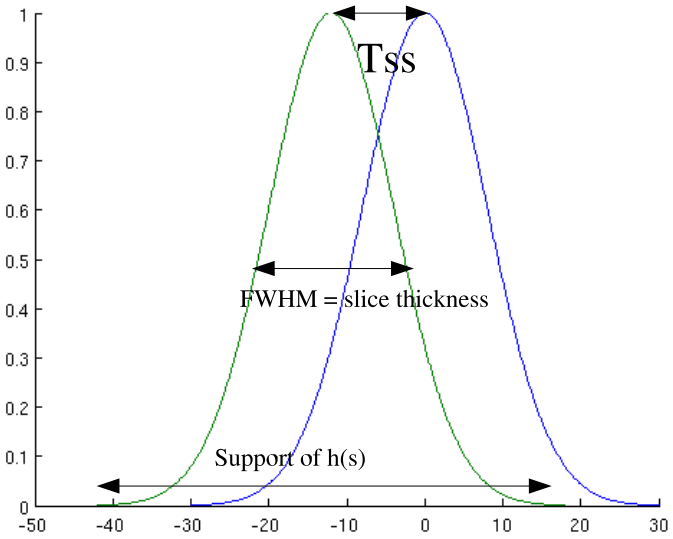

Figure 20: Dramatic illustration of cross talk interference from two slice planes. The support of the profile is greater than the sampling distance or slice width, T_{SS} in V. Full width at half maximum (FWHM) is the slice thickness.

of $\mathbf{s} \in \Omega$. This is an important result in multi-slice MRI, since the image artifact known as cross-talk interference is precisely the effect of overlapping slice regions. Fig. 20 illustrates cross-talk interference, where the sampling distance, or slice width, is less than the support of the slice selection profile. Slice thickness is the full width at half maximum. In these cases only, there will also be non-zero values included off the diagonal entries in the positive definite, symmetric autocorrelation matrix of the amplitude error,

$$\mathbf{R}_{\mathbf{e}_A\mathbf{e}_A} = \mathsf{E}[\mathbf{e}_A\mathbf{e}_A^T], \tag{82}$$

where $\mathbf{e}_A$ is the vector of sampled error amplitudes from the amplitudes of the LRSs. Otherwise, if all of the LRSs share both the same slice profile and precision of error, then the autocorrelation matrix is simply

$$\mathbf{R}_{\mathbf{e}_A\mathbf{e}_A} = \left(\sigma_e^2 \int_\Omega h^2(\mathbf{s})d\mathbf{s}\right)\mathbf{I}, \tag{83}$$

where $\mathbf{I}$ is the identity matrix. Indeed, the MS conditions results in an autocorrelation matrix of this form when there is not any slice-to-slice overlap.

3.2.1 ML Estimation

For the Fast Spin Echo-Inversion Recovery (FSE- IR) multi-slice acquisition used by Berstein et al. and Reich et al., the SNR measured is sufficiently high enough to substitute the Rician PDF of the corrupted amplitude as a Gaussian PDF [5, 62]. This means the likelihood of amplitude parameters, (measured amplitudes denoted as $\mathbf{y}_A$), is

$$p(\mathbf{y}_A|\mathbf{x}_A) = \frac{1}{\sqrt{(2\pi)^M |det(\mathbf{R}_{\mathbf{e}_A\mathbf{e}_A})|}} e^{-(\mathbf{y}_A - \mathbf{H}\mathbf{x}_A)^T \mathbf{R}^{-1}_{\mathbf{e}_A\mathbf{e}_A}(\mathbf{y}_A - \mathbf{H}\mathbf{x}_A)/2}. \tag{84}$$

Equivalently, the ML estimate that maximizes Eq. (84) minimizes the weighted LS estimate:

$$\hat{\mathbf{x}}_{A,ML} = \arg\min_{\mathbf{x}} (\mathbf{y}_A - \mathbf{H}\mathbf{x}_A)^T \mathbf{R}^{-1}_{\mathbf{e}_A\mathbf{e}_A}(\mathbf{y}_A - \mathbf{H}\mathbf{x}_A). \tag{85}$$

If $\mathbf{R}_{\mathbf{e}_A\mathbf{e}_A}$ is of the form given in Eq. (83), and the functional

$$L(\mathbf{x}_A) = (\mathbf{y}_A - \mathbf{H}\mathbf{x}_A)^T \mathbf{R}^{-1}_{\mathbf{e}_A\mathbf{e}_A}(\mathbf{y}_A - \mathbf{H}\mathbf{x}_A), \tag{86}$$

then setting $\nabla_{\mathbf{x}_A} L(\mathbf{x}_A) = 0$ leads to the normal equation

$$\mathbf{H}^T \mathbf{R}^{-1}_{\mathbf{e}_A\mathbf{e}_A} \mathbf{H}\hat{\mathbf{x}}_{A,ML} = \mathbf{H}^T \mathbf{R}^{-1}_{\mathbf{e}_A\mathbf{e}_A} \mathbf{y}_A, \tag{87}$$

and the weighted LS solution or ML estimate reduces to

$$\hat{\mathbf{x}}_{A,ML} = (\mathbf{H}^T \mathbf{R}^{-1}_{\mathbf{e}_A\mathbf{e}_A} \mathbf{H})^{-1} \mathbf{H}^T \mathbf{R}^{-1}_{\mathbf{e}_A\mathbf{e}_A} \mathbf{y}_A. \tag{88}$$

3.3 POCS algorithms

The structure of the MS matrix, H, has the properties of a matrix that represents the transmission/emission computed tomography imaging process. Since the sum of every column and row in H is non-zero, every HR pixel is measured and every LR pixel has information about the HRI. Moreover, the consistent parameters of both equal pixel sizes and slice selection profiles in the LRSs allow an equal contribution from any two HR pixels:

$$\sum_{i=1}^{M} [\mathrm{H}]_{ij} = \sum_{i=1}^{M} [\mathrm{H}]_{ij'} \quad 1 \le j, j' \le N, \tag{89}$$

and similarly from any two LR pixels:

$$\sum_{j=1}^{N} [\mathrm{H}]_{ij} = \sum_{j=1}^{N} [\mathrm{H}]_{i'j} \quad 1 \le i, i' \le M. \tag{90}$$

If the columns of H are normalized to one (i.e, $[\mathrm{H}]_{ij} \leftarrow \frac{[\mathrm{H}]_{ij}}{\sum_{i=1}^{M}[\mathrm{H}]_{ij}}$), then the contribution matrix can be interpreted as a transition matrix or a set of probabilities from a HR pixel to a detector or a LR pixel. Some iterative techniques to solve linear systems of non-negative coefficients or transitional probabilities based on the projection onto convex sets (POCS) formalism have established their convergence to be a minimizer of a weighted least squares functional from any initial guess. This is equivalent to a ML estimate without any regularization, given in Eq. (87). These include simultaneous algebraic reconstruction techniques (SART) [37, 43]. Since the reconstructions work on the amplitude in the MRI data, non-negativity is expected in the true image. Therefore, to avoid any negativity in the estimate, correction can be applied multiplicatively on a positive initial estimate rather than additively. Thus, we included the multiplicative algebraic reconstruction technique (MART), which maximizes the Shannon entropy consistent with available data [9]. MART is intended for nonnegative solutions, where the forwarding matrx also has nonnegative entries. Other families of reconstruction techniques in the computed tomography domain, not implemented in this work, include the iterative back-projection, filtered back-projection and expectation maximization algorithms. The expectation maximization algorithm has been used for a Poisson counting process as opposed to a environment with Gaussian noise. In comparison to the filtered back-projection algorithm, the POCS method demonstrates better performance when the data is noisy, dynamic, inconsistent and over-determined [37]. Furthermore, the filtered back projection algorithm has been shown to neither work well on localized tomographic projections nor on a small number of projections. Elad and Feuer recognize the iterative back-projection algorithm as an error relaxation algorithm that has the same additive form in updating and correcting the error as the algebraic reconstruction techniques [22].

3.3.1 Algebraic Reconstruction Technique

The algebraic reconstruction technique (ART) is a basic form of the POCS algorithms [37, 43]. The $(l+1)^{th}$ estimate is projected sequentially from the l^{th} estimate to the nearest admissible solution in the next convex set. This can be cast into an constrained optimization

problem so that the $(l+1)^{th}$ estimate of $\mathbf{x}$ is

$$\hat{\mathbf{x}}^{(l+1)} = \arg\min_{\mathbf{x}} ||\mathbf{x} - \hat{\mathbf{x}}^{(l)}||_2 \qquad \text{subject to} \quad \mathbf{y}_{i_{(l+1)}} = \mathrm{H}_{i_{(l+1)}}\mathbf{x}, \tag{91}$$

where H_{i_l} is the i_l^{th} row or hyperplane of H and $i_l = (l \mod M) + 1$ for cyclical control of constraints. Eq. (91) is derived in [46] so that the $(l+1)^{th}$ estimate is updated as

$$\hat{\mathbf{x}}^{(l+1)} = \hat{\mathbf{x}}^{(l)} + \lambda_l \frac{\mathbf{y}_{i_l} - \left\langle \mathrm{H}_{i_l}, \hat{\mathbf{x}}^{(l)} \right\rangle}{\|\mathrm{H}_{i_l}\|_2^2}. \tag{92}$$

The relaxation factor is λ_l, where the convergence to $\mathbf{x}$ is satisfied when $\lambda_l \in [0, 2]$. If there is a solution to $\mathbf{y} = \mathrm{H}\mathbf{x}$, then the sequence, $\{||\mathbf{x} - \hat{\mathbf{x}}^{(l)}||_2\}_{l=0}^{\infty}$ is decreasing and $\{\hat{\mathbf{x}}^{(l)}\}_{l=0}^{\infty}$ converges to the solution closest to $\hat{\mathbf{x}}^{(0)}$. If there does not exist a solution (i.e., inconsistent case), then $\{\hat{\mathbf{x}}^{(l)}\}_{l=0}^{\infty}$ converges not to one point, but to a different point for each constraint. These points are known as a limit cycle and it remains unknown if it is possible to compute the least-squares solution from it.

3.3.2 Simultaneous Algebraic Reconstruction Technique

One advantage of simultaneous additive reconstruction (SART) over ART is its guaranteed convergence to a LS solution for inconsistent cases [37]. It also known as the generalized Landweber iteration method. The next estimate is a weighted sum of all hyperplane projections from the previous estimate [43]:

$$\hat{\mathbf{x}}^{(l+1)} = \hat{\mathbf{x}}^{(l)} + \mathrm{H}^T \Lambda (\mathbf{y} - \mathrm{H}\hat{\mathbf{x}}^{(l+1)}). \tag{93}$$

Λ contains the relaxation coefficients for each of the solution sets. For an averaging effect on all of the solutions, the structure of Λ is a diagonal matrix with all non-zero diagonal entries equal to $\frac{1}{M}$, where M is the number of equations. In this case, i.e., $\Lambda = \lambda \mathbf{I}$, convergence occurs if $||\mathrm{H}^T\mathrm{H}||_2 < 2$ for $\hat{\mathbf{x}}^{(0)} = 0$.

3.3.3 Multiplicative Algebraic Reconstruction Technique

In multiplicative ART (MART) given in [9], the reconstructed image has the lowest information content consistent with the fidelity and is intended for positive solutions. That is, the entropy of a RV,

$$h(\mathbf{x}) = -\int_{S(\mathbf{x})} p(\mathbf{x}) \log p(\mathbf{x}), \tag{94}$$

is maximized over its sample space, $S(x)$, while maintaining its fidelity. In other words, MART is a constrained optimization problem that can be expressed as

$$\hat{\mathbf{x}}_{MART} = \arg\min_{\mathbf{x}} \sum_{n=1}^{N} \mathbf{x}_n \ln \mathbf{x}_n \qquad \text{subject to} \quad \mathbf{y} = \mathrm{H}\mathbf{x}. \tag{95}$$

After applying Lagrangian multipliers to the expression, the n^{th} element of $\hat{\mathbf{x}}$ is expressed as

$$\hat{\mathbf{x}}_n^{(l+1)} = \left(\frac{\mathbf{y}_{i_l}}{\left\langle \mathrm{H}_{i_l}, \hat{\mathbf{x}}^{(l)} \right\rangle} \right)^{\lambda_l \mathrm{H}_{i_l n}} \hat{\mathbf{x}}_n^{(l)}, \tag{96}$$

where $\lambda_l \in (0, 1]$ with an initial positive vector $\hat{\mathbf{x}}^{(0)}$, i.e., $\hat{\mathbf{x}}_n^{(0)} > 0, \quad \forall n \in [0, N]$. Consistent cases show that MART converges to a maximum entropy solution yet its convergence behavior is unstable from noisy measurements of inconsistent data [9].

3.4 Computation of the Multi-Stack Observation Model

Accurate discretization of the forwarding model is needed for faithful reconstructions. This is where the i^{th} LR voxel and j^{th} HR voxel intersect in space. In the Multi-Stack model, this means computing

$$[\mathrm{H}]_{ij} = \int_{S_j} h(\mathrm{R}_r(\mathbf{s} - \mathrm{V}\mathbf{n}))d\mathbf{s}, \tag{97}$$

where S_j is the space for the j^{th} voxel of $\mathbf{x}$. The parallel sub-pixel spatial shifts previously used in SR has made the computation of the observation model, H, tractable. The LR voxels have always been multiples of the HR voxels with aligning boundaries. Thus, the shared space is a cuboid and computing its volume is accomplished with multiplication that simplifies the construction of H. Otherwise, if the LR warp is any affine transformation or the PSF is more than a box function, the computation of H presents a challenge for accurate discretization. This is indeed true for MS, where the rotation matrix, R_r (see Eq. (63)), leads to skewed boundaries between the LR and HR voxels. In general, the intersection of two voxels is a convex polytope, as Fig. 21 illustrates. Analytically computing the volume of a convex polytope is cited as a difficult problem with one such algorithm given in [42]. This technique is computationally expensive and not feasible with present workstation power. Weighing the volume with the PSF in the integrand further compounds the difficulty of analytic computation. Furthermore, the huge size of H makes the analytical methods of

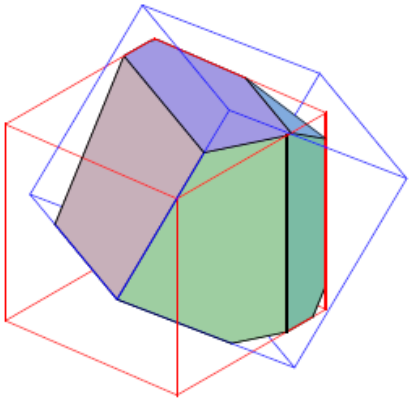

Figure 21: Convex polytope with shaded surfaces given by the intersection of two voxels.

computing all its elements simply impractical despite its sparseness from a small PSF and its banded structure.

Until recently, the SR literature has neither focused directly on the ways of computing H for affine warps nor the effects it has in the SRR when it is numerically approximated. In the CT domain, reconstructions based on POCS have suffered from salt and pepper noise when there are poor approximations used for computing H [38]. This effect in CT can be mitigated by increasing the number of projections for an averaging effect on the error. However, in SR there are much fewer projections, or LRIs, and the accuracy of the approximation is a definite issue. It has seemed to be an overlooked issue in SR, perhaps mainly due to the simple warps, i.e., translational. The circular symmetry[3] of the PSFs on the imaging sensors used in the majority of the SR so far has simplified the approximation as well. For example, Tipping et al. approximate the contribution from a LR and a HR image using Gaussian forms that depend only on the physical distance from the center location of the pixels [79]. That is, the ij^{th} entry of H is approximated as

$$[\hat{\mathrm{H}}]_{ij} = \exp\left(-\frac{||T_{\mathbf{x}}(i) - T_{\mathbf{y}}(j)||^2}{\sigma^2}\right), \tag{98}$$

where $T_{\mathbf{x}}(i) : \mathbb{Z} \rightarrow \mathbb{R}^3$ and $T_{\mathbf{y}}(j) : \mathbb{Z} \rightarrow \mathbb{R}^3$ transform row and column indices in H to the corresponding physical center space coordinates of the HRI and the LRIs, respectively. The

[3] A 2-D function with polar coordinates r and $\theta, h(r,\theta)$ is circularly symmetric if $h(r,\theta) = h(r,\theta')\forall\theta', \theta$.

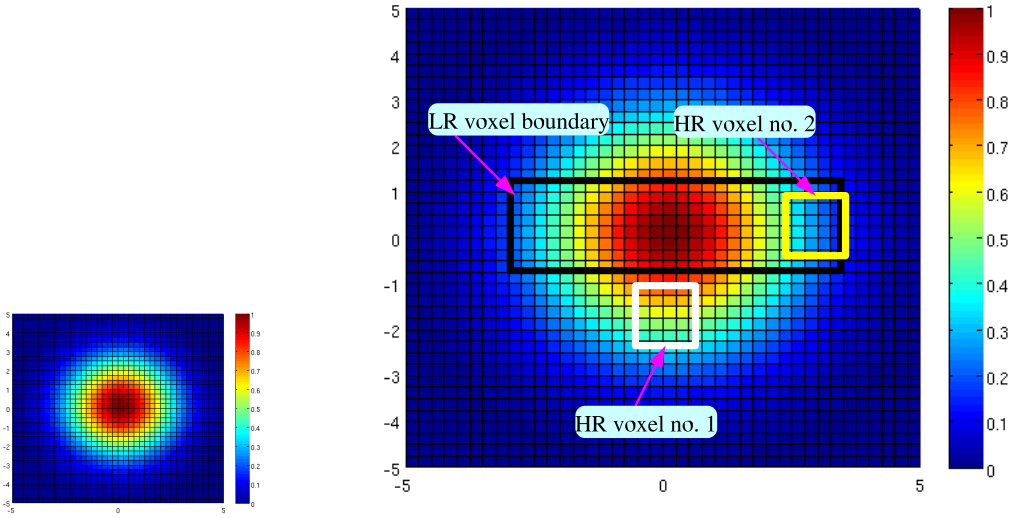

(a) (b)

Figure 22: Contribution modelling used in Eq. (98) from [79]. (a) A circularly-symmetric Gaussian PSF used in a LR pixel. (b) Overlayed boundaries of a rectangular LR pixel on the modeled Gaussian PSF with two different HR pixels. In this contribution model, the non-intersecting HR voxel (no. 1) gives an inaccurate higher contribution than the actual intersecting HR voxel (no. 2).

width of the PSF is related to σ. This approximation model works well when the PSF is or is approximately circularly-symmetric and the voxel is square [79]. However, if a pixel of a LRI is rectangular, as is the case in multi-slice MRI, then this approximation poorly approximates the contribution. This effect is demonstrated in Fig. 22. The shape of the LR and HR voxels are rectangle and square, respectively. Thus, the LR voxel effectively has a long and short axis. A HR voxel that is adjacent to a LRI voxel in the direction of its short axis is not covered, but this will lead to a higher contribution than a HR voxel that is already included in the direction of the long axis. Furthermore, the approximation leads to large inefficient computation and memory requirements, because the infinite support of Eq. (98) produces nonzero entries everywhere in $\hat{\mathrm{H}}$. Without any clipping or thresholding schemes, both computation and memory requirements have asymptotic orders of $O(MN)$.

Rochefort appropriately made some of these observations about the numerical approximation of models by providing quantitative comparisons in the SRRs based on different

construction methods of H when the warps include affine transformations [63]. In their methods, Rochefort et al. first assume the continuous HRI can be represented by the discrete HR estimate with interpolation kernels based on B-splines [60]. Then, the construction of H is divided into three categories based on point-wise interpolation: (1) exact (2) convolve-then-warp and, (3) warp-then-convolve approximations. Exact computation is limited to only translational warps with box PSFs, and certainly could not apply to MS. The convolve-then-warp approximation assumes the warp can be well-approximated with translational motion typically due to the small support region of the PSF. As a consequence, it is unable to capture rotations, sheers, or scale variations very well. The rotation matrices in MS would thus be disqualified from using the convolve-then-warp method. The warp-then-convolve approximation leads to expressing the estimate of the HRI with samples of the true HRIs that are weighted with a warped B-spline kernel function. Results demonstrate high precision for rotational warps in the SRR, thus proving it to be a strong candidate for constructing the MS observation model. Rochefort et al. further recognize that even this construction method is inaccurate for scale changes and propose a new construction method of H based on L^2 function approximation that goes well beyond the requirements of the MS warp.

Prior to the construction methods of Rochefort et al., we developed our own competing construction method for the MS observation model. In hindsight, the warp-then-convolve approximation by Rochefort et al. may have been useful for constructing the MS observation matrix for its accuracy and efficiency. Nevertheless, this alternative is based on stepping through every voxel of the LRIs with accuracy controlled by the length of the stride. For every step made within a LR voxel, the corresponding location in image space of the HRI is determined by evaluating the location of the warp. This means every step will contribute to some entry in H. The process of stepping may omit computing some space of the voxel with an error in volume proportional to the step stride. Otherwise, stepping will include partially computing the volume of an outside neighboring voxel. The algorithm is given in Appendix C and Fig. 23 illustrates the maximum error of the volume computed for a given step size, δ, in comparison with the true volume of the voxel. If the PSF is a box car, (i.e.,

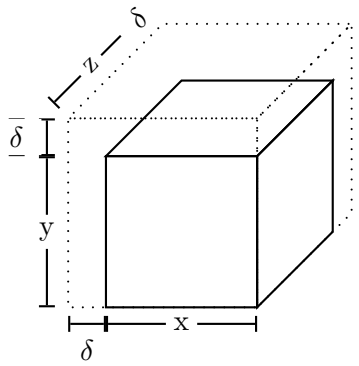

Figure 23: A LR voxel with a solid line and its computed boundary with a dotted-line.

unity) and the sides have lengths, x, y, and z, then the normalized error in the volume of a HR voxel is bounded by

$$e_{voxel}(\delta) < \frac{(x+\delta)(y+\delta)(z+\delta) - xyz}{xyz} \quad (99)$$

$$= \frac{\delta(xy+xz+yz) + \delta^2(x+y+z) + \delta^3}{xyz}. \quad (100)$$

Clearly, $e_{voxel}(\delta) \to 0$ as $\delta \to 0$. Asymptotic analysis of the running time for the construction algorithm given in Appendix C is $O(\frac{M|\mathsf{supp}(h)|}{\delta^3})$, where $\mathsf{supp}(h) = \{\mathbf{s}|h(\mathbf{s}) \neq 0\}$ and $|\mathsf{supp}(h)|$ is its volume. Hence, the error in volume for each voxel can be directly attenuated at the cost of a longer running time in its construction.

3.4.1 Measuring the Fidelity of the Construction

To avoid confusing the fidelity of the above construction method to the performance of a SRR technique, the estimate of H, denoted as $\hat{\mathrm{H}}(\delta)$, should be compared directly with its true value. Of course, this is not possible in general. An experiment needs to be restricted to observation models where H can be computed without any error. Hence, we will compare our construction method with an observation process of parallel sub-pixel spatial shifts, where the LR voxels are multiples of the HR voxels, share boundaries, and use a box PSF. This way, H is pre-determined. The metric,

$$e_{\hat{\mathrm{H}}}(\delta) = \frac{||\mathrm{H} - \hat{\mathrm{H}}(\delta)||_F}{||\mathrm{H}||_F}, \quad (101)$$

indicates the normalized error from the discretization of the observation model. Computing Eq. (101) with realistic matrix sizes presents a further computational challenge of L^2 norms.

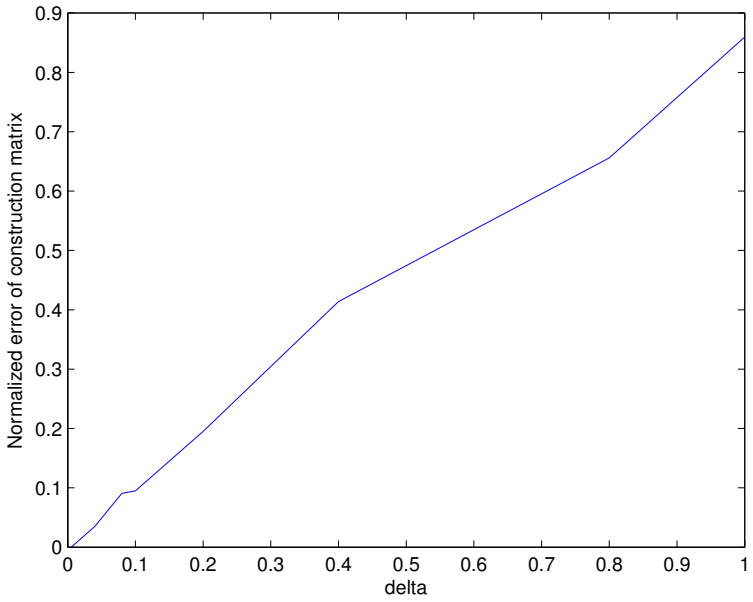

Figure 24: Frobenius norm of construction error as a function of the step size, δ.

Instead, the Frobenius norm is used to plot the normalized construction error as a function of δ. In this case, there were eight LRIs with a pixel size equal to eight HR pixels, borders aligned, with parallel one HR pixel shifts. The plot of Eq. (101) in this configuration is shown in Fig. 24, which agrees with the convergence of error in Eq. (99).

3.5 Conclusion

Multi-Stack is an instance of the E&F SR observation model that departs from the traditional sub-pixel shifts and, instead, relies on rotational warps. The derived noise of MS remains uncorrelated and Gaussian, provided there is no cross-talk interference, which leads to equivalences in the least-squares and maximum-likelihood estimates. Each acquisition resembles a localized tomographic projection that recommends the use of related algebraic reconstruction techniques from the computed tomography domain. The construction (or system) error for the discrete observation model can be made sufficiently close to zero from the true known discrete model by adjusting the step size.

CHAPTER IV

VALIDATION OF MULTI-STACK

The evaluation of the Multi-Stack method includes testing on both synthetic and real Fast Spin Echo-Inversion Recovery (FSE-IR) multi-slice MRI data given in this chapter. Maximum-likelihood (ML) estimation is applied so that there is not any bias in the SRR. The three main experiments to support MS validation in this chapter are as follows.

1. The forwarding model of the multi-slice MR imaging method using the Shepp-Logan phantom (SLP) is simulated, followed by super-resolution reconstruction.

2. A scan of an ex-vivo brain with the MS protocol is acquired. Then the SRR is compared to one HR scan of comparable resolution. SNR efficiencies are then measured.

3. Six data sets of in-vivo brains[1] using the FSE-IR multi-slice acquisition with the MS protocol are acquired, followed by super-resolution reconstruction.

4.1 Simulated Multi-Stack Experiments

The purpose of using synthetic data is to rule out any complication such as motion or unknown blurring. Parameters in the observation model include the

1. number of LRIs: P,

2. slice selection profile: $h(\mathbf{s})$,

3. slice thickness or the support of slice selection profile: $\mathsf{supp}(h(\mathbf{s}))$,

4. sampling period of slice selection profiles, T_{SS}, and

5. SNR of data.

[1]Human subject experiments were carried out with Institutional Review Board approval.

Each of these parameters has been varied in a series of simulations using the standard Shepp-Logan Phantom (SLP) from computed tomography (CT) for the validation process of MS using the ART, SART, and MART. Since the true underlying image (ground truth) is known, the fidelity of the reconstructions can be observed using the normalized mean square error (NMSE):

$$e_{NMSE} = \frac{\|\mathbf{x} - \hat{\mathbf{x}}\|_2}{\|\mathbf{x}\|_2}. \tag{102}$$

A fully-determined inversion problem can be configured with a variety of acquisition parameters. To evaluate the robustness of MS, comparisons are carried out of NMSE dynamics for fully-determined inversion problems with equal hypothetical acquisition times but varying numbers of LRIs, with correspondingly varied slice thickness. Under- and over-determined MS systems are tested as well with either the number of LRIs or the slice thickness changed.

4.1.1 Computing Ground Truth

To make correct quantitative comparisons between the SRR and the ground truth, the SLP needs to have the same sampling rate as the HR image. The hard-limited boundaries or discontinuities of the ellipses in the SLP causes aliasing at any sampling rate, as shown in Fig. 25. This is a recognized problem, causing singularities at the edges of the ellipsoids in some computed tomography reconstructions [85]. In avoiding aliasing from a low sampling rate we have first sampled the SLP on a HR lattice of 2048×2048 pixels and then used a low pass filter followed by down-sampling to a 256×256 grid. We observed that the sampling grid of 2048×2048 showed an imperceptible amount of pixelation when compared to grids of yet higher resolution.

4.1.2 Super-resolution Reconstruction using Different Step Sizes

The estimation of H for the sub-pixel shifts using the algorithm from Appendix C can be constructed so that it is sufficiently close to its true value by adjusting the step size parameter of the sampled voxel overlap, δ (see Appendix 3.4). However, the degree of error for $\hat{\mathrm{H}}(\delta)$ using rotational warps instead of translational warps remains unknown. While it may be difficult to compute H with a known precision for a MS configuration, the NMSE of the SRR using varying step sizes can be determined as a function of δ. Fig. 27 shows

(a) (b) (c)

Figure 25: (a)Sampled version of the SLP on 256×256 lattice after down-sampling from low-pass filtered 2048×2048 lattice with a (b) cropped portion and a (c) cropped portion of an aliased SLP.

several NMSE vs. iteration plots using the ART with equal parameters in the SRR except for different values of δ. The plot shows diminishing differences in NSME as $\delta \to 0$. Unless otherwise stated, all experiments hereafter will use a δ value of 0.01 spatial units.

4.1.3 Generating Projection Data

Generating the MS synthetic data should preserve its high quality and minimize the effects of interpolation from rotation. The SLP lattice with size 2048×2048 is used as the input to the discretized observation model forcing the PSF to be up-sampled by a factor of 8 in each dimension so that it is consistent with the sampling rate. Nearest neighbor, bilinear, and bicubic interpolation methods can be used to determine the values at rotated grid points. Already, this fine lattice should diminish the interpolation effects once it is down-sampled to the designated lattice of 256×256. The interpolation results given by DiBella et al. were used as a guideline for selecting the appropriate scheme for generating the projection data [18]. Their results show low error levels in computed tomography related reconstructions for simulated projections that use bilinear and bicubic interpolation. This agrees with our own experiments given in Table 6. The normalized error from the estimate of the projected interpolated data, $\hat{\mathbf{y}}$, and the projected true data, $\hat{\mathrm{H}}(\delta)\mathbf{x}$, approach each other as the lattice density increases. Hereafter, the bicubic interpolation method was used to generate the MS synthetic data using a lattice of 2048×2048.

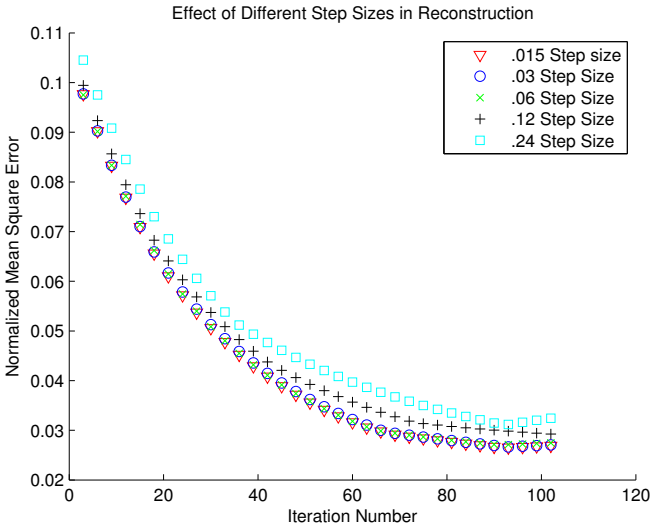

Figure 26: Effect of NMSE from different step integration sizes given in Appendix C.

Table 6: Normalized error in estimating noiseless projection data for 8 LR images, 8 pixel slice thickness, $\delta = 0.01$.

Interpolation	$\frac{\|\hat{\mathrm{H}}(\delta)\mathbf{x}-\hat{\mathbf{y}}\|}{\|\hat{\mathrm{H}}(\delta)\mathbf{x}\|}$ 2048×2048	$\frac{\|\hat{\mathrm{H}}(\delta)\mathbf{x}-\hat{\mathbf{y}}\|}{\|\hat{\mathrm{H}}(\delta)\mathbf{x}\|}$ 1024×1024	$\frac{\|\hat{\mathrm{H}}(\delta)\mathbf{x}-\hat{\mathbf{y}}\|}{\|\hat{\mathrm{H}}(\delta)\mathbf{x}\|}$ 512×512
Nearest Neighbor	.009	.021	.04
Bilinear	.005	.012	.021
Bicubic	.003	.009	.015

4.1.4 Reconstructing a Point Source

The impulse response can help characterize the artifacts in the SRRs. The impulse response for each LRS is a blur in the slice selection direction. Figure 27 shows the impulse response using 8 LRSs, 8 pixel slice thickness, and a box PSF. The SRRs using ART, MART, and SART are given in Fig. 27(j,k,l). The full width at half maximum measurements are 1.9, 1.1, and 2.0 pixels for ART, MART and SART, respectively.

4.1.5 Simulation Results

The following images show the center portion of the SRRs that captures the dynamics, fidelity, and residual artifacts from the various cases described in Table 7. These images correspond to the NMSE minima from the error vs iteration plots, which are also shown. Center line profiles of some of the selected SRRs and their deviation from ground truth (Fig. 28) are included. One iteration using either the ART and MART is a composition of

projections over all M sets.

Table 7: Figure listing of SLP experiments with varying parameters.

Case	Figures of SRRs	Plots of NMSE & Line Profiles
Ground Truth Image	28(b)	28(c)
No. of LRIs, P	29	30
Slice thickness	31	32
SNR	33	34
Gaussian PSF	35	36
Equal stack to slice thickness	37	38
Cross-talk Interference	39	40
Long iterations	-	42
Relaxation rates (λ)	-	41

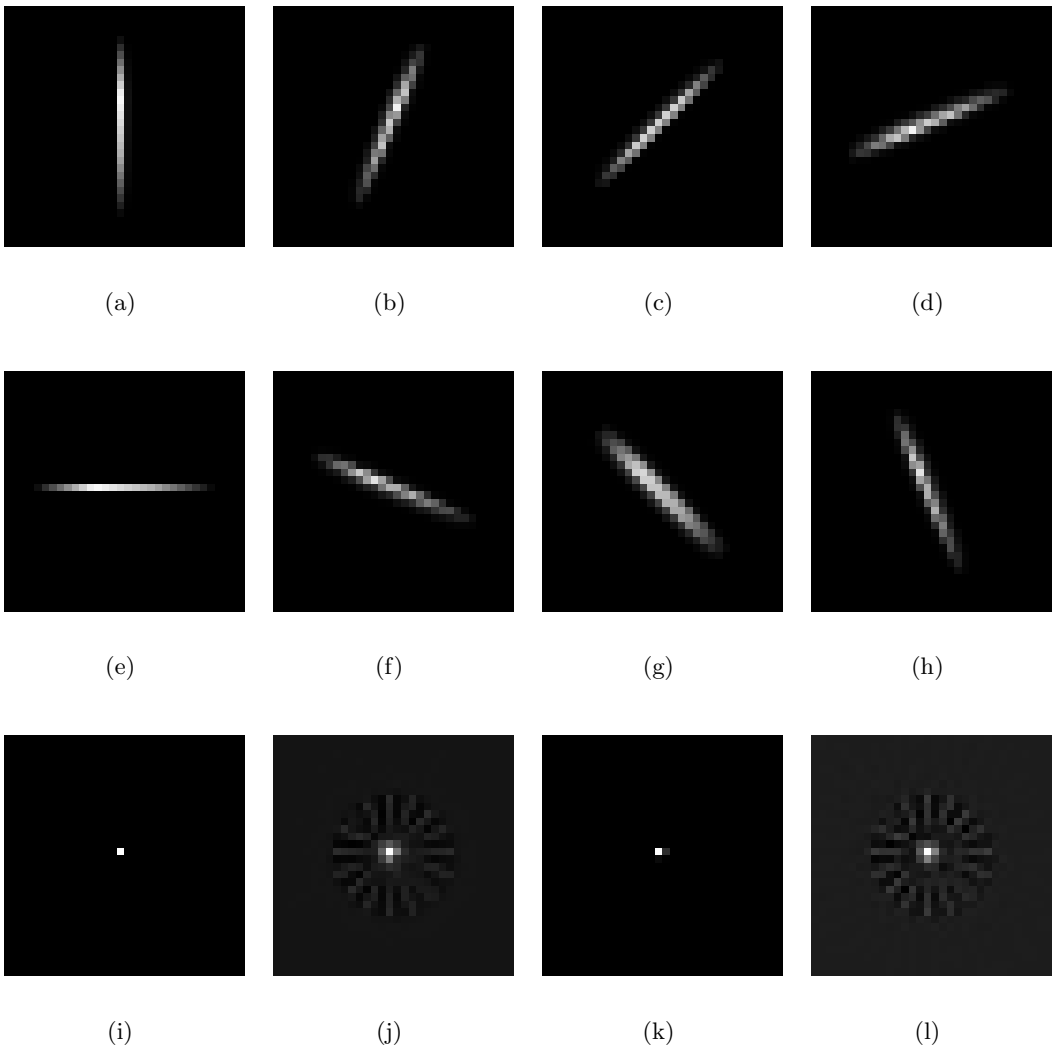

Figure 27: (a-h) The impulse response for a Multi-Stack configuration using 8 LRSs, 8 pixel slice thickness and distance with a box slice selection function from a (i) point source. The SRRs using the (j) ART (k) MART and (l) SART methods.

(a) (b) (c)

Figure 28: (a) True SLP with (b) cropped portion and its (c) line profile.

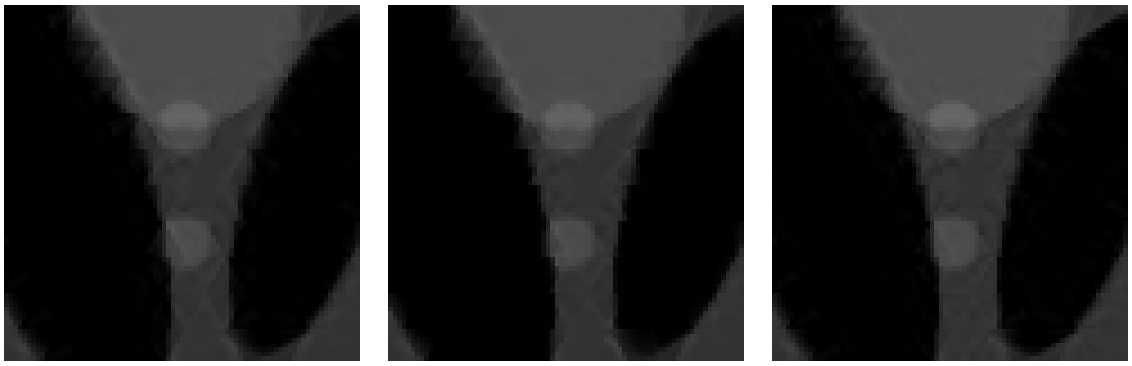

(a) (b) (c)

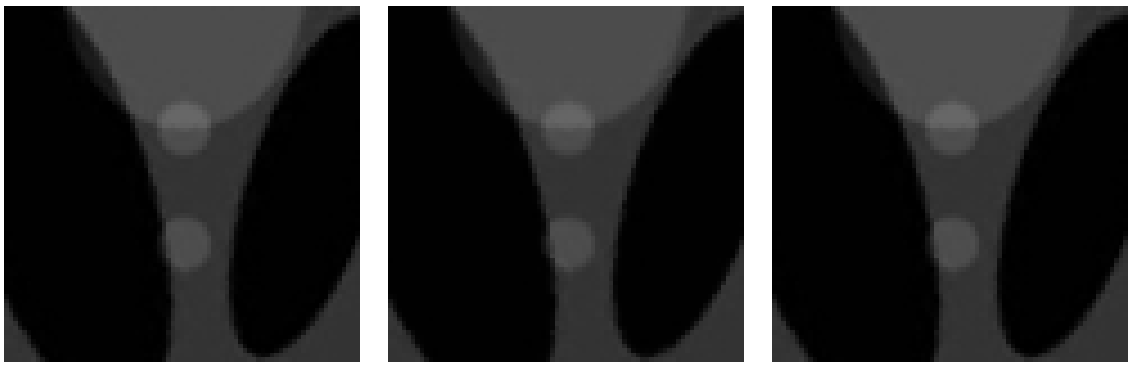

(d) (e) (f)

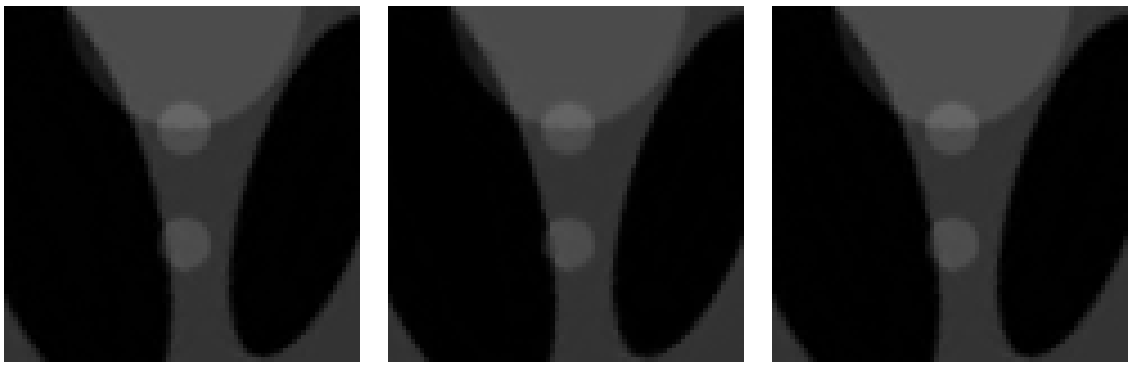

(g) (h) (i)

$\frac{M}{N}$	ART	MART	SART
0.3750 (under-)	(a)	(b)	(c)
1 (fully-)	(d)	(e)	(f)
1750 (over-)	(g)	(h)	(i)

Figure 29: Under-, fully-, and over-determined SRRs using POCS on a noiseless SLP at constant 8 pixel slice thickness, box PSF, and relaxation factor, $\lambda = 10^{-3}$ for (a-c) 3, (d-f) 8, (g-i) and 11 LRIs. The measurements-to-uknowns is $\frac{M}{N}$. Images correspond to NMSE minima.

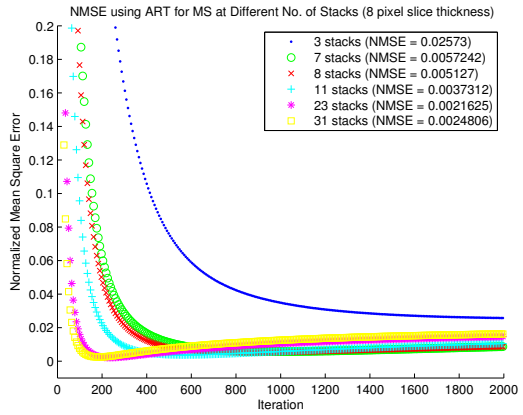

(a)

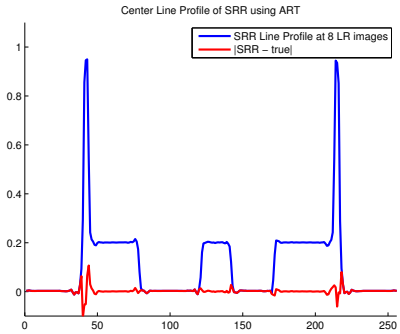

(b)

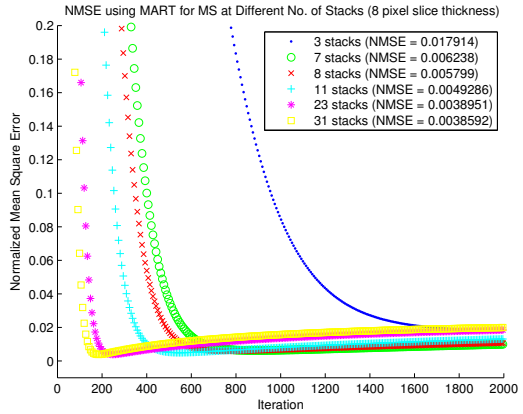

(c)

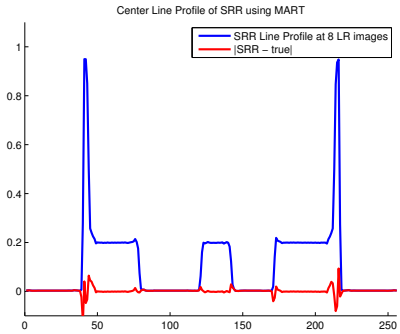

(d)

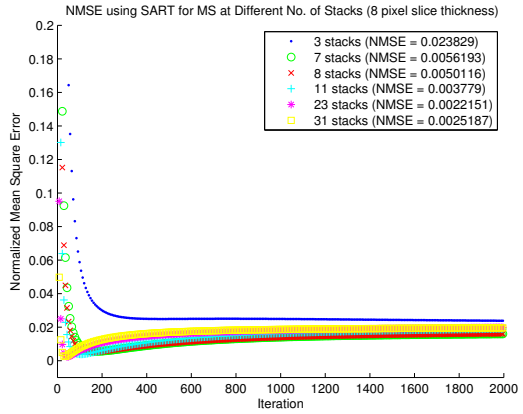

(e)

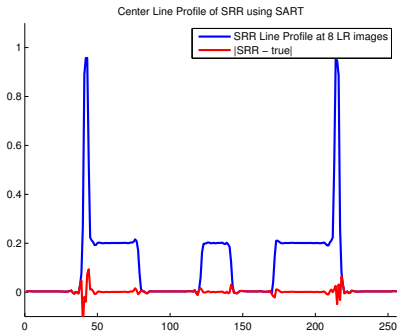

(f)

Figure 30: NMSE vs. Iteration at varying number of LRIs using BOX PSF for (a) ART, (c)MART and (e)SART with center line profiles at 8 LRIs.

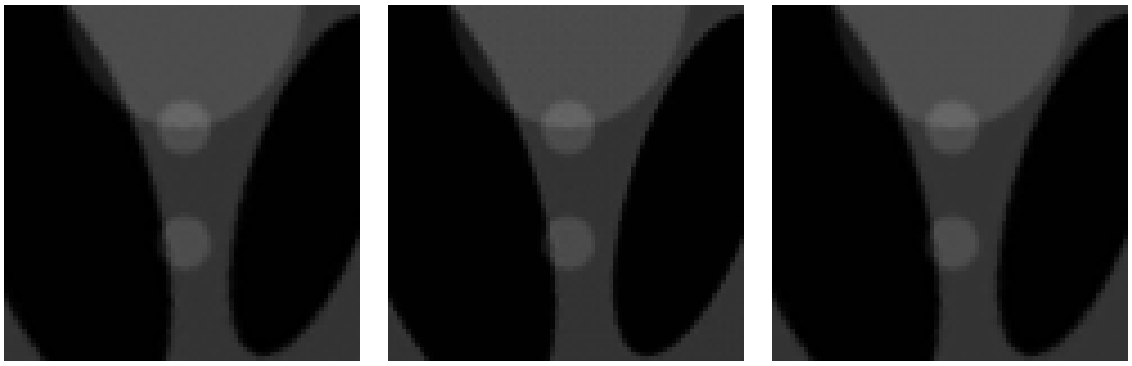

(a) (b) (c)

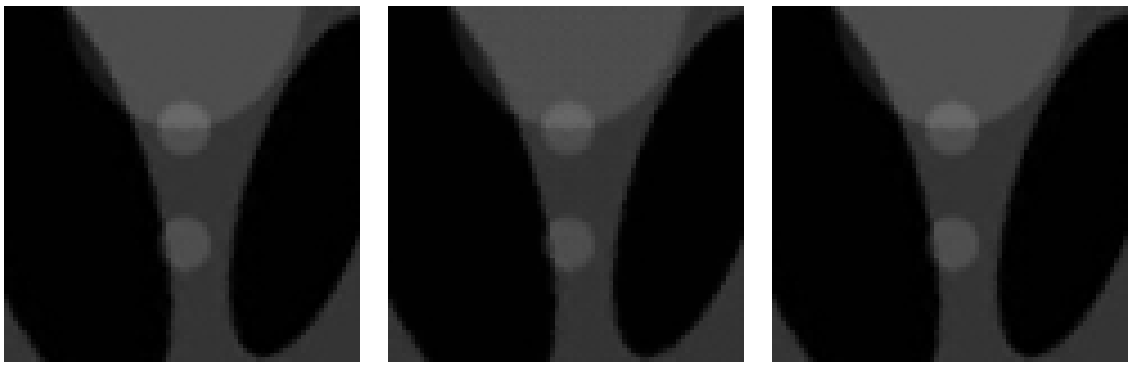

(d) (e) (f)

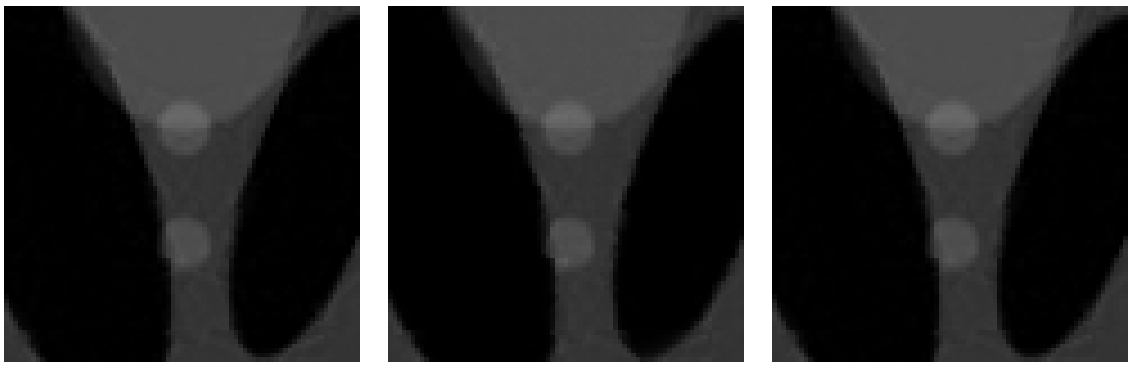

(g) (h) (i)

Pixel Thickness	ART	MART	SART
4 (over-)	(a)	(b)	(c)
8 (fully-)	(d)	(e)	(f)
16 (under-)	(g)	(h)	(i)

Figure 31: Under-, fully-, and over-determined SRRs using ART, SART, and MART on noiseless SLP data for varying slice thickness at constant eight LRIs, box PSF, equal relaxation factors at $\lambda = 10^{-3}$, (a-c) 4, (d-f) 8, (g-i) and 16 pixel slice thickness.

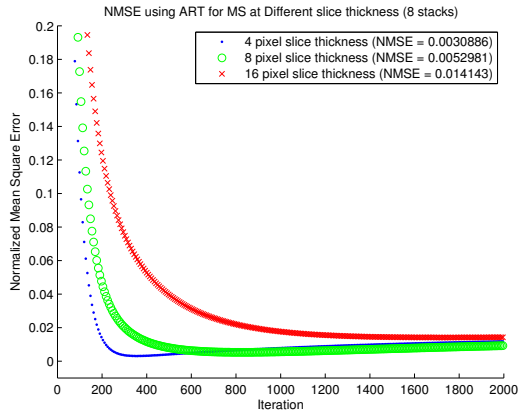

(a)

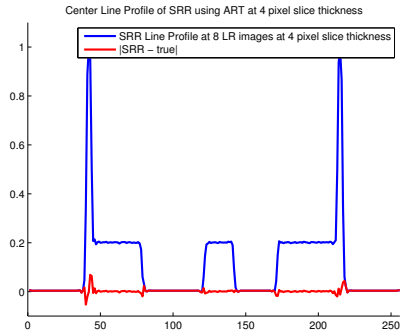

(b)

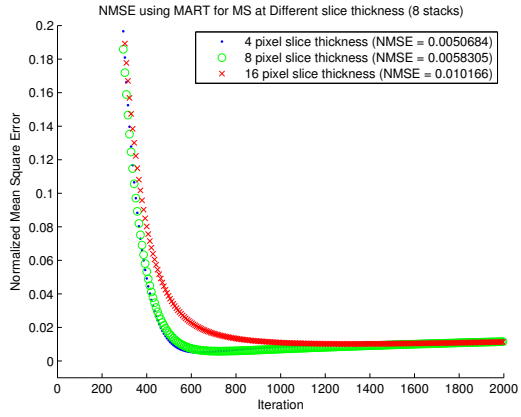

(c)

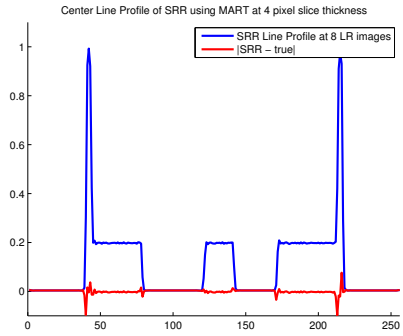

(d)

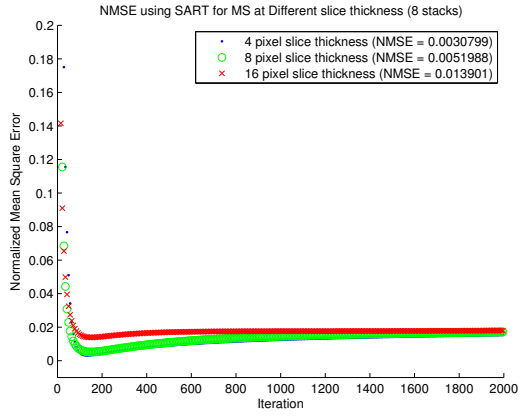

(e)

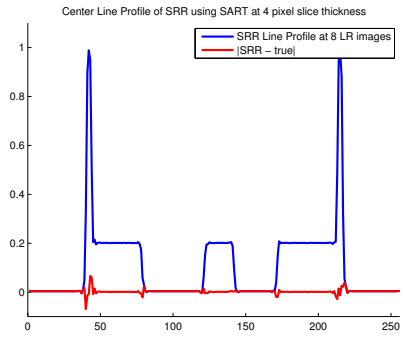

(f)

Figure 32: NMSE vs. Iteration at varying slice thickness using eight LRIs for ART, SART and MART.

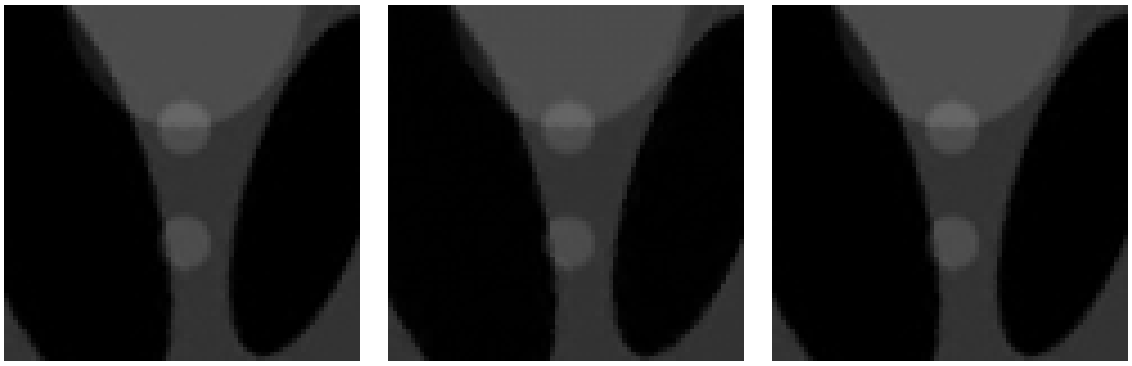

(a) (b) (c)

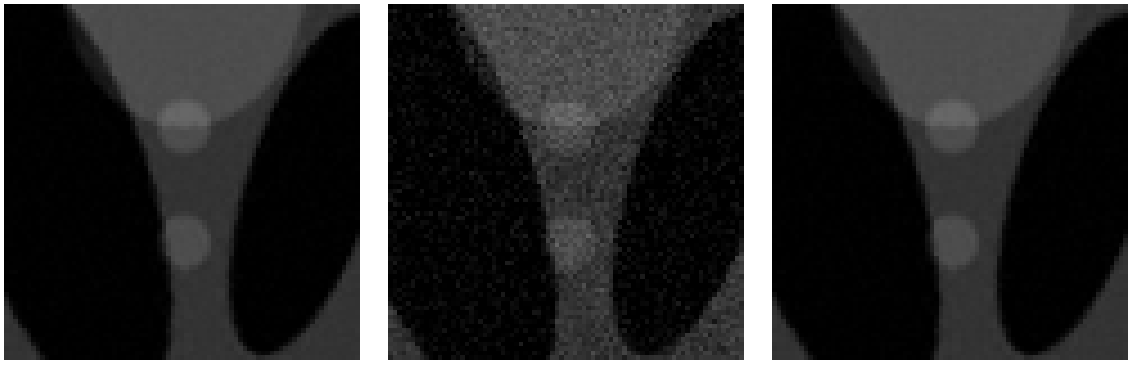

(d) (e) (f)

(g) (h) (i)

SNR	ART	MART	SART
76dB	(a)	(b)	(c)
56dB	(d)	(e)	(f)
36dB	(g)	(h)	(i)

Figure 33: Fully-determined SRRs using ART, SART, and MART on noisy SLP data at constant eight pixel slice thickness and eight LRIs, box PSF, equal relaxation factors at $\lambda = 10^{-3}$, (a-c) 76 dB, (d-f) 56dB, (g-i) and 36dB.

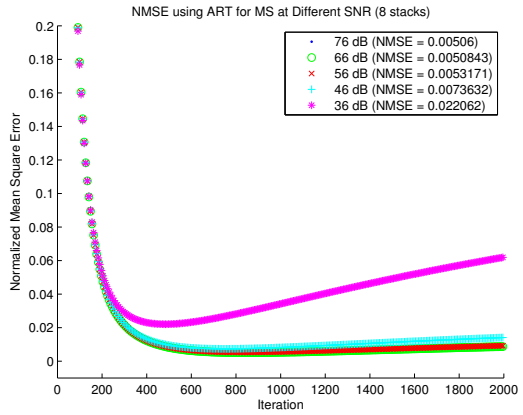

(a)

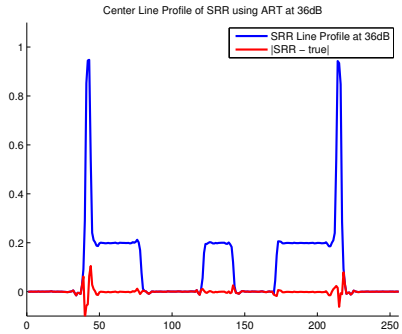

(b)

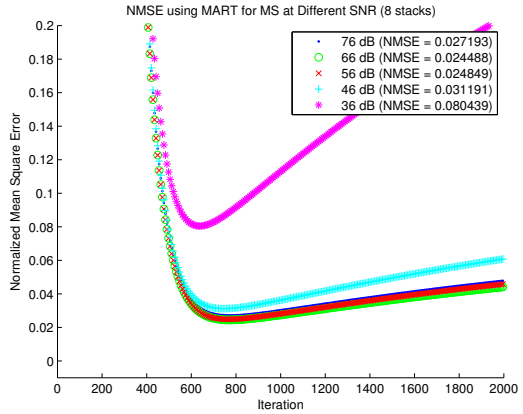

(c)

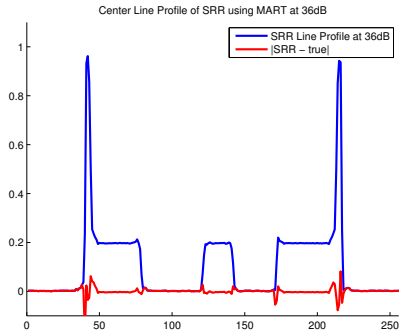

(d)

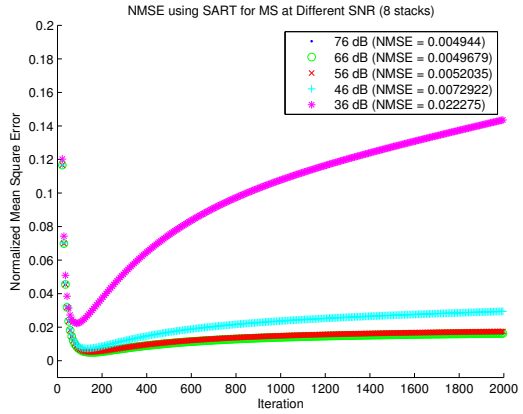

(e)

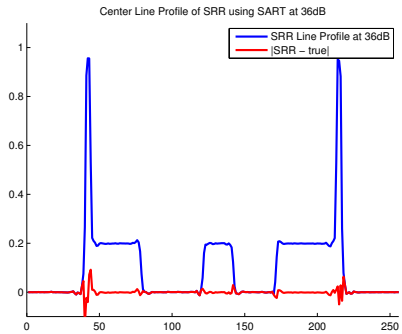

(f)

Figure 34: NMSE vs. Iteration at varying SNR using eight LRIs and eight pixel slice thickness for ART, SART and MART.

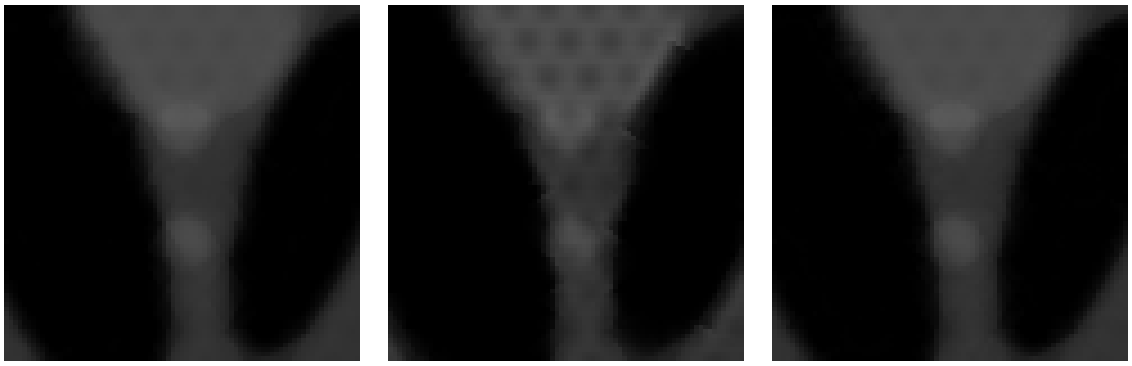

(a) (b) (c)

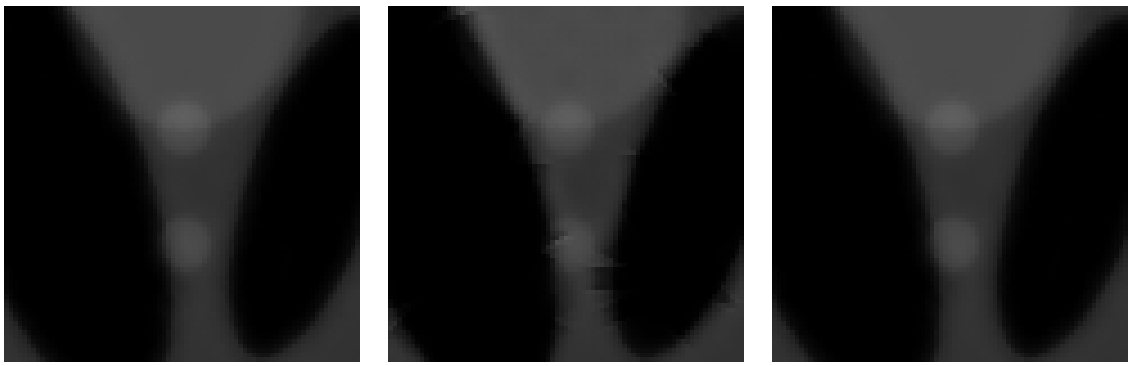

(d) (e) (f)

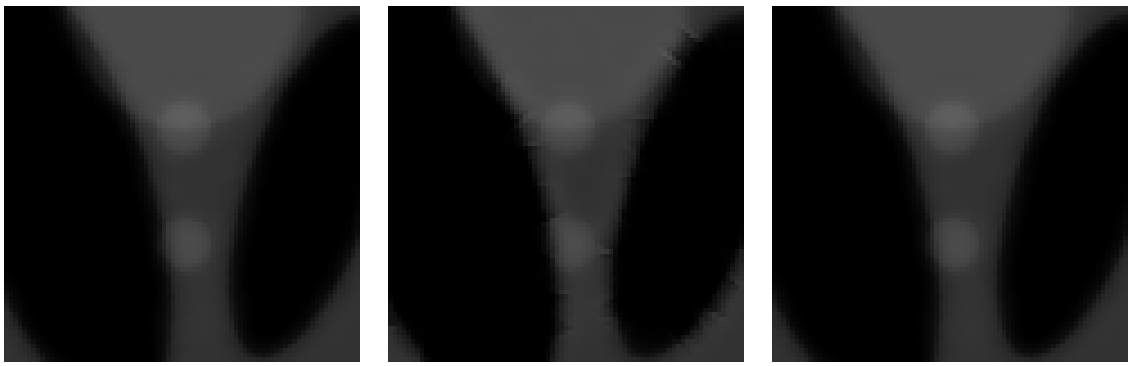

(g) (h) (i)

$\frac{M}{N}$	ART	MART	SART
0.3750 (under-)	(a)	(b)	(c)
1 (fully-)	(d)	(e)	(f)
1.3750 (over-)	(g)	(h)	(i)

Figure 35: Under-, fully-, and over-determined SRRs using ART, SART, and MART on noiseless SLP data for varying number of LRIs at constant eight pixel slice thickness, Gaussian PSF (FWHM = slice distance =8 pixels), equal relaxation factors at $\lambda = 10^{-3}$, (a-c) 3 LR images, (d-f) 8 LRIs, (g-i) and 11 LRIs. The ratio of measurements to unknowns is given as $\frac{M}{N}$.

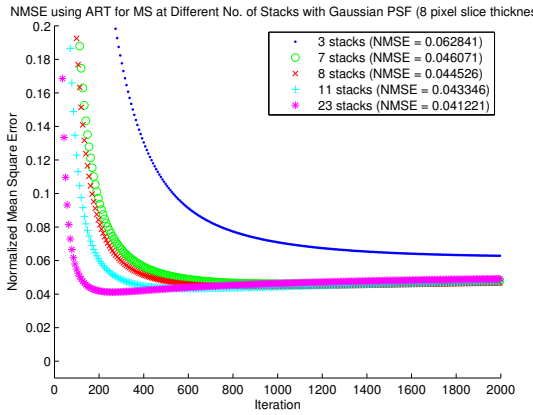

(a)

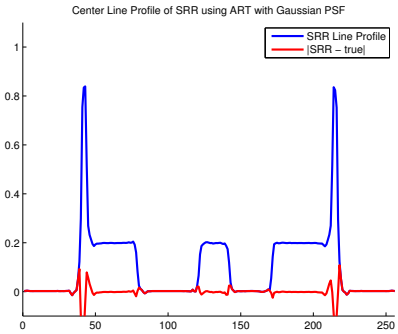

(b)

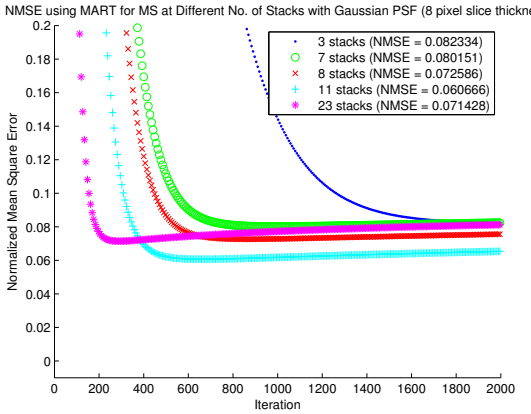

(c)

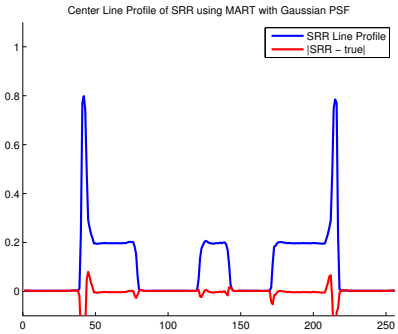

(d)

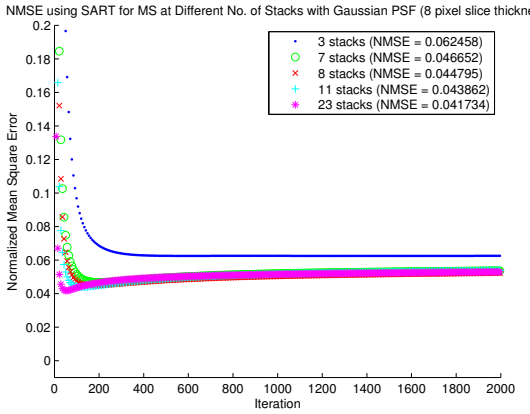

(e)

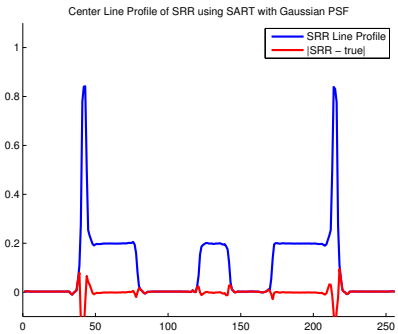

(f)

Figure 36: NMSE vs. Iteration at varying number of LRIs using Gaussian PSF (FWHM = slice distance =8 pixels) for (a) ART, (b)MART and (c)SART.

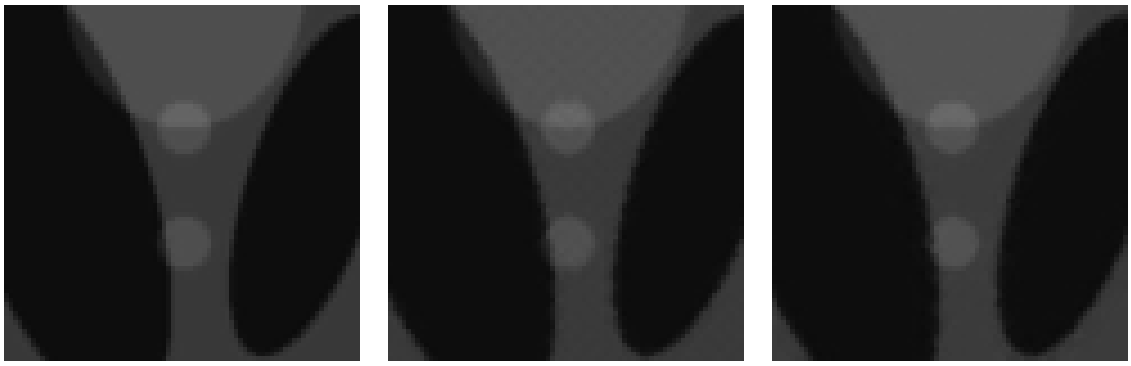

(a) (b) (c)

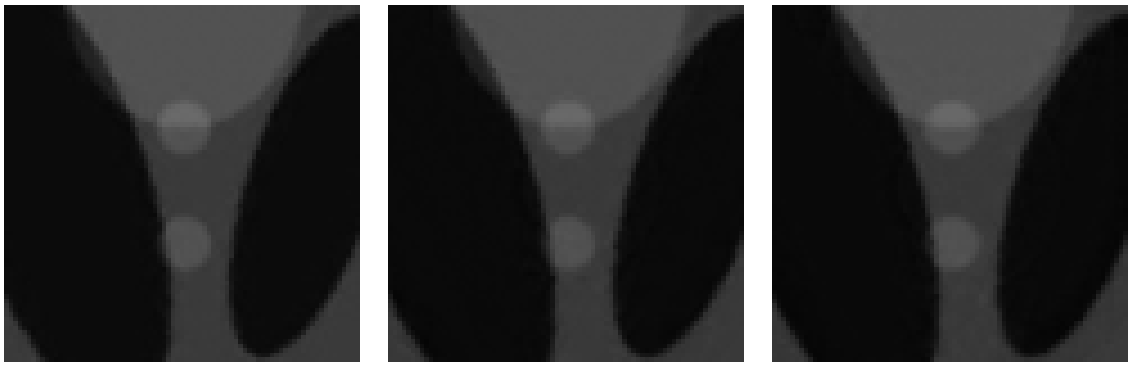

(d) (e) (f)

(a) 2/2	(b) 4/4	(c) 6/6
(d) 8/8	(e) 10/10	(f) 12/12

Figure 37: SRRs using ART for MS at Equal number of LRIs to thickness ratios

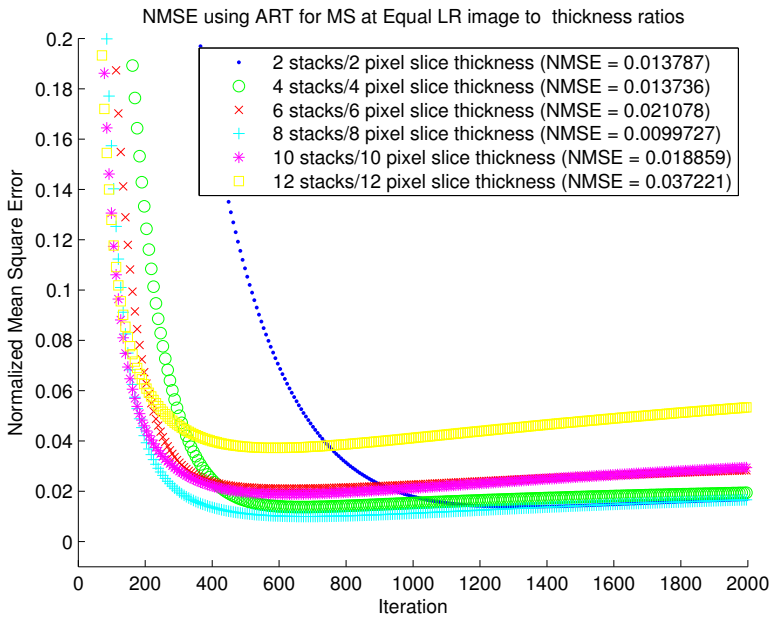

(a)

Figure 38: NMSEs vs Iterations using ART for MS at Equal number of LRIs to thickness ratios

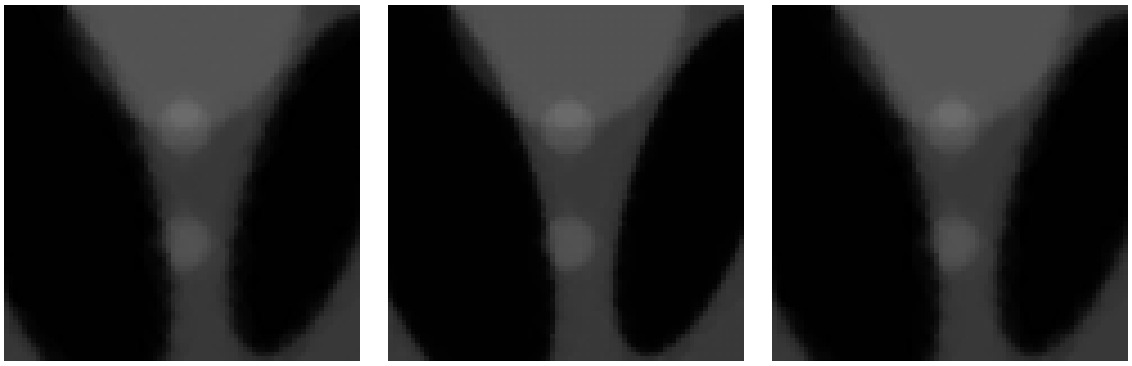

(a) (b) (c)

Figure 39: SRRs using POCS for overlapping PSFs or cross-talk interference (8 pixel slice thickness, 6 pixel slice distance) (a) ART (b) MART (c) SART

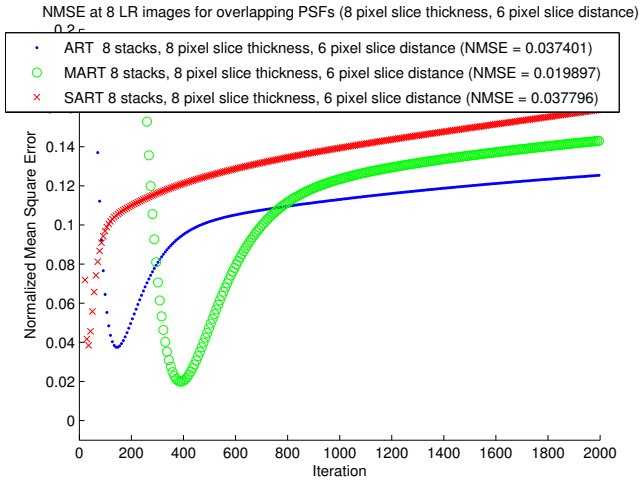

(a)

Figure 40: NMSEs vs Iterations using POCS for overlapping PSFs or cross-talk interference (8 pixel slice thickness, 6 pixel slice distance).

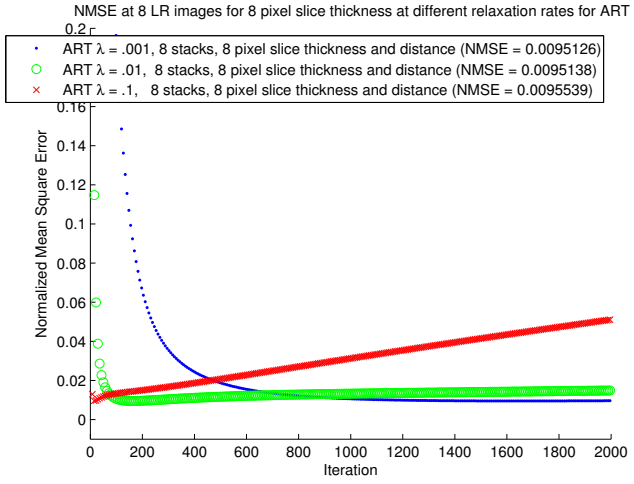

(a)

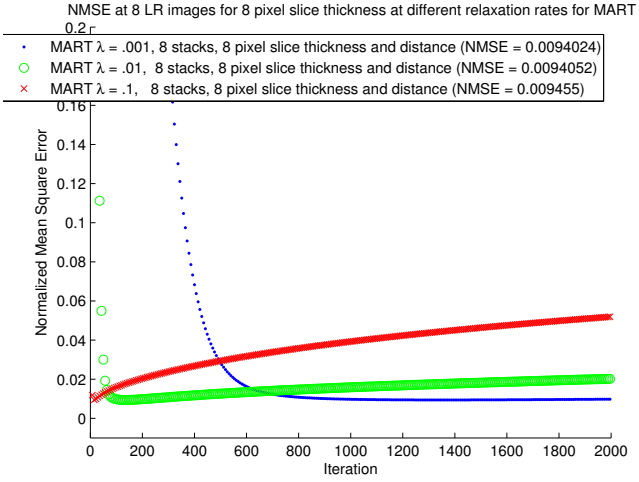

(b)

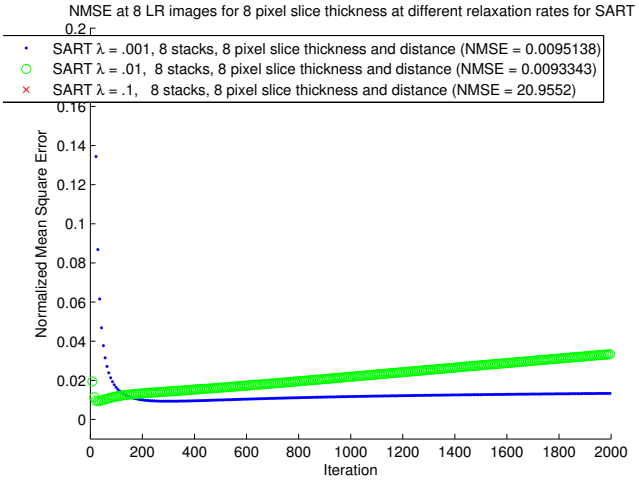

(c)

Figure 41: NMSE vs. Iteration at different relaxation rates λ=.001, .01, .1, using the (a) ART, (b)MART and (c)SART.

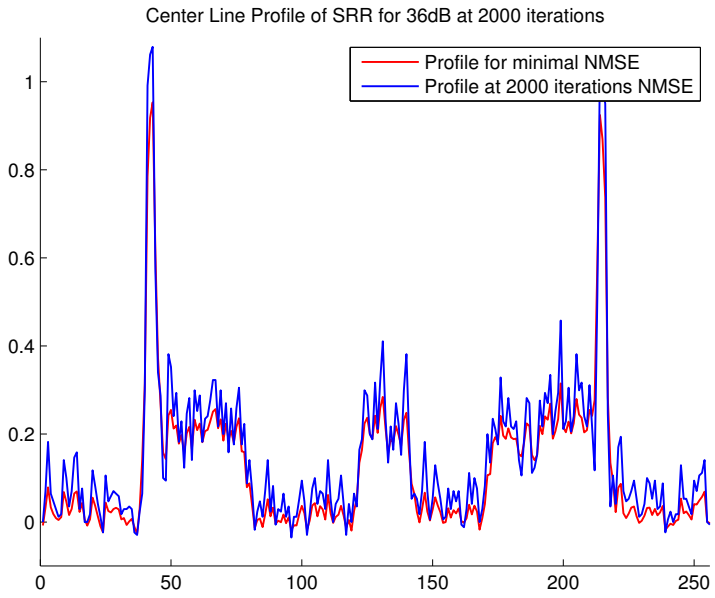

(a)

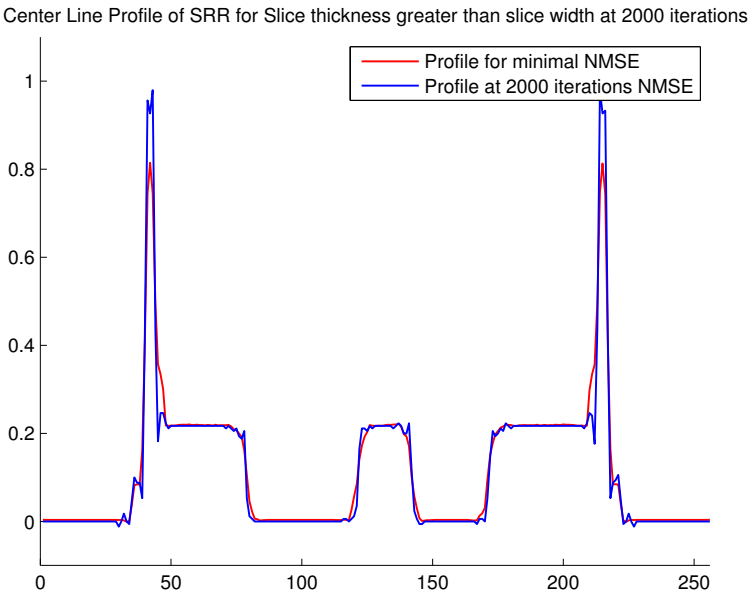

(b)

Figure 42: SLP line profile at 2000 iterations, where NMSE diverges from minima (a) 36 dB (b) slice thickness less than slice distance.

4.1.6 Multi-Stack Observations on Shepp-Logan Phantom Data

Increasing the number of LRIs while maintaining a constant slice thickness and width (Figs. 29 and 30) for the slice profile shows monotonically decreasing NMSE levels for the ART, SART, and MART. Over-determined cases for MS show diminishing returns on lower NMSE for an increasing number of LRIs. Image artifacts for the under-determined systems include partial blurring and streaking similar to that seen in under-determined computed tomography reconstructions, and some overshoot at sharp edges. The visual differences in the SRRs become indiscernible as MS moves from a fully- to an over-determined case. However, overshoot artifact near edges persists in the SRRs despite increases in the number of LRIs, as shown in the center line profiles (Fig. 30(b,d,f)). These same observations apply for the varying size of the slice thickness given a constant number of LRIs (Figs. 31 and 32). The MART returned higher NMSE levels than ART and SART for noisy data (Figs. 33 and 34) and the difference is noticeable in the SRR of the SLP. The SNR at 36dB showed increasing NMSE deviation from the ground truth after a given number of iterations. This is mainly attributed to the nature of iterative methods. They recover low before high-frequency content, and the increase in NMSE is due to the exclusive recovery of the high-frequency noise [50]. The Gaussian envelope slice excitation gives comparable results to the box-PSF (Figs. 29 and 36). The under-determined case in MART for a Gaussian PSF shows a waffle-like artifact in the SRR (Fig. 35(b)). The under-determined case in ART and SART for a Gaussian PSF show blurred edges and comparatively less streaking artifact than the equivalent box-PSF SRRs in Figs. 29. The equal LRI-to-thickness ratio of one yields comparable NMSE levels (Figs. 37 and 38). Increasing the LRIs for the equal image-to-thickness ratio shows faster convergence rates towards a minimum but faster rates to higher NMSE levels. In the case of cross-talk interference, a window of low NMSE levels are shown (Figs. 39 and 40) with the MART demonstrated as superior to the other techniques. The edge overshoot exacerbates as the iterations go beyond the optimal iteration (in the NMSE sense) for some of the selected SRRs, as shown in Fig. 42. Consequently, iterating longer does not always give the best (NMSE) results when using ML estimates. Decreasing the relaxation values (λ) results in a slower convergence towards their respective minima.

However, smaller relaxation values give lower NMSE values. Increasing the relaxation values also increases the rate of divergence once the reconstruction goes beyond the optimal NMSE value, as shown in Fig. 41. The stopping criterion remains a challenge, suggesting the use of regularization and priors on the HRI estimate. There is a high correlation between the information in neighboring tomographic projections in CT domain [31]. As a way to further improve the convergence rate of the ART, Hounsfield ordered the tomographic projections in such a manner that successive tomographic projections are well separated during the reconstruction. This arrangement could be easily applied to MS as well so that the total sum difference of consecutive scanning orientations is maximized. For example, instead of scanning four scans that are ordered in the system matrix as $\{0^o, 45^o, 90^o, 135^o\}$, the system becomes $\{0^o, 90^o, 45^o, 135^o\}$. Thus the sum of consecutive differences changes from 270^o to 360^o.

4.2 Multi-Stack Experiments on MRI Data

Seven MRI data studies were used to validate the MS approach to SR. Six studies are of in-vivo brain specimens from healthy human volunteers while the remaining is an ex-vivo brain. The scanning orientation with respect to the anatomy in all studies is distributed from the sagittal (with a slice plane normal in the left-right direction) to coronal (with a slice plane normal in the front-back direction) back to sagittal. This means the LR imagery of any scan becomes apparent through any multi-planar reformat (MPR) in the axial direction. Therefore, each image plane in the axial direction of the HR estimate is a separate 2-D SRR problem. This reduction in dimensionality thus reduces the computational complexity as well. The number, P, of LRSs ranged from six to eight and were all fully-determined.

Similar to the synthetic experiments, the SRR effects using a variety of parameters are studied on the first in-vivo study. This includes the type of algorithm, the number of iterations, and the size of the HR pixel. Results of these figures are outlined in Table 12. The remaining five studies are included in Appendix E. All studies include an edge measurement (Appendix 4.2.1) in the SRR as well as a MPR (using bilinear interpolation views) of the SRR with corresponding MPRs of one sagittal and one coronal LRSs. The purpose is to

demonstrate and quantify the resolution improvement in the SRR compared to the LR imagery. Appendix D details the procedure for measuring the slice selection profile.

4.2.1 Measuring Edge Width

The degree of resolution improvement in the SRR from the LRSs is measured by edge widths. Therefore, spatially consistent samples of edges of the in-vivo scans are selected from the LRIs (along the slice selection direction) and the SRR. Using the technique given in [27], the width of an edge is first measured by least-squares fitting it to a sigmoid function of the form:

$$p(t) = \frac{1}{1 + e^{-a(t-c)}}. \tag{103}$$

The width is inversely proportional to a, where 80% of the rise height in the function is equivalent to

$$width(pixels) = \frac{4.4}{a}. \tag{104}$$

An example of the sigmoid function for edge measurement is given in Fig. 43.

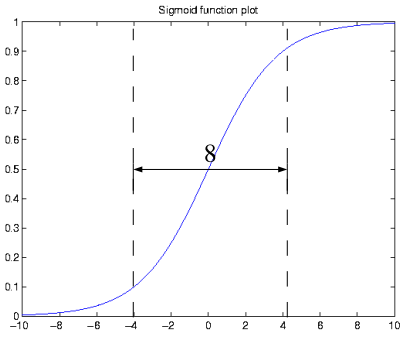

Figure 43: Sigmoid plot with an edge width of 8 units.

4.2.2 Ex-vivo Study

Results from the ex-vivo study are shown in this subsection. Table 8 gives a listing of the figures and tables as a navigational aid. Table 9 shows the relevant acquisition parameters of the LRS with Fig. 44 showing the MPRs in the axial direction of all six LRSs. A HR scan is included in this study with acquisition parameters given in Table 10. Its purpose is to provide a SNR efficiency and fidelity quality comparison to the SRR computed from the LR acquisitions. The SNR efficiency is defined in [27] as

$$\text{SNR efficiency} = \frac{\text{SNR}}{\sqrt{\text{Acquisition time(sec)}}}, \tag{105}$$

where SNR is measured as

$$\text{SNR} = \frac{\mathsf{E}(\Omega_{\text{foreground}})}{\sigma_{\text{background}}}. \tag{106}$$

$\Omega_{\text{foreground}}$ is a region of high intensity where its mean is the expected value. $\sigma_{\text{background}}$ is the standard deviation in pixel intensity of a background region. The measurements for both the SRR and the HR scan are sampled from the same spatial regions for consistency. Fig. 45 shows the MPRs of one sagittal and one coronal scan while Fig. 46 shows the MPRs of the SRR and HR scan. Edge and SNR efficiency measurements are also given (Fig. 47 and Table 11).

Table 8: Ex-vivo study No. 1: Figure and table listing.

Description	Figures	Tables
LRS parameters	-	9
Axial view of all LRSs	44	-
HR scan parameters	-	10
MPRs of two LRSs	45	-
MPRs of HR scan and SRR	46	-
Edge Measurements	47	-
SNR efficiency Measurements	-	11

Table 9: Ex-vivo study No. 1: LRS parameters.

P	6
$M_1 \times M_2 \times M_3$	$30 \times 256 \times 256$
LRS FOV	220×220
LR slice thickness	$5mm$
LR slice distance	$5mm$
SRR voxel Size	$0.859 \times 0.859 \times 0.859\ mm^3$
Pulse Sequence	3DFZ
$T_E/T_I/T_R$	4.2/(N/A)/30 ms
Excitation angle	90^o
Scan time (min:sec)	3:00

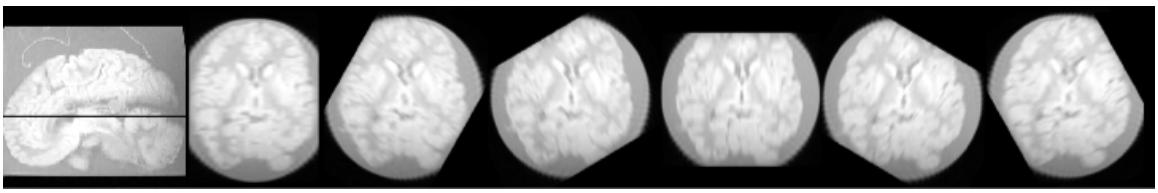

Figure 44: Ex-vivo study No. 1: Sagittal view from one of six LR stacks with the reformatted axial views of all six input multi-slice stacks (sagittal, coronal scans) using the 3-D gradient echo pulse sequence at 30°, slice thickness = 5 mm, in-plane pixel resolution $= 0.859 \times 0.859\ mm^2$.

Table 10: Ex-vivo study No. 1: HR scan parameters.

$M_1 \times M_2 \times M_3$	$200 \times 256 \times 256$
LRS FOV	220×220
LR slice thickness	$0.75mm$
LR slice distance	$0.75mm$
Pulse Sequence	3DFZ
$T_E/T_I/T_R$	4.2/(N/A)/30 ms
Scan time (hour:min:sec)	7:00:00

Table 11: Ex-vivo study No. 1: SNR efficiencies.

Method	SNR	Total time(min:sec)	SNR efficiency
Multi-Stack SRR	39.5	23:06	1.06
High resolution scan	66.3	420:00	0.42

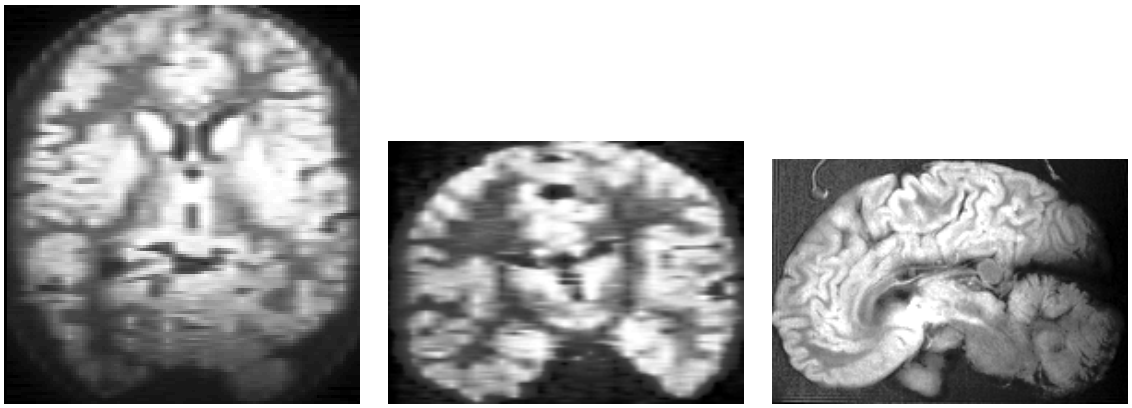

(a) (b) (c)

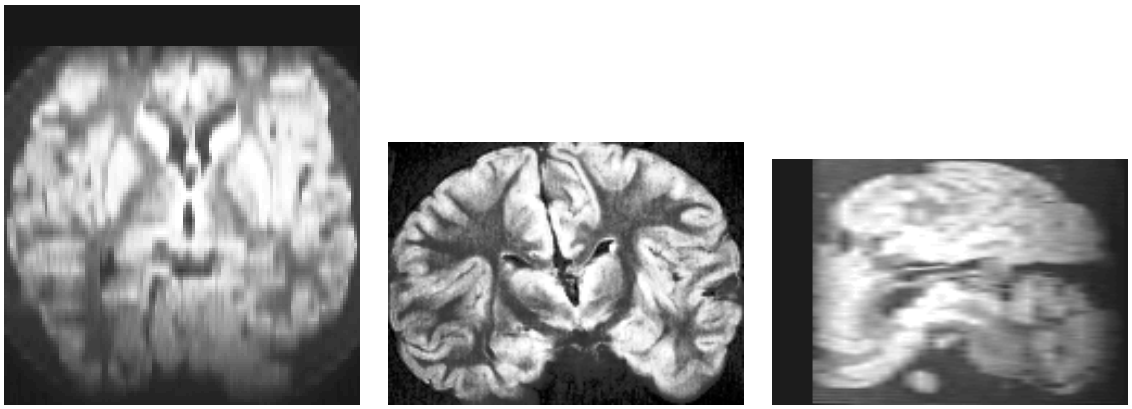

(d) (e) (f)

(a) Axial MPR of sagittal LR stack	(b) Coronal MPR of sagittal LR stack	(c) Sagittal original LR slice
(d) Axial MPR of coronal LR stack	(e) Coronal original LR slice	(f) Sagittal MPR of coronal LR stack

Figure 45: Ex-vivo study No. 1: MPRs of the LRSs (a-c) Axial, coronal, and sagittal views of a sagittal scan (voxel = 0.859 $mm \times 5\ mm \times 0.859mm$) (d-f) Axial, coronal, and sagittal views of a coronal scan (voxel = 5 $mm \times 0.859\ mm \times 0.859\ mm$).

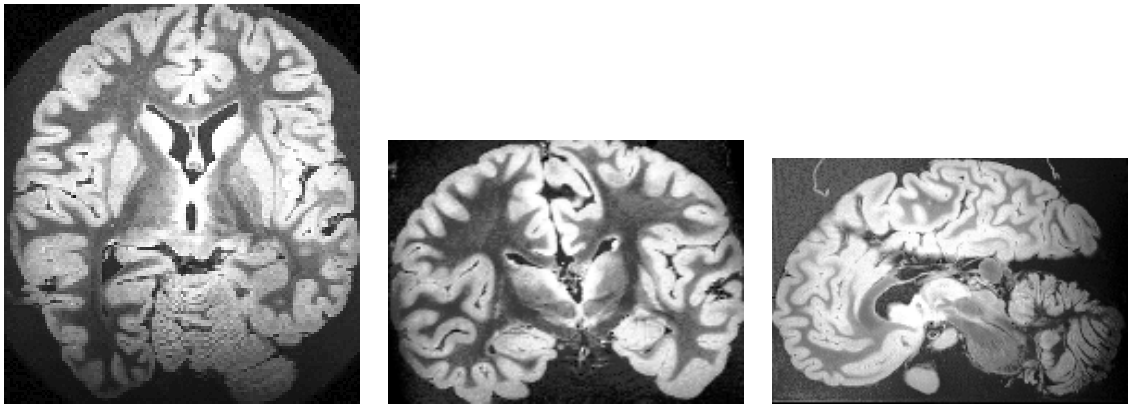

(a) (b) (c)

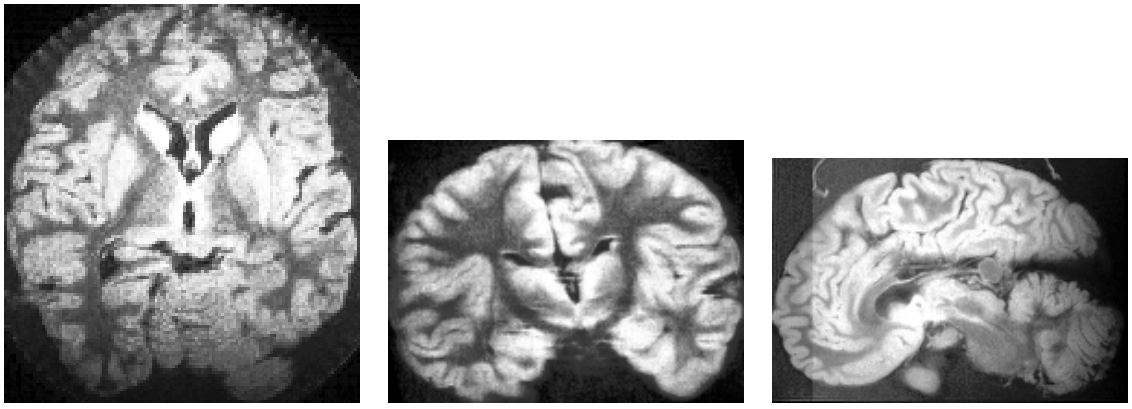

(d) (e) (f)

(a) Axial HR scan	(b) Coronal HR scan	(c) Sagittal HR scan
(d) Axial SRR	(e) Coronal SRR	(f) Sagittal SRR

Figure 46: Ex-vivo study No. 1: HR and SRR comparison using MPRs (a-c) Axial, coronal, and sagittal views of the HR 3-D scan (voxel = 0.75 mm × 0.75 mm × 0.75 mm) (d-f) Axial, coronal, and sagittal views of the SRR using ART (voxel = 0.859 mm × 0.859 mm × 0.859 mm)

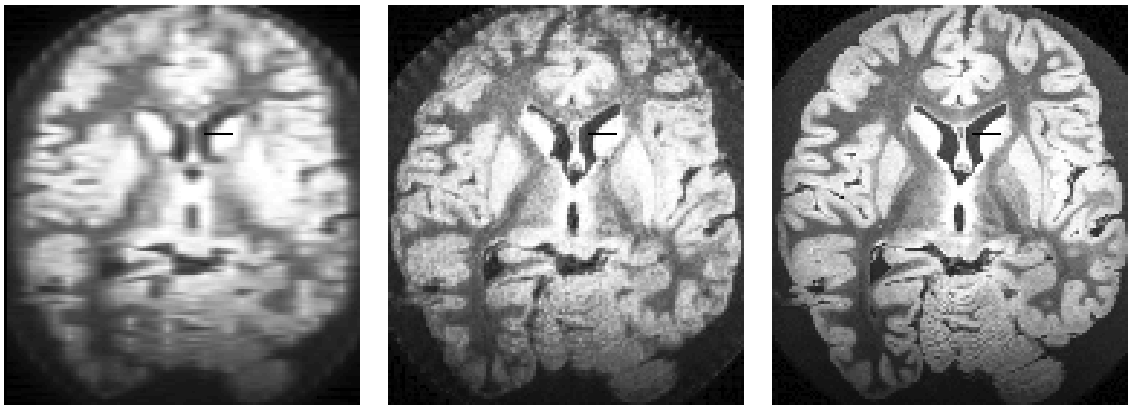

(a) (b) (c)

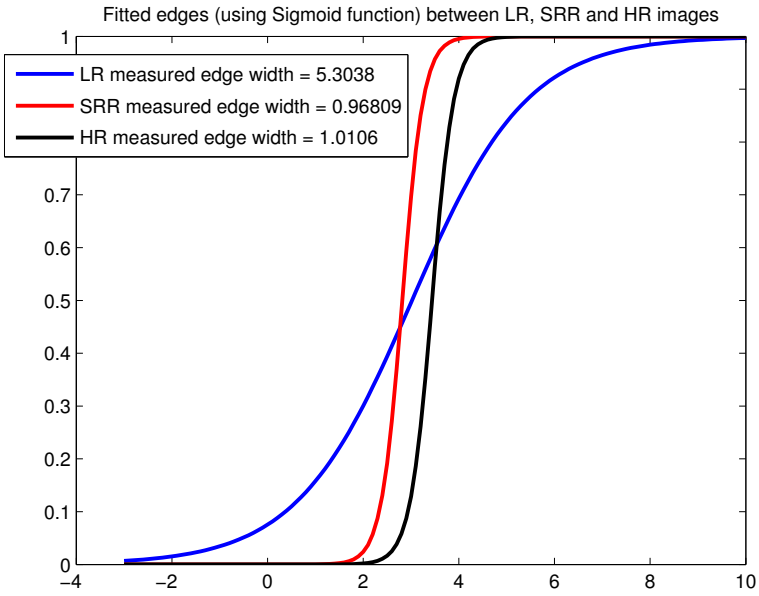

(d)

Figure 47: Ex-vivo study No. 1: (a) LR, (b) SRR, and (c) HRIs (d) with Fitted sigmoid function on selected edge (denoted in black).

4.2.3 In-vivo Studies

Only results from in-vivo study No. 1 are shown in this subsection; the remaining five are given in Appendix E. Table 12 gives a listing of the figures and tables as a navigational aid. Different algorithms, iterations and pixel sizes were introduced to capture any differences from the SRRs. MPRs of one sagittal and one coronal of the LRSs along with the SRR are shown in Fig. 55.

Table 12: In-vivo Study No. 1: Figure and table listing.

Case	Figures	Tables
LRS parameters	-	13
Different Algorithms	48	-
Different Iterations	49	-
Different Iterations	50	-
Different HR pixel sizes	51, 52, 53	-
Edge measurement	54	-
MPR views of two LRIs and SRR	55	-

Table 13: In-vivo Study No. 1: LRS parameters.

P	6
$M_1 \times M_2 \times M_3$	$48 \times 512 \times 512$
LRS FOV	220×220
LR slice thickness	$5mm$
LR slice distance	$5mm$
SRR voxel Size	$5.0 \times 0.4297 \times 0.4297\ mm^3$
Pulse Sequence	Fast-Spin Echo-Inversion Recovery (FSE-IR)
$T_E/T_I/T_R$	85/190/4830 ms
Excitation angle	90^o

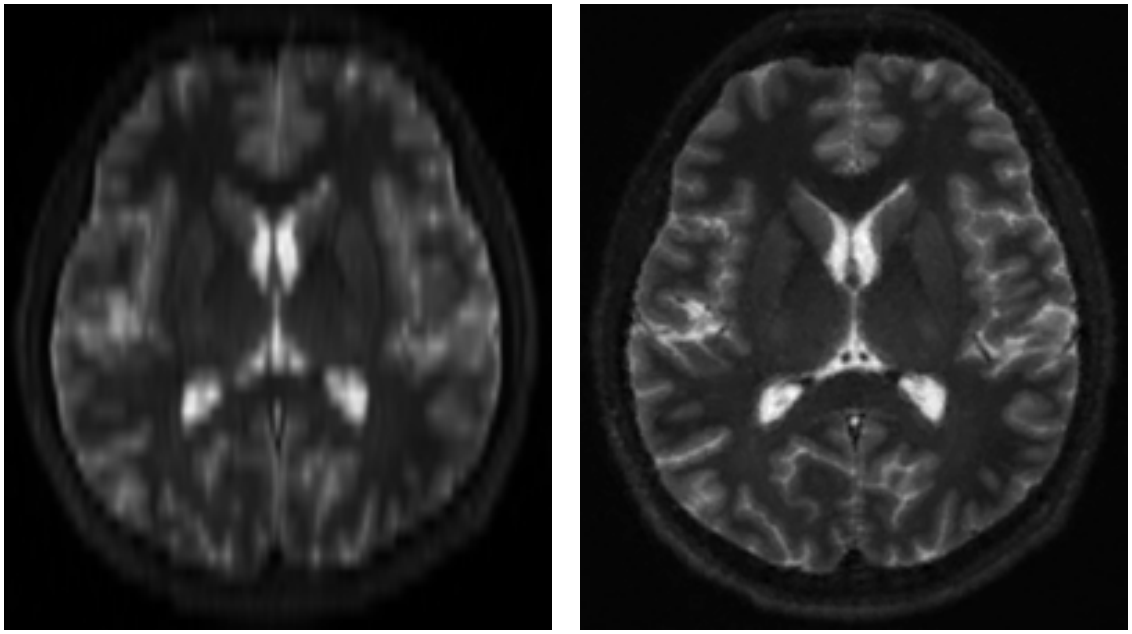

(a)

(b)

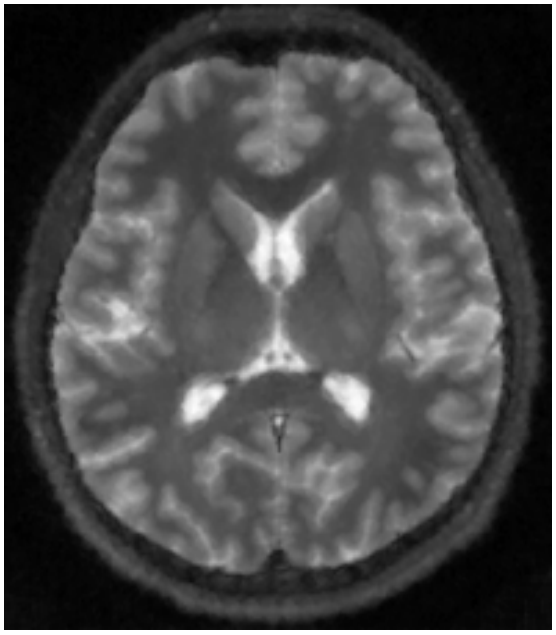

(c)

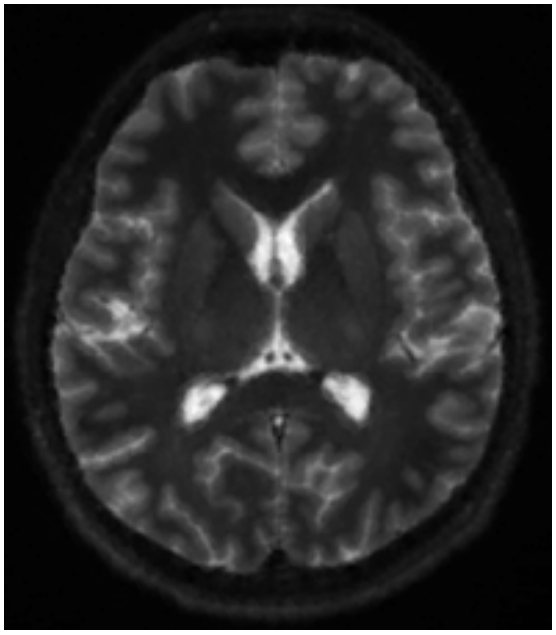

(d)

Figure 48: In-vivo Study No. 1: (a) One of the six LRIs (sagittal) using a multi-planar reformat; Pixel Res = $5.0 \times 0.8594\ mm^2$. SRR using (b) ART (c) MART (d) SART Pixel Res = $0.8594 \times 0.8594\ mm^2$ (over-determined case) at 200 iterations.

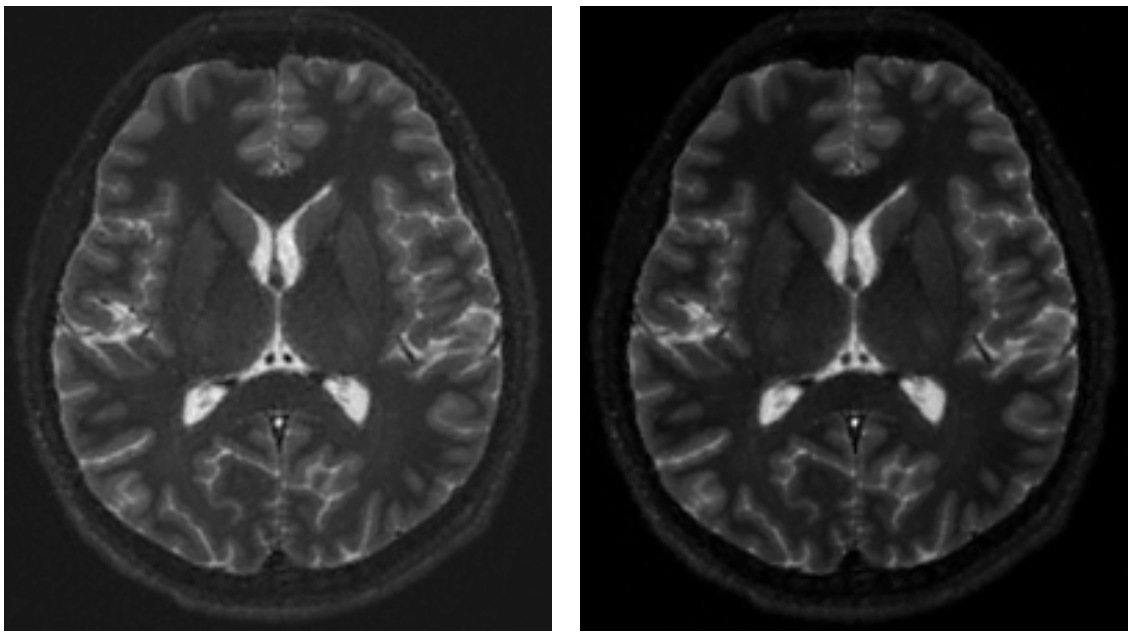

(a) (b)

Figure 49: In-vivo Study No. 1: SRR using (a) SART at 800 iterations (b) MART at 1000 iterations; Pixel Res = 0.8594 $\times$ 0.8594 mm^2.

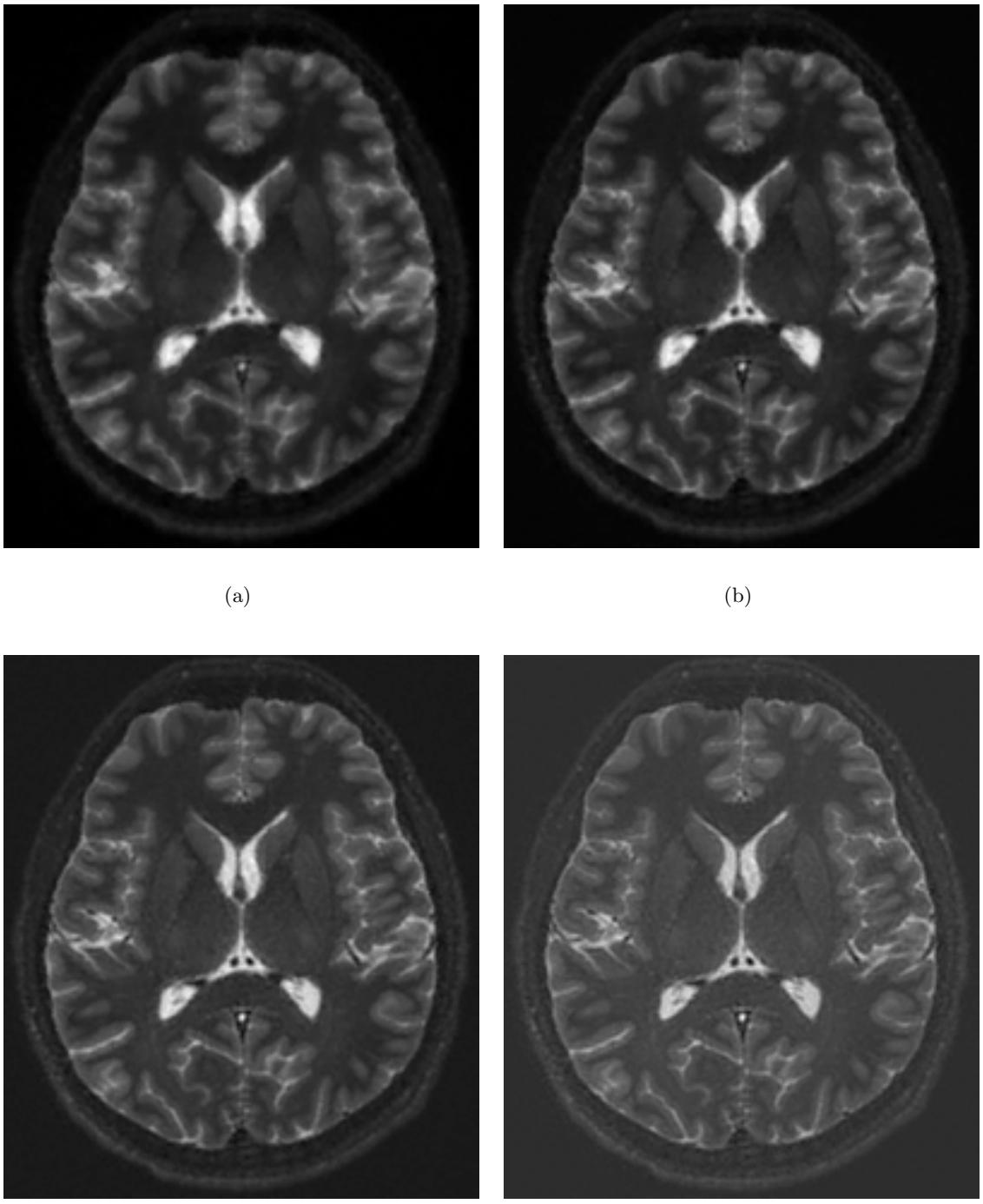

(a) (b)

(c) (d)

Figure 50: In-vivo Study No. 1: Over-determined case: SRR using ART at (a) 100 (b) 200 (c) 500 (d) 1000 iterations with HR estimate pixel size = .8594 × .8594.

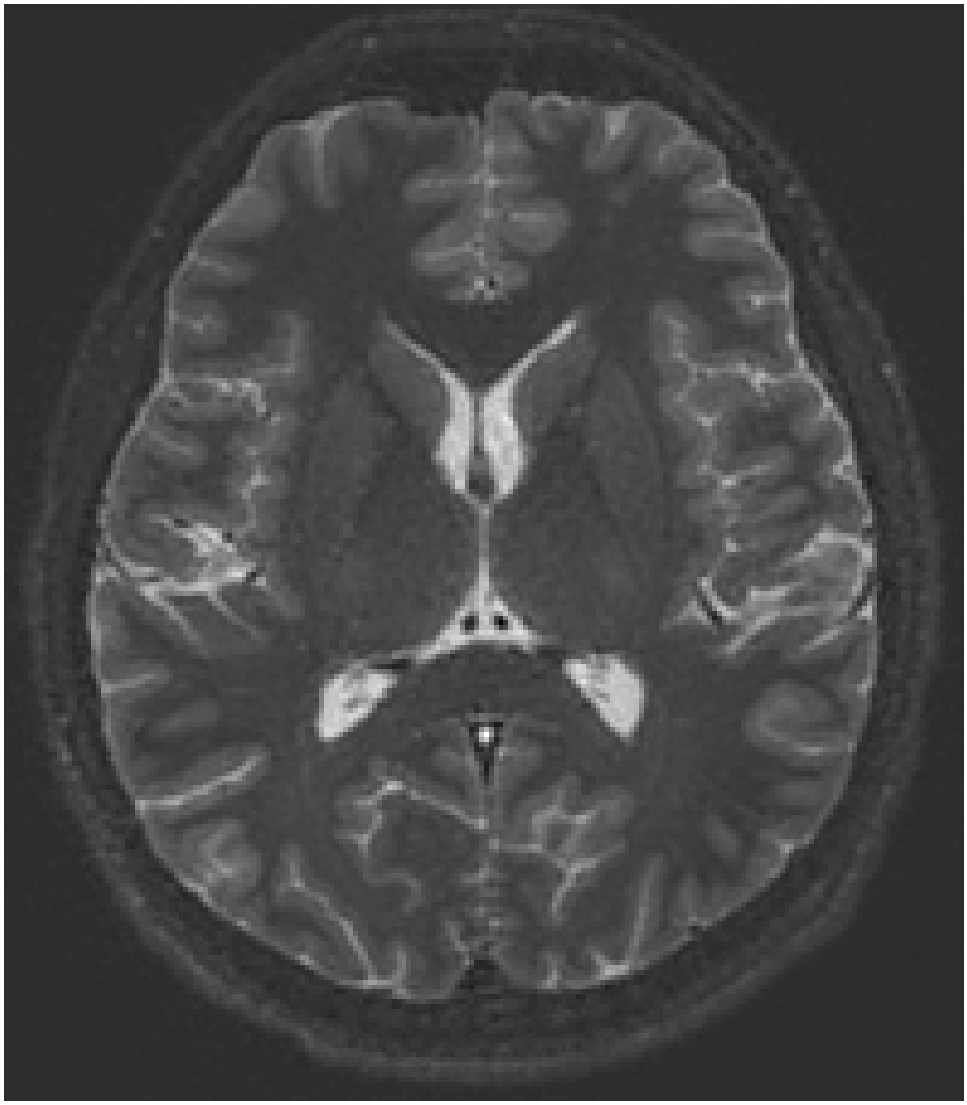

(a)

Figure 51: In-vivo Study No. 1: Over-determined case: SRR using ART at 1000 iterations; Pixel size=$0.8594 \times 0.8594 mm^2$.

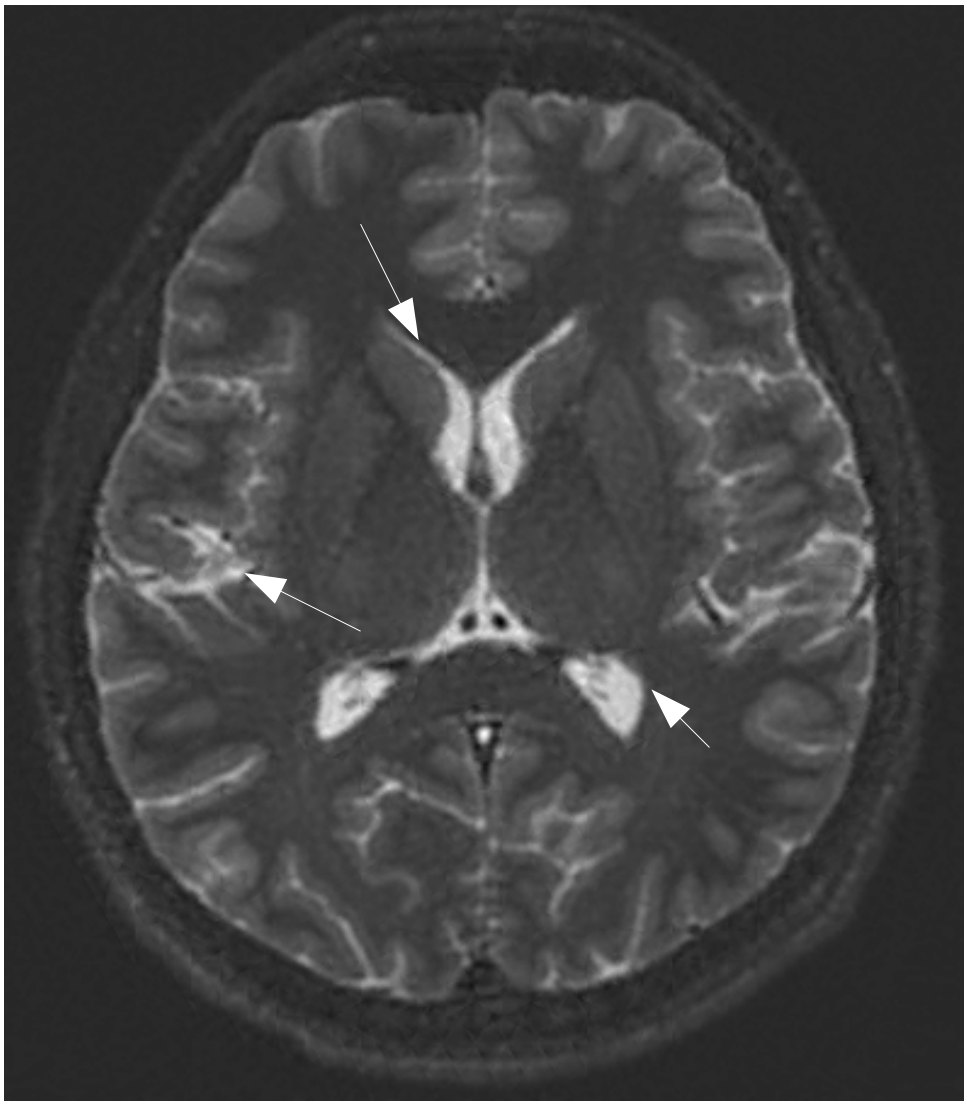

(a)

Figure 52: In-vivo Study No. 1: Fully-determined cases SRR using ART at 1000 iterations; Pixel size = $0.4297 \times 0.4297 mm^2$. White arrows denote some of the edge differences from the under- and over-determined cases.

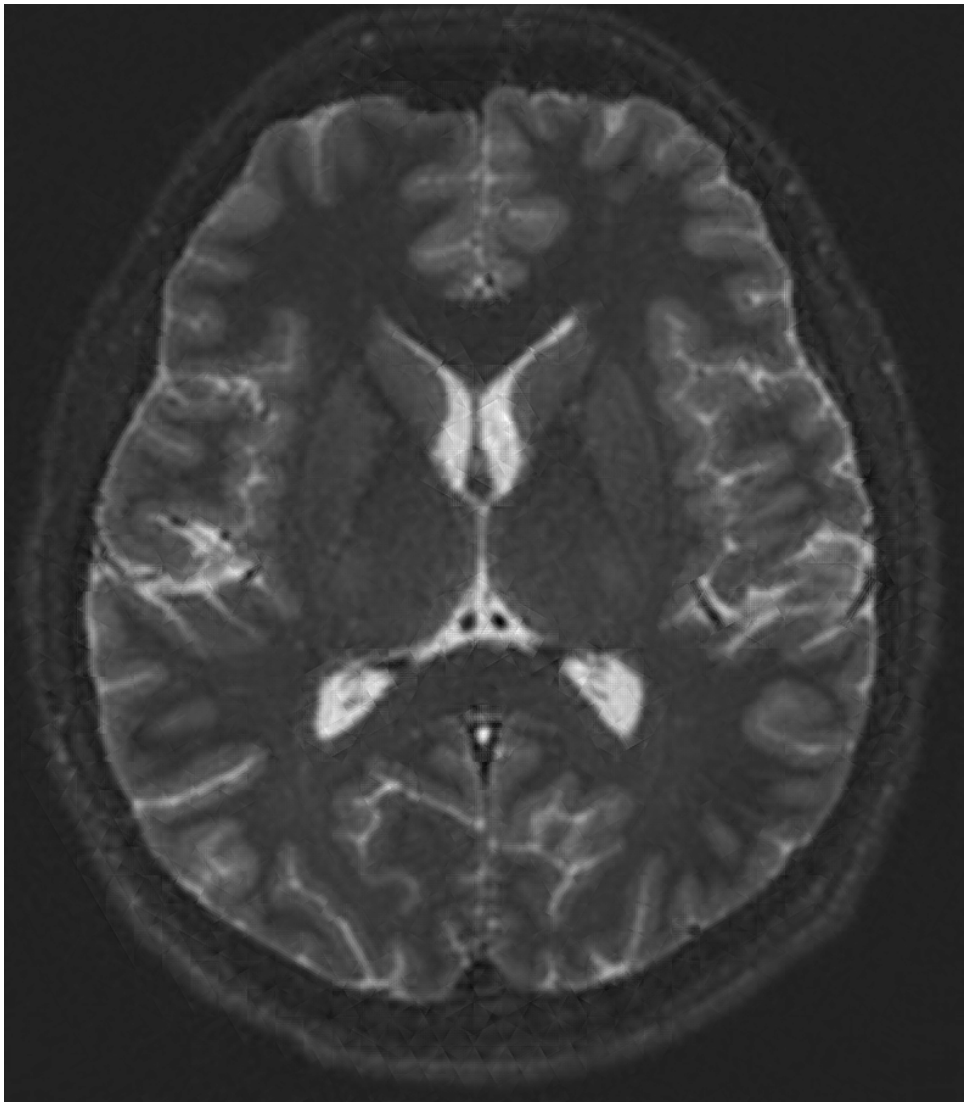

(a)

Figure 53: In-vivo Study No. 1: Under-determined case: SRR using ART at 1000 iterations; Pixel size = 0.2148 $\times$ 0.2148 mm^2.

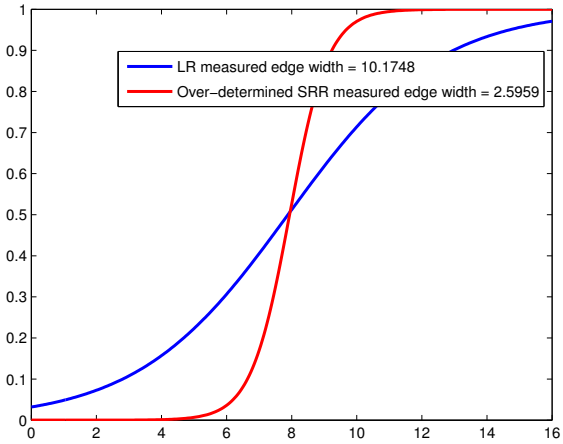

(a)

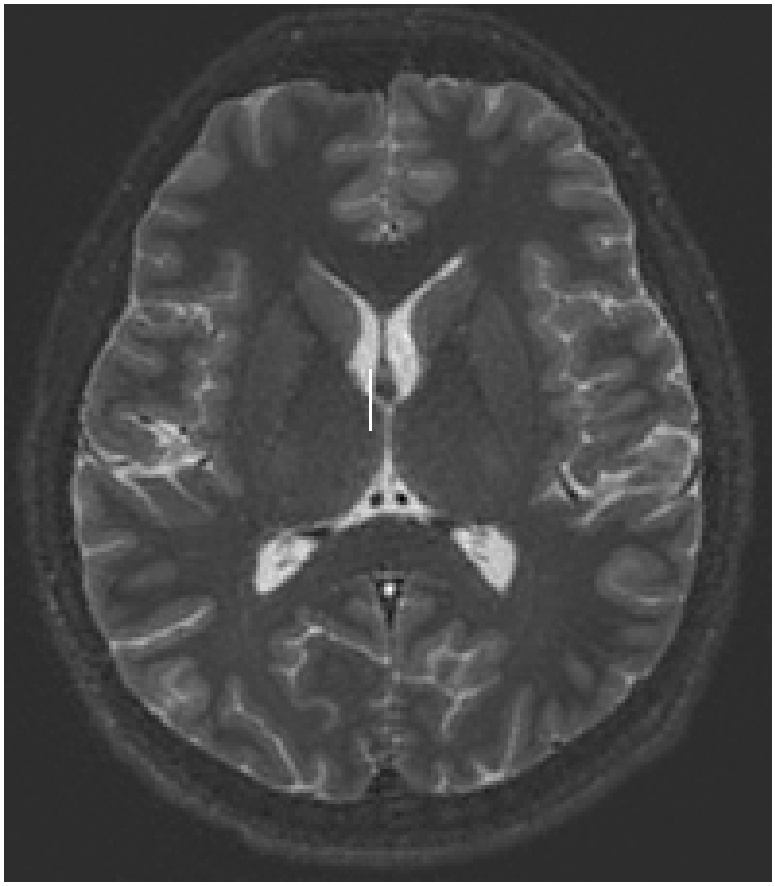

(b)

Figure 54: In-vivo Study No. 1: (a) Edge measurement from (a) SRR image at 1000 iterations; Pixel size = 0.8594 × 0.8594 mm^2.

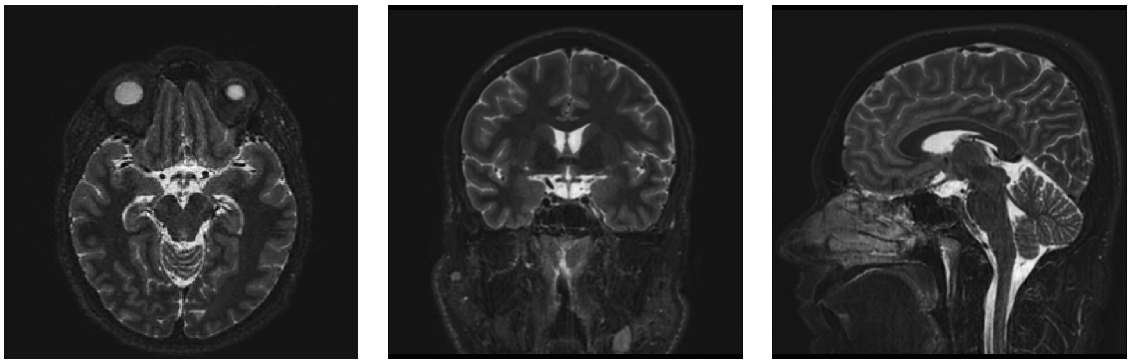

(a) (b) (c)

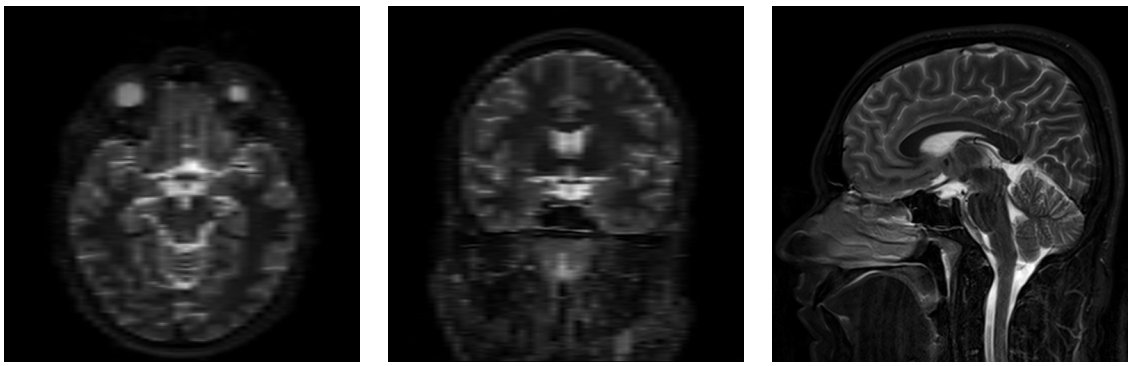

(d) (e) (f)

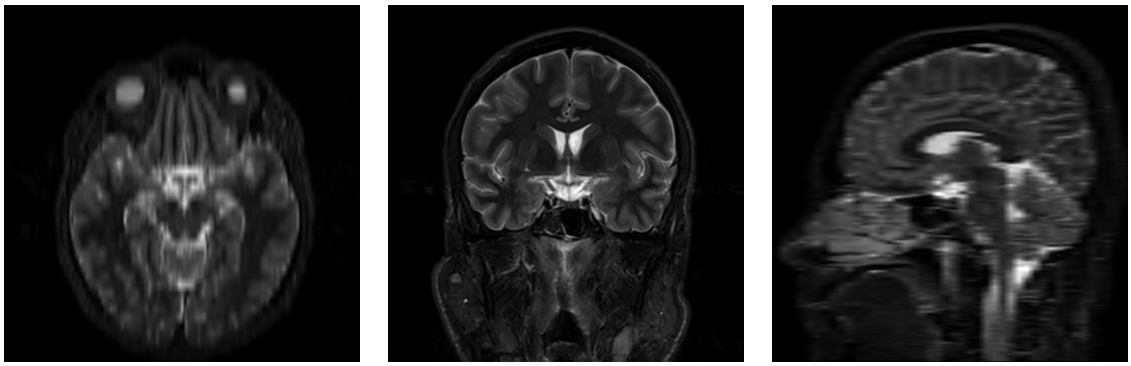

(g) (h) (i)

(a) Axial SRR view	(b) Coronal SRR view	(c) Sagittal SRR view
(d) Axial MPR of sagittal LR stack	(e) Coronal MPR of sagittal LR stack	(f) Sagittal original LR slice
(g) Axial MPR of coronal LR stack	(h) Coronal original LR slice	(i) Sagittal MPR of oronal LR stack

Figure 55: In-vivo Study No. 1: (a-c) Axial, coronal, and sagittal views of the SRR using ART (voxel = 0.8594 mm × 0.8594 mm × 0.8594 mm) (d-f) Axial, coronal, and sagittal views of a sagittal scan (voxel = 5 mm × 0.8594 mm × 0.8594 mm) (g-i) Axial, coronal, and sagittal views of a coronal scan (voxel = 0.8594 mm × 5 mm × 0.8594 mm).

4.2.4 Multi-Stack Observations on MRI Data

Table 14: Width of Edge Measurements for FSE-IR multi-slice MRI data.

Study	Width of LRI	Width of SRR	Improvement ratio
Ex-vivo	5.30	0.96	5.52
In-vivo No. 1	10.17	2.60	3.91
In-vivo No. 2	9.19	2.81	3.27
In-vivo No. 3	N/A	N/A	N/A
In-vivo No. 4	10.08	3.81	2.65
In-vivo No. 5	8.04	3.08	2.61
In-vivo No. 6	11.05	5.29	2.09

The algorithms applied to study no. 1 give comparable SRRs for the over-determined case in Fig. 48. Some of the soft-tissue structure of the brain shown in the SRRs at 200 iterations remains blurry that are then only resolved at either 800 or 1000 iterations, as shown in Fig. 49.

Truth is unknown using the LR multi-slice data sets. Thus, one SRR over another can undergo subjectively preferable treatment. However, the issue of stopping during the iterative reconstruction process may be aided by observing the edges containing both the background region (i.e., outside the brain) and soft tissues. These edges are where the region of support for the image function ends. Our ability to identify the locations of these particular edges implies that there is prior knowledge of the image. Heterogeneity in the background is not expected. In the previously observed SLP experiments, edge overshoot grows with respect to those iterations that are subsequent to the optimal iteration (in the NMSE sense). We assume the same behavior of the error for the cases of real multi-slice data as well. As edge overshoot becomes more apparent in the background at the brain boundary, it can be assumed that the current iteration would exceed the optimal iteration. This can be observed in the SRR from Fig. 50(c) and (d). As the SRR estimate goes from 500 to 1000 iterations, speckle from edge overshoot becomes more apparent suggesting that iterating further would cause an increase in NMSE.

In some of the data sets, the LRIs do not fully cover the brain and thus the outer field of view in the reconstruction is slightly sampled. Reconstruction artifacts in these under-determined regions visually appears to be limited, but includes a residual blurring effect

also observed in the under-determined SLP reconstructions. If the most relevant anatomy is centered in the field of view, acquisition time may be saved in this fashion by allowing a certain degree of image quality degradation in less relevant peripheral structures.

Only slight changes occur, such as sharper edges, when the pixel size of the HR estimate is decreased from a over-determined to fully-determined system, as shown in Figs. 51 and 52. Arrows are used in the imagery in Fig. 52 to highlight any differences. Noise is slightly more apparent in the fully-determined case as well. The under-determined case in Fig. 53 does not show any new edge definition or content. Furthermore, it shows some streaking artifacts in the center of brain anatomy. SNR efficiency measurements of the SRR and the 7 hour HR scan is shown in Table 11.

The MPRs capture isotropic HR in the SRR (Fig. 55). The MPRs from study numbers 2, 4, 5, and 6 show similar improvement in isotropic HR (Figs. 75), (78), (80), (82)). For example, in study number 5, a comparison of the reformatted LR views in the in-vivo scan (Figs. 80(d-i)) with the corresponding SRR (Figs. 80(a-c)) clearly illustrates the resolution improvement in the slice selection direction. Fig. 80(a) shows an axial view of the SRR compared to the LR MPRs of Figs. 80(d,g). Fig. 80(b) and Fig. 80(c) show the coronal and sagittal views of the SRR compared to the LR MPRs of Figs. 80(e,h) and Figs. 80(f,i), respectively. The Globus Pallidus internal and external are resolved clearly in all dimensions, and this is not the case in the individual LR stacks (see arrows). Comparing the sagittal view of the SRR (Fig. 80(c)) with the corresponding native high in-plane resolution image (Fig. 80(f)) of the input stack data, we observe new details in the SRR in many locations due to mitigation of partial volume effects[2]. White matter tracts and cereberal spinal fluid spaces in the cerebellum clearly show improved definition. Similar observations may be made comparing the coronal SRR view (Fig. 80(b)) with the corresponding coronal input stack image. In particular, the sharper delineation of the brain stem boundary in the SRR image is observed.

The degree of improvement in the measured widths of the edges are comparable as shown

[2]The partial volume effect is the phenomenon where voxels in an image represent more than one tissue type.

from Table 14. The SRR from study no. 3 (see Fig. 76) shows a ghosting-like artifact near edge boundaries that strongly indicates a mis-alignment between the LRIs. Chapter (5) is dedicated to a new MS observation that corrects for motion between LRSs.

4.3 Execution Times

All reconstructions were executed on an Intel Xeon CPU 3.20GHz 16GB RAM machine with GNU/Linux. In the SLP experiments, executing 2000 iterations, (relaxation rates = .01) on a fully determined system (8 LR stacks at 8 pixel slice thickness) for our implementations of ART, MART, and SART took 49, 1355 and 95 seconds, respectively. The under- and over-determined SLP cases had comparable execution times. The translational symmetry along the readout direction in the ex-vivo brain, and in-vivo brain, allowed repeated use of the system matrix for each reconstructed slice. Constructing the fully-determined system matrix (at $\delta = 0.01$) for the SLP experiment lasted six minutes. ART reconstruction for these experiments took under 2 seconds per slice at 100 iterations for 250 slices totaling 500 seconds. We note that computing the system matrix is calculated only once for problems with translational symmetry. For known problem geometries the matrix may be pre-computed, pre-conditioned and stored, thus not further affecting the actual reconstruction time. One key advantage of MART and ART is their ability to temporarily work on incomplete data. Since the MS data is acquired sequentially over the LRS, a sequential image reconstruction technique can be used in parallel during the acquisition process, which thus gives computational advantages to the ART and MART over SART.

4.4 Conclusion

The MS approach to SR is validated through the tests given on synthetic and real FSE-IR multi-slice MRI data. Supporting experiments demonstrated resolution improvement in the slice selection direction but also improved in-plane resolution in multi-slice scans, due to reduction in partial volume averaging. We have presented image reconstructions which show isotropic high resolution otherwise only found with 3-D MRI acquisitions, and the high contrast currently only obtained from 2-D multi-slice MRI acquisitions. Multi-Stack experiments on simulated data resulted in super-resolution reconstructions of high fidelity.

Additive correction methods were found superior to multiplicative methods, confirming known results for conventional tomographic reconstruction. SRRs from real data revealed new anatomical features while simultaneously attenuating partial volume image artifact. The method carries promise to improve spatial resolution in clinically feasible data acquisitions for planning and navigation of deep-brain images for minimally invasive image-guided neurosurgery.

CHAPTER V

MULTI-STACK MODELED WITH MOTION

To minimize any motion in the LRSs, minimizing the time between them is desirable. In some of the in-vivo studies given in Chapter 4, queueing all the LR acquisitions on the scanner software increased the throughput of the overall process. In some of these in-vivo experiments, the interval between the 3-minute LR acquisitions was reduced to 5 seconds. This decrease in time certainly decreases the potential for any head motion of the patient. Further improvements based on parallel imaging techniques using multiple RF receiving coils can further decrease the acquisition time as well [61]. When MRI is used as a surgical navigation aid for the intended brain-related diseases, the rigid stereotactic frame that is attached to the head effectively eliminates involuntary movement. Yet Multi-Stack is untested to date with a stereotactic frame as well as other applications. Therefore, motion correction between the LRIs may be necessary for the SR technique of MS. One of the six validation MRI studies (No. 3 in Appendix E.0.2) shows a ghosting-like artifact (see Fig. 76) in the SRR that indicates a mis-registration between some the LRIs. This chapter addresses the issues of motion in MS. We limit our analysis to a rigid head motion of the LRSs, instead of a deformable one. The hard non-deformable skull that holds the brain in place with constant cerebral spinal fluid pressure justifies considering only this type of motion. Furthermore, we assume that any motion is only between the acquistions of the LRSs and not during them. If there is motion during a LR acquisition, motion artifacts will manifest and the LRS is to be repeated immediately. In this chapter, MS is re-modeled to account for motion between LRSs. Motion estimation methods are reviewed with a perspective towards MS. Then, results and observations based on both a synthetic data set and the mentioned in-vivo study (no. 3) are given, followed by concluding remarks.

5.1 The Multi-Stack Formula with Rigid Motion

The MS observation model in Eq. (60) will now be modified to account for an unknown rigid motion so that the r^{th} LRI becomes

$$y_r[\mathbf{n}] = \int_\Omega x(\mathrm{A}_r\mathbf{s} + \mathbf{b}_r)h(\mathrm{R}_r(\mathbf{s} - \mathrm{V}\mathbf{n}))d\mathbf{s} + e_r[\mathbf{n}]. \tag{107}$$

The matrix, $\mathrm{A}_r \in SO(3)$, is parameterized by three rotations, $\phi_r, \varphi_r, \psi_r$, about the origin:

$$\mathrm{A}_r = \mathrm{A}(\phi_r, \varphi_r, \psi_r) = \begin{pmatrix} 1 & 0 & 0 \\ 0 & \cos\phi_r & -\sin\phi_r \\ 0 & \sin\phi_r & \cos\phi_r \end{pmatrix} \begin{pmatrix} \cos\varphi_r & 0 & -\sin\varphi_r \\ 0 & 1 & 0 \\ \sin\varphi_r & 0 & \cos\varphi_r \end{pmatrix} \begin{pmatrix} \cos\psi_r & -\sin\psi_r & 0 \\ \sin\psi_r & \cos\psi_r & 0 \\ 0 & 0 & 1 \end{pmatrix}, \tag{108}$$

and $\mathbf{b}_r \in \mathbb{R}^3$ is the translational component from the origin. For notational clarity, these six parameters are concatenated into $\mathbf{v}_r = [\phi_r \ \varphi_r \ \psi_r \ \mathbf{b}_r^T]^T$. Thus, the effective warps of $x(\mathbf{s})$ are now unknown and need to be incorporated into the estimation process so that

$$\mathbf{y}_r = D_r C_r F_r(\mathbf{v}_r)\mathbf{x} + \mathbf{e}_r, \tag{109}$$

or

$$\mathbf{y} = \mathbf{H}(\mathbf{v})\mathbf{x} + \mathbf{e}, \tag{110}$$

where $\mathbf{v} = [\mathbf{v}_1^T \cdots \mathbf{v}_p^T]^T \in \mathbb{R}^{6P\times 1}$. The matrix $\mathbf{H}$ is now a function of the motion parameters, $\mathbf{v}$. If the LRIs are registered (i.e, $\mathbf{v} = \mathbf{0}$, or equivalently, $\mathrm{A}_r = \mathbb{I}, \mathbf{b}_r = \mathbf{0}$), then the ij^{th} entry of $\mathbf{H}$ in Eq. (63) holds. Any motion invalidates Eq. (63). However, a substitution of variables in Eq. (107), given in Appendix J, expresses the LRI as

$$y_r[\mathbf{n}] = \int_\Omega x(\mathbf{s})h(\mathrm{R}_r(\mathrm{A}_r^{-1}\mathbf{s} - (\mathrm{A}_r^{-1}\mathbf{b}_r + \mathrm{V}\mathbf{n})))d\mathbf{s} + e_r[\mathbf{n}], \tag{111}$$

so that the ij^{th} contribution of H is

$$[\mathrm{H}]_{ij} = \int_{S_j} h(\mathrm{R}_r(\mathrm{A}_r^{-1}\mathbf{s} - (\mathrm{A}_r^{-1}\mathbf{b}_r + \mathrm{V}\mathbf{n})))d\mathbf{s}, \tag{112}$$

where S_j is the space from the j^{th} LR voxel.

5.2 Motion Estimation Methods

Recognizing that $\mathbf{y}$ is non-linear with respect to $\{\mathrm{A}_r, \mathbf{b}_r\}_{r=1}^P$ in Eq. (107), simultaneous estimation of these motion and HRI variables have been recast into a Bayesian formalism

[29, 58, 79]. The ML estimates,

$$\hat{\mathbf{x}}_{ML}, \hat{\mathbf{v}}_{ML} = \arg\max_{\mathbf{x},\mathbf{v}} p(\mathbf{y}|\mathbf{x}, \mathbf{v}), \tag{113}$$

can be reduced so that the likelihood of a LRI depends only on its own motion parameters:

$$p(\mathbf{y}|\mathbf{x}, \mathbf{v}_r) = \prod_{r=1}^{P} p(\mathbf{y}_r|\mathbf{x}, \mathbf{v}_r). \tag{114}$$

Then, according to [39], if the likelihood of the parameters without motion is Gaussian, then it maintains its familiar form of

$$p(\mathbf{y}|\mathbf{x}, \mathbf{v}) \propto \exp(-\frac{1}{2}(\mathbf{y} - \mathbf{H}(\mathbf{v})\mathbf{x})^T \mathbf{R}_{\mathbf{ee}}^{-1}(\mathbf{y} - \mathbf{H}(\mathbf{v})\mathbf{x})). \tag{115}$$

As mentioned in Appendix 2.4.3, Eq. (113) can be generally solved by (1) inference (2) alternating minimization, or (3) sequential techniques.

5.2.1 Inference

In general, the process of inference requires marginalization of the likelihood function. In [79], Tipping et al. apply this principle by solving for

$$\hat{\mathbf{v}}_{ML} = \arg\max_{\mathbf{v}} p(\mathbf{y}|\mathbf{v}) \tag{116}$$

$$= \arg\max_{\mathbf{v}} \int_{S(\mathbf{x})} p(\mathbf{y}|\mathbf{x}, \mathbf{v}) p(\mathbf{x}) d\mathbf{x}, \tag{117}$$

where $S(\mathbf{x})$ is the sample space of $\mathbf{x}$. In their case, $\mathbf{x}$ in Eq. (117) was specified as a zero mean Normal RV, which greatly simplified the distribution of measurements conditioned on the motion transformations to yet another Gaussian distribution. This avoids both the direct integration of Eq. (117) and drawing from the sample space of $\mathbf{x}$ (i.e., enumerating S($\mathbf{x}$)). However, this method is not readily applicable if priors on the HRI are absent. In general, inference is computationally infeasible. Furthermore, aside from using Gaussian priors, other HR prior forms used to evaluate Eq. (117) were not addressed in their work.

5.2.2 Alternating minimization

Alternating minimization (AM) optimizes a two argument function for one variable while the other is fixed in a given iteration and vice-versa in the following iteration [15]. Algorithm (1)

Algorithm 1 Alternate minimization algorithm for estimation of $\mathbf{x}$ and $\mathbf{v}$.

Require:

$\tau_{\mathbf{v}}$ and $\tau_{\mathbf{x}}$ are the convergence tolerances for $\mathbf{v}$ and $\mathbf{x}$.

1: $l \leftarrow 0$
2: $\hat{\mathbf{v}}^{(l)} \leftarrow \mathbf{0}$
3: $\hat{\mathbf{x}}^{(l)} \leftarrow \mathbf{0}$
4: **repeat**
5: $\quad \hat{\mathbf{x}}^{(l+1)} \leftarrow \arg\max_{\mathbf{x}} p(\mathbf{y}|\mathbf{x}, \hat{\mathbf{v}}^{(l)})$
6: $\quad \hat{\mathbf{v}}^{(l+1)} \leftarrow \arg\max_{\mathbf{v}} p(\mathbf{y}|\hat{\mathbf{x}}^{(l+1)}, \mathbf{v})$
7: $\quad l \leftarrow l + 1$
8: **until** $||\hat{\mathbf{x}}^{(l)} - \hat{\mathbf{x}}^{(l-1)}|| \leq \tau_{\mathbf{x}}$ and $||\hat{\mathbf{v}}^{(l)} - \hat{\mathbf{v}}^{(l-1)}|| \leq \tau_{\mathbf{v}}$
9: **return** $\hat{\mathbf{x}}^{(l)}, \hat{\mathbf{v}}^{(l)}$

is an instance of this decoupled optimization technique for solving Eq. (113). The sequential technique is a special case of alternating minimization that iterates only once.

There have been experimental comparisons of the simultaneous and decoupled approaches to the problems of both reconstruction and motion estimation [13]. For example, Chung et al. show lower error levels in their results for the simultaneous approach as opposed to an instance of a decoupled approach for their experiments. If the convergence conditions for alternating minimization, given in Appendix F are satisfied, then

$$\lim_{l\to\infty} p(\mathbf{y}|\hat{\mathbf{x}}^{(l)}, \hat{\mathbf{v}}^{(l)}) = \max_{\mathrm{x,v}} p(\mathbf{y}|x, v). \tag{118}$$

Appendix F continues to apply these convergence conditions for the alternating minimization technique based on Eq. (115).

Note however, that every refinement of $\hat{\mathbf{x}}$ (line 5 in Algorithm (1)) requires re-computing $\mathbf{H}(\hat{\mathbf{v}})$ given by Eq. (112). In our construction method (see Appendix (C)), computation time is $O(\frac{M|\mathsf{supp}(h)|}{\delta^3})$. Yet, it still remains to compute the optimal value of $\hat{\mathbf{v}}$ using the current estimate of $\mathbf{x}$. Recognizing that the down-sampling does not change as a function of $\hat{\mathbf{v}}$, this part of the process can be reversed. That is, the r^{th} LRI after it is up-sampled becomes

$$D_r^{-1}(\mathbf{y}_r - \mathbf{e}_r) = C_r F_r(\mathbf{v}_r)\mathbf{x}. \tag{119}$$

This is the basis for much of the SR work in motion estimation [6]. This is similar to the iterative back-projection algorithm from Eqns. (49) and (50). Certainly, the exact down-sampling is not invertible and consequently, interpolation is substituted as the inverse to D_r

instead. So rather than finding motion estimates of the LRIs to a reference LRI, they are first up-sampled. However, naively applying gradient descent techniques to solve for $\mathbf{v}_r$ in $F_r(\mathbf{v}_r)$ remains an immense challenge since it is a matrix-valued function that has a matrix-valued argument, $F_r(\mathbf{v}_r) : \mathbb{R}^{6P\times 1} \rightarrow \mathbb{R}^{N\times N}$. In this case, its gradient is a matrix with $6PN^2$ elements. As an alternative, block matching techniques or registration algorithms are often successfully used in practice.

5.2.3 Block Matching and Registration algorithms

The different types of block matching metrics used for SR include the sum of absolute differences, mean-square error, and normalized cross-correlation [6]. However, these particular methods are intensity-based, which are inflexible with respect to any variations in contrast within the LRIs nor do they use any known PDF of the imagery. Furthermore, the non-convexity of the registration problem can trap the current motion estimate into local minima if the initial estimates are inaccurately initialized [59]. This is indeed conceivable in MS because the disjoint field of views from in-vivo case no. 5 may falsely align the black backgrounds together (see Appendix E.0.4 Fig. 80(e)(g)). Hence, we use a mutual information metric over a subset of the field of view in our motion estimation method.

Mutual information is the shared information of two RVs that is independent of either their modality or intensity. A reference volume, $x(\mathbf{s})$, and a test volume, $y(\mathbf{s})$, are matched using a rigid transformation, $(\mathrm{A}, \mathbf{b} \in SO(3) \times \mathbb{R}^3)$, so that their mutual information is maximized. That is,

$$\hat{\mathrm{A}}, \hat{\mathbf{b}} = \arg\max_{\mathrm{A},\mathbf{b}} I(x(\mathbf{s}), y(\mathrm{A}\mathbf{s} + \mathbf{b})) \tag{120}$$

where

$$I(x, y) \quad = \quad h(x) - h(x|y) \tag{121}$$

The entropy and conditional entropy functions are $h(.)$ and $h(.|.)$, respectively, (see Eq. (94)). Since the unknown PDF of the HRI is needed for entropy estimation, they are approximated through Parzen windows [84, 33]. These constitute a superposition of smooth symmetric kernels (i.e, Gaussian, box-car, B-spline, etc) centered on the intensity of each pixel sample.

In other words, an estimate of the PDF is given by

$$\hat{P}(x(s)) = \sum_{t \in S(x(s))} K(x(s) - t), \tag{122}$$

where $K(.)$ is the kernel, and $S(x(s))$ are the samples of $x(s)$. As the number of samples increase and the process is ergodic, the Parzen window estimates approaches the true PDF. Wells et al. estimated the gradient of the mutual information with respect to the transformation, $\hat{\nabla}_{(\mathrm{A,b})} I(x(s), y(\mathrm{A}s + \mathbf{b}))$, based on the estimate of the PDF given in Eq. (122). This is then used as part of an additive update in a steepest descent algorithm so that

$$(\hat{\mathrm{A}}, \hat{\mathrm{b}}) \leftarrow (\hat{\mathrm{A}}, \hat{\mathrm{b}}) + \alpha \hat{\nabla}_{(\hat{\mathrm{A}}, \hat{\mathrm{b}})} I(x(s), y(\hat{\mathrm{A}}s + \hat{\mathbf{b}})), \tag{123}$$

where α is the rate of change.

Multi-resolution techniques that are often used in registration algorithms prevent an optimization from becoming trapped into local extremum. Optimization is repeated multiple times each at different levels of pixel resolution. A coarse optimization always preceeds a finer one and the final motion estimate for one level is the initial estimate to the next level. Multi-resolution is most useful when the reference and test volumes are significantly mis-aligned. While the misalignments of the LRIs are not negligible for SR, we have observed that they are close to each other. Hence, a multi-resolution scheme is not critical for efficient performance and we have not included it in our method. However, the varying field of views observed in some of the multi-slice scans restricts the registration over their shared space. Consequently, the r^{th} LRI is modified as

$$y_r[\mathbf{n}] = \int_{\Omega_r} x(\mathrm{A}_r \mathbf{s} + \mathbf{b}_r) h(\mathrm{R}_r(\mathbf{s} - \mathrm{V}\mathbf{n})) d\mathbf{s} + e_r[\mathbf{n}], \tag{124}$$

where $\Omega_r \subseteq \Omega$. Thus, the region for matching is, at most, the common field of view, or

$$\Omega' \subseteq \bigcap_{r=1}^{P} \Omega_r. \tag{125}$$

5.3 Implementation

To account for motion in the MS model, Eq. (119) indicates that the r^{th} up-sampled LRI should be registered against the r^{th} warped and convolved version of $x(\mathbf{s})$. Therefore, the

motion estimation problem is evaluated over the shared field of view, $\Omega^{'}$, of all the LRIs as

$$\hat{\mathrm{A}}_r, \hat{\mathbf{b}}_r = \arg\max_{\mathrm{A}_r, \mathbf{b}_r} I(\ \ x(\mathrm{A}_r \mathrm{R}_r^{-1}\mathbf{s} + \mathbf{b}_r) * h(\mathbf{s}),\ \ y(s) \uparrow \mathrm{V}\ \ ), \tag{126}$$

where $\uparrow$ is the up-sampling process with factors given in the diagonal entries of V from Eq. (59). Bicubic interpolation is the effective up-sampling method. Algorithm (2) outlines the steps for solving Eq. (126), which is the applied motion estimation for line 6 of Algorithm (1). The motion parameters are thus updated using the final SRR after it reaches the desired number of iterations in the assignment: $\hat{\mathbf{x}}^{(l+1)} \leftarrow \arg\max_{\mathbf{x}} p(\mathbf{y}|\mathbf{x}, \hat{\mathbf{v}}^{(l)}))$. Therefore, $\mathrm{H}(\hat{\mathbf{v}})$ is recomputed after each new motion estimate and the translational symmetry initially assumed in the frequency-encoded axis will not be satisfied if motion exists in this direction. Consequently, the series of decoupled 2-D inversions is now one 3-D inversion problem that is solved using the ART. To speed the convergence of the alternating minimization algorithm, the initial HR estimate for a given iteration is the final SRR from the previous one.

Algorithm 2 $\hat{\mathbf{v}} \leftarrow \arg\max_{\mathbf{v}} p(\mathbf{y}|\hat{\mathbf{x}}, \mathbf{v})$

Require:

$\hat{\mathbf{x}}$ is the current HR estimate
V is the diagonal matrix containing the down-sampling rates for each dimension
$h(\mathbf{s})$ is the slice selection function
$\{\mathrm{R}_r\}_{r=1}^{P}$ are known rotation matrices
$\{\hat{A}_r^{(0)}, \hat{\mathbf{b}}_r^{(0)}\}_{r=1}^{P}$ are the initial transformation estimates
$\{\tau_{\mathrm{A}_r}, \tau_{\mathbf{b}_r}\}_{r=1}^{P}$ are convergence criteria
$\Omega^{'}$ is the registration region

1: **for** $r \leftarrow 1 : P$ **do**
2: $\quad \mathbf{y}_r^{\uparrow} \leftarrow \mathbf{y}_r \uparrow \mathrm{V}$ {Use bicubic interpolation}
3: $\quad l \leftarrow 0$
4: $\quad$ **repeat**
5: $\quad\quad \hat{\mathbf{x}}_{warp} \leftarrow \hat{x}(\hat{\mathrm{A}}_r^{(l)}\mathrm{R}_r^{-1}\mathbf{s} + \hat{\mathbf{b}}_r^{(l)})$ {Use bicubic interpolation}
6: $\quad\quad \hat{\mathbf{x}}_{blur} \leftarrow \hat{\mathbf{x}}_{warp} * h$
7: $\quad\quad (\hat{\mathrm{A}}_r^{(l+1)}, \hat{\mathrm{b}}_r^{(l+1)}) \leftarrow (\hat{\mathrm{A}}_r^{(l)}, \hat{\mathrm{b}}_r^{(l)}) + \hat{\nabla}_{(\hat{\mathrm{A}}_r^{(l)}, \hat{\mathrm{b}}_r^{(l)})} I(\hat{\mathbf{x}}_{blur}, \mathbf{y}_r^{\uparrow})|_{\Omega'}$
8: $\quad\quad l \leftarrow l + 1$
9: $\quad$ **until** $||\hat{\mathrm{A}}_r^{(l)} - \hat{\mathrm{A}}_r^{(l-1)}|| \leq \tau_{\mathrm{A}_r}$ and $||\hat{\mathbf{b}}_r^{(l)} - \hat{\mathbf{b}}_r^{(l-1)}|| \leq \tau_{\mathbf{b}_r}$
10: **end for**
11: **return** $\{\hat{A}_r^{(l)}, \hat{\mathbf{b}}_r^{(l)}\}_{r=1}^{P}$

5.4 Experimental Results

Results using the alternating minimization technique and the mutual information metric for motion estimation are reported using both synthetic and FSE-IR multi-slice MRI data.

5.4.1 Synthetic motion

For the synthetic data, the SLP was translated and rotated according to the values given in Table 15. The 2-D domain reduces the number of rotations and translation components from three to one and three to two, respectively. Each of the eight LRIs has eight pixel slice thickness and distance without any noise with a box PSF for a fully-determined system. Fig. 58 shows the six SRRs corresponding to the motion correction estimates using Algorithm (1) with their NMSE vs iteration plots given in Fig. 56). This figure reflects the intermediate results from Algorithm (1). Each of the six curves, denoted in the legend by "i^{th} iteration", corresponds to a SRR process from the alternating minimization algorithm whose input is the set of LRIs that are motion corrected. The reference volume for the motion corrected LRIs for this i^{th} curve is the SRR result from the previous SRR, i.e., the $(i-1)^{th}$. The initial estimate to the i^{th} SRR is the result from the 1000^{th} iteration in the ART used in the previous $(i-1)^{th}$ SRR process. The figure also includes the NMSE plot for reconstruction without any motion for comparison with its corresponding SRR in Fig. 57.

The normalized rotation and translational difference errors, defined as

$$e_{\theta_r} = \left| \frac{\theta_r - \hat{\theta}_r}{\theta_r} \right|, \tag{127}$$

and

$$e_{\mathbf{b}_r} = \frac{||\mathbf{b}_r - \hat{\mathbf{b}}_r||}{||\mathbf{b}_r||}, \tag{128}$$

respectively, are shown in Fig. 59 for each alternating minimization iteration. A 1% stopping criteria in the registration and alternating minimization algorithms (τ_{A} and $\tau_{\mathbf{b}}$) was chosen.

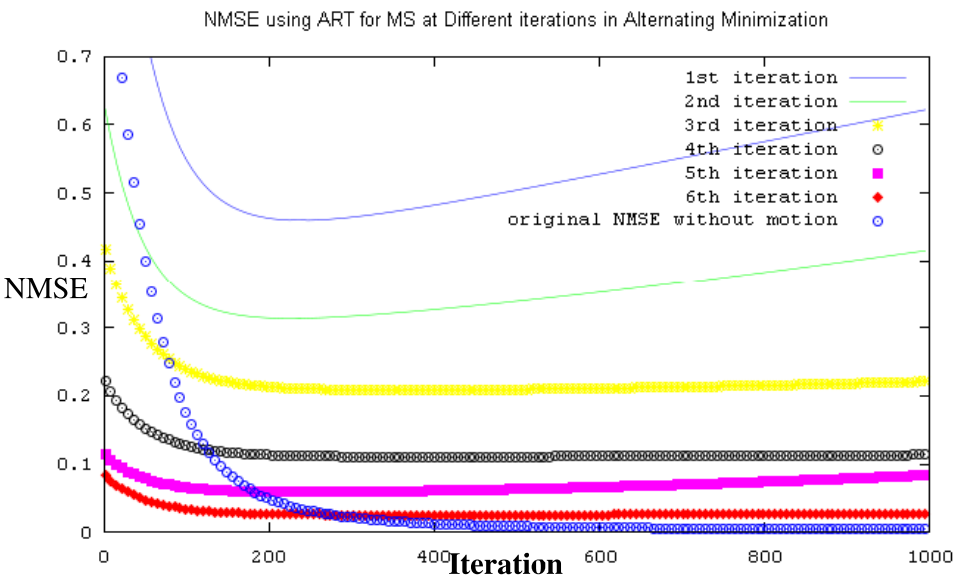

Figure 56: Synthetic motion and SR estimation experiment: NMSE vs Iteration plot for each Alternating minimization iteration of Algorithm (1). The corresponding SRRs of each iteration are given in Fig. 58 using the initial motion vectors from Table 15. The initial estimate to the SRR are the final estimate from the previous SRR in the alternating minimization. The NMSE vs iteration plot for no motion is also given.

Figure 57: Synthetic motion and SR estimation experiment: SLP SRR without any motion.

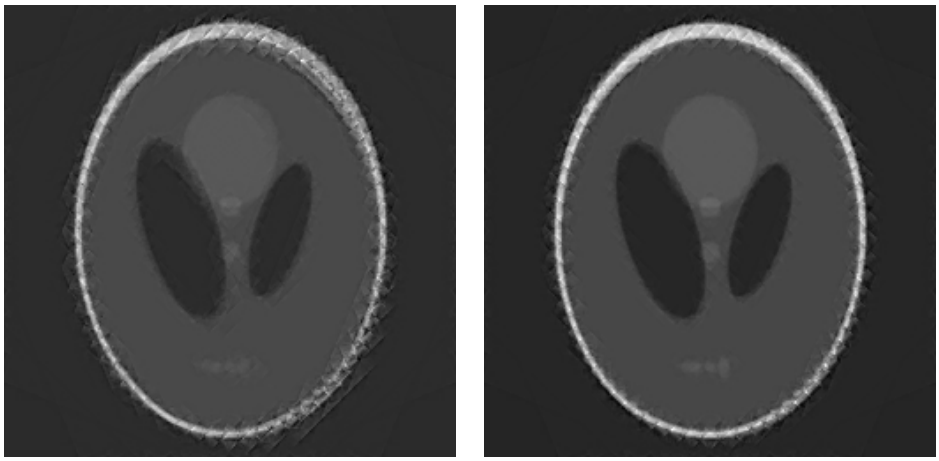

(a)

(b)

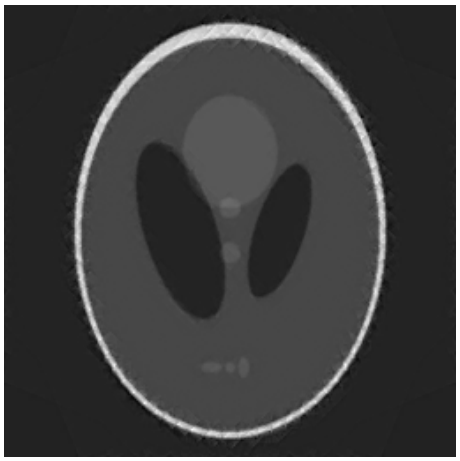

(c)

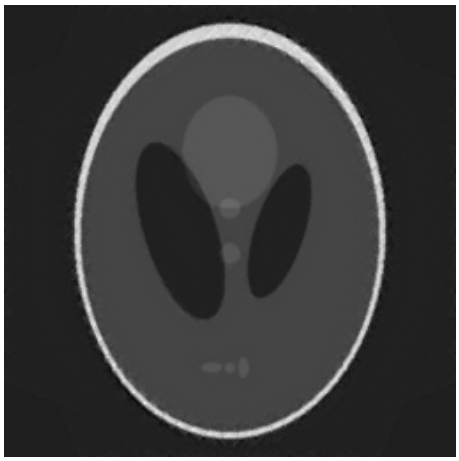

(d)

(e)

(f)

Figure 58: Synthetic motion and SR estimation experiment: Each image corresponds to a SRR after motion correction using the initial motion vectors given in Table 15. These are SRRs of the (a) Initial (no motion correction) (b) 2^{nd} (c) 3^{rd} (d) 4^{th} (e) 5^{th} and (f) 6^{th} iteration of Algorithm (1) using the motion correction from Algorithm (2).

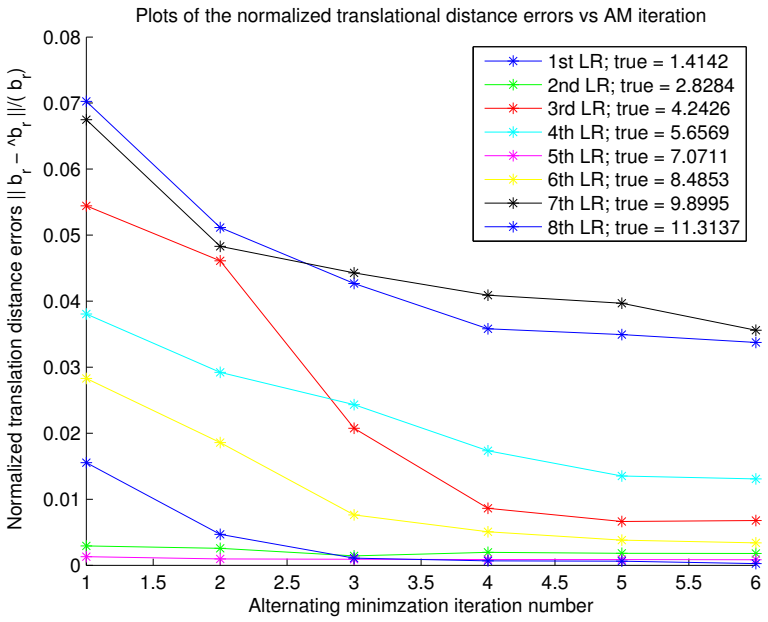

(a)

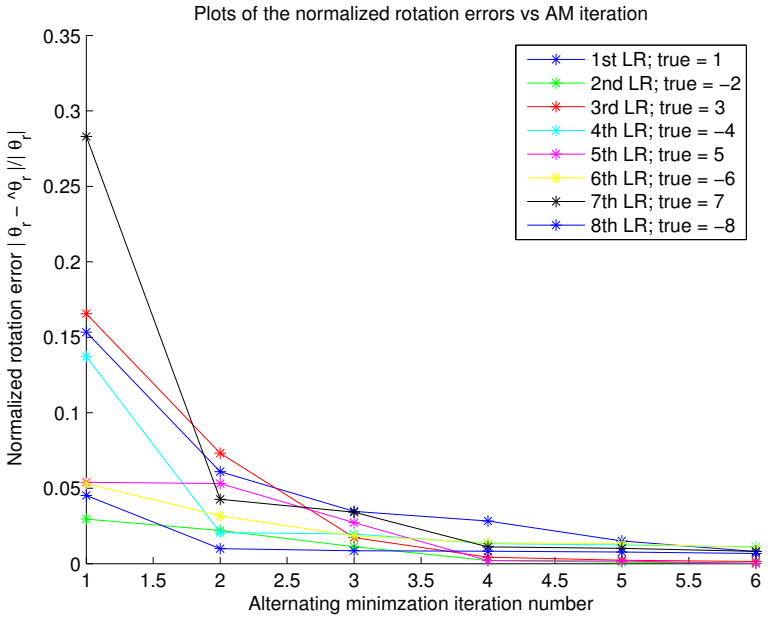

(b)

Figure 59: Synthetic motion and SR estimation experiment: Plots of the normalized errors vs alternating minimization iteration for (a) translational distances (e_{d_r}) (b) rotations (e_{θ_r}).

Table 15: Synthetic motion and SR estimation experiment: Eight LRIs artificially rotated and translated.

LRI No., r	Rotation, θ_r	Translation vector, $\mathbf{b}_r$
1	1	[1 -1]
2	-2	[-2 2]
3	3	[3 -3]
4	-4	[-4 4]
5	5	[5 -5]
6	-6	[-6 6]
7	7	[7 -7]
8	-8	[-8 8]

5.4.2 Multi-slice MRI Data

In-vivo study No. 3 in Chapter four showed a ghosting artifact in the SRR (see Fig. 76). Therefore, we relied on this study to be the data in our super-resolution with motion experiment. Fig. 60(a,c,e) simultaneously show MPRs of both the first and last acquired LR sagittal scans using checkerboard patterns without any motion correction. These are both sagittal scans separated by 30^o in their scanning orientation. Fig. 60(b,d,f) show the checkerboard of the two LRSs again. However, these three MPRs correspond to the transformation using the motion correction estimates after the final (third) iteration of the alternating minimization algorithm. The final estimates in Table 16 results from three iterations in the repeat-until loop from Algorithm (1). Fig. 61(a,c,e) and (b,d,f) show the MPRs of the SRR with and without motion correction, respectively. Fig. 61(b,d,f) is the SRR from the third and final iteration in the repeat-until loop from Algorithm (1). A 1% stopping criteria in the registration and alternating minimization algorithms (τ_{A} and $\tau_{\mathbf{b}}$) was chosen using three iterations of the alternating minimization technique and 1000 iterations of the ART. All of the field of views from the six LRSs covered the head, so the region for matching included the entire volume of the brain. In this study, the slice selection profile was not measured, and a box-PSF was used instead.

Table 16: Multi-slice MRI data motion and SR estimation experiment: Six LR volumes and their estimated rotations and translations after the third iteration from the alternating minimization algorithm.

LRI No., r	Rotations (degrees): $\theta_r, \varphi_r, \psi_r$	Translation (mm): $\mathbf{b}_r$
1	0.02,-0.11,0.09	[0.29 0.13 0.09]
2	-0.35,-0.11,0.19	[-0.35 -0.27 0.09]
3	1.78,-0.13,2.00	[-0.49 2.49 2.1]
4	1.35,-0.11,3.35	[-0.24 2.85 1.09]
5	1.1,-2.87,2.39	[1.71 2.44 0.97]
6	1.22,-3.17,1.67	[1.65 2.51 1.45]

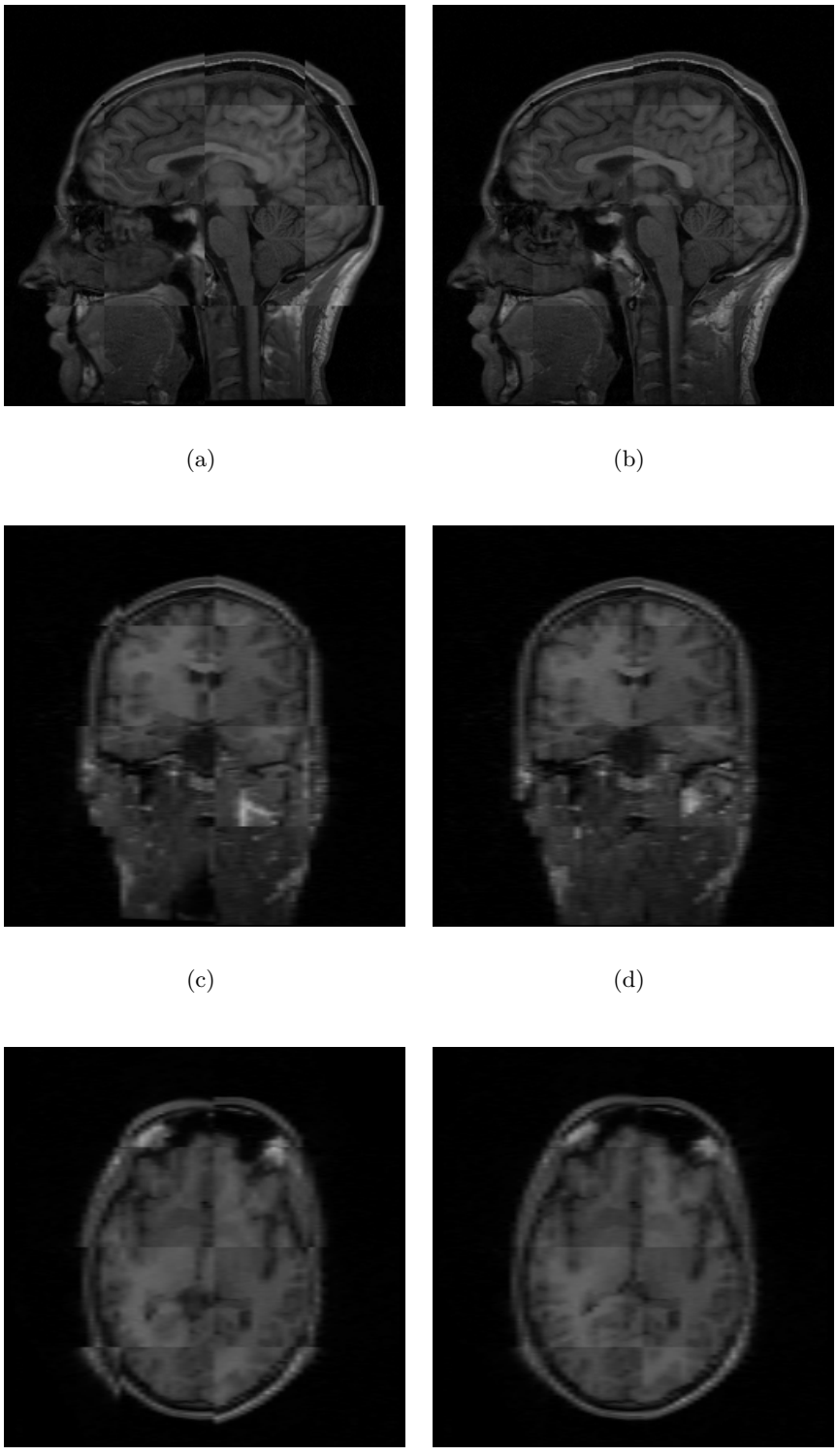

(a) (b)

(c) (d)

(e) (f)

(a) Sagittal view of two LRIs without motion correction	(b) Sagittal view of two LRIs with motion correction
(c) Coronal view of two LRIs without motion correction	(d) Coronal view of two LRIs with motion correction
(e) Axial view of two LRIs without motion correction	(f) Axial view of two LRIs with motion correction

Figure 60: Multi-slice MRI data motion and SR estimation experiment: In-vivo study No. 3: Checkerboard imagery of two sagittal LRSs (30^o difference in scanning orientation) with and without motion correction using the alternating minimization technique. The LRIs in (b,d,f) correspond to the transformation using the motion correction estimates after the final (third) iteration of the alternating minimization algorithm.

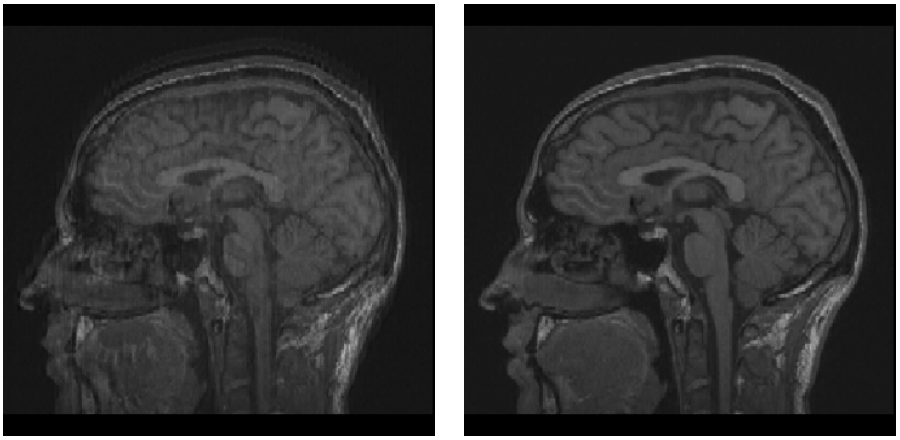

(a) (b)

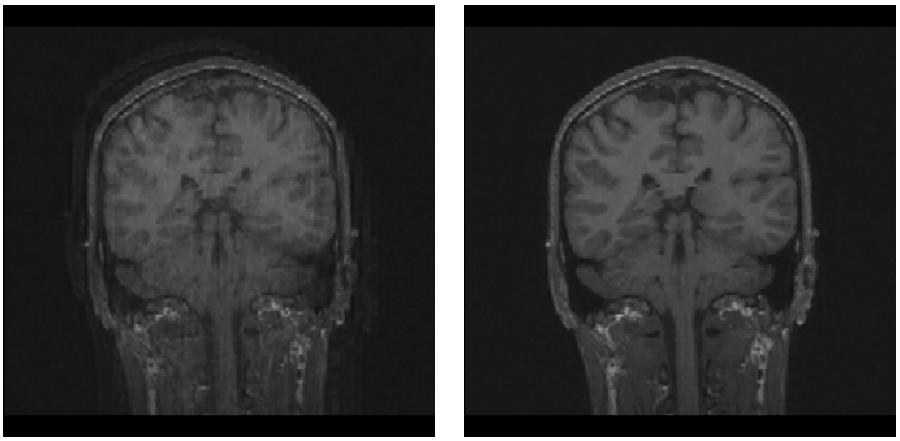

(c) (d)

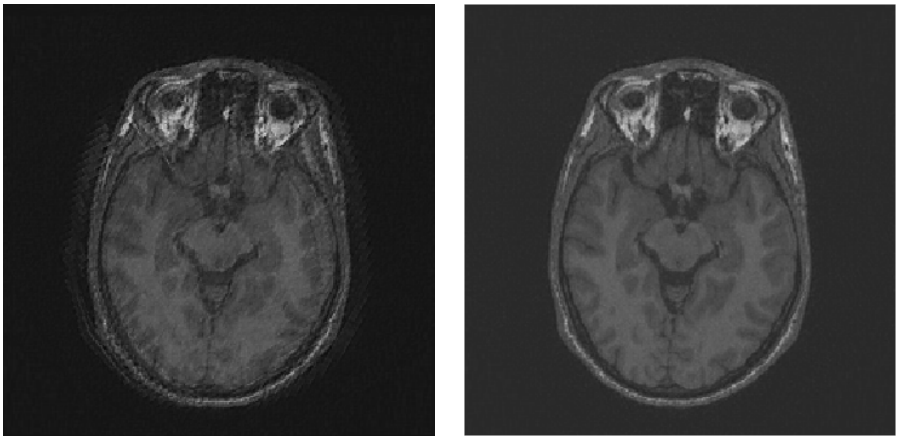

(e) (f)

(a) Sagittal SRR without motion correction	(b) Sagittal SRR with motion correction
(c) Coronal SRR without motion correction	(d) Coronal SRR with motion correction
(e) Axial SRR without motion correction	(f) Axial SRR with motion correction

Figure 61: Multi-slice MRI data motion and SR estimation experiment: SRR using alternating minimization technique (a-c) Axial, coronal, and sagittal views of the SRR without motion correction using ART (voxel = 1 mm × 1 mm × 1 mm) (d-f) Axial, coronal, and sagittal views of the SRR using alternating minimization (after 3 iterations) motion correction with ART (1000 iterations) voxel = 1 mm × 1 mm × 1 mm).

5.5 Observations

5.5.1 Synthetic motion

Each subsequent acquired LRS shows increasing motion distances for in-vivo study no. 3 (e.g., see Table 16). This motion between the first and last LRS is apparent in the checkerboard imagery (Fig. 60(a,c,e)), especially at the head and background boundary. After motion correction and inspection of Fig. 60)(b,d,f), the two images align well at each other's boundaries. This results in a clear and informative SRR shown in Fig. 61(b,d,f).

5.5.2 Multi-slice Data

Each subsequent acquired LRS shows increasing motion distances for in-vivo study no. 3 (e.g., see Table (16)). This motion between the first and last LRS is apparent in the checkerboard imagery (Fig. (60)(a,c,e)), especially at the head and background boundary. After motion correction and inspection of Fig. (60)(b,d,f), the two images align well at each other's boundaries. This results in a clear and informative SRR shown in Fig. (61)(b,d,f).

5.5.3 Execution Times

Software included the GNU/Linux, Brainwork and ITK tools [33]. The alternating minimization technique executing on an Intel Xeon CPU 3.20GHz 16GB RAM machine lasted approximately one hour using the SLP data set. Each iteration of the alternating minimization technique took approximately ten minutes with six iterations; approximately one minute for the SRR (1000 iterations using ART), six minutes to construct and update the new contribution matrix, and three minutes to perform registration correction ($\alpha = .1$ in Eq. (123)). Execution of the in-vivo data set lasted approximately 36 hours. Each of the three iterations of the alternating minimization algorithm took 12 hours ($\delta = 0.01$ is the parameter in constructing H); ten hours to compute the contribution matrix, one hour for the ART, and the remaining one hour for registration. The great loss in speed for the 3-D version of MS is best explained with the extra dimension. In 2-D, the running time to compute the contribution matrix is proportional to $O(\frac{M|\mathsf{supp}(h)|}{\delta^2})$. The 3-D introduces another δ in the denominator (i.e., $O(\frac{M|\mathsf{supp}(h)|}{\delta^3})$), causing a slow-down factor of 100× at

$\delta = 0.01$. However, the process of computing the contribution matrix is distributed over the LRI voxels. Consequently, Algorithm (3) from Appendix C can be arranged so that run time experiences a speed-up factor that scales linearly with the number of processing elements.

5.6 Conclusion

MS re-modeled with rigid motion between LRSs is a feasible approach to SR in multi-slice MRI. The simulated motion experiments of synthetic data return SRRs of high fidelity comparable to one without motion when using the alternating minimization technique. However, CPU time emerges as a new bottleneck in this technique. Incorporating the mutual information metric has made our approach to the motion estimation problem for SR novel enough to warrant further study.

CHAPTER VI

SAMPLING STRATEGIES OF SUPER-RESOLUTION IN MULTI-SLICE MRI

MS is a feasible approach to achieving SR for MRI, but its performance as compared to the parallel sub-pixel shift method of Greenspan et al. remains to be determined [27]. This chapter begins with head-to-head experimental comparisons using MS and the conventional "Parallel Stack" (PS) approach using both simulated and real multi-slice MRI data. So far, we have assumed prior knowledge of the slice excitation, but a key measure of robustness of a SR technique is its response to uncertainty in the slice profile. With a phantom as a measurement tool for the slice excitation profile, as described in Appendix (D), the profile shape may be estimated for a certain pulse sequence. Otherwise the slice profiles will remain unknown, as well as the effects they will have on the SRR. Therefore, we expanded the comparative evaluation by testing the approaches for their response to system error in addition to measurement error. Furthermore, we recognize that the ML estimates used so far, are generally ill-conditioned. That is, a small change in the measurements may cause a large change in the ML estimate. Information may be lost in observation as well (i.e., a linear forwarding system with a nonempty null space) and so some components can never be recovered, regardless of the SRR technique. Therefore, as a regularized approach, we explore a maximum a-posteriori (MAP) solution to emphasize smoothness in our HRI prior so that overshoot artifacts at sharp edges in previously observed SRRs are attenuated.

6.1 Observation Model Comparison of Parallel- and Multi-Stack

The modeled degradation processes of PS and MS are similar. Their input to the SRR consists of the LRIs after Fourier reconstruction, where the slice excitation is modeled as a convolution of the HRI with the slice profile. Both techniques have the same effective

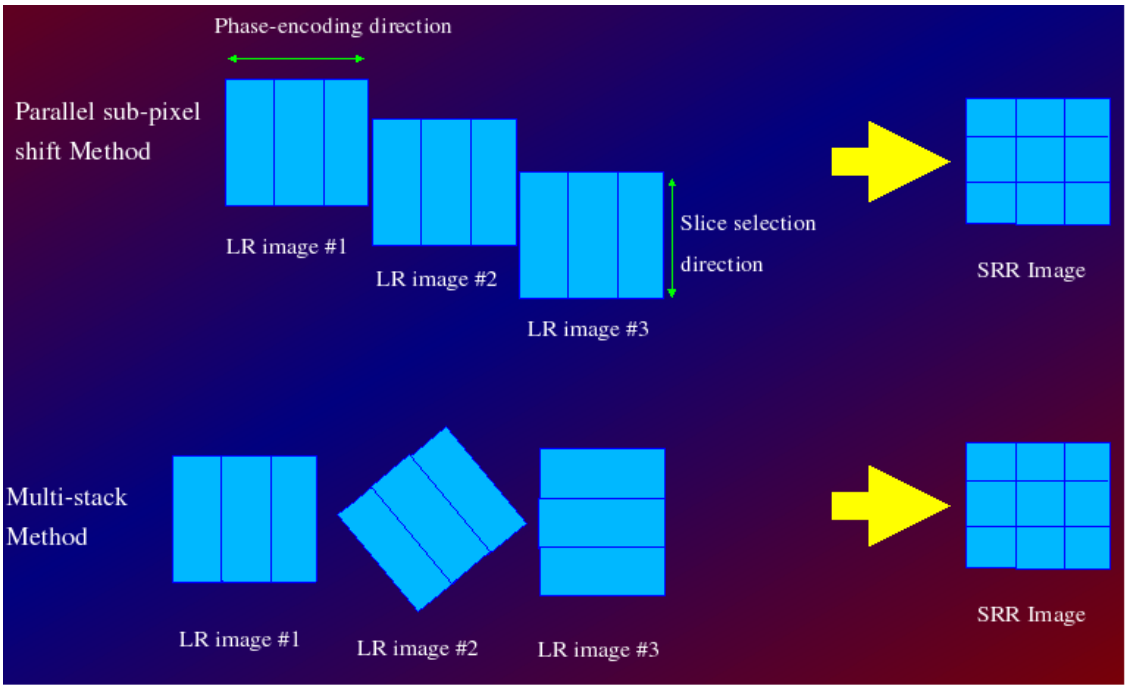

Figure 62: Multi-Stack vs Parallel-stack illustration

down-sampling and blurring functions so that the r^{th} LRI in either case is

$$y_r[\mathbf{n}] = \int_{\Omega_r} x(\mathbf{s}) h_r(\mathbf{s} - \mathrm{V}\mathbf{n}) d\mathbf{s} + e_r[\mathbf{n}], \tag{129}$$

where $e_r[\mathbf{n}]$ is the additive noise term (see Appendix (3.1)). Their difference is the warp acting on the PSF:

$$PS: \quad h_r(\mathbf{s}) = h(\mathbf{s} + \phi_r) \qquad \phi_r = [0 \;\; 0 \;\; \frac{T_{SS}(r-1)}{P}]^T, \tag{130}$$

$$MS: \quad h_r(\mathbf{s}) = h(\mathrm{R}_r\mathbf{s}) \qquad \mathrm{R}_r = \begin{pmatrix} 1 & 0 & 0 \\ 0 & \cos\theta_r & -\sin\theta_r \\ 0 & \sin\theta_r & \cos\theta_r \end{pmatrix}, \quad \theta_r = \frac{180(r-1)}{P}, \tag{131}$$

where T_{SS} is the slice selection sampling period given as the last diagonal entry in V. Figure 62 illustrates the difference between the two methods. As an example, a set of multi-planar reformats (MPR) of the LRIs for both the PS and MS methods are shown in Fig. 63).

Analysis of $e_r[\mathbf{n}]$ in Eq. (129) for the PS approach is similar to that of MS given in

Appendix B so that

$$\mathsf{E}[\Re(e_r[\mathbf{n}])] = 0 \tag{132}$$

$$\mathsf{Cov}(\Re(e_r[\mathbf{n}])\Re(e_r[\mathbf{m}])) = \sigma_e^2 \int_\Omega h(\mathbf{s} - \mathrm{V}\mathbf{n} + \phi_r)h(\mathbf{s} - \mathrm{V}\mathbf{m} + \phi_r)d\mathbf{s}, \tag{133}$$

which leads to a ML and LS estimate equivalence.

6.2 Singular Value Decomposition Experiment

The susceptibility of error by the SR techniques of MS or PS is first examined using singular value expansion (SVE) and singular value decomposition (SVD). These numerical tools decompose any linear transformation into a set of orthonormal basis functions that quantitatively indicate their sensitivity to input error. The intrinsic model of observations for MS and PS could either be ill-conditioned or rank-deficient.

6.2.1 Theory of Singular Value Expansion and Decomposition

In general, a linear continuous process can be represented by a Fredholm integral of the first kind in the form

$$\int_0^1 H(s,t)x(t)dt = y(s) \quad 0 \le s \le 1, \tag{134}$$

where $y(s)$ is known, and $x(s)$ is the sought solution. The kernel, $H(s,t)$, can be decomposed into its singular value expansion as

$$H(s,t) = \sum_{i=1}^{\infty} \sigma_i u_i(s) v_i(t), \tag{135}$$

where $u_i(s)$ and $v_i(t)$ are its orthonormal functions such that

$$(u_i, u_j) = (v_i, v_j) \tag{136}$$

$$= \delta(i-j), \tag{137}$$

where

$$(a,b) \equiv \int_0^1 a(t)b(t)dt. \tag{138}$$

These are analogous to the ortho-normal vectors used in SVD for a matrix, H. That is,

$$\mathrm{H} = \mathrm{U}\Sigma\mathrm{V}^H \tag{139}$$

$$= [\mathbf{u}_1, \cdots, \mathbf{u}_M]\mathrm{diag}(\sigma_1, \cdots, \sigma_L)[\mathbf{v}_1, \cdots, \mathbf{v}_N]^H, \tag{140}$$

where $L = \text{rank(H)} \leq \min(M, N)$, $\text{UU}^H = \mathbb{I} \in \mathbb{R}^{M \times M}$, and $\text{VV}^H = \mathbb{I} \in \mathbb{R}^{N \times N}$. The numbers, $\{\sigma_i\}_{i=1}^{L}$, are the non-negative singular values, or amplitude gains, that map the set of basis functions in the domain of $H(s,t)$, $\{u_i(s)\}_{i=1}^{M}$, to the set of basis functions in its co-domain, $\{v_i(s)\}_{i=1}^{N}$. Using Eq. (135), the solution can be represented as

$$x(t) = \sum_{i=1}^{L} \frac{(u_i, y)}{\sigma_i} v_i(t). \tag{141}$$

The ratio, $\frac{(u_i,y)}{\sigma_i}$, is the amplitude gain of $v_i(t)$ contributing to the solution $x(t)$. If the numerator in the ratio shares the same decay rate as its respective singular value, then numerical anomalies may be mitigated. Otherwise, if the representation is to be approximated on a machine with a finite precision, the number may be compromised, thus affecting the solution estimate. The disparity or ratio of the largest and smallest singular values, defined as the condition number of the matrix, indicates the susceptibility to error in a system. While it may be difficult or impossible to capture this information analytically, in practice it is has been observed that the singular functions $u_i(s)$ increase with the number of oscillations crossing zero for a decreasing σ_i. The Riemann-Lebesgue lemma indicates that the inner product approaches 0 as the number of zero crossings increases[1].

Thus, a quantitative measure of PS and MS systems can be derived from the singular values and the number of zero crossings in the singular vectors of H.

6.2.2 Experiment Design

The asymptotic running time to compute the SVD of a matrix is proportional to the same asymptotic time in its direct inversion (i.e., $O(N^3)$ for a $N \times N$ matrix). The computation relies on an eigenvalue decomposition for both H^HH and HH^H, known as QR factorization [26], which expresses the matrix as a product of orthogonal and upper triangular matrices. In any case, SVD computation remains infeasible for a matrix whose size is comparable to a realistic forwarding model for SR. As an alternative to large scale SVD, a significantly smaller system with the same number of unknowns as equations for both SR methods has been set up in this experiment, as shown in Table 17.

[1]Riemann-Lebesgue lemma: If $u(s)$ is a continuous function on $[0,1]$, then $\int_0^1 u(s)e^{j\lambda s}ds \to 0$ as $\lambda \to \infty$.

Table 17: SVD experiment: SR configurations for PS and MS.

SR Method	P	LR pixel resolution	HR pixel resolution	PSF	M	N
PS	4	16×4	16×16	Box	256	256
MS	4	16×4	16×16	Box	256	256

6.2.3 Results

Fig. 64 shows plots of the singular values for the PS and MS methods using QR matrix factorization with a box slice encoding profile using the configuration in Table 17. Their condition numbers and number of zero crossings are given in Table 18). Tables (19 and 20 show the computed condition numbers at configurations with different numbers of LRIs (P) and slice thicknesses (T_{SS}), for MS and PS, respectively. The entries with ∞-values in Tables (19) and (20) indicate under-determined systems that possess zero-valued singular values. Smaller condition numbers can be interpreted as providing better conditioning to input error in the SRR process.

Table 18: SVD experiment: Condition Numbers of SRR methods.

Configuration	Condition Number ($\frac{\sigma_{max}}{\sigma_{min}}$)	Total Zero Crossings
Parallel stack	36.0764	32196
Multi stack	32.1831	31013

Table 19: SVD experiment: Condition Number for MS.

$\frac{P}{T_{SS}}$	2	4	6	8
2	14.00	11.00	13.03	14.28
4	∞	18.31	19.00	32.00
6	∞	∞	38.00	41.00
8	∞	∞	∞	33.88

6.2.4 Conclusion

According to the configurations given in Tables (19), (18), and (20), MS and PS share comparable condition numbers as well as zero crossings in their singular vectors. However, in these tested cases, MS is shown to be slightly more well-posed than PS. Increasing the size of both systems while maintaining its fully-determined attribute results in monotonically increasing condition numbers. This indicates that the both SR techniques become

Table 20: SVD experiment: Condition Number for PS.

$\frac{P}{T_{SS}}$	2	4	6	8
2	24.00	24.40	24.58	24.95
4	∞	36.08	41.00	36.00
6	∞	∞	40.00	46.00
8	∞	∞	∞	39.85

increasingly more ill-conditioned as more measurements and unknowns are introduced into the observation process.

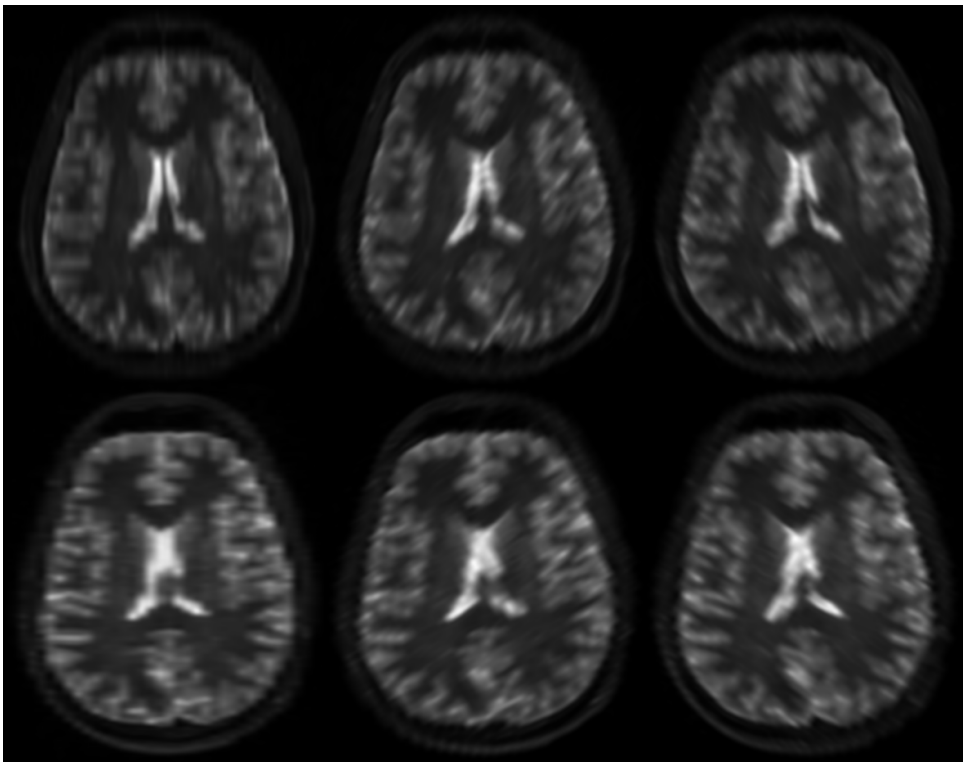

(a)

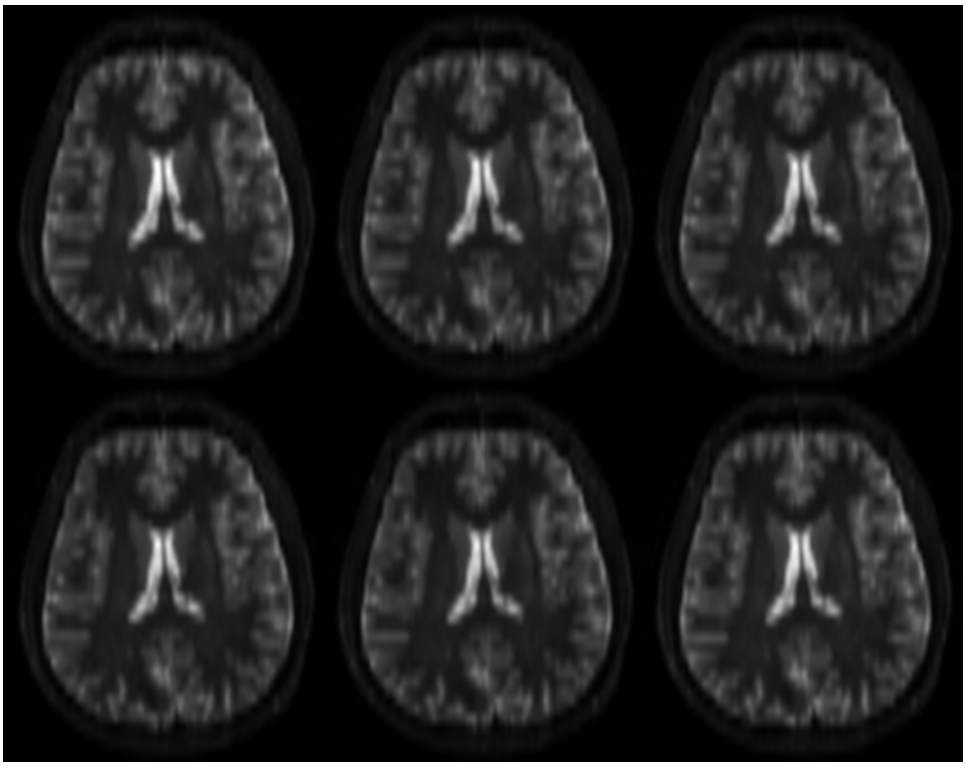

(b)

Figure 63: MS vs PS in-vivo scan experiment: MPRs of the LRSs from (a) MS, and (b) PS. The slice selection for PS is in the vertical direction.

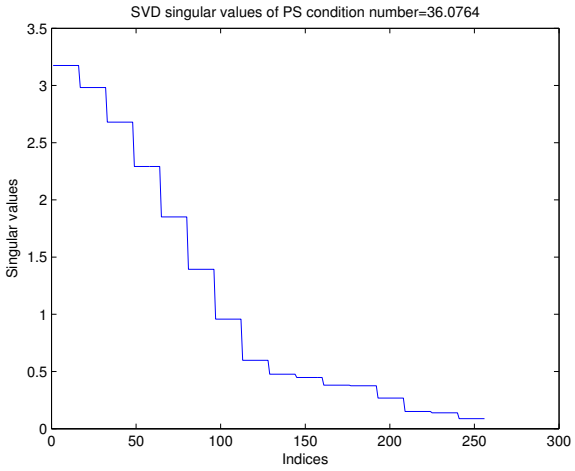

(a)

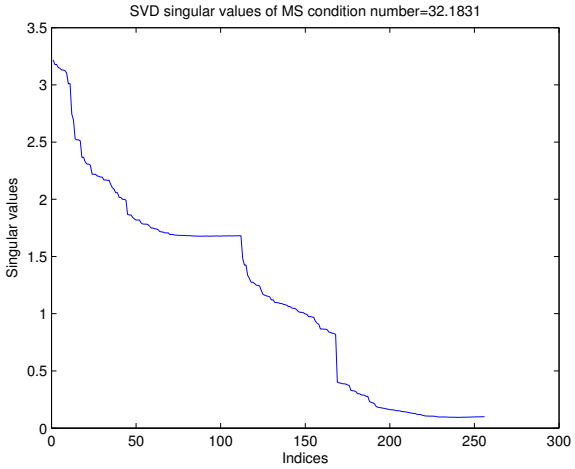

(b)

Figure 64: SVD experiment: Plot of singular values of the (a) PS and (b) MS methods

6.3 Regularization with a Gibbs Prior

An ill-posed problem is a system with a non-empty null space[2] and thus a unique solution does not exist. Yet some of these solutions may be more meaningful than others. Certainly, this holds true for the observations made in the under-determined MS SLP cases shown in Chapter 4. For example, the absence of any streaking artifacts already observed in the SRRs would be more desirable than their presence. Therefore, in order to obtain a meaningful and accurate approximation in a Bayesian framework, stabilizing either MS and PS requires the use of a prior. According to the MAP expression,

$$\hat{\mathbf{x}}_{MAP} = \arg\max_{\mathbf{x}}(\log p(\mathbf{y}|\mathbf{x}) + \log p(\mathbf{x})), \tag{142}$$

the HRI requiring a PDF for $\mathbf{x}$ is often based on a Gibbs prior from a Markov Random Field in image processing and tomographic reconstruction:

$$p(\mathbf{x}) \propto \exp(-\lambda||\mathrm{L}\mathbf{x}||^2), \tag{143}$$

where λ indicates the strength of some stability operator, L [34]. This can be the identity, first order derivative, Laplacian, etc. In other words, image roughness is penalized in the solution. Combining this term with the ML expression already derived for MS (see Eq. (85)) results in the MAP estimate

$$\hat{\mathbf{x}}_{MAP}(\lambda) = \arg\min_{\mathbf{x}} \|\mathbf{y} - \mathbf{H}\mathbf{x}\|^2 + \lambda \|\mathrm{L}\mathbf{x}\|^2 . \tag{144}$$

The ability to determine a suitable λ is essential to obtaining an acceptable solution to the discrepancy between fidelity and smoothness. Either the solution can be over- or under-smoothed for large or small values of λ, respectively. In theory, λ is chosen to minimize the predictive mean square error

$$PMSE(\lambda) = ||\mathrm{H}\mathbf{x} - \mathrm{H}\hat{\mathbf{x}}_{MAP}(\lambda)||^2, \tag{145}$$

but this requires direct knowledge of $\mathbf{x}$ or the statistics of the error norm. Instead, techniques such as the generalized cross-validation or L-curve methods have been applied that

[2]The null space of a matrix, H, is denoted as $N(\mathrm{H}) \equiv \{x|\mathrm{H}x = 0\}$

automatically solve for λ with the solution [78]. If an arbitrary measurement is removed in the reconstruction, then cross-validation predicts the best estimate for λ so that this solution remains close to the solution that would otherwise include the measurement. Chung et al. give experimental results that over-estimate λ based on generalized cross validation while Tenorio makes claims that the same technique leads to small values of λ [14, 78]. The L-curve method plots the norms of the fidelity versus the prior as a function of λ (leading to a L-shape). The selection of λ corresponds to the point of highest curvature. Rather than using these techniques for finding an optimal λ and contending with the mentioned claims, we want to observe and evaluate the behavior of the algorithm subject to different choices for the parameter λ. As a guideline, the regularization parameter is selected between the smallest and largest value of the singular values [14].

In any case, once λ is selected, the MAP solution of Eq. (144) satisfies

$$(\mathbf{H}^T\mathbf{H} + \lambda\mathbf{L}^T\mathbf{L})\mathbf{x} = \mathbf{H}^T\mathbf{y}. \tag{146}$$

Without the use of regularization, the LS estimate, given as the solution to the normal equation (see Eq. (87)), in terms of the variables from its SVD (Eq. (139)), becomes

$$\hat{\mathbf{x}}_{LS} = \sum_{i=1}^{L} \frac{1}{\sigma_i}(\mathbf{u}_i^T\mathbf{y})\mathbf{v}_i. \tag{147}$$

If the singular components are either zero or small enough that the machine precision, denoted as ϵ, is compromised (i.e., $\sigma_i < \epsilon$), then the scaling factor of $\frac{1}{\sigma_i}$ will deviate considerably from the true scaling factor. Consequently, this results in large errors between the true solution and its estimate. However, expressing the regularized solution from Eq. (146) with the SVD variables using $\mathrm{L} = \mathbb{I}$, changes the solution to

$$\hat{\mathbf{x}}_{MAP} = \sum_{i=1}^{L} \frac{\sigma_i^2}{\sigma_i^2 + \lambda^2}(\mathbf{u}_i^T\mathbf{y})\mathbf{v}_i. \tag{148}$$

The change in gains, $\frac{1}{\sigma_i} \mapsto \frac{\sigma_i^2}{\sigma_i^2+\lambda^2}$, thus stablizes the MAP solution when $\sigma_i < \epsilon$.

The method to solve for a MAP SRR is straightfoward. Eggermont et al. use the ART to find the regularized solution in Eq. (146) [21]. The matrix equation used by the ART

solves for

$$[\mathbf{H} \;\; \lambda\mathbf{L}] \begin{pmatrix} \mathbf{x} \\ \mathbf{v} \end{pmatrix} = \mathbf{y}, \tag{149}$$

with initial conditions, $\hat{\mathbf{x}}^{(0)} = 0$, and $\hat{\mathbf{v}}^{(0)} = 0$. The upper component, $\mathbf{x}$, in the vector of Eq. (149) is shown to converge to the regularized solution, i.e., $\hat{\mathbf{x}}^{(\infty)}$, that satisfies Eq. (146). Therefore, we solve for

$$\mathbf{H}^{'}\mathbf{x}^{'} = \mathbf{y}, \tag{150}$$

where $\mathbf{H}^{'} = [\mathbf{H} \;\; \lambda\mathbf{L}]$ and $\mathbf{x}^{'} = [\mathbf{x}^T \;\; \mathbf{v}^T]^T$ and take the upper component of $\mathbf{x}^{'}$ as the regularized SRR.

6.4 Experimental comparison of Multi-Stack and Parallel-Stack

Three SR experiments for both PS and MS techniques were conducted using the SLP and real multi-slice MRI data. Real multi-slice MRI data includes an inanimate object (grapefruit) to show a comparison using data absent of motion as a possible confounding factor, and also of a volunteer subject to assess in-vivo performance. The reconstruction algorithms include using the ART with and without Tikhonov regularization based on the Gibbs prior (see Eq. (143)). We substituted the variables given in Eq. (150) for the regularization cases and use $\mathrm{L} = \mathbb{I}$.

6.4.1 Phantom Simulations

Using the simulated forwarding described in Chapter 4, experimental variables in the SLP experiments were the slice thickness, slice profile, and noise level. The SRR effects from introducing uncertainty in the slice profile is accomplished through inconsistent slice profile functions between the forwarding model and the inverse model used as part of the SRR. The forwarding model is a Gaussian function with the full width at half maximum (FWHM) equal to the slice thickness. The corresponding slice profile function in the inverse model is an ideal box with its width equal to the FWHM in the forward model, as shown in Fig. 65. The original SR process is now

$$(\mathrm{H} + \mathrm{E})\mathbf{x} = \mathbf{y} + \mathbf{e}, \tag{151}$$

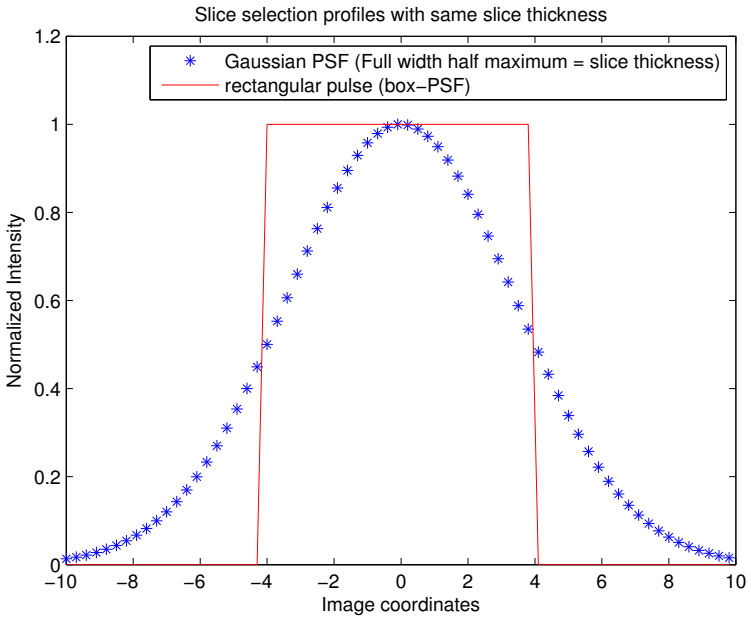

Figure 65: MS vs PS: Plots of different slice selection profiles

where E denotes the system error. The regularization parameter, λ, was sampled at $\{0.1, 1, 2, 10\}$ with $\mathrm{L} = \mathbb{I}$, to empirically select a value balancing fidelity and energy levels.

6.4.2 MRI of Inanimate Object

A grapefruit was scanned to rule out possible motion between stacks. Two sets of six scans were acquired by the MS and the PS protocols on a 1.5T Philips Intera Scanner (R11), with otherwise identical parameters: TE=40ms, TR=3000ms, TI=190ms, flip angle=90, 256x256 pixels on a 160mm in-plane square field of view, using partial-Fourier acquisition; contiguous 3.6mm slices with in-plane resolution = 0.6mm; scan time 3 min per stack. All scans had the same readout direction. The angular increment between MS stacks was 30. The PS stacks were scanned at 0.6 mm slice offset increments. The slice profile of the scans was determined using a separate scan of a resolution phantom.

6.4.3 In-vivo Brain Scan

Two sets of six scans were acquired by the MS and the PS protocols on a 3T Siemens Trio/TIM (Rev. 4BV13A) with otherwise identical parameters: multi-slice IR-FSE, echo train length = 17, TE=85 ms, TR=4830 ms, TI=190ms, flip angle=90, 512x512 image grid on a square 220 mm field of view from 271 phase encodings, NEX=1; contiguous 4.8 mm slices; scan time 3 min/stack. The readout direction, common to all scans, was orthogonal to the transverse plane. The angular increment between MS stacks was 30. The five sub-pixel shifts from the reference scan all shared 0.8 mm increments

6.5 Results

6.5.1 Phantom Simulations

Fig. 66 shows details from the SLP ground truth, MS and PS reconstructions (2000 iterations), respectively, using eight noiseless contiguous stacks of eight pixel slice thickness. Fig. 67 shows the SLP SRRs with and without regularization. The figure also shows corresponding vertical center line (see Fig. 67) profiles (left) and difference with truth (right). Figure 68 shows the NMSE vs iteration plots of MS for both the noiseless ideal fully-determined and noisy cases with and without regularization. Fig. 69(a) shows comparative NMSE evolution for noiseless and noisy data. Fig. 69(b) compares the effect on NMSE of inconsistent slice profile information in the reconstruction process using the slice profiles from Fig. 65.

6.5.2 MRI of Inanimate Object

Axial views of the grapefruit are shown in Fig. 70. A slice reformatted from a single LR scan is shown in Fig. 70(a). The MS and PS images are shown in Fig. 70(b-c), at 2000 iterations. The voxel size in the reconstructions is $0.6mm^3$.

6.5.3 In-vivo Brain Scan

A set MPRs of the LRIs for both PS and MS are shown in Fig. 63. The shared slice selection for PS is in the vertical direction. A reformatted axial view through one of six LR In-vivo brain scans is shown in Fig. 72 for reference. Regularized reconstructions ($\lambda = 1$) for PS

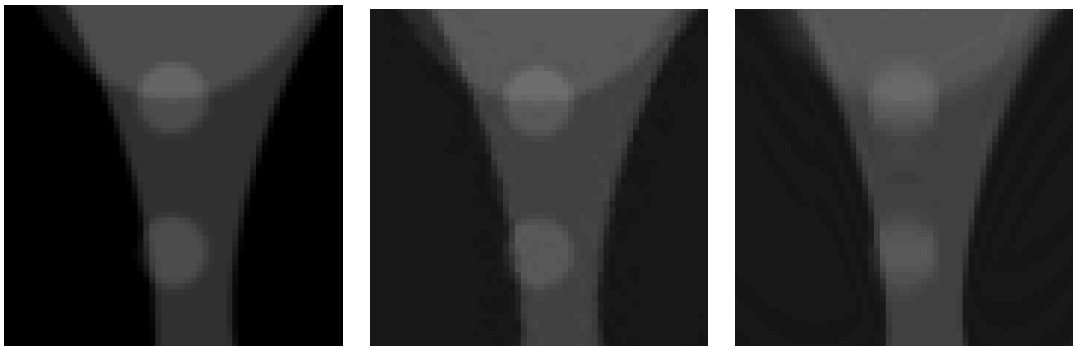

(a) (b) (c)

Figure 66: MS vs PS: Detail of SLP at center of SRRs (a) Truth (b) MS (c) PS.

and MS are shown in Fig. 72(b) and Fig. 72(c), respectively. The pixel size in the output grid is: $0.8 \times 0.8mm^2$.

6.6 Discussion

Simulation experiments showed lower NMSE (Fig. 69(a)) for MS than for PS in both the noiseless and noisy cases. MS also reaches an optimal value in a fewer number of iterations than the PS with the ART algorithm. This improvement in the rate of convergence for MS over PS in the ART can be attributed to the angles between the hyper-planes. By choosing two hyper-planes (i.e., rows of H) that have a wide angle between them, the number of iterations to reach their intersection of admissible solutions is is fewer than the two hyper-planes that have a narrow angle. Iterative reconstruction with additive correction recovers low before high frequency content. The increasing NMSE in Fig. 69)(a) for reconstruction from noisy data may be attributed to recovery of high-frequency noise. Line profiles in Fig. 67 reveal ripple artifact at edges, which includes persistent ringing artifact in the slice selection direction for the PS method. Ripple wavelength is linked to slice thickness, and the number of periods grows with continued iteration. Between the line plots of the error, as shown in Fig. 67(a) and (b), MS seems to have shorter amplitude and ripple wavelengths compared to PS. Intermediate reconstruction estimates showed trade-offs between unresolved edges and increased ringing. The MS method expresses isotropic

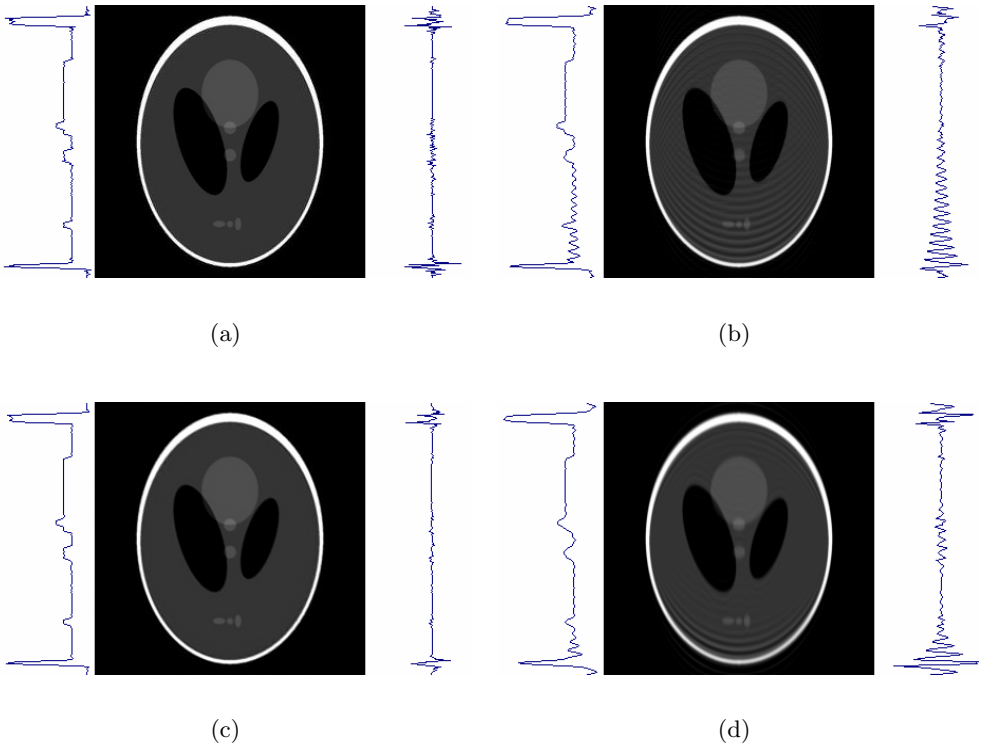

(a) (b)

(c) (d)

No Regularization	(a) MS	(b) PS
Regularization, $\lambda = 1$	(c) MS	(d) PS

Figure 67: MS vs PS: To the left of each image an intensity profile is shown, and to the right of each image profile are shown (amplified consistently relative to the intensity profiles) to show difference with the ideal SLP (Fig. 66).

local overshoot at step edges. Regularized versions of both approaches (Fig. 66) attenuate edge ringing at a penalty in edge resolution. The NMSE for regularized versions in the noisy fully-determined MS cases levels off as opposed to the un-regularized version, where all cases are shown in Fig. 68. As λ increases from 0.1 to 10 in Fig. 68, the NMSE increases. This observation agrees intuitively with the dynamics, because the penalty on the fidelity component in the energy function decreases relative the prior component. Residual artifact levels after regularization are visibly higher for PS. Visually, the regularized HR estimates for $\lambda = 0.1$, had little effect to the rippling and overshoot artifact while solutions for $\lambda = 2$ and $\lambda = 10$ sacrificed edge definition, especially in the high contrast regions. $\lambda = 1$ is the recommended value based on this data. In Fig. 69(b) we can observe that MS yields a considerably lower NMSE (13%) than the PS approach (40%) when the slice selection

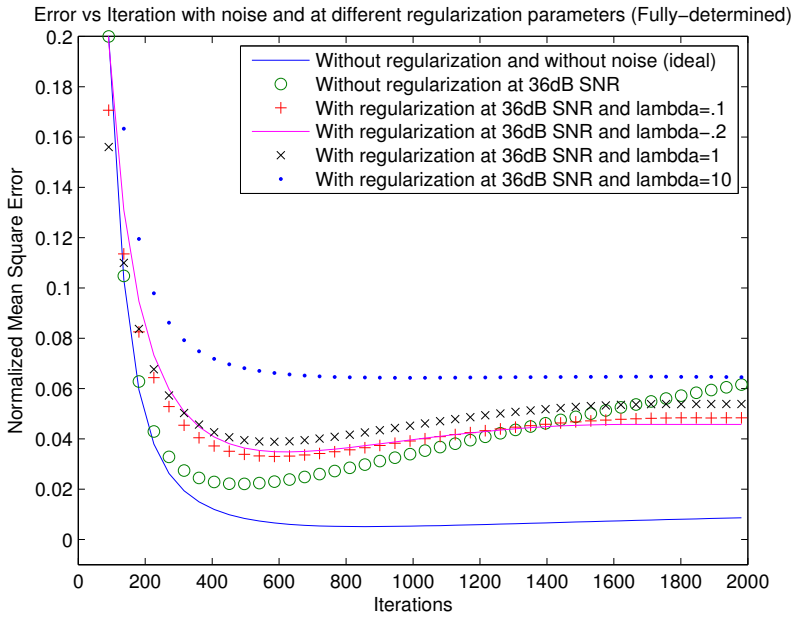

Figure 68: Error vs Iteration with noise and at different regularization parameters for Multi-Stack (Fully-determined: 8 LRIs, 8 pixel slice thickness, box PSF).

profile is inconsistent between the forward and inverse modeling.

The edges of grapefruit wedges and the capillaries within the wedges are resolved more clearly in the MS method than by the PS method, which shows residual resolution anisotropy. Image reconstruction results for the in-vivo brain experiment showed visual differences using the MS and PS techniques. Sulcal cerebral spinal fluid spaces and narrow gray matter tracts lateral to caudate nucleus are better visualized with MS than by PS reconstruction as shown with white arrows in Fig. 72(a).

6.7 Conclusion

We have presented a set of experiments on synthetic and real MRI data to compare two sampling strategies in SR for MRI. SVD reveals better conditioning for MS than PS for small test cases. Reconstruction from multiple slice stacks at different slice orientations (MS) outperformed reconstruction from multiple parallel overlapping slice stacks (PS) at sub-pixel location offsets. Quantitative error metrics were of the same order of magnitude without system error, but slightly better for MS. MS responds considerably better than PS if

system error or slice profile modeling error is present. Residual image artifacts were different for the two methods. Both methods show some overshoot ripple artifacts at sharp edges, but in MS these have much shorter wavelength and are moderated better by regularized reconstruction.

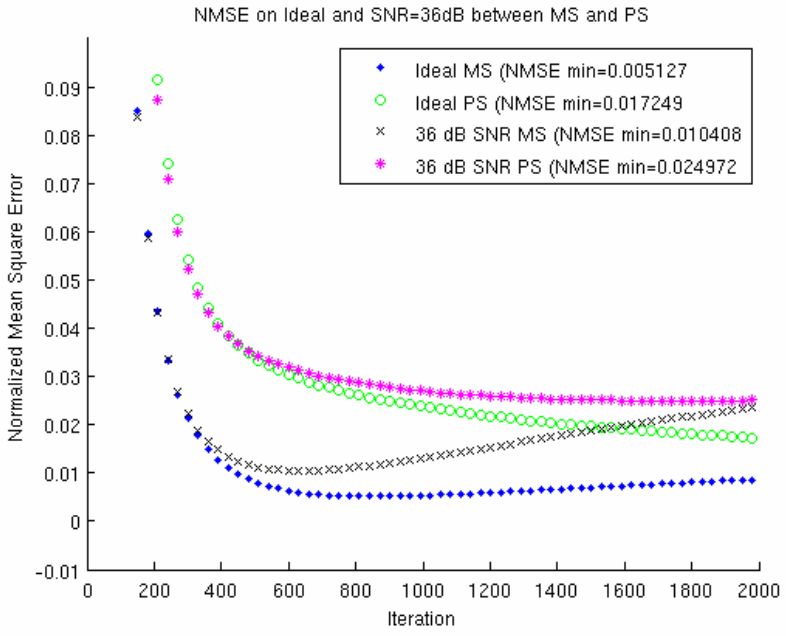

(a)

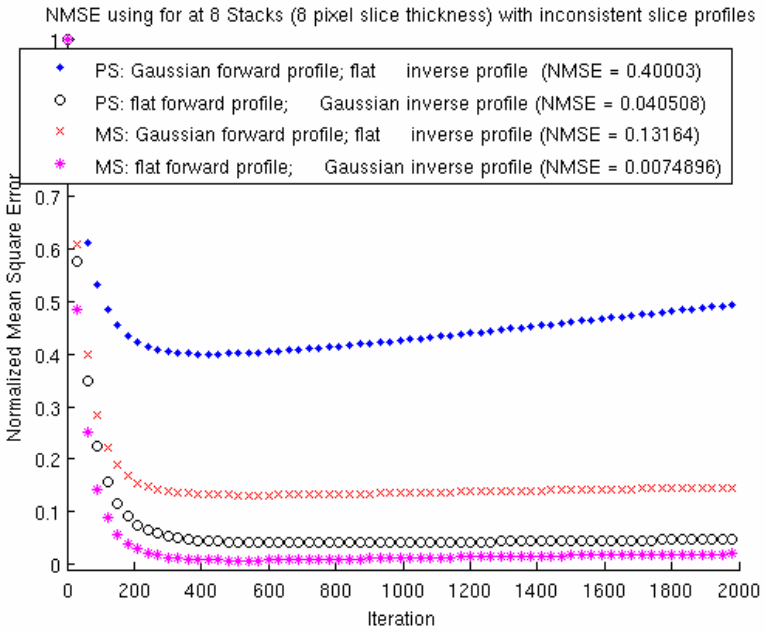

(b)

Figure 69: MS vs PS: NMSE in reconstructions from (a) noiseless and noisy data, (b) inconsistent slice profiles.

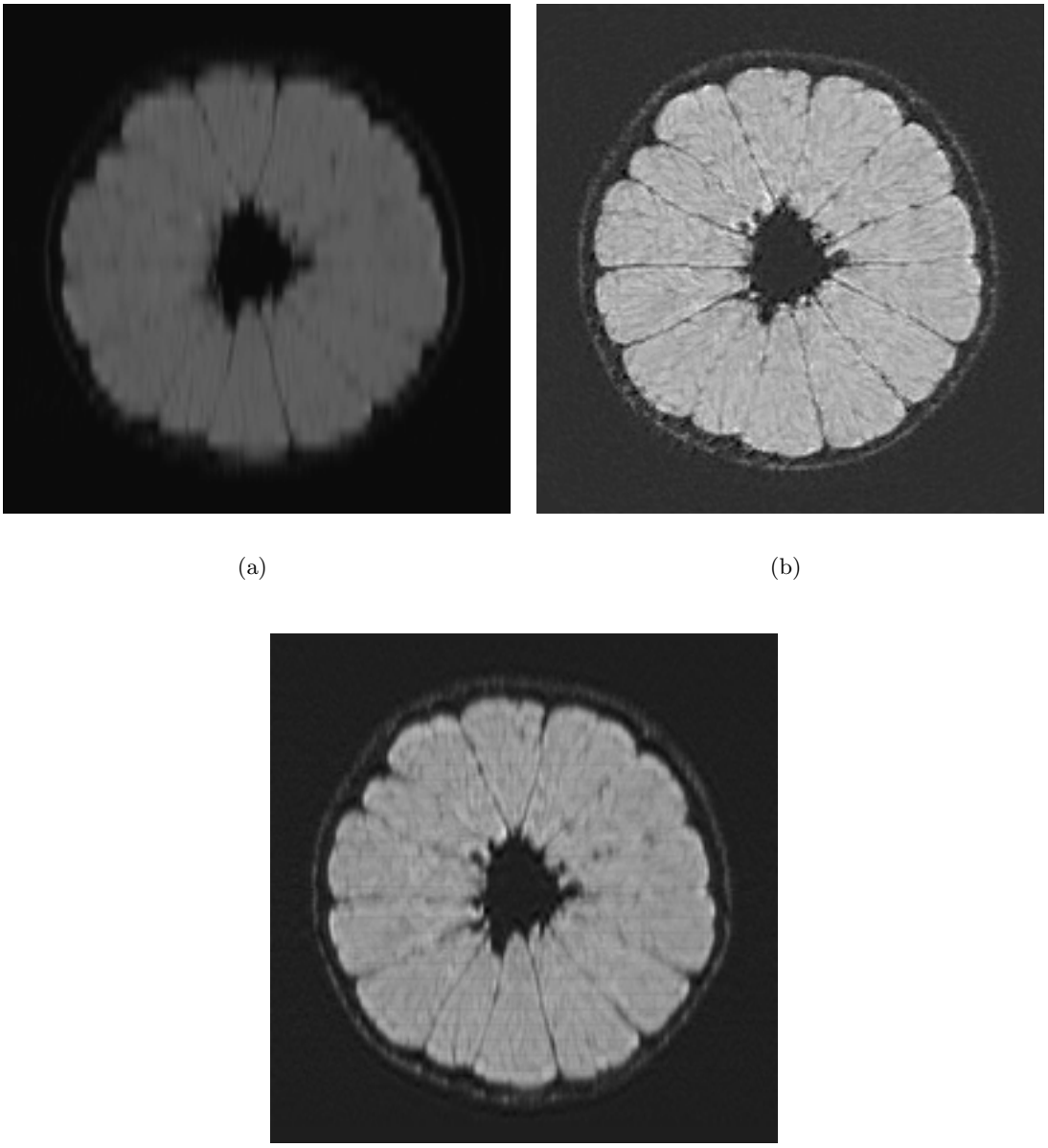

(a) (b)

(c)

Figure 70: MS vs PS: Reconstructions from grapefruit scans. (a) Reformat through a single LR slice stack, oriented at 30 degrees from vertical axis; (b) MS reconstruction from 6 stacks; (c) PS reconstruction from 6 slice stacks. The slice selection for PS is in the vertical direction.

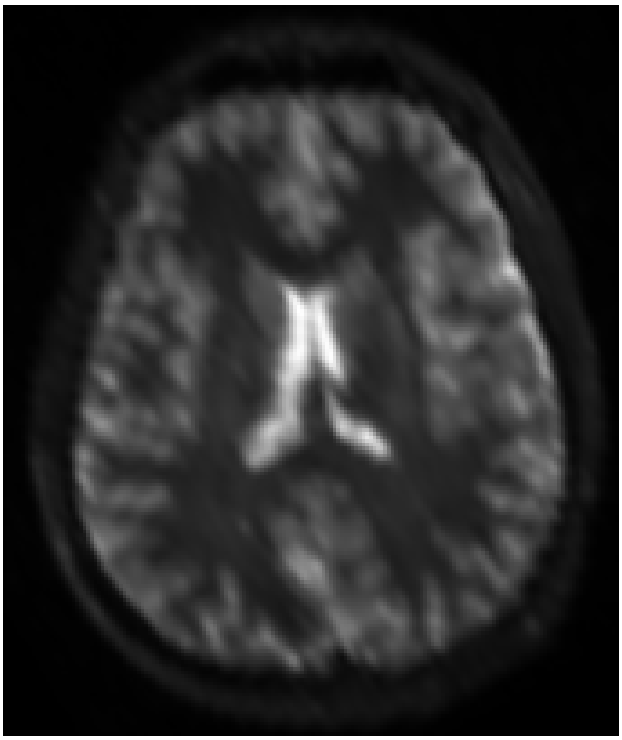

(a)

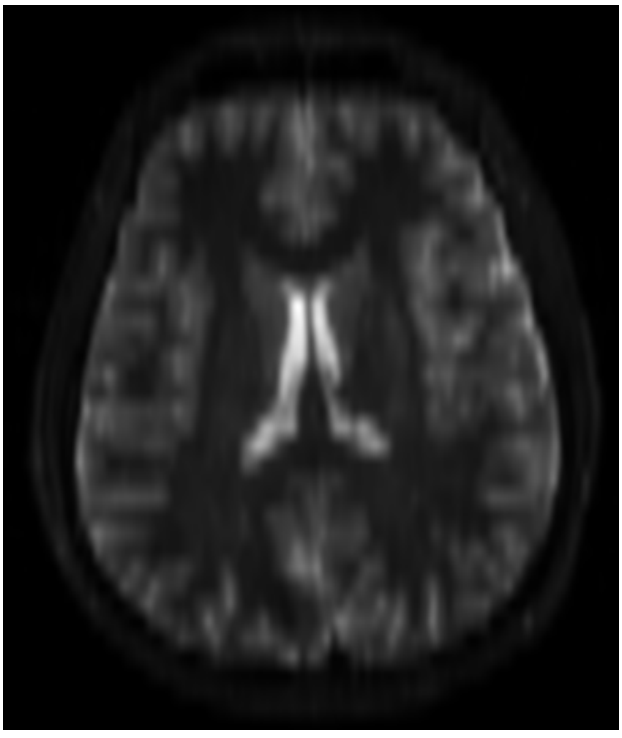

(b)

Figure 71: MS vs PS: MPR (bilinear interpolation) of two low-resolution coronal scans used for (a) MS oriented 30^o from vertical axis used and (b) PS. The slice selection for PS is in the vertical direction.

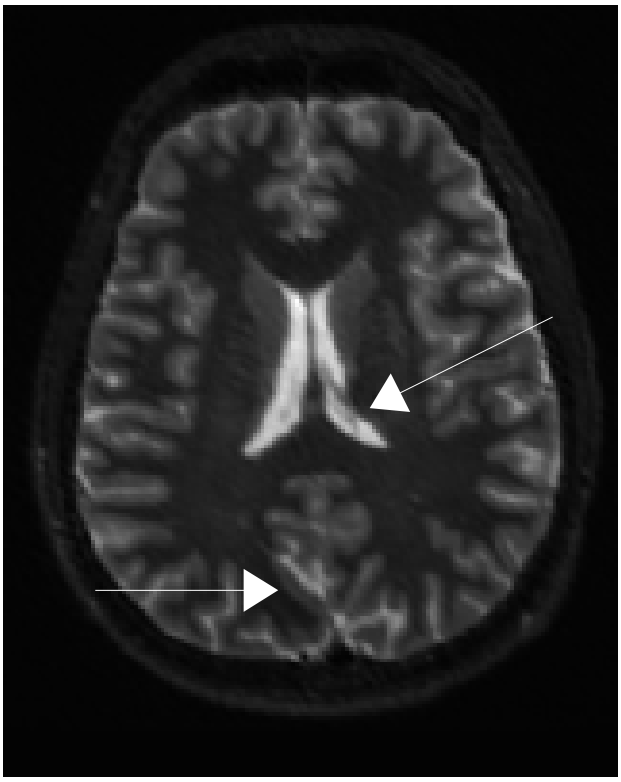

(a)

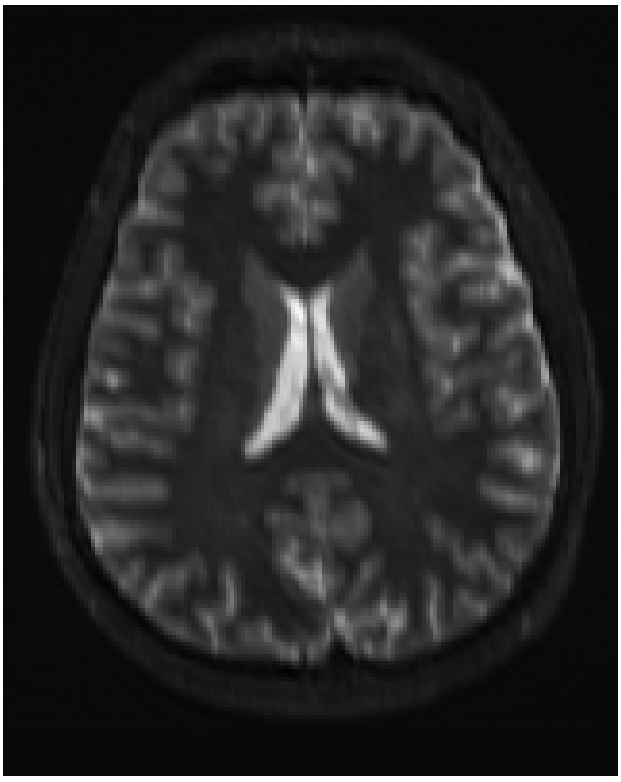

(b)

Figure 72: MS vs PS: In-vivo scans. (a) MS and (b) PS SRRs from 6 multi-slice stacks of a normal brain. White arrows highlight show some differences between two reconstructions.

CHAPTER VII

CONCLUSION

The central goal of this research was to achieve resolution enhancement of multi-slice MRI images using a super-resolution technique known as Multi-Stack. The following specific findings are given as follows [71, 70, 69, 72].

- Super-resolution reconstruction methods resulting in high fidelity were developed by adapting projection reconstruction methods in the computed tomography domain.
- Using synthetic data, the robustness of the projection reconstruction methods was demonstrated by their ability to produce a) stable results with improved resolution for under-determined problems, b) isotropic resolution for fully determined problems and, c) noise reduction for over-determined problems.
- The algebraic reconstruction techniques recovered low before high-frequency content with increasing iterations. As the number of unknowns increased (i.e., decreasing the pixel size estimate of the high resolution image), both the number of iterations and computation time per iteration needed to reconstruct the estimate of the high resolution image increased.
- The time needed for super-resolution reconstruction with present PC computation power is on the order of minutes and hours for separable 2-D and 3-D inversions, respectively. The time and accuracy needed to construct the observation model for super-resolution is directly controlled and thus mitigated through the use of a stepping parameter. The time to construct 2-D and 3-D contributions with realistic data sizes is on the order of minutes and hours, respectively.
- Six of the seven Multi-Stack data sets successfully combined the benefits of Multi-slice acquisition efficiency with the high resolution comparable with traditional 3-D

encoding. Improved edge widths measured in the super-resolution reconstruction from the low-resolution images support this finding. The seventh scan was corrupted by subject motion in between individual low-resolution stack acquisitions.

- The alternating minimization algorithm is an effective approach for rigid motion correction between low-resolution acquisitions needed for super-resolution. Results from synthetic data showed error levels in reconstructions comparable to the error levels from motion-free data. The alternating minimization algorithm applied to the Multi-slice data set with initially unknown motion converged to a solution that showed visual improvement compared to the reconstruction without motion correction. Correction of this motion within the super-resolution reconstruction achieved comparable resolution improvements with the Multi-Stack data sets without motion.

- Compared to the conventional sub-pixel parallel shift method, the Multi-Stack method delivered superior isotropic resolution, less overshoot at edges, faster convergence, and improved attenuation of ripple artifacts by use of regularization based on the Gibbs prior. Furthermore, Multi-Stack showed significantly lower error levels than Parallel-stack when system error was introduced.

APPENDIX A

THE MULTI-STACK FORMULA

A.1 Standard Representation

According to Eq. (60), the warp and sampling is applied to the PSF, $h(\mathbf{s})$ and not the image. The one-to-one mapping of the matrix warp permits a change of variables to this equation so that it can be expressed in the standard E&F form of warp, convolve, and sampling of the image, itself. Starting with Eq. (60)

$$y_r[\mathbf{n}] = \int_{\Omega} x(\mathbf{s}) h(\mathrm{R}_r(\mathbf{s} - \mathrm{V}\mathbf{n}))d\mathbf{s} + e_r[\mathbf{n}]. \tag{152}$$

Let $\mathbf{s}^{'} = \mathrm{R}_r(\mathbf{s} - \mathrm{V}\mathbf{n})$, then

$$\begin{aligned} \mathbf{s} &= \mathrm{R}_r^{-1}(\mathbf{s}^{'} + \mathrm{R}_r\mathrm{V}\mathbf{n}) && (153)\\ &= \mathrm{R}_r^{-1}\mathbf{s}^{'} + \mathrm{V}\mathbf{n}, && (154) \end{aligned}$$

and

$$\begin{aligned} \frac{d\mathbf{s}}{d\mathbf{s}^{'}} &= (\mathrm{R}_r^{-1})^T && (155)\\ d\mathbf{s} &= |(\mathrm{R}_r^{-1})^T| d\mathbf{s}^{'}. && (156) \end{aligned}$$

The transpose of an ortho-normal matrix is its inverse, i.e., $(\mathrm{R}_r^{-1})^T = \mathrm{R}_r$, which simplifies its Jacobian. Hence,

$$d\mathbf{s} = d\mathbf{s}^{'}, \tag{157}$$

The support of the image, Ω, remains the same in the area of integration so that

$$y_r[\mathbf{n}] = \int_{\Omega} x(\mathrm{R}_r^{-1}\mathbf{s}^{'} + \mathrm{V}\mathbf{n}) h(\mathbf{s}^{'}) d\mathbf{s}^{'} + e_r[\mathbf{n}]. \tag{158}$$

The variable $\mathbf{s}^{'}$ can be simplified to

$$y_r[\mathbf{n}] = \int_{\Omega} x(\mathrm{R}_r^{-1}\mathbf{s} + \mathrm{V}\mathbf{n}) h(\mathbf{s}) d\mathbf{s} + e_r[\mathbf{n}]. \tag{159}$$

Thus, the LRI can be expressed by the a warp, convolution, and downsampling operation from the E&F model as

$$y_r[\mathbf{n}] = ((x \circ \mathrm{R}_r^{-1}) * h)(-\mathrm{V}\mathbf{n}). \tag{160}$$

A.2 Standard Representation with rigid motion

Accounting for rigid motion, the MS model is

$$y_r[\mathbf{n}] = \int_\Omega x(\mathrm{A}_r\mathbf{s} + \mathbf{b}_r)h(\mathrm{R}_r(\mathbf{s} - \mathrm{V}\mathbf{n}))d\mathbf{s} + e_r[\mathbf{n}], \tag{161}$$

where $\{\mathrm{A}_r, \mathbf{b}_r\}_{r=1}^P$ are the motion parameters. Letting,

$$\mathbf{s}^{'} = \mathrm{A}_r\mathbf{s} + \mathbf{b}_r, \tag{162}$$

$$\mathbf{s} = \mathrm{A}_r^{-1}(\mathbf{s}^{'} - \mathbf{b}_r), \tag{163}$$

the derivative is

$$\begin{aligned} \frac{d\mathbf{s}}{d\mathbf{s}^{'}} &= (\mathrm{A}_r^{-1})^T & (164)\\ d\mathbf{s} &= |(\mathrm{A}_r^{-1})^T| d\mathbf{s}^{'} & (165)\\ &= d\mathbf{s}^{'}. & (166) \end{aligned}$$

Substituting Eq. (219) into the PSF argument from Eq. (218) gives

$$\mathrm{R}_r(\mathbf{s} - \mathrm{V}\mathbf{n}) = \mathrm{R}_r(\mathrm{A}_r^{-1}\mathbf{s}^{'} - (\mathrm{A}_r^{-1}\mathbf{b}_r + \mathrm{V}\mathbf{n})). \tag{167}$$

Hence,

$$y_r[\mathbf{n}] = \int_\Omega x(\mathbf{s}^{'})h(\mathrm{R}_r(\mathrm{A}_r^{-1}\mathbf{s}^{'} - (\mathrm{A}_r^{-1}\mathbf{b}_r + \mathrm{V}\mathbf{n})))d\mathbf{s}^{'} + e_r[\mathbf{n}], \tag{168}$$

and the new contribution of the ij^{th} in entry H becomes

$$[\mathrm{H}]_{ij} = \int_{S_j} h(\mathrm{R}_r(\mathrm{A}_r^{-1}\mathbf{s} - (\mathrm{A}_r^{-1}\mathbf{b}_r + \mathrm{V}\mathbf{n})))d\mathbf{s}. \tag{169}$$

The warp, convolution, and down-sampling applied directly to $x(\mathbf{s})$ gives

$$y_r[\mathbf{n}] = \int_\Omega x(\mathrm{A}_r(\mathrm{R}_r^{-1}\mathbf{s} + \mathrm{V}\mathbf{n}) + \mathbf{b}_r)h(\mathbf{s})d\mathbf{s}. \tag{170}$$

APPENDIX B

DERIVATION OF MULTI-STACK ERROR

This section derives the PDFs of the output error given by Multi-Stack. It is known that the MS error for the r^{th} LRS is

$$e_r[\mathbf{n}] = \int_{\Omega} e(\mathbf{s})h(\mathrm{R}_r(\mathbf{s} - \mathrm{V}\mathbf{n}))d\mathbf{s}, \tag{171}$$

where

$$\Re(e(\mathbf{s})) \sim \mathsf{N}(0, \sigma_e^2), \tag{172}$$

$$\Im(e(\mathbf{s})) \sim \mathsf{N}(0, \sigma_e^2), \tag{173}$$

$$\mathsf{Cov}(\Re(e(\mathbf{s}))\Re(e(\mathbf{t}))) = \delta(\mathbf{s} - \mathbf{t})\sigma_e^2, \tag{174}$$

$$\mathsf{Cov}(\Im(e(\mathbf{s}))\Im(e(\mathbf{t}))) = \delta(\mathbf{s} - \mathbf{t})\sigma_e^2. \tag{175}$$

The real and imaginary components of Eq. (171) are each sums of IID Gaussian RVs, which according to the Central Limit Theorem must also be a Gaussian RV [65]:

$$\mathsf{E}[\Re(e_r[\mathbf{n}])] = \int_{\Omega} \mathsf{E}[\Re(e(\mathbf{s}))]h(\mathrm{R}_r(\mathbf{s} - \mathrm{V}\mathbf{n}))d\mathbf{s} \tag{176}$$

$$= 0. \tag{177}$$

The covariance between two different samples, $\mathbf{n}$ and $\mathbf{m}$, becomes

$$
\begin{aligned}
\mathsf{Cov}(\Re(e_r[\mathbf{n}])\Re(e_r[\mathbf{m}])) &= \mathsf{E}[\Re(e_r[\mathbf{n}])\Re(e_r[\mathbf{m}])] - \mathsf{E}[\Re(e_r[\mathbf{n}])]\mathsf{E}[\Re(e_r[\mathbf{m}])] && (178)\\
&= \mathsf{E}[\Re(e_r[\mathbf{n}])\Re(e_r[\mathbf{m}])] && (179)\\
&= \mathsf{E}[\int_\Omega \Re(e(\mathbf{s}))h(\mathrm{R}_r(\mathbf{s}-\mathrm{V}\mathbf{m}))d\mathbf{s}\int_\Omega \Re(e(\mathbf{t}))h(\mathrm{R}_r(\mathbf{t}-\mathrm{V}\mathbf{n}))d\mathbf{t}] && (180)\\
&= \mathsf{E}[\int_\Omega\int_\Omega \Re(e(\mathbf{s}))h(\mathrm{R}_r(\mathbf{s}-\mathrm{V}\mathbf{n}))\Re(e(\mathbf{t}))h(\mathrm{R}_r(\mathbf{t}-\mathrm{V}\mathbf{m}))d\mathbf{t}d\mathbf{s}] && (181)\\
&= \int_\Omega\int_\Omega \mathsf{E}[\Re(e(\mathbf{s}))\Re(e(\mathbf{t}))]h(\mathrm{R}_r(\mathbf{s}-\mathrm{V}\mathbf{n}))h(\mathrm{R}_r(\mathbf{t}-\mathrm{V}\mathbf{m}))d\mathbf{t}d\mathbf{s} && (182)\\
&= \int_\Omega\int_\Omega \sigma_e^2\delta(\mathbf{s}-\mathbf{t})h(\mathrm{R}_r(\mathbf{s}-\mathrm{V}\mathbf{n}))h(\mathrm{R}_r(\mathbf{t}-\mathrm{V}\mathbf{m}))d\mathbf{t}d\mathbf{s} && (183)\\
&= \sigma_e^2\int_\Omega\left(\int_\Omega \delta(\mathbf{s}-\mathbf{t})h(\mathrm{R}_r(\mathbf{s}-\mathrm{V}\mathbf{n}))d\mathbf{s}\right)h(\mathrm{R}_r(\mathbf{t}-\mathrm{V}\mathbf{m}))d\mathbf{t} && (184)\\
&= \sigma_e^2\int_\Omega h(\mathrm{R}_r(\mathbf{t}-\mathrm{V}\mathbf{n}))h(\mathrm{R}_r(\mathbf{t}-\mathrm{V}\mathbf{m}))d\mathbf{t} && (185)\\
&= \sigma_e^2\hat{h}_r(\mathbf{n},\mathbf{m}) && (186)
\end{aligned}
$$

where

$$\hat{h}_r(\mathbf{n},\mathbf{m}) = \int_\Omega h(\mathrm{R}_r(\mathbf{s}-\mathrm{V}\mathbf{n}))h(\mathrm{R}_r(\mathbf{s}-\mathrm{V}\mathbf{m}))d\mathbf{s}. \quad (187)$$

The variance is

$$
\begin{aligned}
\mathsf{Var}(\Re(e_r[\mathbf{n}])) &= \mathsf{Cov}(\Re(e_r[\mathbf{n}])\Re(e_r[\mathbf{n}])) && (188)\\
&= \sigma_e^2\hat{h}_r(\mathbf{n},\mathbf{n}). && (189)
\end{aligned}
$$

The autocorrelation between two samples, $\mathbf{n}$ and $\mathbf{m}$, becomes

$$
\begin{aligned}
\mathsf{R}_{\Re(e_r[\mathbf{n}])\Re(e_r[\mathbf{n}])}(\mathbf{n},\mathbf{m}) &= \mathsf{E}[\Re(e_r[\mathbf{n}])\Re(e_r[\mathbf{m}])] && (190)\\
&= \mathsf{Cov}(\Re(e_r[\mathbf{n}])\Re(e_r[\mathbf{m}])) && (191)\\
&= \sigma_e^2\hat{h}_r(\mathbf{n},\mathbf{m}). && (192)
\end{aligned}
$$

The same derivations apply for $\Im(e_r[\mathbf{n}])$.

APPENDIX C

CONSTRUCTION OF MULTI-STACK MATRIX

Algorithm 3 Constructing H

Require:

All P LRIs have size $M_1 \times M_2 \times M_3$ with PSF $h(\mathbf{s}) : \mathbb{R}^3 \to \mathbb{R}$

$\{R_r\}_{r=1}^{P}$ are the rotation warps with sampling matrix V

δ is the step length

$T_{\mathbf{x}}(\mathbf{s}) : \mathbb{R}^3 \to \mathbb{R}^3$ transforms from physical to image coordinates of the HR image

The discrete HR image, $\mathbf{x}$, has size $N_1 \times N_2$ with support region Ω

Ensure:

$\hat{\mathrm{H}}$ is the constructed observation model

$M \leftarrow PM_1M_2M_3$

$N \leftarrow N_1N_2$

$\hat{\mathrm{H}} \leftarrow \mathbf{0} \in \mathbf{R}^{M \times N}$

$\Lambda = (\Lambda_1, \Lambda_2, \Lambda_3) \leftarrow \mathsf{supp}(h)$

for $r \leftarrow 1 : P$ **do**

  for $m_1 \leftarrow 1 : M_1$ **do**

    for $m_2 \leftarrow 1 : M_2$ **do**

      for $m_3 \leftarrow 1 : M_3$ **do**

        $i \leftarrow m_1 + (m_2 - 1)M_1 + (m_3 - 1)M_1M_2 + (r - 1)M_1M_2M_3$

        $\mathbf{m} \leftarrow [m_1, m_2, m_3]^T$

        for $s_1 \leftarrow \min(\Lambda_1) : \delta : \max(\Lambda_1)$ **do**

          for $s_2 \leftarrow \min(\Lambda_2) : \delta : \max(\Lambda_2)$ **do**

            for $s_3 \leftarrow \min(\Lambda_3) : \delta : \max(\Lambda_3)$ **do**

              $\mathbf{s} \leftarrow [s_1, s_2, s_3]^T$

              $\mathbf{s}' \leftarrow \mathrm{R}_r(\mathbf{s} + V\mathbf{m})$

              if $\mathbf{s}' \notin \Omega$ **then**

                break

              end if

              $\mathbf{t} \leftarrow T_{\mathbf{x}}(\mathbf{s}')$

              $\mathbf{t}' \leftarrow (\lfloor \mathbf{t}_1 \rfloor, \lfloor \mathbf{t}_2 \rfloor, \lfloor \mathbf{t}_3 \rfloor)$

              $j \leftarrow t_1' + (t_2' - 1)N_1 + (t_3' - 1)N_1N_2$

              $[\hat{\mathrm{H}}]_{ij} \leftarrow [\hat{\mathrm{H}}]_{ij} + \delta^3 h(\mathbf{s})$

            end for

          end for

        end for

      end for

    end for

  end for

end for

return $\hat{\mathrm{H}}$

APPENDIX D

MEASURING THE SLICE SELECTION PROFILE

To measure the slice excitation profile, a physical phantom is scanned using the same acquisition parameters as the LRSs. The phantom has an acrylic housing containing thin ramps made from a paramagnetic homogeneous material that slant downward, as shown in a coronal view from one of the LRSs in Fig. 73(a). The material is water doped with $CuSO_4$, causing a short T_1 relaxation time. During scanning, slice excitation intercepts the material at different spatial locations producing the transverse imagery, as shown in Fig. 73(c). The intensity portion along the ramp is common to this slice plane. Since the ramp is homogeneous, any change in image intensity indicates a change in the slice selection profile. The ramp geometry, shown in Fig. 73(b), produces imagery of the slice selection profile that is stretched and is computed with the angle of the ramp:

$$x = z\tan(a). \tag{193}$$

From one of the ramps, rows of pixels in either the phase- or frequency-encoding direction and denoted by the overlayed sigma symbol in Fig. 73(c) are averaged to reduce the measured noise in the profile function. Fig. 73(d) shows the measured profile. The information is corrected by Eq. (193) that is then included as the slice selection profile in the multi-slice LRSs.

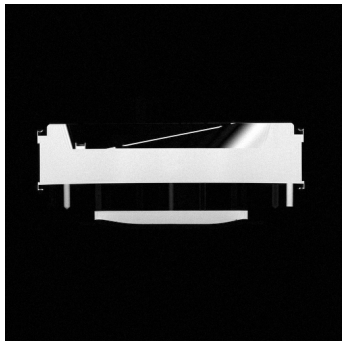

(a)

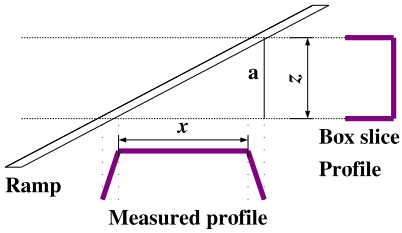

(b)

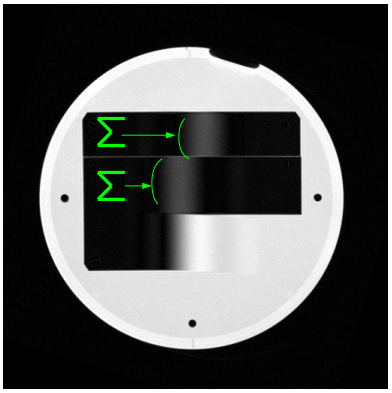

(c)

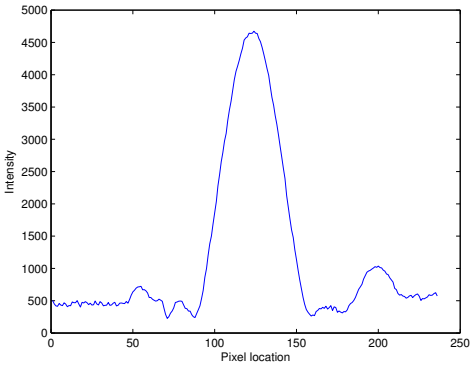

(d)

Figure 73: Experiment to measure slice selection profile: (a) Coronal view of phantom used for measurement containing ramp (b) Schematic side view of the homogenous ramp; z is the direction of the slice selection which is measured in the dimension of x; a is the incident angle of the ramp. (c) Axial view showing an intensity along the ramps common to the slice plane with denoted summation in green against the slice selection direction (d) the added 1-D strips of the slice selection function to reduce noise.

APPENDIX E

VALIDATION RESULTS FOR MULTI-STACK CONTINUED

The remaining five in-vivo studies (2 - 6) for validation are shown here. Each study has a MPR of one LRS and a SRR with a consistent edge measurement, MPRs of a sagittal and coronal LRS and the SRR. Table 21 gives a listing of the figures and tables as a navigational aid.

Table 21: Figure and table listing for the remaining In-vivo studies.

Study No.	Appendix	LR Parameters Table	Axial views of LR, SRR & edge fits	MPRs Figures of LRSs & SRR
2	E.0.1	22	74	75
3	E.0.2	23	-	76
4	E.0.3	24	77	78
5	E.0.4	25	79	80
6	E.0.5	26	81	82

E.0.1 In-vivo Study No. 2

Table 22: In-vivo Study no. 2: LRS parameters.

P	6
$M_1 \times M_2 \times M_3$	$48 \times 512 \times 512$
LRS FOV	220×220
LR slice thickness	$5mm$
LR slice distance	$5mm$
SRR voxel Size	$5.0 \times 0.4296 \times 0.4296\ mm^3$
Pulse Sequence	Fast-Spin Echo-Inversion Recovery (FSE-IR)
$T_E/T_I/T_R$	85/190/4830 ms
Excitation angle	90^o

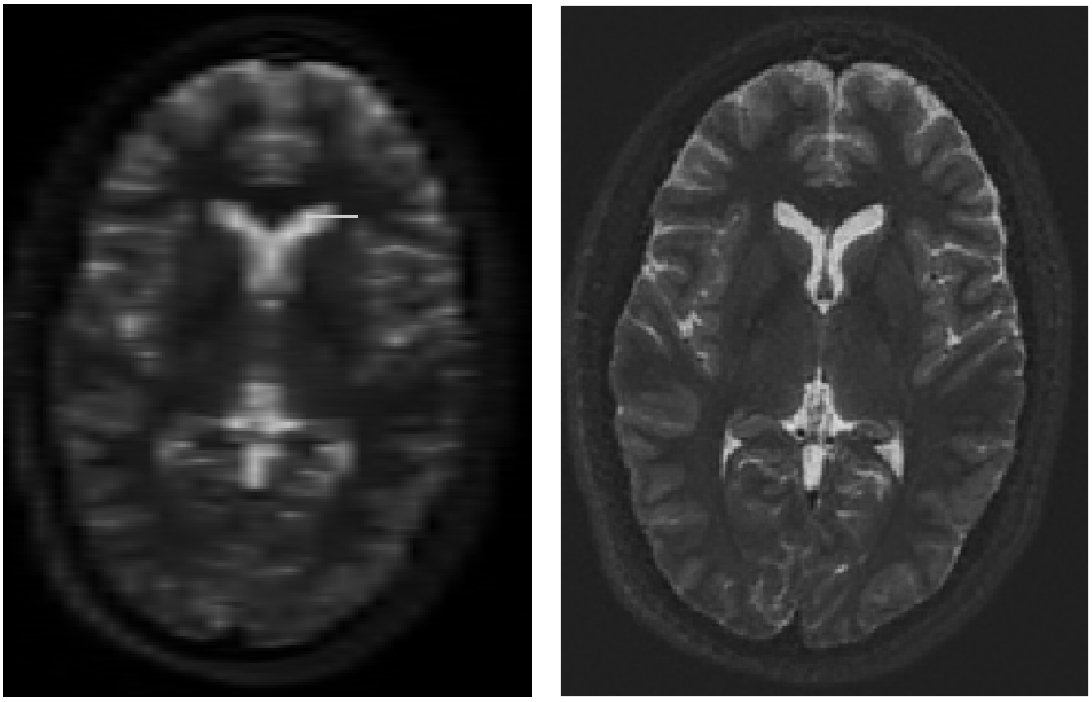

(a) (b)

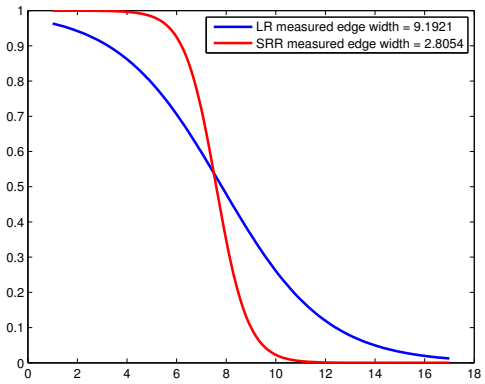

(c)

Figure 74: In-vivo Study no. 2: (a) MPR of a sagittal LRS; (b) SRR with denoted edge measurement; (c) Measured edge curve with LR and SRR images.

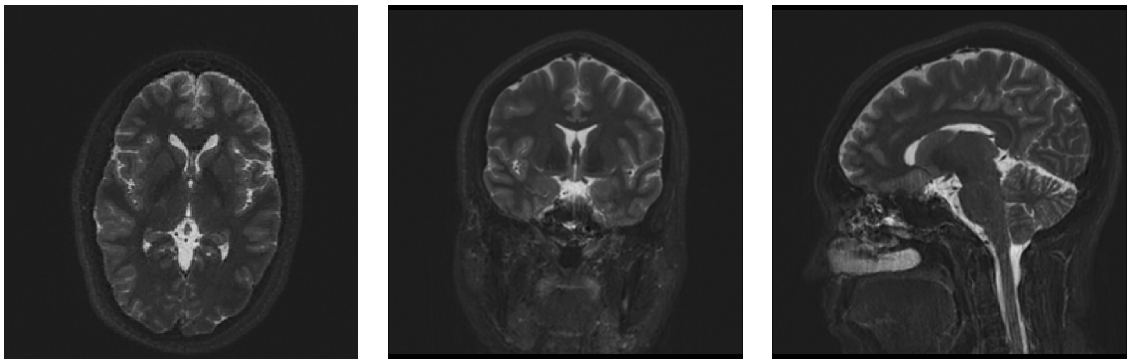

(a) (b) (c)

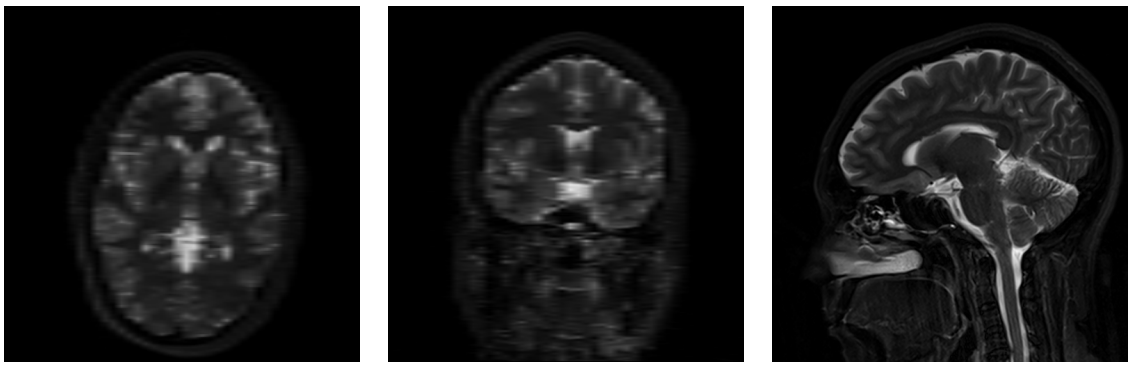

(d) (e) (f)

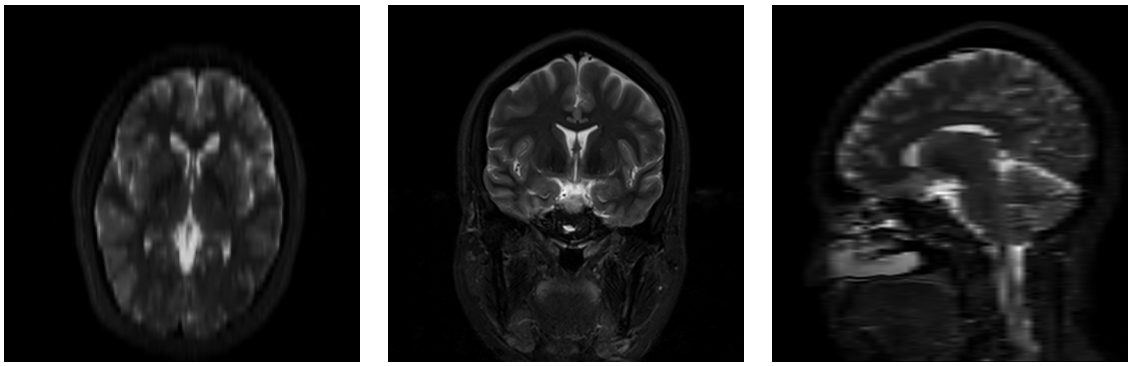

(g) (h) (i)

(a) Axial SRR view	(b) Coronal SRR view	(c) Sagittal SRR view
(d) Axial MPR of sagittal LR stack	(e) Coronal MPR of sagittal LR stack	(f) Sagittal original LR slice
(g) Axial MPR of coronal LR stack	(h) Coronal original LR slice	(i) Sagittal MPR of Coronal LR stack

Figure 75: In-vivo Study no. 2: (a-c) Axial, coronal, and sagittal views of the SRR using ART (voxel = 0.8594 mm × 0.8594 mm × 0.8594 mm) (d-f) Axial, coronal, and sagittal views of a sagittal scan (voxel = 5 mm × 0.8594 mm × 0.8594 mm) (g-i) Axial, coronal, and sagittal views of a coronal scan (voxel = 0.8594 mm × 5 mm × 0.8594 mm).

E.0.2 In-vivo Study No. 3

Table 23: In-vivo Study no. 3: LRS parameters.

P	6
$M_1 \times M_2 \times M_3$	$63 \times 256 \times 256$
LRS FOV	256×256
LR slice thickness	$4mm$
LR slice distance	$4mm$
SRR voxel Size	$1 \times 1 \times 1\ mm^3$
Pulse Sequence	3DFZ
$T_E/T_I/T_R$	3.68/ (N/A) /7.49 ms
Excitation angle	20^o

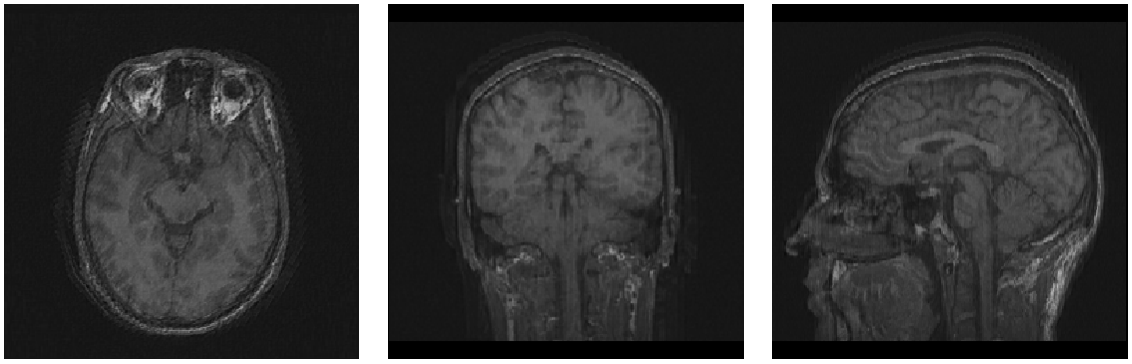

(a) (b) (c)

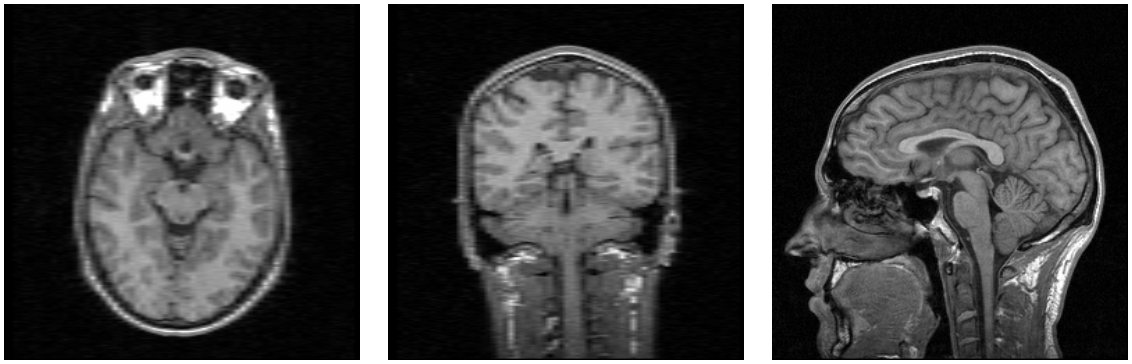

(d) (e) (f)

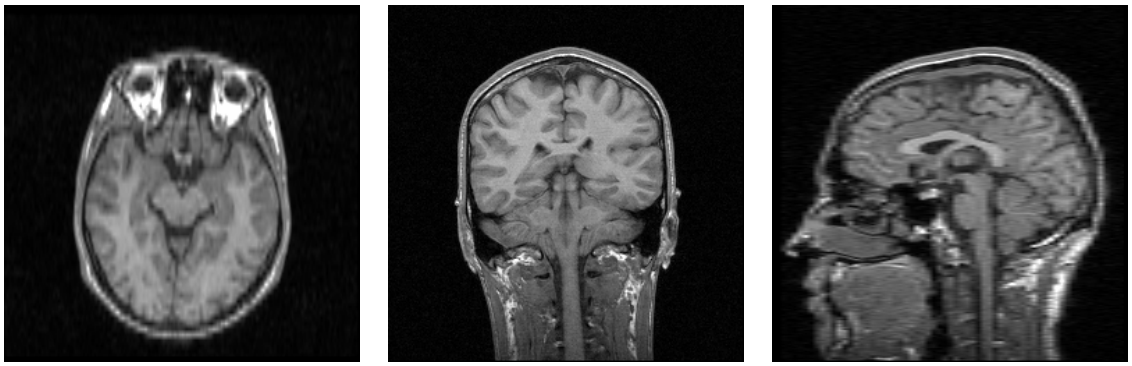

(g) (h) (i)

(a) Axial SRR view	(b) Coronal SRR view	(c) Sagittal SRR view
(d) Axial MPR of sagittal LR stack	(e) Coronal MPR of sagittal LR stack	(f) Sagittal original LR slice
(g) Axial MPR of coronal LR stack	(h) Coronal original LR slice	(i) Sagittal MPR of oronal LR stack

Figure 76: In-vivo Study no. 3: (a-c) Axial, coronal, and sagittal views of the SRR using ART (voxel = $1\ mm \times 1\ mm \times 1\ mm$) (d-f) Axial, coronal, and sagittal views of a sagittal scan (voxel = $4\ mm \times 1\ mm \times 1\ mm$) (g-i) Axial, coronal, and sagittal views of a coronal scan (voxel = $1\ mm \times 4\ mm \times 1\ mm$).

E.0.3 In-vivo Study No. 4

Table 24: In-vivo Study no. 4: LRS parameters.

P	
$M_1 \times M_2 \times M_3$	$44 \times 256 \times 256$
LRS FOV	$240 \times 240\ mm^2$
LR slice thickness	$5mm$
LR slice distance	$5mm$
SRR voxel Size	$5 \times 1.07 \times 1.07\ mm^3$
Pulse Sequence	FSE-IR
$T_E/T_I/T_R$	140/90/3606 ms
Excitation angle	90^o

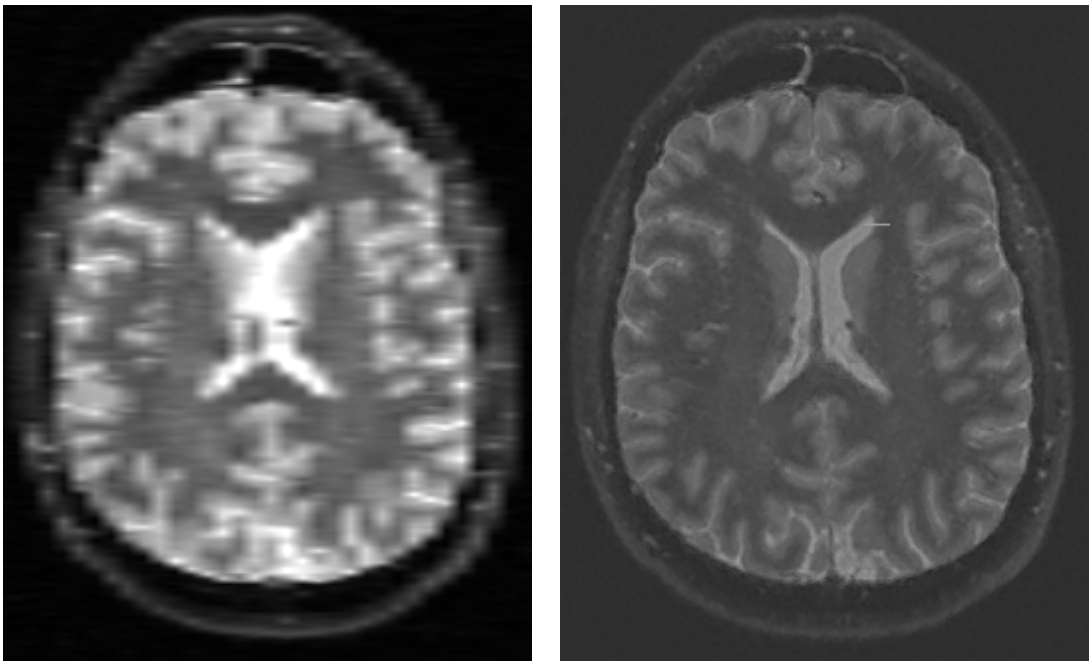

(a) (b)

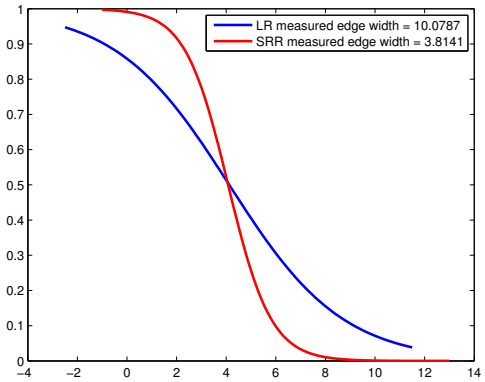

(c)

Figure 77: In-vivo Study no. 4: (a) MPR of a sagittal LRS; (b) SRR with denoted edge measurement; (c) Measured edge curve with LR and SRR images.

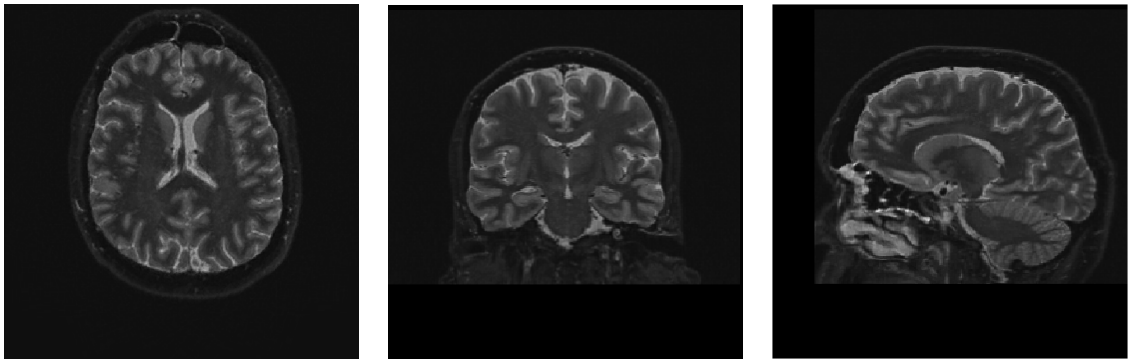

(a) (b) (c)

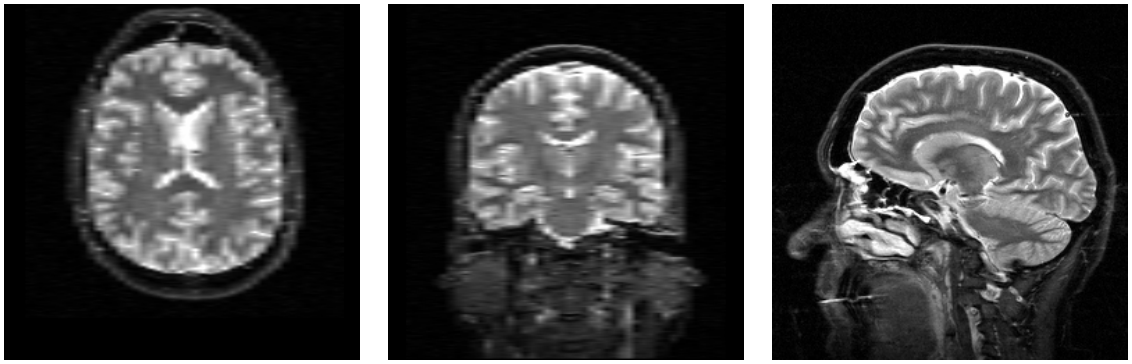

(d) (e) (f)

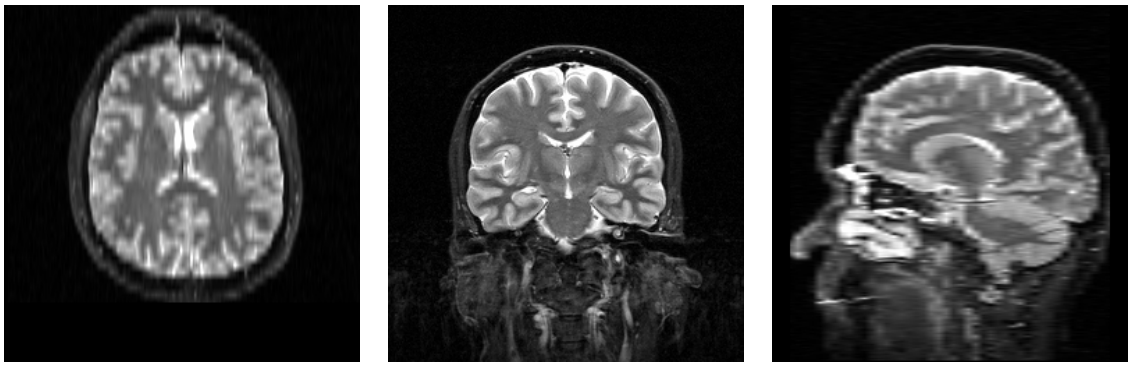

(g) (h) (i)

(a) Axial SRR view	(b) Coronal SRR view	(c) Sagittal SRR view
(d) Axial MPR of sagittal LR stack	(e) Coronal MPR of Sagittal LR stack	(f) Sagittal original LR slice
(g) Axial MPR of coronal LR stack	(h) Coronal original LR slice	(i) Sagittal MPR of coronal LR stack

Figure 78: In-vivo Study no. 4: (a-c) Axial, coronal, and sagittal views of the SRR using ART (voxel = 0.94 mm × 0.94 mm × 0.94 mm) (d-f) Axial, coronal, and sagittal views of a sagittal scan (voxel = 5 mm × 0.94 mm × 0.94 mm) (g-i) Axial, coronal, and sagittal views of a coronal scan (voxel = 0.94 mm × 5 mm × 0.94 mm).

E.0.4 In-vivo Study No. 5

Table 25: In-vivo Study no. 5: LRS parameters.

P	
$M_1 \times M_2 \times M_3$	$44 \times 256 \times 256$
LRS FOV	$240 \times 240\ mm^2$
LR slice thickness	$5\ mm$
LR slice distance	$5\ mm$
SRR voxel Size	$0.5 \times 0.5 \times 0.5\ mm^3$
Pulse Sequence	FSE-IR
$T_E/T_I/T_R$	14/170/3606 ms
Excitation angle	90^o

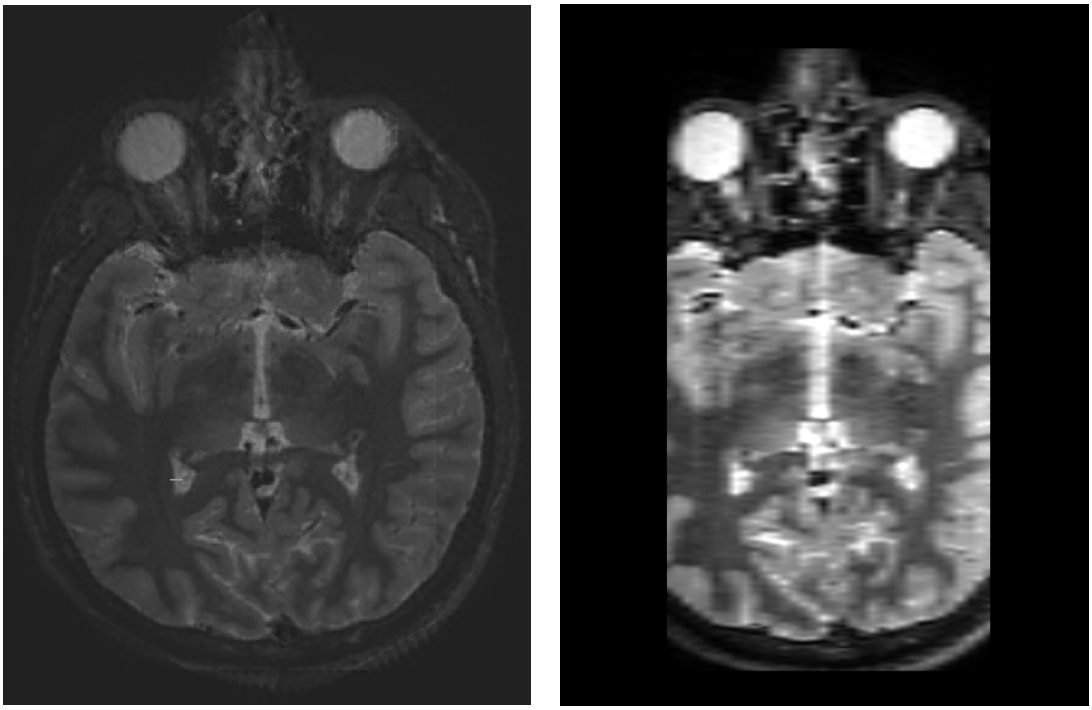

(a) (b)

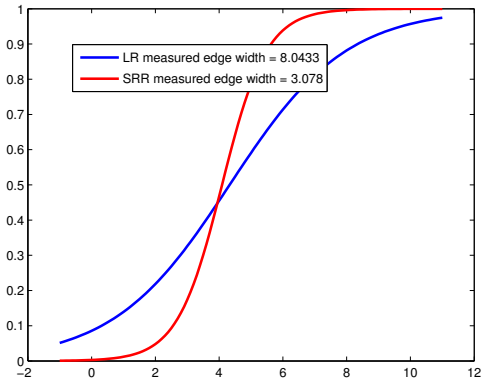

(c)

Figure 79: In-vivo Study no. 5: (a) MPR of a sagittal LRS; (b) SRR with denoted edge measurement; (c) Measured edge curve with LR and SRR images.

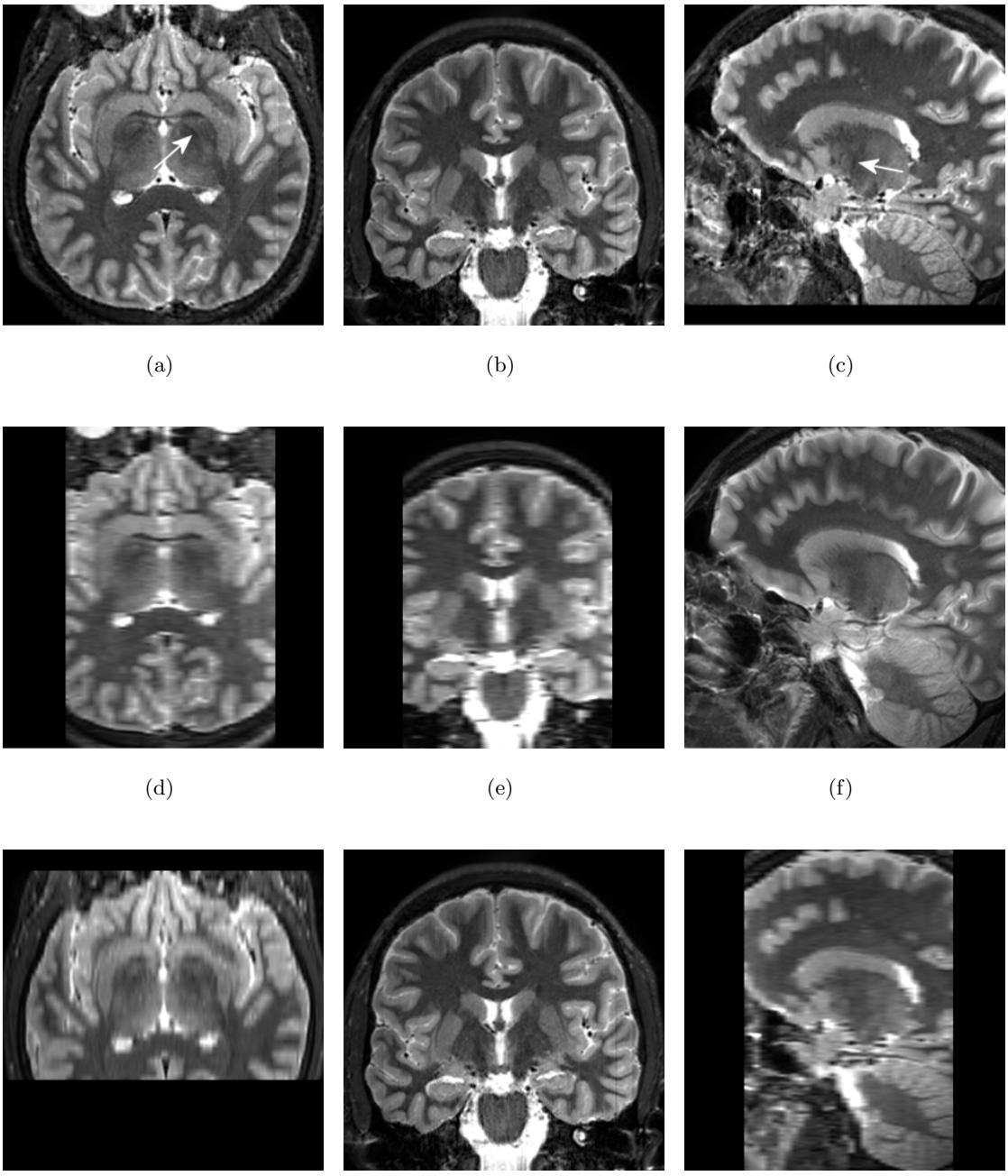

(a) (b) (c)

(d) (e) (f)

(g) (h) (i)

(a) Axial SRR view	(b) Coronal SRR view	(c) Sagittal SRR view
(d) Axial MPR of sagittal LR stack	(e) Coronal MPR of sagittal LR stack	(f) Sagittal original LR slice
(g) Axial MPR of coronal LR stack	(h) Coronal original LR slice	(i) Sagittal MPR of coronal LR stack

Figure 80: In-vivo Study no. 5: (a-c) Axial, coronal, and sagittal views of the SRR using the ART (voxel size = 0.5 mm × 0.5 mm × 0.5 mm) (d-f) Axial, coronal, and sagittal views of one sagittal multi-slice stack (voxel size = 3 mm × 0.46875 mm × 0.46875 mm) (g-i) Axial, coronal, and sagittal views of one coronal multi-slice stack (voxel size = 0.46875 mm × 3 mm × 0.46875 mm).

E.0.5 In-vivo Study No. 6

Table 26: In-vivo Study no. 6: LRS parameters.

P	
$M_1 \times M_2 \times M_3$	$48 \times 512 \times 512$
LRS FOV	$220 \times 220\ mm^2$
LR slice thickness	$4.8mm$
LR slice distance	$4.8mm$
SRR voxel Size	$0.5 \times 0.47 \times 0.47\ mm^3$
Pulse Sequence	FSE-IR
$T_E/T_I/T_R$	85/190/4830 ms
Excitation angle	90^o

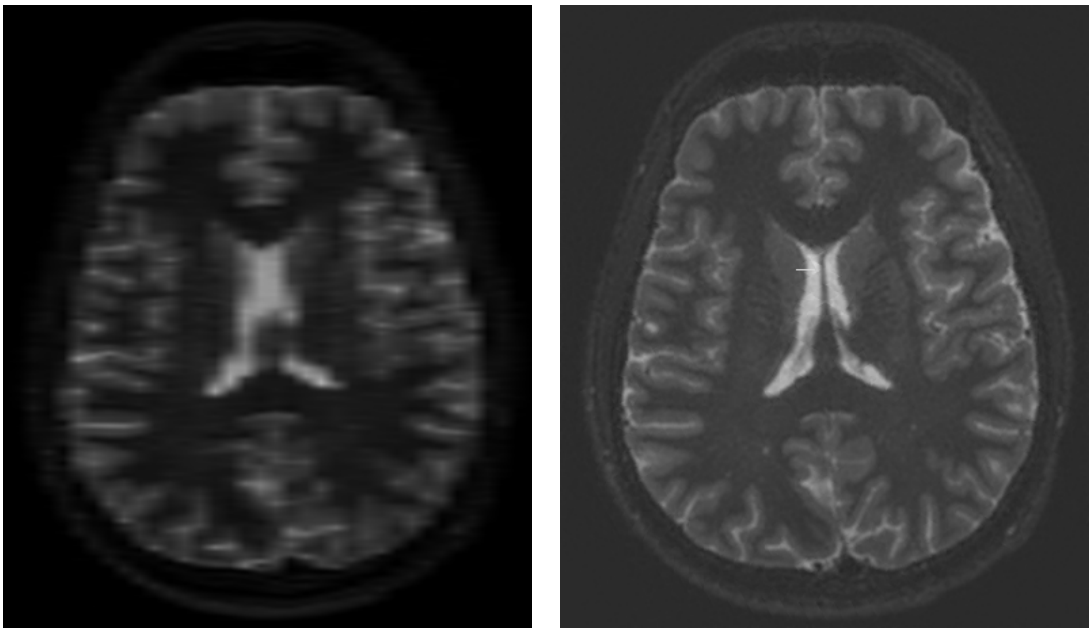

(a) (b)

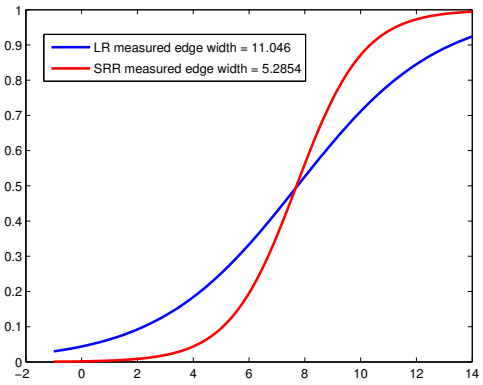

(c)

Figure 81: In-vivo Study no. 6: (a) MPR of a sagittal LRS; (b) SRR with denoted edge measurement; (c) Measured edge curve with LR and SRR images.

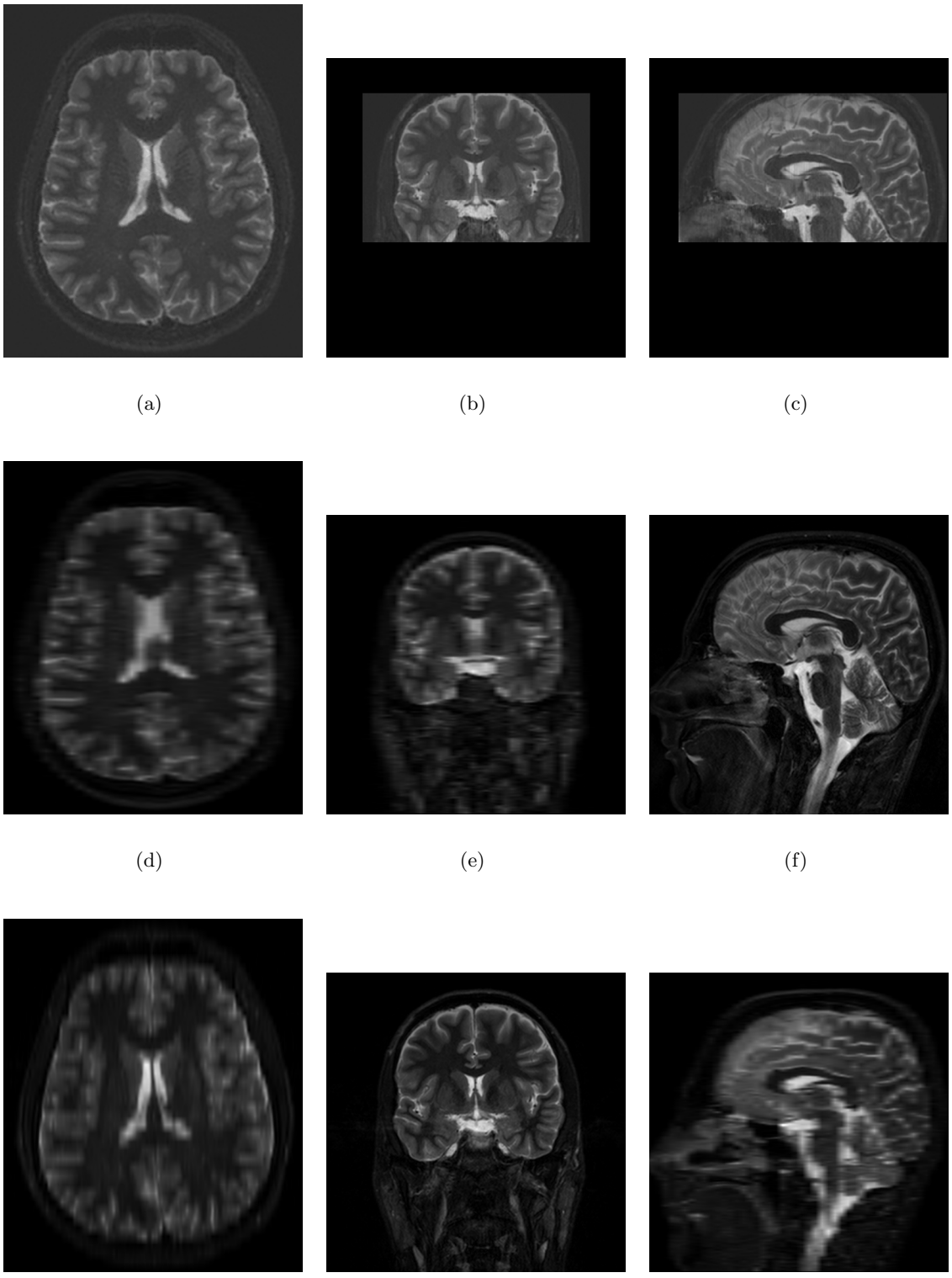

(a) (b) (c)

(d) (e) (f)

(g) (h) (i)

(a) Axial SRR view	(b) Coronal SRR view	(c) Sagittal SRR view
(d) Axial MPR of sagittal LR stack	(e) Coronal MPR of sagittal LR stack	(f) Sagittal original LR slice
(g) Axial MPR of coronal LR stack	(h) Coronal original LR slice	(i) Sagittal MPR of oronal LR stack

Figure 82: In-vivo Study no. 6: (a-c) Axial, coronal, and sagittal views of the SRR using ART (voxel = $0.5 \times 0.47 \times 0.47\ mm^3$) (d-f) Axial, coronal, and sagittal views of a sagittal scan (voxel = $4.8\ mm \times 0.43\ mm \times 0.43\ mm$) (g-i) Axial, coronal, and sagittal views of a coronal scan (voxel = $0.43\ mm \times 4.8\ mm \times 0.43\ mm$).

APPENDIX F

CONDITIONS FOR ALTERNATING MINIMIZATION

The likelihood,

$$p(y|x,v) \propto e^{-\frac{1}{2}(y-H(v)x)^T R(y-H(v)x)}, \tag{194}$$

is to be maximized. Then,

$$\begin{aligned} \hat{x},\hat{v} &= \arg\max_{x,v} p(y|x,v) && (195)\\ &= \arg\min_{x,v} (y-H(v)x)^T R(y-H(v)x). && (196) \end{aligned}$$

We want to show that

$$f(x,v) = (y-H(v)x)^T R(y-H(v)x) \tag{197}$$

converges to a global minimum using the alternating minimization technique based on MS conditions on x and v, given as Algorithm (1) in Chapter 5.2.2:

$$\lim_{l\to\infty} f(\hat{\mathrm{x}}^{(l-1)}, \hat{\mathrm{v}}^{(l-1)}) = \min_{(\mathrm{x},\mathrm{v})} f(x,v). \tag{198}$$

The necessary conditions the alternating minimization algorithm needs to satisfy so that Eq. (198) holds, are as follows [15].

If $\forall \tilde{x} \in \mathbb{R}^{*N\times 1}, \tilde{v} \in \mathbb{R}^{6P\times 1}$

$$\arg\min_x f(x,\tilde{v}) \neq 0, \tag{199}$$

$$\arg\min_v f(\tilde{x},v) \neq 0, \tag{200}$$

then Eq. (198) holds.

If $\arg\min_x f(x,\tilde{v}) = 0$, then equivalently, for any $\tilde{v}$:

$$\begin{aligned} \forall x \neq 0 \quad ||y-H(\tilde{v})(0)|| &\leq ||y-H(\tilde{v})x|| && (201)\\ ||y|| &\leq ||y-H(\tilde{v})x||. && (202) \end{aligned}$$

Since x is the magnitude component and H only has non-negative values (satisfied by the MS conditions) any component in $H(\tilde{v})x$ will be nonnegative and hence any component in $y - H(\tilde{v})x$ will be less than the corresponding component in y. This means $||y|| > ||y - H(\tilde{v})x||$ and thus $\arg\min_x f(x, \tilde{v}) \neq 0$.

Since the motion accompanying MS includes a rigid transformation, its one-to-one mapping with unit Jacobian (see Appendix J) preserves the total energy before and after its warp. That is,

$$\int_\Omega x^2(s)ds = \int_\Omega x^2(A_r s + b_r)ds. \tag{203}$$

This means that the total energy for the projection of x by $H(v)$ for any v is the same as any other $v' \neq v$. That is,

$$||H(v)|| = ||H(v')|| \quad \forall v \neq v'. \tag{204}$$

APPENDIX G

GENERALIZED SAMPLING EXPANSION THEOREM APPLIED FOR MULT-STACK

The corollary on the well-posedness for the generalized sampling expansion (GSE) theorem, given in Chapter (2.4.2), is based on the transfer characteristics of the channels. [7]. The problem of reconstruction using interpolation methods based on the GSE is ill-posed if at least one of the interpolation kernels is not square-integrable. (Ill-posed is the sense that the variance of the reconstruction error is unbounded when noisy samples are used.) The interpolation problem is well-posed if the matrix, $\mathbf{H}(\omega)$, given in Eq. (30) from the GSE theorem has a determinant bounded away from zero over the bandwidth of the true signal. This condition has been directly applied to the set of uniform delays (i.e., sub-pixel shifts with a box point spread function) from the low-resolution images and was shown to be well-posed (see Eq. (36)). We apply here the same corollary on a Multi-Stack sampling configuration needed to evaluate the determinant of $\mathbf{H}(\omega)$. Note however, the Multi-Stack method is 3-D and so the N-D generalized sampling expansion theorem is first stated.

Generalized Sampling Theorem in N Dimensions 1 *A $[\sigma_1, ..., \sigma_N]$-bandlimited square-integrable input signal, $x(\boldsymbol{s}) : \mathbb{C}^N \rightarrow \mathbb{C}$, can be reconstructed from P independent linear shift invariant systems $\{h_r(\boldsymbol{s})\}_{r=1}^{P}$ sampled at $\frac{1}{P}^{th}$ the Nyquist rate along each dimension, i.e., with a diagonal (rectangular) sampling matrix V whose diagonal terms are $\frac{P\pi}{\sigma_i}$ if*

$$\mathbf{H}(\omega_1, \omega_2, ..., \omega_N) = \mathbf{H}(\omega) = \begin{pmatrix} H_1(\omega) & ... & H_P(\omega) \\ H_1(\omega + \boldsymbol{c}) & ... & H_P(\omega + \boldsymbol{c}) \\ \vdots & & \vdots \\ H_1(\omega + (P-1)\boldsymbol{c}) & ... & H_P(\omega + (P-1)\boldsymbol{c}) \end{pmatrix} \tag{205}$$

is non-singular $\forall \omega_i \in [-\sigma_i, -\sigma_i + \frac{2\sigma_i}{P}]$ where $\boldsymbol{c} = [\frac{2\sigma_1}{P}, ..., \frac{2\sigma_N}{P}]$.

If so, then if

$$\Phi(\omega, \boldsymbol{s}) = \begin{pmatrix} \Phi_1(\omega, \boldsymbol{s}) \\ \vdots \\ \Phi_P(\omega, \boldsymbol{s}) \end{pmatrix}, \tag{206}$$

is a solution to

$$\mathbf{H}(\omega)\Phi(\omega, \boldsymbol{s}) = \boldsymbol{b}(\boldsymbol{s}), \tag{207}$$

where

$$\boldsymbol{b}(\boldsymbol{s}) = \begin{pmatrix} 1 \\ e^{j\boldsymbol{c}^T\boldsymbol{s}} \\ \vdots \\ e^{j(P-1)\boldsymbol{c}^T\boldsymbol{s}} \end{pmatrix}, \tag{208}$$

then the r^{th} interpolation kernel is

$$\varphi_r(\boldsymbol{s}) = \frac{P}{2\sigma} \int_{-\sigma_N}^{-\sigma_N+\frac{2\sigma_N}{P}} \cdots \int_{-\sigma_1}^{-\sigma_1+\frac{2\sigma_1}{P}} \Phi_r(\omega, s) e^{j\omega^T\boldsymbol{s}} d\omega_1 \cdots d\omega_N, \qquad r = 1, ..., P. \tag{209}$$

Thus, the original signal is expressed by

$$x(\boldsymbol{s}) = \sum_{r=1}^{P} \sum_{n_1=-\infty}^{\infty} \cdots \sum_{n_N=-\infty}^{\infty} y_r(V\boldsymbol{n})\varphi_r(\boldsymbol{s} - V\boldsymbol{n}), \tag{210}$$

where $\boldsymbol{n} = [n_1, \cdots, n_N]$ and $y_r[\boldsymbol{n}]$ is the output from the r^{th} channel.

According to Brown et al., the $det(\mathbf{H}(\omega))$ must be bounded away from zero for all $\omega_i \in [-\sigma_i, -\sigma_i + \frac{2\sigma_i}{P}]$ if the generalized sampling problem is to be well-posedness [7].

If the slice profile with Fourier transform pair, $h(\mathbf{s}) \leftrightarrow H(\omega)$, undergoes an (invertible) affine transformation, $\mathbf{s} \mapsto \mathrm{A}\mathbf{s} + \mathbf{b}$, then this Fourier pair becomes

$$h(\mathrm{A}\mathbf{s} + \mathbf{b}) \leftrightarrow |\mathrm{A}^{-T}| e^{j2\pi(\mathrm{A}^{-1}\mathbf{b})^T\omega} H(\mathrm{A}^{-T}\omega), \tag{211}$$

where $|.|$ denotes the determinant. Equation (211) can thus be substituted into $det(\mathbf{H}(\omega))$. In general, the i^{th} row, r^{th} column for $\mathbf{H}(\omega)$, from Eq. (205) is

$$[\mathbf{H}]_{ir}(\omega) = H_r(\omega + (i-1)\mathbf{c}). \tag{212}$$

Continuing with the affine transformation, the GSE for the r^{th} channel, (i.e., $h_r(\mathbf{s}) = h(\mathrm{A}_r s + \mathbf{b}_r)$) gives

$$[\mathbf{H}]_{ir}(\omega) = |\mathrm{A}_r^{-T}| e^{j2\pi(\mathrm{A}_r^{-1}\mathbf{b}_r)^T(\omega+(i-1)\mathbf{c})} H(\mathrm{A}_r^{-T}(\omega + (i-1)\mathbf{c})). \tag{213}$$

In the case of Multi-Stack, the linear shift-invariant channels are rotated versions of the same slice excitation profile. This means $\mathrm{A}_r = \mathrm{R}_r$ and $\mathbf{b}_r = 0$. Furthermore, $|\mathrm{R}_r| = 1$ with $\mathrm{R}_r^{-T} = \mathrm{R}_r$, which leads to

$$[\mathbf{H}]_{ir}(\omega) = H(\mathrm{R}_r(\omega + (i-1)\mathbf{c})). \tag{214}$$

The slice profile function, $h(\mathbf{s})$, can be substituted into Eq. (214) for evaluation of its determinant as a function of its frequency, ω. In general, the frequency- and phase-encoding directions in MRI are based on a truncated Fourier series (see Eq. (52)). Therefore, we treat these as separable filters in the frequency spectrum from the slice selection direction so that

$$\begin{aligned} H(\omega) &= H(\omega_{SS}, \omega_{FE}, \omega_{PE}) && (215) \\ &= H_{SS}(\omega_{SS})\Delta k^2 \sum_{n_1=-M_1/2}^{M_1/2-1} \delta(\omega_{PE} - n_1\Delta k) \sum_{n_2=-M_2/2}^{M_2/2-1} \delta(\omega_{FE} - n_2\Delta k), && (216) \end{aligned}$$

where Δk is the sampling distance in $\boldsymbol{k}$-space and SS, FE, and PE denote the slice selection, frequency- and phase-encoding directions, respectively. M_1 and M_2 are the number of samples in frequency- and phase-encoding directions, respectively, and $H_{SS}(\omega_{SS})$ is the frequency response of the slice profile function. Subsituting Eq. (216) into Eq. (214),

$$[\mathbf{H}]_{ir}(\omega) = H_{SS}(\omega_{SS}^{'})\Delta k \sum_{n_1=-M_0/2}^{M_1/2-1} \delta(\omega_{PE}^{'} - n_1\Delta k) \sum_{n_2=-M_0/2}^{M_2/2-1} \delta(\omega_{FE} - n_2\Delta k), \tag{217}$$

where $\omega_{SS}^{'} = \omega_{PE}\sin\theta_r + \omega_{SS}\cos\theta_r$ and $\omega_{PE}^{'} = \omega_{PE}\cos\theta_r - \omega_{SS}\sin\theta_r$. Without further knowledge of the slice profile function, the entries of $\mathbf{H}(\omega)$, and consequently its determinant cannot be simplified to a closed form. However, this derivation can be thus be used as a guideline and starting point for further work using the GSE.

APPENDIX H

LIST OF SYMBOLS

Table 27: Table of symbols.

Variable	Description
$y(\boldsymbol{s})$	low resolution measured image
ρ	proton-density
T_1	longitudinal decay rate of magnetic moment
T_2	transverse decay rate of magnetic moment
T_E	echo time; time between RF excitation and signal acquisition
$\boldsymbol{k}$-space	Fourier space used in MRI sampling
$x(\mathbf{s})$	true image
$\mathbf{x}$	unaliased discrete vector of true image
$\hat{\mathbf{x}}$	estimate vector of true image
P	number of low resolution images
$\mathbf{y}_r$	r^{th} discrete low resolution image lexicographically ordered
D_r	r^{th} down-sampling matrix
C_r	r^{th} blur matrix
F_r	r^{th} warp matrix
$\mathbf{e}_r$	r^{th} vector of measured error
$\mathbf{y}$	discrete vector of all P measured images
H	contribution matrix representing forward process of true image to measured images
M	number of measurements; number of rows in H
N	number of high resolution pixels; number of columns in H
$X(\omega)$	continuous Fourier transform of $x(\mathbf{s})$
$Y_r(\omega)$	continuous Fourier transform of $y(\mathbf{s})$
$h_r(\mathbf{s})$	point spread function of r^{th} image; synonymous with slice profile function
$H_r(\omega)$	continuous Fourier transform of $h_r(\mathbf{s})$
σ	bandwidth of $x(s)$
σ_i	i^{th} singular value of H (sorted in descending order)
$\mathbf{Y}_r^s[l]$	r^{th} discrete Fourier transform of $\mathbf{y}$
δ	step parameter in constructing H
ϕ_r	r^{th} phase offset in $h_r(\mathbf{s})$
φ_r	r^{th} interpolation kernel for reconstruction of $x(\mathbf{s})$
$\mathbf{H}(\omega)$	system matrix from the Generalized Sampling Expansion
$p(\mathbf{x})$	probability distribution function prior for high resolution image
$\mathbf{v}$	motion parameters of low resolution images
R_r	r^{th} rotation matrix for Multi-Stack
V	diagonal sampling matrix in Multi-Stack
Ω	region of support in the high resolution image or set of Fourier samples
S_j	space for the j^{th} voxel of $\mathbf{x}$
$\mathsf{N}(0, \sigma_e^2)$	Normal/Gaussian distribution with zero mean and variance σ_e^2 for measurement noise
$h(\mathbf{x})$	entropy of a random variable, $\mathbf{x}$
e_{NMSE}	normalized mean square error of estimate and true image
A_r	rotation matrix for the r^{th} low resolution image
$\mathbf{b}_r$	translation vector for the r^{th} low resolution image
$\mathbf{v}_r$	rigid motion vector of r^{th} low resolution image
$\mathbf{v}$	concatenated motion vectors of $\mathbf{v}_r$
Σ	diagonal matrix of non-increasing singular values, σ_i, of H
U	ortho-normal matrix with left singular vectors of H
V	ortho-normal matrix with right singular vectors of H
L	matrix from Gibbs Prior to stabilize estimate of $\mathbf{x}$
λ	strength of stability operator

APPENDIX I

LIST OF ACRONYMS

Table 28: List of Acronyms.

Acronym	Phrase
AM	alternating minimization
ART	algebraic reconstruction technique
CFT	continuous Fourier transform
CT	computed tomography
DFT	discrete Fourier transform
E&F	Elad and Feuer
FWHM	full width at half maximum
FSE	Fast Spin Echo
GSE	Generalized Sampling Expansion
HR	high resolution
HRI	high resolution image
IBP	iterative back-projection
IID	independent and identically distributed
IR	Inversion Recovery
LR	low resolution
LRI	low resolution image
LRS	low resolution scan
LSI	linear shift-invariant
MAP	maximum a posterior
MART	multiplicative algebraic reconstruction technique
ML	maximum-likelihood
MOTSA	multiple overlapping thick slab acquisition
MPR	multi-planar reformat
MRI	magnetic resonance imaging
MS	Multi-Stack
N/A	not available
NMSE	normalized mean square error
PDF	probability density function
POCS	projection onto convex sets
PS	parallel-stack
PSF	point-spread function
RF	radio frequency
RV	random variable
SART	simultaneous algebraic reconstruction technique
SLP	Shepp-Logan phantom
SNR	signal-to-noise ratio
SR	super-resolution
SRR	super-resolution reconstruction
SVD	singular value decomposition
SVE	singular value expansion

APPENDIX J

CHANGE OF REGISTRATION VARIABLES IN MULTI-STACK

Accounting for rigid motion, the MS model is

$$y_r[\mathbf{n}] = \int_{\Omega} x(\mathrm{A}_r\mathbf{s} + \mathbf{b}_r)h(\mathrm{R}_r(\mathbf{s} - \mathrm{V}\mathbf{n}))d\mathbf{s} + e_r[\mathbf{n}], \tag{218}$$

where $\{\mathrm{A}_r, \mathbf{b}_r\}_{r=1}^{P}$ are the motion parameters. Letting,

$$\mathbf{s}^{'} = \mathrm{A}_r\mathbf{s} + \mathbf{b}_r, \tag{219}$$

$$\mathbf{s} = \mathrm{A}_r^{-1}(\mathbf{s}^{'} - \mathbf{b}_r), \tag{220}$$

the derivative is

$$\begin{aligned} \frac{d\mathbf{s}}{d\mathbf{s}^{'}} &= (\mathrm{A}_r^{-1})^T & (221)\\ d\mathbf{s} &= |(\mathrm{A}_r^{-1})^T|d\mathbf{s}^{'} & (222)\\ &= d\mathbf{s}^{'}. & (223) \end{aligned}$$

Substituting Eq. (219) into the PSF argument from Eq. (218) gives

$$\mathrm{R}_r(\mathbf{s} - \mathrm{V}\mathbf{n}) = \mathrm{R}_r(\mathrm{A}_r^{-1}\mathbf{s}^{'} - (\mathrm{A}_r^{-1}\mathbf{b}_r + \mathrm{V}\mathbf{n})). \tag{224}$$

Hence,

$$y_r[\mathbf{n}] = \int_{\Omega} x(\mathbf{s}^{'})h(\mathrm{R}_r(\mathrm{A}_r^{-1}\mathbf{s}^{'} - (\mathrm{A}_r^{-1}\mathbf{b}_r + \mathrm{V}\mathbf{n})))d\mathbf{s}^{'} + e_r[\mathbf{n}], \tag{225}$$

and the new contribution of the ij^{th} in entry H becomes

$$[\mathrm{H}]_{ij} = \int_{S_j} h(\mathrm{R}_r(\mathrm{A}_r^{-1}\mathbf{s} - (\mathrm{A}_r^{-1}\mathbf{b}_r + \mathrm{V}\mathbf{n})))d\mathbf{s}. \tag{226}$$

The warp, convolution, and down-sampling applied directly to $x(\mathbf{s})$ gives

$$y_r[\mathbf{n}] = \int_{\Omega} x(\mathrm{A}_r(\mathrm{R}_r^{-1}\mathbf{s} + \mathrm{V}\mathbf{n}) + \mathbf{b}_r)h(\mathbf{s})d\mathbf{s}. \tag{227}$$

APPENDIX K

GRADIENT OF REGISTRATION PARAMETERS IN MULTI-STACK

$$p(\mathbf{y}|\mathbf{x},\mathbf{v}) = \frac{1}{\sqrt{(2\pi)^M |det(\mathbf{R_{ee}})|}} e^{-\frac{1}{2}(\mathbf{y}-\mathbf{H(v)x})^T \mathbf{R_{ee}}^{-1}(\mathbf{y}-\mathbf{H(v)x})}. \tag{228}$$

For ease of notation let

$$f(v) = e^{-(y-H(v)x)^T R(y-H(v)x)} : \mathbb{R}^{P\times 1} \rightarrow \mathbb{R} \tag{229}$$

where $v \in \mathbb{R}^{P\times 1}$ and $H(v) : \mathbb{R}^{P\times 1} \rightarrow \mathbb{R}^{M\times N}$. We want to find the value of v that minimizes $f(v)$.

$$\nabla_v f(v) : \mathbb{R}^{P\times 1} \rightarrow \mathbb{R}^{P\times 1} \tag{230}$$

This will involve computing $\nabla_v H(v)$, which is a matrix-valued function that has a matrix-valued argument that results in a tensor $\nabla_v H(v) : \mathbb{R}^{MP\times N}$

$$\nabla_v H(v) = \tag{231}$$

compute $\nabla_v f(v)$:

$$\nabla_v f(v) \quad = \quad e^{-(y-H(v)x)^T R(y-H(v)x)} \nabla_v \left(-(y-H(v)x)^T R(y-H(v)x)\right) \tag{232}$$

REFERENCES

[1] "http://www.uni.edu/walsh/basalganglia-2.jpg,"

[2] Atasoy, H., Nuyan, O., Tunc, T., Yorubulut, M., Unal, A., and Inan, L., "T2-weighted MRI in Parkinson's disease; Substantia Nigra Pars Compacta Hypointensity Correlates with the Clinical Scores," *Neurol India*, vol. 52, pp. 332–337, 2004.

[3] Avriel, M., *Nonlinear Programming: Analysis and Methods*. Dover Publishing, 2003.

[4] Basser, P., Pajevic, S., Pierpaoli, C., Duda, J., and Aldroubi, A., "In-vivo Fiber Tractography using DT-MRI Data," *Mag Reson Med*, vol. 44, pp. 625–32, 2000.

[5] Bernstein, M., Thomasson, D., and Perman, W. H., "Improved Detectability in Low Signal-to-noise Ratio Magnetic Resonance Images by Means of a Phase-corrected Real Reconstruction," *Med. Phys.*, vol. 16, pp. 813–817, 1989.

[6] Borman, S., Robertson, M., and Stevenson, R. L., "Block-matching Sub-pixel Motion Estimation from Noisy, Under-sampled Frames - an Empirical Performance Evaluation," in *In SPIE Visual Communications and Image Processing*, pp. 1442–1451, 1999.

[7] Brown, J. and Sa-Ngsari, K., "Sampling Reconstruction of N-dimensional Band-limited Images After Multilinear Filtering," *IEEE Transactions on Circuits and Systems*, vol. 36, pp. 1025–1038, 1989.

[8] Brummer, M., Mersereau, R., Eisner, R., and Lewine, R., "Automatic Detection of Brain Contours in MRI Data Sets," *IEEE Trans. Med. Imag.*, vol. 12, pp. 153–166, 1993.

[9] Byrne, C., "Iterative Image Reconstruction Algorithms Based on Cross-entropy Minimization," *IEEE Transactions on Image Processing*, vol. 2, pp. 96–103, 1993.

[10] Carmi, E., Liub, S., Alona, N., Fiata, A., and Fia, D., "Resolution Enhancement in MRI," *Magnetic Resonance Imaging*, vol. 24, pp. 133–154, 2006.

[11] Cheung, K., "A Multidimensional Extension of Papoulis Generalized Sampling Expansion with the Application in Minimum Density Sampling in Advanced Topics in Shannon Sampling and Interpolation Theory," 1993.

[12] Cheung, K. and R.J. Marks, I., "Ill-posed Sampling Theorems," *IEEE Transactions on Circuits and Systems*, vol. 32, pp. 481–484, 1985.

[13] Chung, J., Haber, E., and Nagy, J., "Numerical Methods for Coupled Super-resolution," *Inverse Problems*, vol. 22, pp. 1261–1272, 2006.

[14] Chung, J., J., J. N., and O'Leary, D., "A Weighted GCV Method for Lanczos Hybrid Regularization," *Technical Report Mathematics and Computer Science Emory University*, vol. TR-2007-004-A, pp. 1–14, 2007.

[15] Csiszar, I. and Tusnady, G., "Information Geometry and Alternating Minimization Procedures," *Statistics and Decisions, Supplement Issue*, vol. 1, pp. 205–237, 1984.

[16] Davis, W., Blatter, D., Harnsberger, H., and Parker, D., "Intracranial MR Angiography: Comparison of Single-volume Three-dimensional Time-of-flight and Multiple Overlapping Thin Slab Acquisition Techniques," *American Journal of Roentgenology*, vol. 163, pp. 915–920, 1994.

[17] DeSabata, A., "Extension of a Finite Version of the Sampling Theorem," *IEEE Transactions on Circuits and Systems*, vol. 41, pp. 821–823, 1994.

[18] DiBella, E., Barclay, A., Eisner, R., and Schafer, R. W., "A Comparison of Rotation-based Methods for Iterative Reconstruction Algorithms," *IEEE Transactions on Nuclear Science*, vol. 43, pp. 3370–3376, 1996.

[19] Drayer, B., "Magnetic Resonance Imaging and Extrapyramidal Movement Disorders," *Eur Neurol*, vol. 29, pp. 9–12, 1989.

[20] Duyn, J., "High-Speed Interlaced Spin-Echo Magnetic Resonance Imaging," *Magn Reson Med*, vol. 43, pp. 905–908, 2000.

[21] Eggermont, P. and Lent, G. H. A., "Iterative Algorithms for Large Partitioned Linear Systems, with Applications to Image Reconstruction," *Linear Algebra and its Applications*, vol. 40, pp. 37–67, 1981.

[22] Elad, M. and Feuer, A., "Restoration of a Single Superresolution Image from Several Blurred, Noisy and Undersampled Measured Images," *IEEE Trans Image Process*, vol. 6, p. 1646 to 1658, 1997.

[23] Feuer, A., "On the Necessity of Papoulis Result for Multidimensional GSE," *IEEE Signal Processing Letters*, vol. 11, no. 4, 2004.

[24] Fischer, H. and Ladebeck, R., *Echo-planar Imaging, Theory, Technique and Application*. Springer Verlag, 1998.

[25] Goelman, G., "Fast 3D T2-weighted MRI with Hadamard Encoding in the Slice Select Direction," *Magn Reson Imag*, vol. 18, p. 939 to 945, 2000.

[26] Golub, G. H. and Loan, C. F. V., *Matrix Computations*. second ed., 1989.

[27] Greenspan, H., Oz, G., Kiryati, N., and Peled, S., "MRI Inter-slice Reconstruction using Super-resolution," *Magnetic Resonance Imaging*, vol. 20, pp. 437–446, 2002.

[28] Hacke, W. and Warach, S., "Diffusion-weighted MRI as an Evolving Standard of Care in Acute Stroke," *Neurology*, vol. 54, p. 1548 to 1549, 2000.

[29] Hardie, R., Barnard, K., and Armstrong, E., "Joint MAP Registration and High-resolution Image Estimation using a Sequence of Undersampled Images," *IEEE Transactions on Image Processing*, vol. 6, p. 16211633, 1997.

[30] Herment, A., Roullot, E., Bloch, I., Jolivet, O., Cesare, A. D., Frouin, F., Bittoun, J., and Mousseaux, E., "Local Reconstruction of Stenosed Sections of Artery Using Multiple MRA Acquisitions," *Magnetic Resonance in Medicine*, vol. 49, pp. 721–742, 2003.

[31] Hounsfield, G. N., "A Method of and Apparatus for Examination of a Body by Radiation such as X-ray or Gamma Radiation," *Patent Specification 1283915 , The Patent Office*, 1972.

[32] Huang, T. and Tsay, R., "Multiple Frame Image Restoration and Registration," *Advances in Computer Vision and Image Processing*, vol. 1, p. 317 to 339, 1984.

[33] Ibanez, L., Schroeder, W., Ng, L., Cates, J., and Hamming, R., "The ITK Software Guide," 2005.

[34] Idier, J. and Giovannelli, J., "Regularized Estimation of Mixed Spectra Using a Crcular GibbsMarkov Model," *IEEE Trans. Signal Processing*, vol. 49, pp. 2201–2213, 2001.

[35] Irani, M. and Peleg, S., "Motion Analysis for Image Enhancement: Resolution, Occlusion, and Transparency," *J Vis Comm Image Rep*, vol. 4, no. 4, pp. 324–35, 1993.

[36] Jerri, A., "The Shannon Sampling Theorem-Its Various Extensions and Applications: A Tutorial Review," *Proc. IEEE*, vol. 65, p. 1565, 1977.

[37] Jiang, M. and Wang, G., "Convergence of the Simultaneous Algebraic Reconstruction Technique," *IEEE Transactions on Image Processing*, vol. 12, pp. 957–961, 2003.

[38] Kak, A. C. and Slaney, M., *Principles of Computerized Tomographic Imaging*. IEEE Press, 1988.

[39] Katsaggelos, A., Molina, R., and Mateos, J., *Super Resolution of Images and Video*. Morgan and Claypool, 2007.

[40] Kelley, D. and Schenck, J., "Very-high-field Magnetic Resonance Imaging: Instrumentation and Safety Issues," *Top Magn Reson Imaging*, vol. 10, 1999.

[41] Kim, S., Bose, N., and Valenzuela, H., "Recursive Reconstruction of High Resolution Image from Noisy Undersampled Multiframes," *IEEE Transactions on Acoustics Speech and Signal Processing*, vol. 38, no. 6, pp. 1013–27, 1990.

[42] Lasserre, J. and Zeron, E., "A Laplace Transform Algorithm for the Volume of a Convex Polytope," *Journal of the ACM*, vol. 48, pp. 1126–1140, 2001.

[43] Lent, A., Herman, G., and Lutz, P., "Relaxation Methods for Image Reconstruction," *Commun. ACM*, vol. 21, pp. 152–158, 1978.

[44] Liang, Z. and Lauterbur, P., *Magentic Resonance Imaging: A Signal Processing Perspective*. IEEE Press, 2000.

[45] Liu, K., Xu, Y., and Loncar, M., "Reduced Slab Boundary Artifact in Multi-slab 3D Fast Spin-echo Imaging," *Magnetic Resonance in Medicine*, vol. 44, pp. 269–276, 2000.

[46] Mailloux, G., Noumeir, R., and Lemieux, R., "Deriving the Multiplicative Algebraic Reconstruction Algorithm (MART) by the Method of Convex Projections (POCS)," *IEEE International Conference on Acoustics, Speech, and Signal Processing*, vol. 5, pp. 457–460, 1993.

[47] Nguyen, N., *Numerical Algorithms for Superresolution*. PhD thesis, Stanford University, 2001.

[48] Oh, C., Hilal, S., Wu, E., and Cho, Z. H., "Phasescrambled RF Excitation for 3D Volume Selective Multislice NMR Imaging," *Magn Reson Med*, vol. 28, p. 290 to 299, 1992.

[49] Oppenheim, A., Schafer, R., and Buck, J., *Discrete-time Signal Processing*. Prentice-Hall, 1999.

[50] Pan, T. and Yagle, A., "Numerical Study of Multigrid Implementations of Some Iterative Image Reconstruction Algorithms," *IEEE Transactions on Medical Imaging*, vol. 10, pp. 572–588, 1991.

[51] Papoulis, A., "A New Algorithm in Spectral Analysis and Band-limited Extrapolation," *IEEE Transactions on Circuits Syst*, vol. 9, pp. 735–742, 1975.

[52] Papoulis, A., "Generalized Sampling Expansion," *IEEE Trans. Circuit Syst.*, vol. 11, pp. 652–654, 1977.

[53] Park, S., Park, M., and Kang, M., "Super-Resolution Image Reconstruction: A Technical Overview," *IEEE Signal Processing Magazine*, pp. 21–36, 2003.

[54] Parker, D., Yuan, C., and Blatter, D., "MR Angiography by Multiple Thin Slab 3-D Acquisition," *Magn. Reson. Med.*, vol. 17, pp. 434–451, 1991.

[55] Patti, A., Sezan, M., and Teklap, A., "High-resolution Image Reconstruction from a Low-resolution Image Sequence in the Presence of Time-varying Motion Blur," in *Proc. ICIP*, pp. 343–347, IEEE, 1994.

[56] Peeters, R., Kornprobst, P., Nikolova, M., Sunaert, S., Vieville, T., Malandain, G., Deriche, R., Faugeras, O., and Hecke, M. N. P., "The Use of Superresolution Techniques to Reduce Slice Thickness in functional MRI," *Int. J. Imaging Syst. Technol.*, 2004.

[57] Peled, S. and Yeshurun, H., "Superresolution in MRI: Application to Human White Matter Fiber Tract Visualization by Diffusion Tensor Imaging," *Magn Reson Med*, vol. 45, pp. 29–35, 2001.

[58] Pickup, L., Capel, D., Roberts, S., and Zisserman, A., "Bayesian Image Superresolution, Continued," in *Advances in Neural Information Processing Systems*, Dec. 2006.

[59] Pickup, L., Roberts, S., and Zisserman, A., "Optimizing and Learning for Superresolution," in *Proceedings of the British Machine Vision Conference*, 2006.

[60] Piegl, L. and Tiller, W., *The NURBS Book*. Springer, 1997.

[61] Pruessmann, K., Weiger, M., Scheidegger, M., and Boesiger, P., "SENSE: Sensitivity Encoding for Fast MRI," *Magnetic Resonance in Medicine*, vol. 42, pp. 952–962, 1999.

[62] Reich, C., Hudgins, P., Sheppard, S., Starr, P., and Bakay, R., "A High-resolution Fast Spin-echo Inversion-recovery Sequence for Preoperative Localization of the Internal Globus Pallidus," *AJNR Am J Neuroradio*, vol. 21, pp. 928–931, 2000.

[63] Rochefort, G., Champagnat, Besnerais, G. L., and Giovannelli, J., "An Improved Observation Model for Super-resolution Under Affine Motion," *IEEE Transactions on Image Processing*, vol. 15, pp. 3325–3337, 2006.

[64] Rosenow, J., Mogilner, A., Ahmed, A., and Reza, A., "Deep Brain Stimulation for Movement Disorders," *Neurological Research*, vol. 26, pp. 9–20, 2004.

[65] Ross, S., *A First Course in Probability*. Prentice-Hall, 1996.

[66] Roullot, E., Herment, A., Bloch, M., Nikolova, M., and Mousseaux, E., "Regularized Reconstruction of 3D High-resolution Magnetic Resonance Images from Acquisitions of Anisotropically Degraded Resolutions," *Proc Int Conf Image Process*, vol. 3, pp. 350–353, 2000.

[67] Sauer, K. and Allebach, J., "Iterative Reconstruction of Band-limited Images from Non-uniformly Spaced Samples," *IEEE Trans. Circuits Syst.*, vol. 34, pp. 1497–1505, 1987.

[68] Scheffler, K., "Superresolution in MRI?," *Magn Reson Med*, vol. 48, p. 408, 2002.

[69] Shilling, R. and Brummer, M., "An Experimental Comparison of Super-resolution Techniques in 2-D Multi-slice MRI.," in *International Society in Magnetic Resonance in Medicine*, 2008.

[70] Shilling, R., Mewes, K., and Brummer, M., "Merging Multiple Multiple Stacks MRI into a Signal Data Volume," in *IEEE International Symposium on Biomedical Imaging*, 2006.

[71] Shilling, R., Ramamurthy, S., and Brummer, M., "Sampling Strategies for Super-Resolution in Multi-slice MRI," in *IEEE International Conference on Image Processing*, 2008.

[72] Shilling, R., Robbie, T., Bailloeul, T., Mewes, K., Mersereau, R. M., and Brummer, M., "A Super-resolution Framework for 3-D High Resolution and High Contrast Imaging Using 2-D Multi-slice MRI," *Accepted and to appear in IEEE Transactions on Medical Imaging*.

[73] Sijbers, J., den Dekker, A. J., Scheunders, P., and Dyck, D. V., "Maximum Likelihood Estimation of Rician Distribution Parameters," *IEEE Trans. Med. Imag.*, vol. 17, pp. 357 – 361, 1998.

[74] Stark, H. and Oskoui, P., "High Resolution Image Recovery from Image- plane Arrays, using Convex Projections," *J. Opt. Soc. Am. A*, vol. 6, pp. 1715–1726, 1989.

[75] Starr, P., Christine, C., Theodosopoulos, P., Lindsey, N., Byrd, D., Mosley, A., and Marks, W., "Implantation of Deep Brain Stimulators into the Subthalamic Nucleus: Technical Approach and Magnetic Resonance Imaging," *J Neurosurg*, vol. 97, pp. 370–387, 2002.

[76] Stergiopoulos, S., *Advanced Signal Processing Handbook: Theory and Implementation for Radar, Sonar, and Medical Imaging Real-Time Systems*. CRC Press, 2001.

[77] Tekalp, A., Ozkan, M., and Sezan, M., "High-resolution Image Reconstruction from Lower-resolution Image Sequences and Space Varying Image Restoration," in *Proc. IEEE Int. Conf. Acoustics, Speech and Signal Processing*, vol. 3, pp. 169–172, IEEE, 1992.

[78] Tenorio, L., "Statistical Regulaization of Inverse Problems," *SIAM Review*, vol. 43, pp. 346–366, 2001.

[79] Tipping, M., Bishop, C., Thrun, S., Becker, S., and Obermayer, K., *Advances in Neural Information Processing Systems*. MIT Press, 2003.

[80] Torrey, H., "Bloch Equations with Diffusion Terms," *Phys. Rev.*, vol. 140, pp. 563–565, 1956.

[81] Ur, H. and Gross, D., "Improved Resolution from Subpixel Shifted Pictures," *CVGIP: Graphical Models and Image Processing*, vol. 54, p. 1816, 1992.

[82] Vitek, J., Bakay, R., Hashimoto, T., Kaneoke, Y., Mewes, K., Zhang, J., Rye, D., Starr, P., Baron, M., Turner, R., and Delong, M., "Microelectrode-guided Pallidotomy: Technical Approach and its Application in Medically Intractable Parkinson's Disease," *J Neurosurg*, vol. 88, pp. 1027–1043, 1998.

[83] Wang, Y. and Lei, T., "Statistical Analysis of MR Imaging and its Applications in Image Modeling," *Proceedings of the IEEE International Conference on Image Processing and Neural Networks*, vol. I, pp. 866–870, 1994.

[84] Wells, W., Viola, P., Atsumi, H., Nakajima, S., and Kikinis, R., "Multi-modal Volume Registration by Maximization of Mutual Information," 1996.

[85] Yu, H., Zhao, S., and Wang, G., "A Differentiable Shepp-logan Phantom and its Applictions in Exact Cone-bean CT," *Physics in Medicine and Biology*, vol. 50, pp. 5583–5595, 2005.

VITA

Richard Z. Shilling grew up in Lancaster, Pennsylvania and Niskayuna, New York and received the Bachelor of Science (with high distinction) degrees in Computer Engineering and Mathematics from the Pennsylvania State University, State College, PA in 1998. He received his Masters of Science in Electrical Engineering at the Georgia Institute of Technology in 2003. He has worked for several companies including General Electric Research and Development, I.B.M., Kulicke and Soffa, Emory University, and Lincoln Laboratories at the Massachusetts Institute of Technology. He has worked under the direction of Dr. Marijn Brummer of Emory University for his doctoral studies for which he will receive the Ph.D. degree in Electrical and Computer Engineering at the Georgia Institute of Technology in May 2009. He has published a journal paper, three conference papers and presented a talk on super-resolution for MRI at a major image processing conference.